Engineering the Multi-Length Scale Structure of Self-Assembled Conjugated Polymer Networks

Gregory Matthew Newbloom

A dissertation

submitted in partial fulfillment of the

requirements for the degree of

Doctor of Philosophy

University of Washington

2014

Reading Committee:

Lilo D. Pozzo, Chair

Samson A. Jenekhe

Jim Pfaendtner

Stuart B. Adler

Program Authorized to Offer Degree:

Chemical Engineering

University of Washington

Abstract

Engineering the Multi-Length Scale Structure of Self-Assembled Conjugated Polymer Networks

Gregory Matthew Newbloom

Chair of the Supervisory Committee:
Dr. Lilo D. Pozzo

Department of Chemical Engineering

Conjugated polymers are a Nobel Prize winning class of materials known for their intrinsic semi-conducting properties and have been used in applications as diverse as organic-based solar cells, transistors, light emitting diodes, sensors and thermoelectric devices. These applications have varying, but optimized, structure and property requirements which often include an interconnected network of conjugated polymers to transport charge. In this work, self-assembly and gelation are explored as a platform to engineer the multi-length scale structure of conjugated polymer networks. A detailed understanding is developed through structural characterization of each stage of the self-assembly process: dissolved polymer, semi-crystalline fiber, fibrillar branching and percolated network formation. Variations in self-assembly conditions were utilized to develop multi-length scale structure-property relationships. Furthermore, a new method to directly incorporate these fibrillar network structures into thin films for organic electronics is discussed. This dissertation will demonstrate our work towards understanding the mechanisms behind conjugated polymer self-assembly in order to provide robust design parameters that can be tuned to generate specific structures, occurring on multiple length scales, and relevant properties for a diversity of applications.

Table of Contents

List of Figures

Figure **Page**

List of Tables

Acknowledgements

I appreciate the countless hours of teaching and mentorship that my advisor, Prof. Lilo Pozzo, has provided to me over the last five years. Her passion for science is contagious and her depth of expertise has pushed me far beyond what I expected when I first joined her group. Thank you to my committee members: Prof. Sam Jenekhe, Prof. Stu Adler, Prof. Jim Pfaendtner and Prof. Amy Shen for your advice over the years.

I am lucky to have collaborated with many talented researchers. Specifically, I would like to thank Dr. Kathleen Weigandt, Pablo de la Iglesia, Prof. Christine Luscombe, Prof. Felix Kim, Dr. Selvam Subramaniyan, Dr. Alpana Ranade, Dr. Marvi Matos, and Stephanie Hoffman for their substantial contributions to this work. I would also like to thank the instrument scientists at NIST and ILL for their help in executing and analyzing our SANS experiments, specifically Dr. Lionel Porcar, Dr. Paul Butler, Dr. Yun Liu, Dr. Matthew Wasbrough and Dr. Jae-Hi Cho. I also appreciate the efforts of my many undergraduate researchers including Aaron West and Andrew Amodei, who took their projects beyond what was expected of them. I am also thankful to the Department of Energy and the National Science Foundation IGERT program for the funding to complete this work.

Finally, I would also like to thank all of the other Pozzo Group Members, including Dr. Kjersta Larson-Smith, Dr. Monica Ospinal-Jimenez, Jeff Richards, Michael Lombardo, Kiran Kanekal and Yuyin Xi for their help through the years. From technical insights to coffee every morning, I could not and would not have wanted to do it without you.

Dedication

To my Lord and Savior, Jesus Christ, who rescued my life because of His immeasurable love.

No words can express the constant need I have for you.

Philippians 2:5-11

And to my wife, Jenny, for her friendship and unwavering support.

Chapter 1

Motivation & Introduction

1.1 The Importance of Tunable Networks Structures

The term "network structure" represents a broad range of morphologies that are present in many material classes. The ability to design multi-length scale features of network structures is critical for their implementation in a variety of applications. In tissue engineering, there is a need to design network scaffolds that can mimic the structure of collagen. In this example, the structure of the network is critical for cell attachment, proliferation and functionality which ultimately determines the effectiveness of the tissue.[1] On the other hand, in water filtration applications there is a need to balance the morphology with the strength of the network. This comes from the requirement for selective transportation of water through nanometer to micrometer sized pores under high pressure conditions.[2] All of this is in contrast with a transportation industry that is engineering light-weight composite materials and has found a need for electrically percolating networks that can be used for static dissipation applications. In this example, it is often carbon nanotubes or metallic nanoparticles that are suspended in a polymer

matrix to form an interconnected and electrically percolating network structure.[3, 4] These examples represent only a tiny fraction of the diversity and applications of network structures.

1.2 Types and Qualities of Different Networks

It is important to understand the relevant structural features of tunable networks, even though a diversity of structures and properties can be difficult to generalize. On a fundamental level, networks allow for the transfer of a material or property over a designated length scale through an interconnected material within a secondary medium (e.g., air, water and polymer). An example of this can be seen in Figure 1.1.

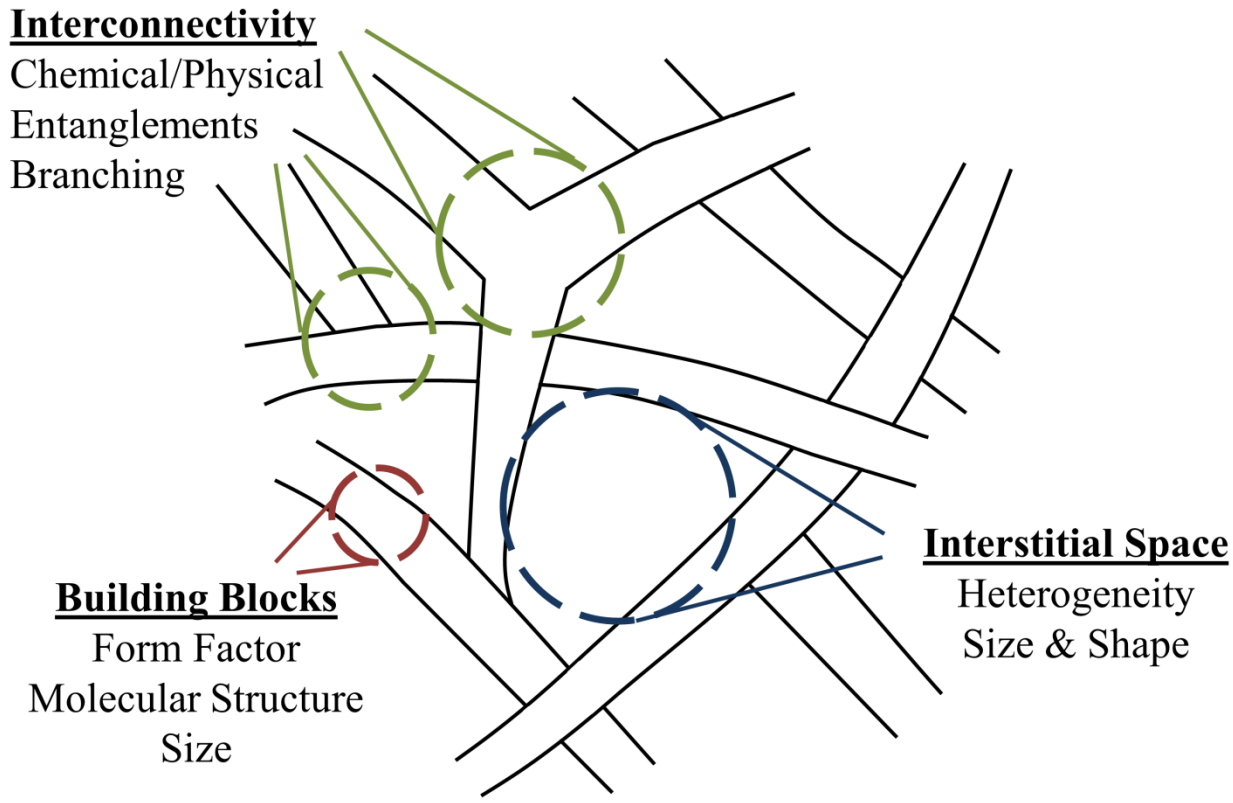

Figure 1.1 – Diagram of a nondescript network structure highlighting various designable material and structural features

There are three fundamental categories that can be used to summarize many of the features within network structures: building blocks, interconnectivity and interstitial space. Often these features can exist on multiple size scales. For example, in a carbon nanotube networks the diameter of the carbon nanotubes (i.e., building block feature) can be between 1-10 nm, while the physical overlaps between the nanotubes (i.e., interconnectivity feature) can exist over several centimeters.[3] While each of these features plays a critical role in network functionality, the relationship between features can often play as significant of a role.

Figure 1.1 points to form factor, molecular structure and size as three examples of the building block feature within a tunable network structure. A larger network structure can be assembled from smaller components of virtually any form factor. For example, polymer functionalized spherical gold nanoparticles have been reported to self-assemble into rod-like structures to form an interconnected network.[5] It is actually quite common for networks to be based on either intrinsically or self-assembled rod-like form factors (e.g., cylinders[3, 6, 7] and parallelpipedons[8-11]). Individual polymer chains also represent a large subsection of network building blocks. These form factors are useful when assembling mesh-like structures and have been utilized successfully to generate "double-network structures" with extremely high mechanical strength.[12, 13] These double network structures utilize the combination of a highly cross-linked polymer network with a non-cross-linked network in order to achieve properties not obtainable with a single network structure. Tunable network structures can even be made from the self-assembly of small molecules (such as GP-1), which assemble into fiber-like structures.[14, 15]

In addition to a variety of form factors, the building block feature of networks often incorporates functionality required for specific applications. These are often achieved through

the molecular structure of the material choice. For example, catalytic activity is possible for metal-organic frameworks (MOFs), which utilize a combination of "metal ions" and ligands to construct a tunable, 3-dimensional network structure.[16] *In vivo* applications require materials to be biologically compatible, which substantially limits the options for network design. However, many biocompatible polymers have been found to form network structures, including poly(ethylene glycol) derivatives[17] and zwitterionic polymers[18]. Networks for organic electronics require both light absorption and the ability to transport charges over length scale between 100 nm - 10 μm. Often conjugated polymers are utilized towards this end and have been shown to form branching fibrillar organogels as well as networks of entangled polymer chains.[10, 19]

The size of the building block is also largely dictated by the application. Currently, many fields are moving towards nanometer scale building blocks.[3, 7, 8, 10, 12, 13, 17] However, networks made from much larger building blocks (millimeter size scale) are already being utilized commercially in applications such as carbon fiber networks in reinforced cement.[6]

Figure 1.1 highlights another crucial feature in tunable network structures: interconnectivity. The interconnectivity of the network structure plays a substantial role in the transportation of material or properties (e.g., stress and electrical charges) over a designated length scale. The largest distinction is whether the network is of chemical or physical nature. Chemical networks rely on covalent bonds to create connectivity within the network structure. In contrast, a physical network relies on Van der Waals forces, hydrogen bonding or electrostatic interactions between building blocks to create an interconnected structure. Chemical networks are the result of a reaction process and therefore polymer-based meshes tend to be a common type of chemical network. These meshes often rely on branched polymers or oligomers to create the interconnectivity and define the mesh size.[12, 13] Examples of physical networks depend

largely on the building block features. In one case, a small molecule organogellator (such as GP-1) formed aggregated network structures via Van der Waals interactions that drive a self-assembly process.[15] Likewise the hydrogen bonding of water and electrostatic interactions between surfactants are some of the driving forces for the self-assembly of wormlike micelle systems that can forms network structures over large length scales.[7]

Two more specific interconnectivity features of physical networks are entanglements and branching. Entanglements are the overlapping, or physical contacts, of self-similar building blocks that allows for the transport of a material or properties over a given length scale. This behavior tends to arise in systems that have high aspect ratio building blocks (Aspect ratio = Length/Diameter). In carbon nanotube composite networks, the physical contact of multiple nanotubes allows for the transport of charges through an otherwise non-conducting polymer matrix.[3] Branching, or bifurcations, can occur in systems where the building block is molecularly branched (i.e., branched polymers) or in systems where the building blocks self-assemble. In the case of self-assembly, branching typically arises from a mismatch in the self-assembly process that allow for a splitting of the building block during formation. Liu and coworkers have adapted the Avrami theory for phase change to mathematically describe the process of branching for the small molecule organogellator GP-1.[15, 20, 21]

Some researchers are also utilizing novel methods to push the boundaries of engineering the interconnectivity feature of network structures. Hoyle and coworkers used thiol-ene reactions to generate polymer mesh structures with nearly defect-free network structures.[22] These "near-perfect" network structures allow hydrogels to approach their theoretical maximum strain limits and allow for a better understanding of intrinsic material properties.[23] Hillhouse and coworkers created double gyroid network structures by controlling the curvature of a silica-surfactant

interface upon self-assembly.[24] These highly porous network structures can be electrochemically coated with other semiconductors to form high efficiency photovoltaic and thermoelectric devices. Furthermore, inorganic network structures have also been formed by using the core of self-assembled surfactant networks as nanoreactors.[25] In this example, the network structure of the organic phase is used to "template" the structure of the inorganic phase and allows for the engineering of interconnected inorganic network structures using colloidal principles.

Figure 1.1 also points to interstitial space as an important feature for tunable network structures. This feature is particularly important when the application relies on the chemistry or properties of the medium. In particular, the heterogeneity of the interstitial space plays a substantial role on the achievable properties. For example, the double gyroid network structures formed by Hillhouse and coworkers allow for the formation of an inverted gyroid structure that can be backfilled with a secondary material.[24] In this case, homogeneity of the interstitial space is required for effective electro-deposition. The homogeneity is also an important factor in networks that are utilized for nanofiltration because the high pressure operating principles are highly dependent on pore sizes.[2, 26]

The size and shape of the interstitial space also plays a crucial role in the application of the network structure. Many polymer mesh structures differ based on the size of the interstitial space between mesh links. Liao and coworkers demonstrated that, as the mesh size decreases and interstitial space was confined, the elastic modulus of the network structure increased.[27] The shape and orientation of the interstitial space is particularly important in polymer electrolyte membranes (PEM). Schmidt-Rohr and Chen used computer simulations to demonstrate that the size, shape and orientation of the interstitial water phase in Nafion PEM significantly affects the methanol diffusion through the membrane.[28]

The building block, interconnectivity and interstitial space features highlighted in Figure 1.1 are an effective way to describe the multi-scale structure of most networks. However, the necessity and specificity of each of these features is highly dependent on the structure and property requirements of the final application.

1.3 Networks for Organic Electronic Applications

Conjugated polymers are a keystone material for developing the next generation of commercial electronic devices. The potential for low-temperature and solution-based processing of semiconducting polymers makes it possible to manufacture inexpensive, large area devices directly on a variety of substrates.[29, 30] These unique features are embraced in the design of organic light emitting diodes (OLEDs) and organic field-effect transistors (OFETs) that are now being incorporated into high-definition electronic displays.[31] Organic photovoltaic (OPVs) devices, also based on conjugated polymers, offer a lower-cost alternative to traditional solar cell technologies. OPVs are also economically well-positioned to capture a significant fraction of the available solar energy (120,000 TW) because of the low material and processing costs as well as the potential for large scale manufacturing.[30, 32, 33] However, the overall efficiency and stability of these devices must be improved before they can make a significant impact in this field.[30, 34]

OLEDs, OFETs and OPVs (as seen in Figure 1.2) have radically different device geometries, design principles and applications. However, they all share one critically important attribute: the need to transport charge through an electrically percolated polymer network. Engineering a network structure that is interconnected and spans the gap between electrodes is one of the grand challenges of designing efficient electronic devices from conjugated polymers.[30, 31, 35, 36] Figure 1.2 highlights some of the design requirements for each of the device applications. To work efficiently, OPVs require a composite p-type/n-type semiconductor active

layer, usually containing a conjugated polymer and a fullerene derivative that effectively absorb visible light, dissociates excitons and transports charges to produce useful current.[36-38] Optimized active layers are often associated with a high p-type/n-type interfacial contact area, the formation of nano-sized domains (< 20 nm) and high electrical connectivity or percolation between vertical electrodes (> 100 nm).[39-43]

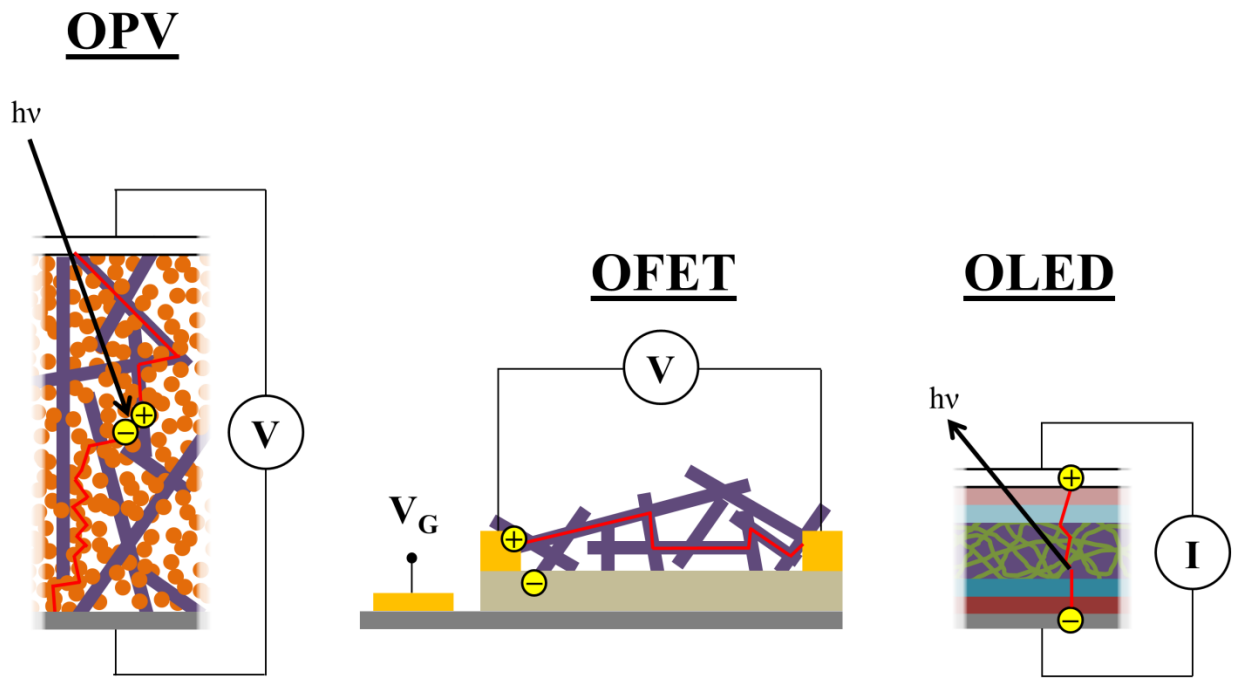

Figure 1.2 – Schematic of an organic photovoltaic (OPV), organic field effect transistor (OFET) and organic light emitting diode (OLED). Yellow circles represent charge carriers while red lines represent the path of the charge carriers.

In contrast, OLED devices are typically made in a layered fashion that does not resemble a typical network structure. However, some researchers have found enhanced performance for white-light emitting organic light emitting diodes (WOLEDS) while using mixed interlayers.[44-46] In this case, a mixed p-type/n-type interlayer (5-30 nm thick) is sandwiched between charge barrier and injection layers. The interlayer should be well mixed and interconnected for

recombination to occur throughout the entire layer thickness. Additionally, the choice of polymers must balance the band energy levels (to determine emission color) and the hole and electron mobility (for efficient charge recombination).[47]

Organic field effect transistors (OFETs) utilize only one material for charge transport, in contrast with the two or more required for OPVs and OLEDs. A network structure with high charge mobility must bridge the two electrodes, which are often > 10 μm apart.[48] Charges are injected across a dielectric barrier and then carried throughout the network structure to the electrode to generate current.

The network structure of organic electronic devices must be engineered to consider the operating constraints of the device. Unfortunately, the morphology of conjugated polymers is sometimes loosely characterized in the literature because of difficulties involved with probing the bulk structure of opaque thin-films and because of their multi-scale nature. Therefore, instead of designing necessary structures to achieve good performance, it is more common to optimize device properties through changes to processing parameters. Frequently, annealing conditions and coating protocols are changed without having a firm understanding of how these affect the multi-scale structure of the conjugated polymers. This leads to a lack of accurate structure-property relationships describing the correlation between a specific network structure and the device performance.[9]

Achieving specific network morphologies for use in organic electronics also becomes increasingly difficult when structural development is strongly coupled to processing conditions. OPVs, for example, are typically produced by coating a solution of dissolved p-type and n-type materials onto a conductive substrate.[39] This produces a film that may or may not phase segregate into the desired structure depending on parameters related to coating conditions and

post-processing annealing (e.g., temperature, solvent vapor pressure and coating speed).[43, 49-51] Operating constraints for ideal OPV photoactive layers suggest that there should be a bicontinuous network structure of mixed p-type and n-type materials, with nanoscale phase segregation, that can vertically bridge the anode and cathode.[29, 34-36, 51-54] The kinetically arrested structure that forms after initial coating usually does not match this description. Instead, various annealing techniques are utilized to further manipulate the photoactive layer usually resulting in increases in device efficiency.[43, 51] Though these techniques often yield better device performance, it is difficult to corroborate that an ideal bicontinuous network structure has been achieved. This is because there are few analytical techniques that can directly and quantitatively probe the multi-scale network structure in these materials. The top surface of thin-films is commonly studied using atomic force microscopy (AFM) or transmission electron microscopy (TEM).[55] Unfortunately, it is unlikely that this surface structure will match the bulk morphology due to the vertical phase segregation that is commonly observed for spin-coated devices.[50, 56, 57] Issues with contrast between the two organic phases and low instrument resolution also make it difficult to extract precise structural information using these techniques. Ginger and coworkers have made significant progress in addressing this issue by directly linking the nanoscale surface morphology to local device performance using photoconductive AFM.[54, 55] However, even these improved techniques are still limited to probing the surface structure of the thin-films.

An alternative method to adjusting the morphology of the network via post-processing is to directly build the desired structure prior to coating. The self-assembly of one component prior to deposition could ensure the formation of a stable and interconnected network that could be beneficial for organic electronic devices. Network formation in conjugated polymers is a common phenomenon at moderate concentrations (> 1 mg/mL). Poly(3-alkylthiophenes)

(P3ATs), Poly(9,9-dioctylfluorene-2,7-diyl) (PF8) and Poly[2-methoxy-5-(2-ethylhexyloxy)-1,4-henylenevinylene)] (MEH-PPV) have all been shown to form organogels in certain solvents.[19, 58-69] One common trait amongst conjugated polymers that self-assemble is the occurrence of π-π stacking. This propensity for π-stacking frequently leads to growth of long crystalline fiber structures that can extend for several micrometers.[30, 58, 59] It has been shown that the fiber cross-section and network structure of P3HT, crystallized prior to coating, could be tuned based on the solvent type.[9] Malik and coworkers further demonstrated that the natural interconnectivity of P3HT in the gel-phase (> 10mg/mL) results in increased charge mobility when compared to traditional spin-cast films of the same composition.[63] The ability to engineer the network phases of conjugated polymers could provide a route towards achieving unique active layer morphologies.

Researchers in the area of conjugated polymers have largely regarded network formation and gelation as a hurdle that needs to be overcome for the benefit of storing and processing electronic inks.[58, 69, 70] The elastic mechanical nature of interconnected networks makes them difficult to process using traditional coating techniques. Our lab has recently made significant progress towards enabling the processing of P3HT organogels from aqueous dispersions through the preparation of microgel particles. The feasibility of the approach was demonstrated by fabricating solar cells.[71] We have also developed a new method to form gels in a confined thin film environment, which will be discussed in Chapter 6. Other researchers have also demonstrated the feasibility of using conjugated polymer organogels in OPVs through both a freeze-drying coating method and organogel sonication to form a homogenous solution.[60, 72] These advances in gel processing make it possible to utilize these percolated networks in real applications. Additionally, research in the field of small-molecule organogel growth suggests

that the network structure of organogels can be effectively tuned by controlling the solubility of the gelator molecules.[14, 73] Despite all of these important results, there are no systematic reports exploring the formation and mesoscale structure of conjugated polymer networks. Therefore, there are no accurate relationships between the multi-scale structural properties of conjugated polymer organogels and charge transport.

1.4 Highlights and Objectives

In this work we present a systematic, multi-scale structural analysis of self-assembled conjugated polymer networks formed at different concentrations, in various aromatic solvents and at different temperatures to inform the ongoing development of percolated networks for organic electronics.

In Chapter 3, we demonstrate the importance of using a multi-length scale structural analysis when developing structure-property relationships for self-assembled networks of P3HT.[9] We identify and characterize the mesoscale morphology of poly(3-hexylthiophene) (P3HT) fibers crystallized through colloidal self-assembly in various aromatic solvents. The network structure of the P3HT is evaluated through *in situ* small angle neutron scattering (SANS) and ultra-small angle neutron scattering (USANS) experiments and by electron microscopy. Through model fitting to the scattering data we were able to determine that P3HT forms network structures in solution prior to deposition. We directly obtain structural parameters such as the volume fraction of P3HT in nanofiber form, the cross-sectional fiber shape and the fractal dimension of the colloidal networks. The structural parameters are shown to be strongly dependent on the solvent choice. *Ex situ* microscopy experiments were also performed to provide complementary structural information such as type and frequency of fibrillar junctions and the

network size. The structural parameters were also analyzed within the context of the hole mobility in organic field effect transistors (OFET).

In Chapter 4, the structural, mechanical and electrical properties of poly(3-hexylthiophene) (P3HT) organogels have been probed during the sol-gel transition through combined rheology, AC dielectric spectroscopy and small angle neutron scattering (SANS).[11] SANS shows that structural features of P3HT gels, which are crucial for the optimization of organic photovoltaic devices, evolve throughout the gelation process. *In-situ* structure-property analyses also demonstrate that there are very different mechanisms for the formation and dissolution of fibers and networks prepared from these polymeric semiconductors. It is determined that P3HT gels form conductive pathways that were maintained even after up to 50% of the fibers re-dissolve upon heating. P3HT organogels formed in different aromatic solvents also show differences of more than two orders of magnitude in conductivity despite having similar nanoscale fiber structures. These results demonstrate the importance of controlling the self-assembled morphology of fiber networks for maintaining optimal electronic properties.

In Chapter 5, we investigate the potential to rationally design an interconnected network of conjugated polymers using the gelation of poly(3-hexylthiophene) (P3HT) as a model system.[10] The three-dimensional network structure is evaluated through small angle neutron scattering (SANS) and ultra-small angle neutron scattering (USANS). The analytical models used for data fitting provide relevant structural parameters over multiple length scales. Structural parameters include the fiber cross-section (height and width), the specific surface area and the network density (i.e. fractal dimension). Simultaneous rheological and conductivity measurements also provide insight into the development of the mechanical and electrical properties of organogels and allow us to propose a detailed gelation mechanism for P3HT. The

fiber shape is found to be relatively independent of the solvent type but P3HT organogels show distinct differences in conductivity, which can be directly linked to differences in the branching network structures.

In Chapter 6, low volatility solvent/non-solvent mixtures were utilized to engineer the structure of poly(3-alkylthiophene) (P3AT) organogels. The ratio of solvent to poor-solvent was manipulated to systematically control the kinetics of self-assembly. Specific solvent mixtures were utilized to produce similar gelation kinetics with polymers of differing alkyl chain length. Simultaneous small angle neutron scattering (SANS) and dielectric spectroscopy was used to probe the structure and the electronic properties of isothermally self-assembled P3ATs. It was determined that alkyl chain length has a dominant effect on the relationship between fiber development and conductivity. Furthermore, using transmission electron microscopy (TEM) and SANS we demonstrate that, for P3HT organogels, lower poor-solvent content leads to fewer fibers with larger network structures while higher poor-solvent amounts leads to more fibers and a network structure that is smaller and more heterogeneous. This leads to opposing effects in terms of the contribution of the solvent quality to the electrical conductivity. An optimum in conductivity is found at different amounts of poor-solvent for each type of polymer. It is also shown that low volatility solvent mixtures allow for the formation of thermoreversible conjugated polymer organogels in thin-films at room temperature.

In Chapter 7, an alternative approach to hybrid photovoltaic (HPV) active layer formation is reported based on the deposition of a metal oxide coating over a porous conjugated polymer network that acts as a structural template. The process was demonstrated by magnetron sputtering of zinc oxide (ZnO) over a dry poly(3-hexylthiophene) (P3HT) organogel network. Structural and optical characterization was performed before and after metal oxide deposition

using a combination of small angle x-ray scattering (SAXS), scanning electron microscopy (SEM) and UV-visible absorption spectroscopy (UV-vis) techniques. Results show negligible degradation of the P3HT organogel layer upon the deposition of the inorganic components. HPV solar cells were successfully demonstrated but they had very low power conversion efficiency (PCE) values. The low efficiency is the result of limited penetration of the inorganic components into the porous P3HT matrix as well as a mismatch in the energy levels of the two materials. Several recommendations are made to substantially increase PCE values for HPV devices fabricated using this new process.

In Chapter 8, we utilize UV-vis spectroscopy, small angle neutron scattering (SANS) and all atom molecular dynamic (AA-MD) simulations to closely probe the relationship between the conformation of dissolved, isolated chains of poly(3-alkylthiophene) polymers and their optical properties. Variations in the radius of gyration and Kuhn length were observed as a function of the length (and structure) of different alkyl chain moieties and the solvent environment. Furthermore, both SANS and MD simulations shows that dissolved P3HT chains are more rigid in solvents where self-assembly and network formation is possible. Shifts in P3AT optical properties were also observed for different solvent environments. However, these changes were not correlated to the changes in polymer conformation. Instead, we demonstrate that the most significant changes in optical properties are explained by accounting for well-established solvent-solute solvatochromic interactions and MD simulations provide further insights into specific polymer-solvent interactions. This chapter also highlights the need for further experiments and molecular simulations that inform the specific role of solvent molecules on local polymer conformation and optical properties.

Together, these chapters will demonstrate that it is possible to engineer a network structure for specific organic electronic applications using gelation and/or network formation as a general platform.

1.5 References

1. Smith, L. A.; Liu, X.; Ma, P. X. *Soft Matter* **2008,** 4, (11), 2144-2149.
2. Matsuura, T. *Desalination* **2001,** 134, (1–3), 47-54.
3. Sandler, J. K. W.; Kirk, J. E.; Kinloch, I. A.; Shaffer, M. S. P.; Windle, A. H. *Polymer* **2003,** 44, (19), 5893-5899.
4. Nam, S.; Cho, H. W.; Kim, T.; Kim, D.; Sung, B. J.; Lim, S.; Kim, H. *Applied Physics Letters* **2011,** 99, (4), 043104-3.
5. Boal, A. K.; Ilhan, F.; DeRouchey, J. E.; Thurn-Albrecht, T.; Russell, T. P.; Rotello, V. M. *Nature* **2000,** 404, (6779), 746-748.
6. Chen, B.; Wu, K.; Yao, W. *Cement and Concrete Composites* **2004,** 26, (4), 291-297.
7. Koehler, R. D.; Raghavan, S. R.; Kaler, E. W. *The Journal of Physical Chemistry B* **2000,** 104, (47), 11035-11044.
8. Samitsu, S.; Shimomura, T.; Heike, S.; Hashizume, T.; Ito, K. *Macromolecules* **2010,** 43, (19), 7891-7894.
9. Newbloom, G.; Kim, F.; Jenekhe, S.; Pozzo, D. *Macromolecules* **2011,** 44, (10), 3801-3809.
10. Newbloom, G. M.; Weigandt, K. M.; Pozzo, D. C. *Macromolecules* **2012,** 45, (8), 3452-3462.
11. Newbloom, G. M.; Weigandt, K. M.; Pozzo, D. C. *Soft Matter* **2012,** 8, (34), 8854-8864.
12. Gong, J. P.; Katsuyama, Y.; Kurokawa, T.; Osada, Y. *Advanced Materials* **2003,** 15, (14), 1155-1158.
13. Na, Y.-H.; Kurokawa, T.; Katsuyama, Y.; Tsukeshiba, H.; Gong, J. P.; Osada, Y.; Okabe, S.; Karino, T.; Shibayama, M. *Macromolecules* **2004,** 37, (14), 5370-5374.
14. Li, J. L.; Yuan, B.; Liu, X. Y.; Xu, H. Y. *Crystal Growth & Design* **2010,** 10, (6), 2699-2706.
15. Liu, X. Y.; Sawant, P. D. *Advanced Materials* **2002,** 14, (6), 421-426.
16. James, S. L. *Chemical Society Reviews* **2003,** 32, (5), 276-288.
17. Sakai, T.; Matsunaga, T.; Yamamoto, Y.; Ito, C.; Yoshida, R.; Suzuki, S.; Sasaki, N.; Shibayama, M.; Chung, U.-i. *Macromolecules* **2008,** 41, (14), 5379-5384.
18. Jiang, S.; Cao, Z. *Advanced Materials* **2010,** 22, (9), 920-932.
19. Wang, P. S.; Lu, H. H.; Liu, C. Y.; Chen, S. A. *Macromolecules* **2008,** 41, (17), 6500-6504.
20. Avrami, M. *Journal of Chemical Physics* **1939,** 7, 1103-1112.

21. Avrami, M. *Journal of Chemical Physics* **1941,** 8, 177-184.
22. Hoyle, C. E.; Lee, T. Y.; Roper, T. *Journal of Polymer Science Part A: Polymer Chemistry* **2004,** 42, (21), 5301-5338.
23. Cui, J.; Lackey, M. A.; Madkour, A. E.; Saffer, E. M.; Griffin, D. M.; Bhatia, S. R.; Crosby, A. J.; Tew, G. N. *Biomacromolecules* **2012,** 13, (3), 584-588.
24. Urade, V. N.; Wei, T.-C.; Tate, M. P.; Kowalski, J. D.; Hillhouse, H. W. *Chemistry of Materials* **2007,** 19, (4), 768-777.
25. Pileni, M.-P. *Nat Mater* **2003,** 2, (3), 145-150.
26. Choi, H.; Stathatos, E.; Dionysiou, D. D. *Desalination* **2007,** 202, (1–3), 199-206.
27. Liao, H.; Munoz-Pinto, D.; Qu, X.; Hou, Y.; Grunlan, M. A.; Hahn, M. S. *Acta Biomaterialia* **2008,** 4, (5), 1161-1171.
28. Schmidt-Rohr, K.; Chen, Q. *Nat Mater* **2008,** 7, (1), 75-83.
29. Hoppe, H.; Sariciftci, N. *Journal of Materials Research* **2004,** 19, (7), 1924-1945.
30. Yang, X. N.; Loos, J.; Veenstra, S. C.; Verhees, W. J. H.; Wienk, M. M.; Kroon, J. M.; Michels, M. A. J.; Janssen, R. A. J. *Nano Letters* **2005,** 5, (4), 579-583.
31. Halls, J., Walsh, CA, Greenham, NC, Marseglia, EA, Friend, RH, Moratti, SC, Holmes, AB. *Nature* **1995,** 376, 498-500.
32. *Basic Research Needs for Solar Energy Utilization*; U.S. Department of Energy: http://www.sc.doe.gov/bes/reports/files/SEU_rpt.pdf, 2005.
33. Wohrle, D.; Meissner, D. *Advanced Materials* **1991,** 3, (3), 129-138.
34. Coakley, K.; McGehee, M. *Chemistry of Materials* **2004,** 16, (23), 4533-4542.
35. Yu, G.; Gao, J.; Hummelen, J. C.; Wudl, F.; Heeger, A. J. *Science* **1995,** 270, (5243), 1789-1791.
36. Yu, G.; Heeger, A. J. *Journal of Applied Physics* **1995,** 78, (7), 4510-4515.
37. Krebs, F. C. *Solar Energy Materials and Solar Cells* **2009,** 93, (4), 394-412.
38. Krebs, F. C.; Gevorgyan, S. A.; Gholamkhass, B.; Holdcroft, S.; Schlenker, C.; Thompson, M. E.; Thompson, B. C.; Olson, D.; Ginley, D. S.; Shaheen, S. E.; Alshareef, H. N.; Murphy, J. W.; Youngblood, W. J.; Heston, N. C.; Reynolds, J. R.; Jia, S.; Laird, D.; Tuladhar, S. M.; Dane, J. G. A.; Atienzar, P.; Nelson, J.; Kroon, J. M.; Wienk, M. M.; Janssen, R. A. J.; Tvingstedt, K.; Zhang, F.; Andersson, M.; Inganäs, O.; Lira-Cantu, M.; de Bettignies, R.; Guillerez, S.; Aernouts, T.; Cheyns, D.; Lutsen, L.; Zimmermann, B.; Würfel, U.; Niggemann, M.; Schleiermacher, H.-F.; Liska, P.; Grätzel, M.; Lianos, P.; Katz, E. A.; Lohwasser, W.; Jannon, B. *Solar Energy Materials and Solar Cells* **2009,** 93, (11), 1968-1977.
39. Moule, A.; Meerholz, K. *Advanced Functional Materials* **2009,** 20, 3028-3036.
40. Shaw, P. E.; Ruseckas, A.; Samuel, I. D. W. *Advanced Materials* **2008,** 20, (18), 3516-3520.
41. Sirringhaus, H.; Brown, P.; Friend, R.; Nielsen, M.; Bechgaard, K.; Langeveld-Voss, B.; Spiering, A.; Janssen, R.; Meijer, E.; Herwig, P.; de Leeuw, D. *Nature* **1999,** 401, 685-688.

42. van Bavel, S.; Sourty, E.; de With, G.; Frolic, K.; Loos, J. *Macromolecules* **2009,** 42, (19), 7396-7403.
43. Yin, W.; Dadmun, M. *ACS Nano* **2011,** 5, (6), 4756-4768.
44. Gao, C.-H.; Shi, X.-B.; Zhou, D.-Y.; Zhang, L.; Wang, Z.-K.; Liao, L.-S. *International Jounral of Photoenergy* **2013,** 831765, 1-7.
45. Lee, J.; Lee, J.-I.; Lee, J. Y.; Chu, H. Y. *Applied Physics Letters* **2009,** 94, (19), 193305-3.
46. Yook, K. S.; Jeon, S. O.; Joo, C. W.; Lee, J. Y. *Journal of Industrial and Engineering Chemistry* **2009,** 15, (3), 420-422.
47. Friend, R. H.; Gymer, R. W.; Holmes, A. B.; Burroughes, J. H.; Marks, R. N.; Taliani, C.; Bradley, D. D. C.; Santos, D. A. D.; Bredas, J. L.; Logdlund, M.; Salaneck, W. R. *Nature* **1999,** 397, (6715), 121-128.
48. Bao, Z.; Dodabalapur, A.; Lovinger, A. J. *Applied Physics Letters* **1996,** 69, (26), 4108-4110.
49. Hoppe, H.; Sariciftci, N. S. *Journal of Materials Chemistry* **2006,** 16, (1), 45-61.
50. Treat, N. D.; Brady, M. A.; Smith, G.; Toney, M. F.; Kramer, E. J.; Hawker, C. J.; Chabinyc, M. L. *Advanced Energy Materials* **2011,** 1, (1), 82-89.
51. Zhang, Y.; Yip, H. L.; Acton, O.; Hau, S. K.; Huang, F.; Jen, A. K. Y. *Chemistry of Materials* **2009,** 21, (13), 2598-2600.
52. Cravino, A.; Sariciftci, N. S. *Journal of Materials Chemistry* **2002,** 12, 1931-1943.
53. Pingree, L.; MacLeod, B.; Ginger, D. *Journal of Physical Chemistry C* **2008,** 112, (21), 7922-7927.
54. Rice, A. H.; Giridharagopal, R.; Zheng, S. X.; Ohuchi, F. S.; Ginger, D. S.; Luscombe, C. K. *ACS Nano* **2011,** 5, (4), 3132-3140.
55. Coffey, D. C.; Reid, O. G.; Rodovsky, D. B.; Bartholomew, G. P.; Ginger, D. S. *Nano Letters* **2007,** 7, (3), 738-744.
56. Kiel, J. W.; Eberle, A. P. R.; Mackay, M. E. *Physical Review Letters* **2010,** 105, (16), 168701-4.
57. Kiel, J. W.; Kirby, B. J.; Majkrzak, C. F.; Maranville, B. B.; Mackay, M. E. *Soft Matter* **2010,** 6, (3), 641-646.
58. Berson, S.; De Bettignies, R.; Bailly, S.; Guillerez, S. *Advanced Functional Materials* **2007,** 17, (8), 1377-1384.
59. Chen, J. H.; Chang, C. S.; Chang, Y. X.; Chen, C. Y.; Chen, H. L.; Chen, S. A. *Macromolecules* **2009,** 42, (4), 1306-1314.
60. Huang, P.-T.; Chang, Y.-S.; Chou, C.-W. *Journal of Applied Polymer Science* **2011,** 122, 233-240.
61. Huang, W. Y.; Huang, P. T.; Han, Y. K.; Lee, C. C.; Hsieh, T. L.; Chang, M. Y. *Macromolecules* **2008,** 41, (20), 7485-7489.
62. Kitts, C. C.; Vanden Bout, D. A. *Polymer* **2007,** 48, 2322-2330.
63. Malik, S.; Jana, T.; Nandi, A. K. *Macromolecules* **2001,** 34, (2), 275-282.

64. Malik, S.; Nandi, A. K. *Journal of Physical Chemistry B* **2004,** 108, (2), 597-604.
65. Malik, S.; Nandi, A. K. *Journal of Applied Polymer Science* **2007,** 103, (4), 2528-2537.
66. Kim, J. Y.; Lee, K.; Coates, N. E.; Moses, D.; Nguyen, T.-Q.; Dante, M.; Heeger, A. J. *Science* **2007,** 317, (5835), 222-225.
67. Lin, Z.-Q.; Shi, N.-E.; Li, Y.-B.; Qiu, D.; Zhang, L.; Lin, J.-Y.; Zhao, J.-F.; Wang, C.; Xie, L.-H.; Huang, W. *Journal of Physical Chemistry C* **2011,** 115, (11), 4418-4424.
68. Chen, C. Y.; Chan, S. H.; Li, J. Y.; Wu, K. H.; Chen, H. L.; Chen, J. H.; Huang, W. Y.; Chen, S. A. *Macromolecules* **2010,** 43, (17), 7305-7311.
69. Koppe, M.; Brabec, C.; Heiml, S.; Schausberger, A.; Duffy, W.; Heeney, M.; McCulloch, I. *Macromolecules* **2009,** 42, (13), 4661-4666.
70. Alcazar, D.; Wang, F.; Swager, T. M.; Thomas, E. L. *Macromolecules* **2008,** 41, (24), 9863-9868.
71. Richards, J. J.; Weigandt, K. M.; Pozzo, D. C. *Journal of Colloid and Interface Science* **2011,** 364, (2), 341-350.
72. Kim, B.-G.; Jeong, E. J.; Park, H. J.; Bilby, D.; Guo, L. J.; Kim, J. *ACS Applied Materials & Interfaces* **2011,** 3, (3), 674-680.
73. Li, J. L.; Liu, X. Y.; Wang, R. Y.; Xiong, J. Y. *Journal of Physical Chemistry B* **2005,** 109, (51), 24231-24235.

Chapter 2

Theory and Use of Primary Experimental Techniques

2.1 Small Angle Scattering

2.1.1 Scattering Principles

Small angle scattering is a non-destructive experimental technique that allows for the structural analysis of complex systems through standard plots and model fitting. It is especially valuable for the structural characterization of networks, because small angle scattering provides inherently multi-length scale information. This technique has been widely utilized in the study of surfactant-based worm-like micelle networks,[1] cross-linked polymer mesh networks,[2] biologically compatible hydrogel networks[3] as well as many other network structures.

Fundamentally, small angle scattering experiments utilize a collimated beam of light, x-rays or neutrons to probe the correlated spatial distribution of atoms within a sample.[4] Figure 2.1 shows the four possible interactions between the particle probe (i.e., light, x-rays or neutrons) and the sample (i.e., atom or molecule). The first is absorption, where the atom absorbs the incident probe which results in a later radiative decay process. The second is transmission, where

the atom does not interact with the probe particle. This is the most common type of interaction in small angle scattering where often more than 90% of the incident beam is transmitted through the sample. The third interaction is elastic scattering, where the probe particle scatters off the atom at a defined angle with no change in momentum. This interaction will be the focus of this chapter. The final interaction is inelastic scattering, where the probe particle scatters off the atom at a defined angle but in this case there is a reduction in the particle energy after interaction. This interaction can provide information about the molecular motion of materials, but is not the focus of this work. All small angle scattering experiments include these four interactions in some ratio to one another.

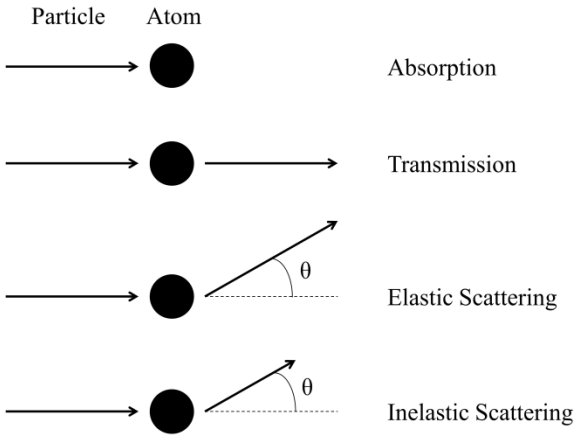

Figure 2.1. The four possible interactions between a collimated probe particle (i.e., light, x-ray or neutron) and an atom.

Neutrons interact with a different part of the atom than x-rays or light. Neutrons will interact with the nucleus of an atom while x-rays and light will interact with the electron cloud. These differences in interactions lead to different experimental design principles and constraints. In this work, we utilize small angle neutron scattering (SANS) and ultra-small angle neutron scattering (USANS) to study the multi-length scale network structure of conjugated polymer networks.

2.1.2 Instrumentation

SANS experiments in this work were performed at either the Center for Neutron Research at the National Institute of Standards and Technology (Gaithersburg, MD) on NG3/NG7, at the High Flux Isotope Reactor (HFIR) at Oak Ridge National Lab (Oak Ridge, TN) on CG2 and at the Institut Laue-Langevin (ILL) in Grenoble, France on D22. The operating principles of these instruments are identical even though SANS experiments were performed in different locations and on different instruments. Figure 2.2 gives a basic outline of a SANS instrument for a continuous reactor source.

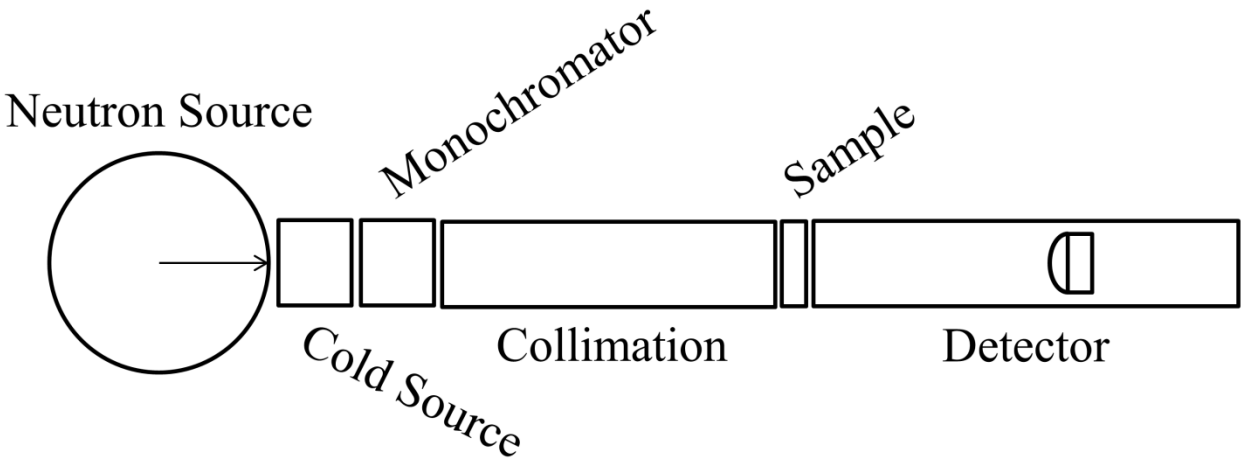

Figure 2.2. Standard elements of a continuous source SANS instrument.

A nuclear reactor is utilized to provide a continuous neutron source where thermal (i.e., fast) neutrons are generated through fission events. These neutrons are then funneled through a "cold source" where they collide with liquid hydrogen or deuterium. This energy transfer process slows down the neutrons before they are sent to the monochromator which is utilized to select a specific neutron wavelength (λ) and wavelength spread ($\Delta\lambda/\lambda$). Monochromatic neutrons then pass through a collimation system where they are focused into a beam with a specific aperture size before hitting the sample. All neutrons that are not absorbed will pass through the sample

and be registered as counts (i.e., intensity) on a 2-dimensional detector. This detector can be moved to different distances (relative to the samples) in order to capture different ranges of scattering angles. It is common for 2-3 detector positions to be utilized to capture the entire accessible range of angles for an instrument.[5]

USANS experiments were all performed at the Center for Neutron Research at the National Institute of Standards and Technology on BT5. These measurements are often performed in addition to SANS to study larger structures (100 nm to 20 μm). USANS utilizes a triple bounce diffraction process to examine ultra-low scattering angles, as seen in Figure 2.3.

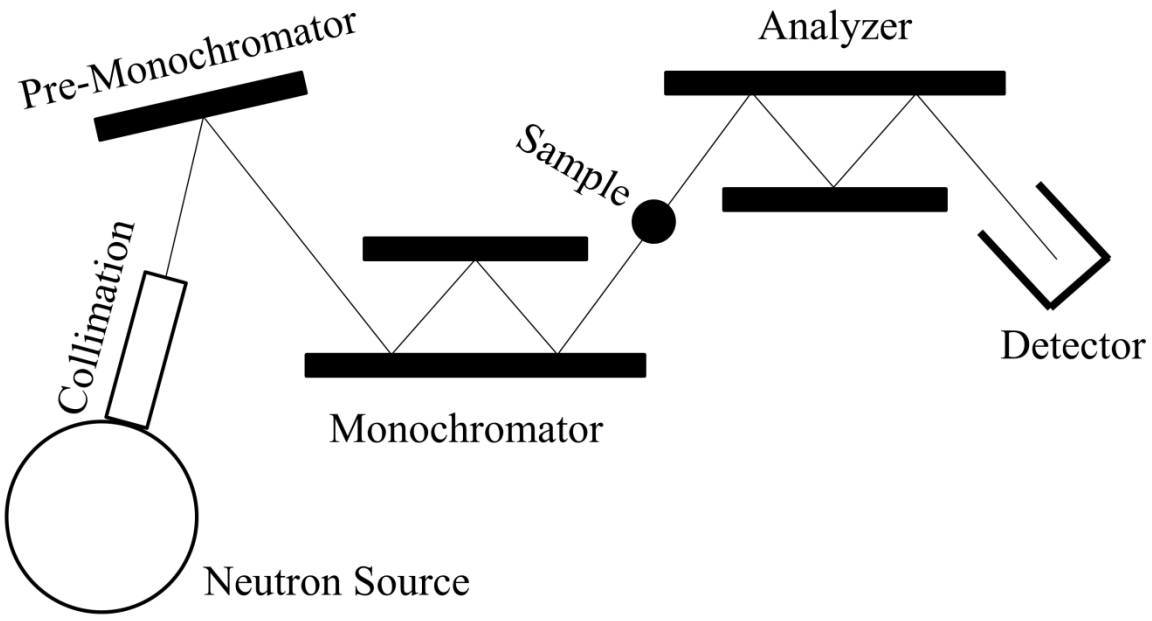

Figure 2.3. NIST CNR USANS instrument diagram

The USANS utilizes thermal neutrons and applies a collimation system before monochromation. Monochromation is applied by reflecting the neutron beam using silicon crystals before the neutron beam passes through the sample. The analyzer crystal is rotated so that the detector is allowed to access different scattering angles. This process typically results in

very low neutron flux-on-sample and therefore only strong scattering systems can be studied with USANS.[6]

2.1.3 Standard Plots

SANS and USANS data are collected in reciprocal space and utilize the scattering vector (q). The scattering vector, also called q-vector, can be determined from the following equation:

$$q = 4\pi \frac{\sin(\theta / 2)}{\lambda} \tag{2.1}$$

where λ is the neutron wavelength and θ is defined as the angle between the incident neutron beam and the scattered neutron. The q-vector typically has units of $Å^{-1}$. The real space equivalent (d) of the q-vector can be calculated using Bragg's Law:

$$d = \frac{2\pi}{q} \tag{2.2}$$

SANS and USANS data must be corrected for background and empty cell scattering before they can be analyzed because neutrons interact with all materials in the beam. The background is typically measured by scattering with nothing in the beam while the empty cell is measured by scattering with just the empty cell in the beam (i.e., no sample). These two-dimension scattering profiles are then subtracted from the two-dimensional sample scattering profile using standard reduction protocols created by the NIST CNR.[7] The two-dimensional scattering intensity (I) of the corrected sample is then averaged about the azimuthal angle, normalized by the neutrons transmitted through the sample and plotted as a function of the scattering vector (q) for both SANS and USANS experiments. This "reduction" process results in a final, one-dimensional function: *I(q)*.

Standard plots are a powerful tool for the characterization of neutron scattering profiles. Two standard plots utilized in this work are the Guinier plot and the Porod plot. The Guinier plot is utilized to determine the radius of gyration (R_g) of a structure.[8] A Guinier plot is generated by plotting the ln($I(q)$) vs q^2, as seen in Figure 2.4 where a sample plot of a nanoparticle solution can be seen. This can be fit with the following equation to extract R_g as long as $q_{min} \cdot R_g < 1$:

$$\ln(I(q)) = \ln(I_o) - \frac{q^2 R_g^{\,2}}{3} \tag{2.3}$$

Figure 2.4 shows the Guinier plot of a gold nanoparticle solution with 5 nm (radius) particles. The linear fit corresponds to an R_g of 3.9 nm and since the radius of sphere is $R_g^2 = 3R^2/5$, this fit corresponds to a particle radius of 5.0 nm, as expected.

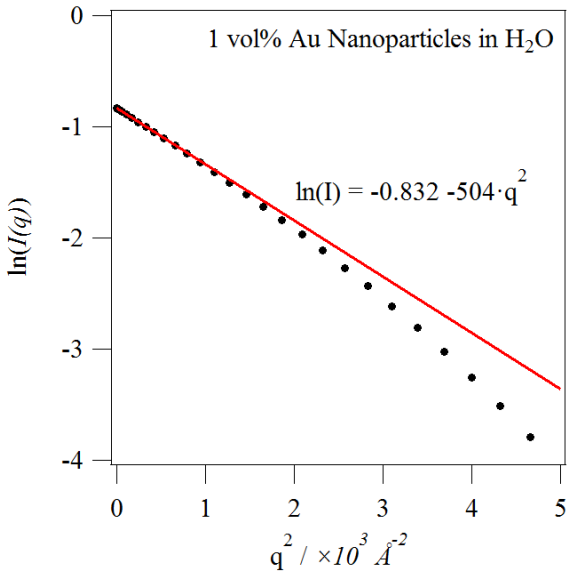

Figure 2.4. Guinier plot the simulated scattering of a 1 vol% Au nanoparticle solution in D_2O with a particle radius of 5 nm.

The Porod plot is utilized to determine the specific surface area (S_v) of a structure.[4] The Porod plot is generated by plotting $I(q) \cdot q^4$ (in absolute intensity) vs q after background

subtraction, as seen in Figure 2.4 where a sample plot of a nanoparticle solution can be seen. The specific surface area of a structure is calculated using the Porod equation:

$$\lim_{q\to\infty}\left[I(q)\cdot q^4\right]=2\pi(\Delta\rho)^2\Sigma \tag{2.4}$$

where Σ is the surface area per volume in units of m^{-1} that can be converted to specific surface area (S_v) in units of m^2/g using the following equation:

$$S_v=\frac{\Sigma}{\rho_m\cdot\phi} \tag{2.5}$$

where ρ_m is the mass density and ϕ is the volume fraction of particles that contribute to the surface area. Figure 2.5 shows that $\lim_{q\to\infty}\left[I(q)\cdot q^4\right]=3\times10^{-7}\ cm^{-1}\cdot\AA^{-4}$, which corresponds to a Σ = 5.8×10^8 m^{-1}. Given that Σ reduces to $3/R$ for a sphere, this would produce a sphere of radius 5.2 nm, which is within 4% of the true radius.

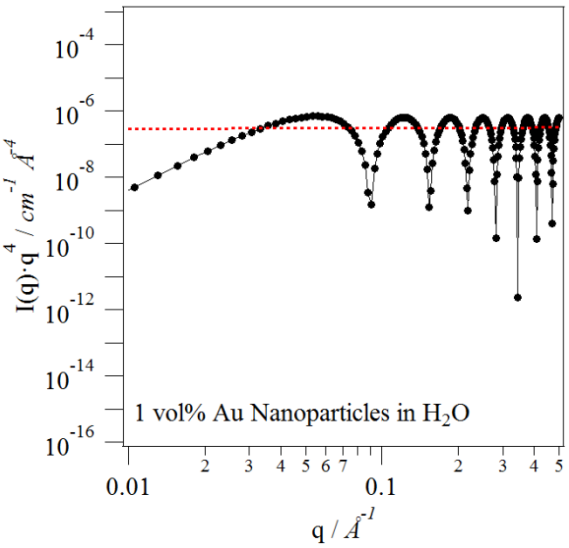

Figure 2.5. Porod plot the simulated scattering of a 1 vol% Au nanoparticle solution in D_2O with a particle radius of 5 nm

The scattering invariant (Q) is another principle which can be utilized to determine volume fraction of scattering objects:[4]

$$Q = \int_0^{\infty} I(q) \cdot q^2 \, dq = 2\pi^2 \phi (1-\phi) \left(\Delta\rho\right)^2 \tag{2.6}$$

The invariant is often utilized to check for self-consistency between the expected and measured particle volume fractions. The Guinier analysis, Porod analysis and invariant analysis can all be performed independent of the scattering form factor or structure factor as long as all of the theory constraints are met.

2.1.4 Form Factor Fitting

The absolute scale elastic (i.e., coherent) scattering intensity is dependent on the five terms as seen below:

$$I(q) = \left(\frac{N}{V}\right) \cdot V_p^{\,2} \cdot (\Delta\rho)^2 \cdot P(q) \cdot S(q) + Bkg \tag{2.3}$$

In Equation 2.3, *N/V* is defined as the number of primary scattering objects per volume of the sample.[4] V_p is the total volume of the primary particle. These terms are often condensed into a volume fraction term (ϕ) to form the more common expression of *I(q)*:

$$I(q) = \phi \cdot (\Delta\rho)^2 \cdot P(q) \cdot S(q) + Bkg \tag{2.4}$$

In Equation 2.3 & 2.4, $\Delta\rho$ refers to the scattering contrast which is the difference between the scattering length density (ρ) of the primary particle and the matrix (e.g., polymer or solvent) it is in. The larger the difference between scattering length densities, the greater the scattering intensity. The scattering length density is related to the sum of the bound coherent scattering length (b_c) of each atom normalized by the molecular volume (v_m):

$$\rho = \frac{\sum_{i=1}^{n} b_{c_i}}{v_m} \tag{2.5}$$

It is possible to tune the scattering length density of either component through partial or full deuteration because of the large difference between the bound coherent scattering lengths of hydrogen and deuterium. The bound coherent scattering lengths of select atoms are presented in Table 2.1.

Table 2.1. Bound coherent scattering lengths (b_c) for different atoms.[9]

Atom	b_c **(fm)**
Hydrogen	-3.74
Deuterium	6.67
Carbon	6.65
Sulfur	2.80
Nitrogen	9.37
Chlorine	11.65
Silicon	4.11

In Equations 2.3 & 2.4, *P(q)* refers to the form factor of the primary particle and *S(q)* refers to the structure factor (i.e., interactions) of the primary particles. If there are no interactions between primary particles *S(q)* = 1. In many cases, the form factor and structure factor can be externally determined or verified using techniques such as scanning or transmission electron microscopy or atomic force microscopy. Finally, in Equation 2.3 & 2.4, *Bkg* refers to the isotropic background scattering of the sample. Background scattering occurs as a result of incoherent scattering in SANS measurements and is most prevalent in samples with high hydrogen concentrations. It is ideal to remove the background scattering before fitting, which can be done by subtracting the flat scattering at high-*q*.

Two software packages are utilized for the fitting of Equation 2.4 to the SANS data in this work: IGOR Pro with NIST Macros[7] and SASView.[10] Both of these programs utilize a least-squares fitting routine to minimize the deviation between scattering profile and model.

Polydispersity is also a crucial component for the proper fitting of SANS data. Figure 2.6 shows the difference in scattering profiles between a monodisperse and polydisperse (10%) gold nanoparticle solution. The oscillation at high-q are smeared out by polydispersity. The polydispersiy of the form factors should be externally verified, and if possible quantified, before being included in the fitting routine in order to reduce the number of unknown variables.

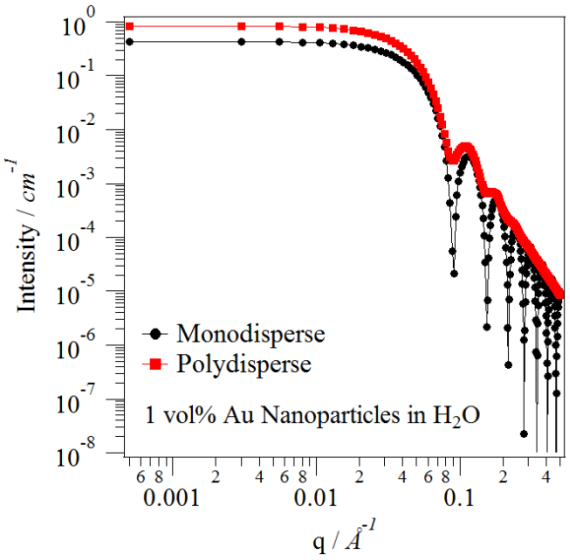

Figure 2.6. Simulated scattering data for a 1 vol% Au nanoparticle solution in D_2O with a particle radius of 5 nm with an without a polydispersity index of 10%.

2.1.5 Conjugated Polymer Network Fitting

Organic electronic devices operate on physical principles that occur over multiple length scales.[11] Therefore, when optimizing the morphology of conjugated polymers it is crucial to study the structure over all relevant length scales for a given application. Small angle scattering is an ideal structural analysis technique because it is inherently multi-scale and much of this work is devoted to the use of SANS for the structural study of conjugated polymer self-assembly and network formation. Figure 2.7 shows a typical SANS and USANS profiles for self-assembled P3HT in p-xylene. The scattering provides structural information over almost 4 orders

of magnitude in length scale (about 3 nm to 16 μm) and thus requires different physical models for different size scales. In this work, the interpretation of SANS and USANS data is approached using the following models and multi-scale approach for every polymer system investigated.

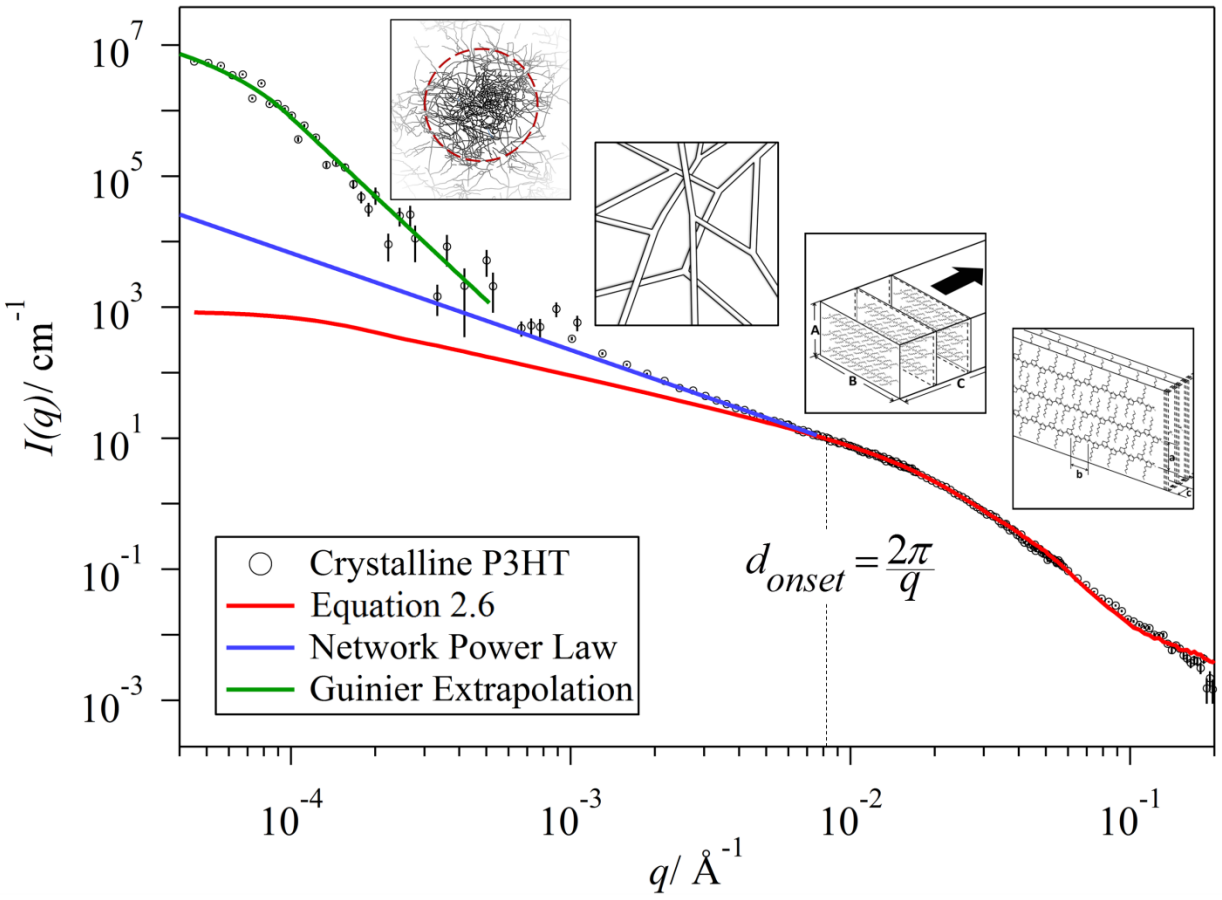

Figure 2.7. Reduced and combined SANS and USANS data from 0.2 wt% P3HT in p-xylene. The data, in absolute scale, is fit using models that describe the structures at different length scales. Equation 2.9 describes the network power law and Equation 2.10 describes the Guinier extrapolation. The insets are schematic representations of the structural features that are characterized at each q-range.

The fibrillar cross-section of self-assembled P3HT is seen at $0.0088 < q$ (Å^{-1}) < 0.07 and can be fit using the parallelepiped model.[12] Chen et al. modeled the small angle x-ray scattering (SAXS) of a P3AT gel with a cylindrical model.[13] However, a parallelepiped model is observed

to better represent the orthorhombic crystal structure of P3AT that is reported by many researchers.[14-16] The scattering intensity in this region is modeled using:

$$I(q)=\phi_v \Psi_f (\Delta\rho_{PP})^2 P_{PP}(q)+\phi_v (1-\Psi_f)(\Delta\rho_{PExV})^2 P_{PExV}(q) \quad (2.6)$$

where ϕ_v is the total volume fraction of polymer, Ψ_f is the fraction of the sample that is a parallelepiped shape (i.e. fibrillar), $\Delta\rho_{PP}$ is the scattering contrast between fibers and solvent, $\Delta\rho_{PExV}$ is the scattering contrast between dissolved chains and solvent, $P_{PP}(q)$ is the parallelepiped form factor and $P_{PExV}(q)$ is the form factor for polymer chains with excluded volume interactions. The parallelepiped form factor, $P_{PP}(q)$, is given by:

$$P_{PP}(q,a,b,c)=\frac{2}{\pi}\int_0^{\pi/2}\int_0^{\pi/2}\left[\left(\frac{\sin(qa\sin\alpha\cos\beta)}{qa\sin\alpha\cos\beta}\right)\left(\frac{\sin(qb\sin\alpha\sin\beta)}{qb\sin\alpha\sin\beta}\right)\left(\frac{\sin(qc\cos\alpha)}{qc\cos\alpha}\right)\right]^2 \sin(\alpha)d\alpha\, d\beta \quad (2.7)$$

where a, b and c are the fibrillar height, width and length, respectively. Only the fibrillar height (a) and width (b) are utilized for fitting because the length of a fiber (c) is typically longer than the parallelepiped model fitting q-range.

In this work, no samples were found to completely assemble into nanofibers, leaving some dissolved polymer coexisting (1-Ψ_f) with the network structure at all times. At low-q, the scattering contribution of this soluble polymer fraction is typically negligible because the fibrillar network dominates the scattering, as seen in Figure 2.8. On the other hand, at very high values of q, there is a non-negligible contribution arising from the dissolved polymer fraction. Therefore, we decided to properly account for the contribution of the dissolved polymer by directly measuring the scattering function of samples that only contain fully dissolved polymer chains (i.e. before they are allowed to self-assembly). The form factor for polymers with excluded volume interactions (P_{PExV}) is utilized to determine the shape of these dissolved chains. [17, 18]

$$P_{PExV}(q,n,a,\nu)=2\int_0^1 dx(1-x)\exp\left[-\frac{q^2a^2}{6}n^{2\nu}x^{2\nu}\right] \tag{2.8}$$

Here, n is the number of segments, a is the statistical segment length and ν is related to conformation of the polymer chain. In order to reduce the number of fitting parameters in Equation 2.6, we fit data from fully dissolved chains at elevated temperatures ($40 < T$ (ºC) < 80) and use the same parameters for the rest of the data. One inherent assumption in this approach is that the conformation of the dissolved polymer fraction is the same at all times during the crystallization process and that only the relative concentration is changing.

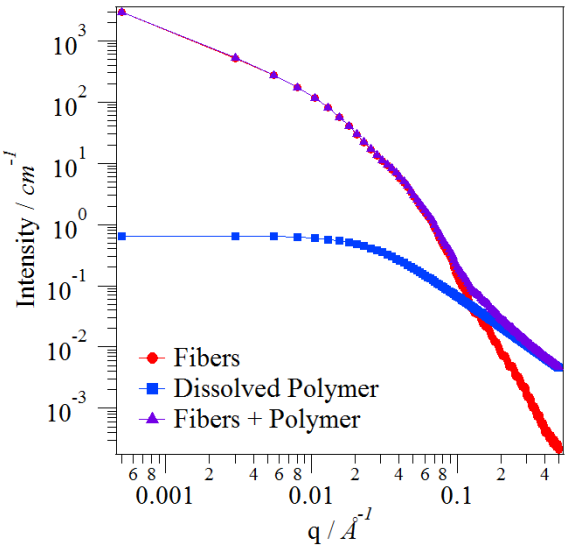

Figure 2.8. Simulated scattering data for conjugated polymer network that is 50% self-assembled fibers ($\Psi_f = 0.5$) and 50% dissolved polymer. Fibers are represented by Equation 2.7, dissolved polymer by Equation 2.8 and the linear combination by Equation 2.6.

We also evaluated the fractal nature of the network using a power-law dependence of:

$$I(q)\approx q^{-D_f^S} \tag{2.9}$$

where D_f^S is the structural fractal dimension.[29] Figure 2.7 shows a clear deviation between the data and the Equation 2.6 fit at $q < 0.0088$ Å^{-1} indicating that, at larger length scales, the scattering is dominated by the network rather than by the form factor of isolated fibers. This

region was fit using a power-law to obtain a fractal dimension (D_f^S) that represents the network structure. This physical interpretation is based on the size scale (70 nm to 900 nm) over which the self-similar feature exists. The onset of self-similar behavior (d_{onset}) represents the maximum dimension over which the individual fibers in the network can be approximated as isolated rod-like structures. The determination of d_{onset} is possible by plotting both data and Equation 2.7, with an arbitrarily sized cross-section, as $I(q)\cdot q^2$ vs q and finding the form factor deviation when the peak of the model is aligned with the peak of the SANS profile, as seen in Figure 2.9.

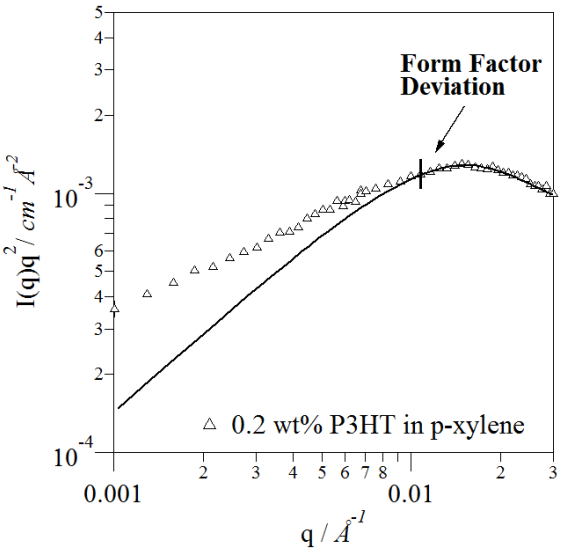

Figure 2.9. $I(q)\cdot q^2$ plot of SANS data, for P3HT crystallized in p-xylene, to highlight the "knee" corresponding to the fibrillar cross-section and the corresponding Equation 2.7 fit. The deviation between the model and scattering is determined from this plot and is utilized to delineate the onset of the fractal region**.**

At the smallest scattering angles in Figure 2.7 ($q < 4\times10^{-4}$ Å^{-1}), the data is fit to a Guinier extrapolation:[8]

$$I(q) = I_0 \exp(-R_g^2 q^2 / 3) \tag{2.10}$$

This low-q behavior is attributed to the interface between a dense nucleation center, or colloidal network particles, and the solvent. This is a surface-dominated scattering region with a power-

law slope that should correspond well with Porod scattering, $I(q) \sim q^{-4}$. The wide range of length scales that are simultaneously analyzed by SANS and USANS in this work (1-10,000 nm) make it essential to use several models to properly analyze the structural features that develop in these complex materials.

2.2 Oscillatory Rheology

Small amplitude oscillatory rheology is used for the characterization of conjugated polymer networks in this work. Rheology is the study of the flow of matter.[19] In oscillatory rheology, either a stress (σ) is applied and a strain (γ) is measured or vice versa. The depiction of an oscillatory stress-strain relationship can be seen in Figure 2.10. Stress is defined as:

$$\sigma = \frac{F}{A} \tag{2.11}$$

where F is the applied force and A is the interfacial area, as seen in Figure 2.11. Strain is defined as:

$$\gamma = \frac{\Delta x}{h} \tag{2.12}$$

where Δx is the linear displacement and h is the gap thickness.

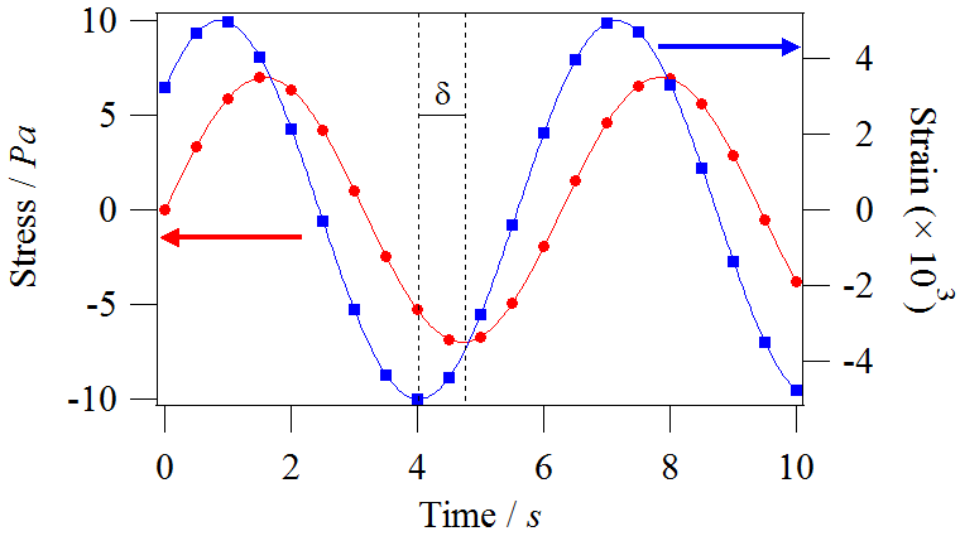

Figure 2.10. Simulated stress-strain relationship for oscillatory rheology measurements

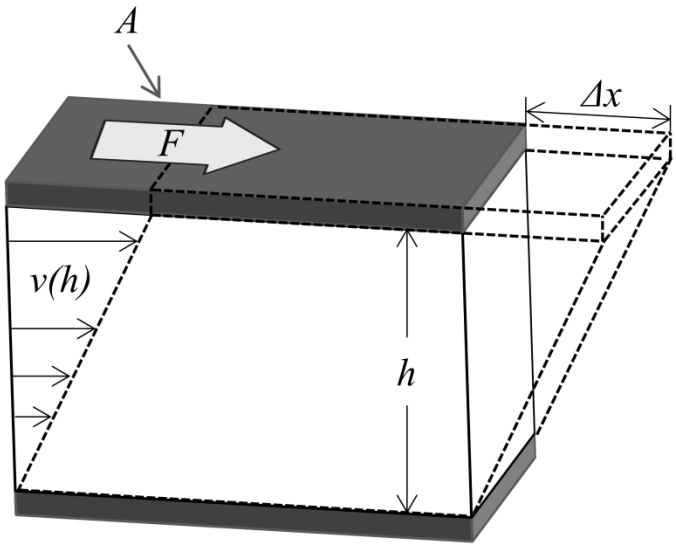

Figure 2.11. Schematic of relevant rheology parameters

For a purely elastic materials, there will be no lag between the applied stress/strain and the measured stress/strain, leading to a phase angle (δ) of 0º. For purely viscous materials, there will be the maximum possible lag between the applied stress/strain and the measured stress/strain, leading to a phase angle (δ) of 90º. Viscoelastic materials, such as conjugated

polymer networks, have both an elastic and a viscous nature and therefore the phase angle falls between 0º and 90º.

A small-amplitude, non-destructive stress must be applied to measure the viscoelastic properties of a conjugated polymer network. The stress limit before network deformation can be determined by performing a stress sweep of the network structure, as seen in Figure 2.12. In this figure, the storage modulus (*G'*) and the loss modulus (*G"*) are reported as a function of shear stress. The storage modulus represents the in-phase stress response (i.e., elastic) while the loss modulus represents the out-of-phase stress response (i.e., inelastic) according to the following equation:

$$\sigma = \gamma_0[G'\sin(\omega t) + G''\cos(\omega t)] \qquad (2.13)$$

where γ_0 is the strain amplitude, t is time and ω is the angular frequency. The linear viscoelastic response (LVR) corresponds to the range over which there is a linear response to increasing stress/strain amplitude.[19] All of the networks probed in this work have a LVR for $\tau < 10$ Pa and therefore a perturbation stress of 0.25 Pa is typically used.

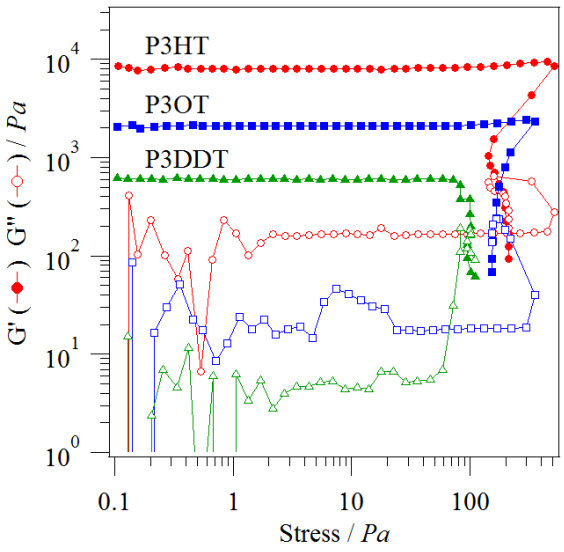

Figure 2.12. Oscillatory rheology stress sweep for a 30 mg/mL P3AT organogels formed in solvent/poor-solvent mixtures. The P3HT gel is in a 47.5 wt% Dodecane/52.5 wt% DCB mixture, the P3OT gel is in a 65.0 wt% Dodecane/35.0 wt% DCB mixture, the P3DDT gel is in a 69.1 wt% Dodecane/30.9 wt% DCB mixture.

Another important attribute of viscoelastic network structures is the frequency behavior at a given stress/strain perturbation. A cross-over (*G'*=G") in the frequency dependent behavior indicates a characteristic relaxation time of the network.[19] Figure 2.13 shows the characteristic frequency sweep of a P3AT network, which are found to be viscoelastic solids over a wide range of frequencies.

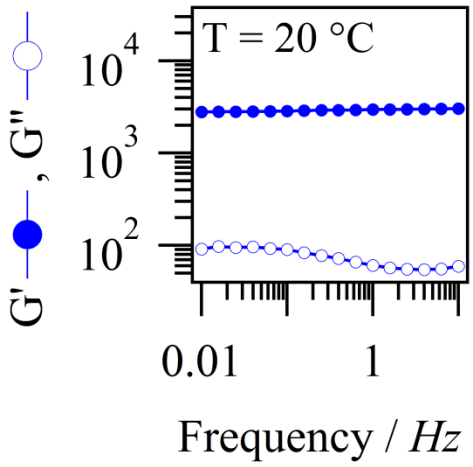

Figure 2.13. Frequency dependent rheology of an equilibrium 30 mg/mL P3HT organogel in p-xylene.

2.3 Dielectric Spectroscopy

AC dielectric spectroscopy is used to probe the electrical properties of P3AT networks. Dielectric spectroscopy (i.e., impedance spectroscopy) is an oscillatory technique with similar principles to rheology. Impedance is the resistance to current flow. Either a current (*I*) is applied and a voltage (*V*) is measured or vice versa. In this work, a sinusoidal voltage is applied and the current is measured. The depiction of a current-voltage relationship can be seen in Figure 2.14.

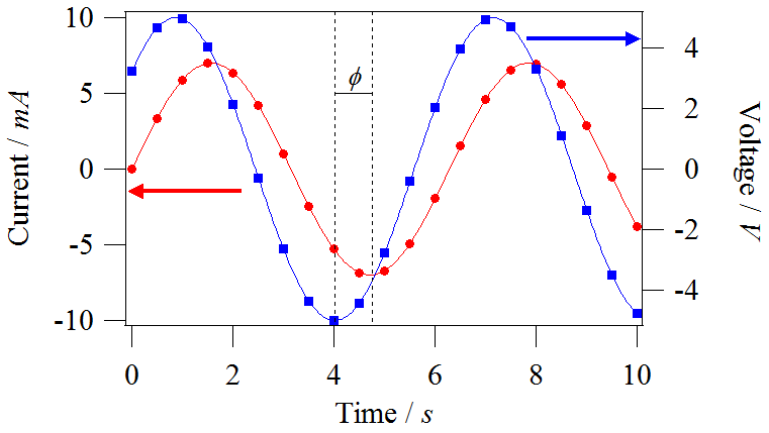

Figure 2.14. Simulated current-voltage relationship for dielectric spectroscopy measurements.

For a purely resistive circuit, there will be no lag between the applied voltage and the measured current, leading to a phase angle (ϕ) of 0º.[20] For purely capacitive circuit, the applied voltage and the measured current will be completely out of phase (ϕ = 90º). It is common for complex circuits, such as conjugated polymer networks, to have both resistive and capacitive elements that change as a function of frequency. In these cases, it can be useful to utilize standard plots.

One of the most useful standard plots in impedance spectroscopy is the Nyquist plot, which plots the resistive impedance (Z') against the reactive impedance (Z'').[20] The impedance can be calculated using:

$$Z = \frac{V_0}{I_0} e^{i\phi} \tag{2.14}$$

$$Z = Z' + i \cdot Z'' \tag{2.15}$$

where V_0 and I_0 are the voltage and current amplitude, respectively. The Nyquist plot of a fully formed conjugated polymer network can be seen in Figure 2.15. The DC resistance of the samples can be determined by the difference between the two ends ($Z'' \rightarrow 0$) of the "semi-circle".[20] More complex equivalent circuit fitting is also possible and is utilized in Chapter 4.

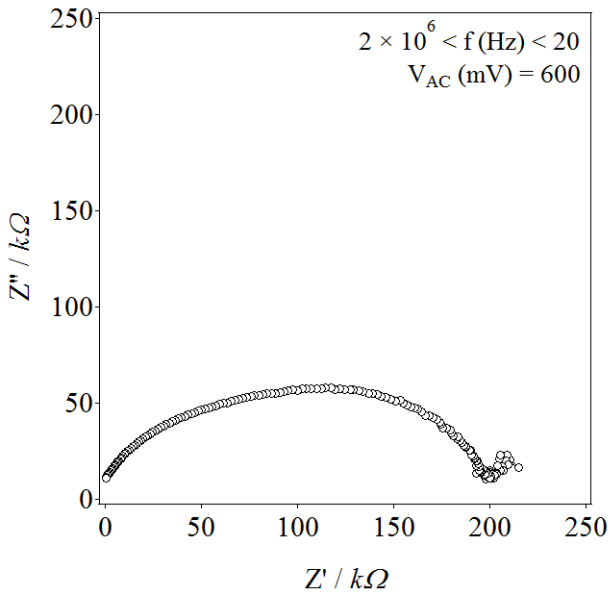

Figure 2.15. Nyquist plot of an equilibrium 30 mg/mL P3HT organogel in 43.9% dodecane/56.1% DCB at 30 °C.

It is often useful to evaluate other data representations, such as the admittance (Y) and complex dielectric constant (ε^*). The admittance is a measurement of how easily a circuit will flow current and can be derived from impedance (Z):[20]

$$Y \equiv \frac{1}{Z} \tag{2.16}$$

$$Y = G + i \cdot B = \frac{Z' - i \cdot Z''}{(Z')^2 + (Z'')^2} \tag{2.17}$$

where G is the conductance and B is the susceptance. The conductance can be utilized to calculate the frequency dependent conductivity (σ) of the sample:

$$\sigma = G \cdot \frac{h}{A} \tag{2.18}$$

where A is the surface area of the electrode and h is the thickness of the sample between electrodes. The complex dielectric constant provides information about the stored energy (ε') within a medium and the dissipated energy within a medium (ε''). These can be calculated using:

$$\varepsilon' = \frac{B \cdot d}{A \cdot \omega \cdot \varepsilon_o} \tag{2.19}$$

$$\varepsilon'' = \frac{G \cdot d}{A \cdot \omega \cdot \varepsilon_o} \tag{2.20}$$

where ε_o is the permittivity of free space (ε_o = 8.854×10-^{12} F/m) and ω is the angular frequency.

For all of these measurements, a small-amplitude voltage must be applied to measure the current-voltage properties of a conjugated polymer network. This perturbation voltage (V_{AC}) should be high enough to produce reasonable data quality (i.e. low noise), but low enough to be within the linear impedance response (LIR) region. The LIR corresponds to the voltage range over which there is a linear response to increasing voltage-current amplitude.[20] Figure 2.16 shows the LIR for P3HT networks formed in different solvents. All networks probed in this work have a LIR for V_{AC} < 0.6 V therefore common perturbation voltages fall within the range of 200 – 600 mV.

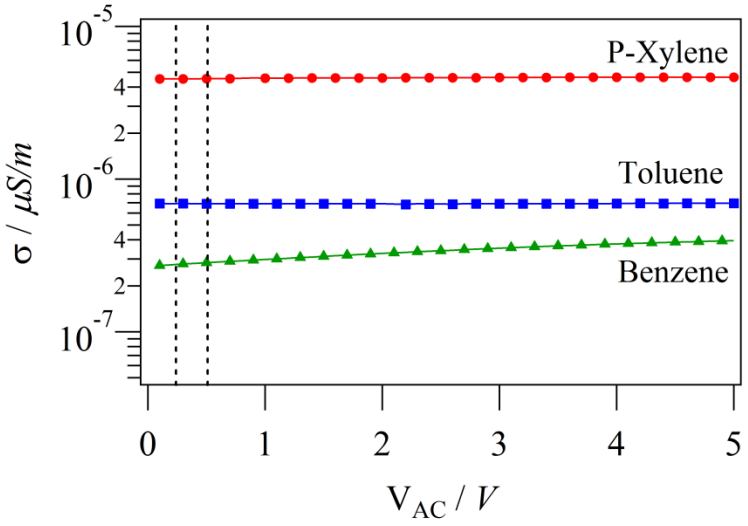

Figure 2.16. AC voltage sweep at 2 kHz of 30 mg/mL P3HT organogels formed in different organic solvents. Dashed lines represent the common V_{AC} range used in these experiments.

2.4 Simultaneous Techniques

In order to optimize the multi-scale structure of conjugated polymer networks, there is a need to understand the self-assembly process and progression of intermediate structures. In this work, we combine three complementary experimental techniques to simultaneously probe structure and property development occurring during the sol-gel transition in P3AT organogels.[18] Three experimental setups allow for direct correlation of structural, mechanical and electrical properties of developing gels. Dielectric-SANS (Figure 2.17) allows for simultaneous probing of the developing structure and electrical properties. Rheology-SANS (Figure 2.18) allows us to simultaneously probe the structural and mechanical properties. Finally, dielectric-rheology (Figure 2.19) provides a direct link between the developing mechanical and electrical properties.

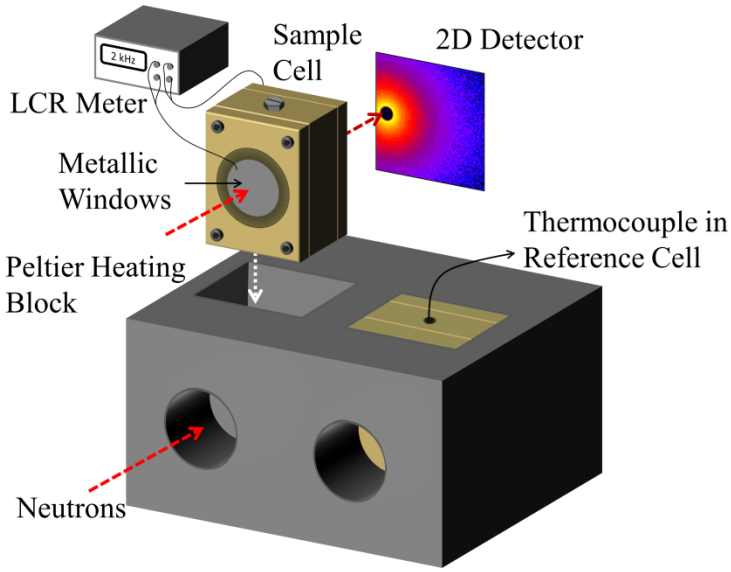

Figure 2.17. Schematic of a simultaneous SANS-dielectric spectroscopy experiment. *Figure designed by Dr. Kathleen Weigandt.*

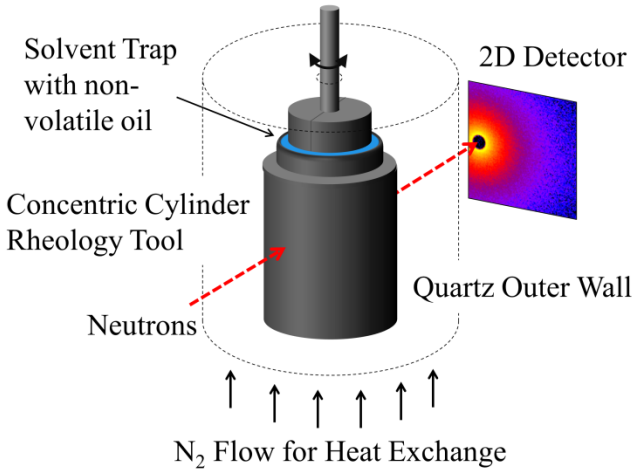

Figure 2.18. Schematic of a simultaneous rheology-SANS experiment. *Figure designed by Dr. Kathleen Weigandt.*

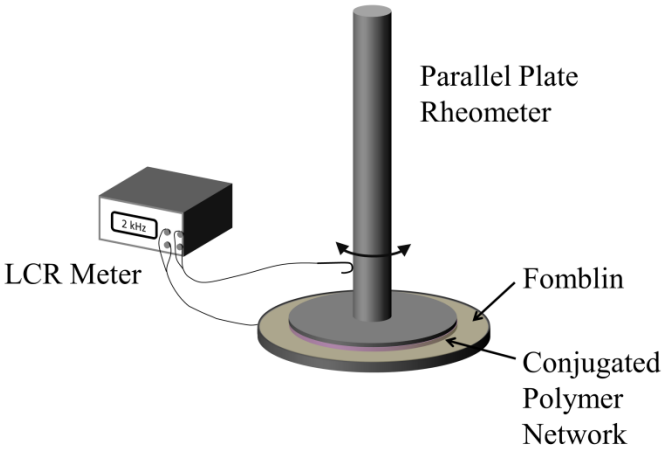

Figure 2.19. Schematic of a simultaneous dielectric spectroscopy-rheology experiment. *Figure designed by Dr. Kathleen Weigandt.*

Figure 2.17 shows the sample environment for a dielectric-SANS experiment which includes a novel, electrically isolated demountable sample cell (polyether ether ketone) with a 1 mm pathlength and polished metal (e.g., aluminum or stainless steel) windows. The hot polymer solution (80 ºC) was loaded into the room temperature sample cell, sealed and then re-heated to 80 ºC to ensure full dissolution of the polymer. Temperature control was maintained by using a

Peltier heating block and the accuracy was monitored by a placing a j-type thermocouple into an identical sample cell filled with ethylene glycol.

The rheology-SANS experiments (Figure 2.18) were performed using an Anton Paar Physica MCR 501 rheometer with a titanium concentric cylinder geometry.[21] A solvent trap filled with a non-volatile, low viscosity silicone oil was utilized to prevent evaporation. After loading the hot (80 ºC) P3AT solution, the samples were re-heated to 80°C to ensure the polymer remained fully dissolved prior to experimentation.

Dielectric-rheology experiments (Figure 2.19) utilized a parallel plate geometry with a ceramic shaft insert that is used to electrically isolated the sample electrodes from the electronics of the rheometer. Electrical contact is created between a gold wire and the upper tool geometry (stainless steel) and also from the bottom tool (stainless steel). The conductivity and other electrical properties are then measured across the sample gap with the parallel plates of the rheometer also acting as parallel electrodes. The use of stainless steel plates ensures that corrosion and oxidation does not impact the electrical measurements. The torque created by the constant frictional resistance of the gold lead wire on the upper tool geometry results in a constant background modulus. To perform an experiment, the bottom plate was pre-heated to 40 °C prior to loading the hot polymer solution (80 °C).[22] Once loaded, the solution was rapidly cooled to induce self-assembly and gelation. After the solution had solidified (~ 1 minute) a fluorinated non-conductive oleophobic liquid (Fomblin Y 25/6) was added to the outer edge of the sample geometry to fully suppress the evaporation of the organic solvent. The gel was then re-heated to 80 °C for 5 minutes to completely re-dissolve the gel before the experiments were performed.

Dielectric-SANS, rheology-SANS and dielectric-rheology also provide identical measurements of the structure, rheology and dielectric properties in different sample environments. Therefore, a comparison of the results from these techniques should yield identical properties when the experimental conditions match. In Figure 2.20, rheology data collected from rheology-SANS and dielectric-rheology are compared for 1 ºC/min temperature sweeps to induce gelation in different solvents. As expected, it is found that there is very good agreement in the rheology from the dielectric-rheology and rheology-SANS experiments despite the different geometries that are used (concentric cylinder and parallel plate fixtures). The only significant difference is observed in the moduli of the samples when they are fully dissolved. This is the result of the friction caused by the wire that is utilized to collect simultaneous electrical measurements (Figure 2.19). Furthermore, there is very good agreement between the shapes and transition temperatures for the normalized dielectric-SANS and dielectric-rheology measurements (Figure 2.21). The consistency between measurement techniques further demonstrates that the combination of complementary rheology-SANS, dielectric-SANS and dielectric-rheology measurements allows for a rigorous analysis of structural-mechanical-electrical property relationships of developing P3HT organogels.

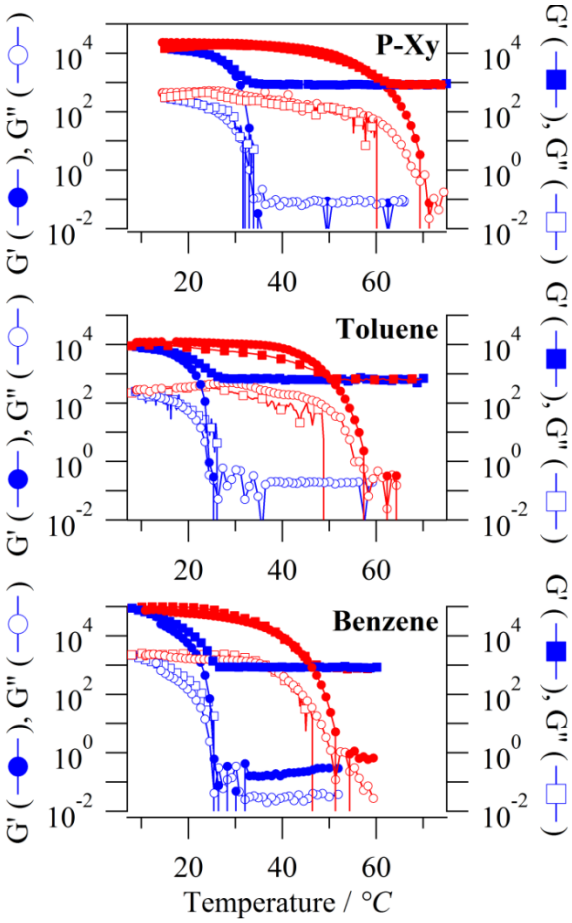

Figure 2.20. Rheology-SANS (left axis) and dielectric-rheology (right axis) of P3HT organogels formed and dissolved in p-xylene, toluene and benzene where *G'* is the elastic modulus and *G"* is the loss modulus. Blue markers represent the cooling ramp (gelation) while red markers represent the re-heating ramp (re-dissolution).

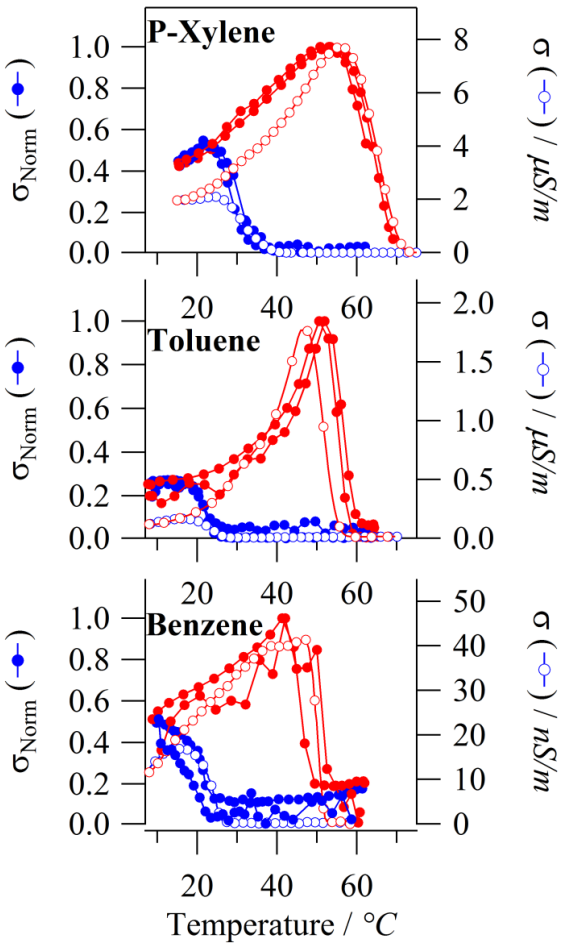

Figure 2.21. Normalized conductivity from dielectric-SANS (left axis) and ac conductivity of dielectric-rheology (right axis) for P3HT organogels formed (blue) and re-dissolved (red) in different organic solvents.

2.5 UV-visible Spectroscopy

UV-visible spectroscopy is utilized to measure the absorbance of conjugated polymers over the UV and visible light spectrum (200 – 1100 nm). Conjugated polymer absorbance is a design parameter for organic photovoltaic devices. High efficiency OPV devices will utilize conjugated polymers with absorbance values that overlap well with the solar spectrum.[16, 23] Figure 2.22 shows the typical absorbance spectrum for a dissolved P3AT in solution.

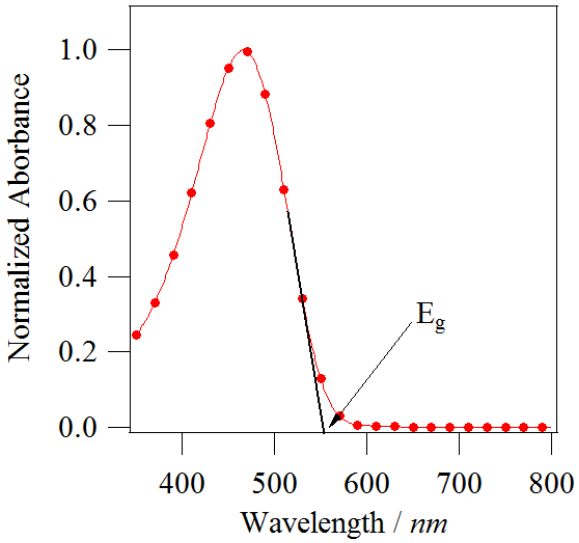

Figure 2.22. Absorbance of 0.02 mg/mL dissolved P3HT in 1,2-dichlorobenzene. The solid black line highlights the bandgap (E_g) extrapolation.

The absorbance of conjugated polymers is strongly dependent on polymer chemistry and the solvent environment. The Beer-Lambert law shows that the absorbance (A) is the product of the concentration (C), sample path length (l) and extinction coefficient (ε):

$$A(\lambda)=C\cdot l\cdot \varepsilon(\lambda) \tag{2.21}$$

The extinction coefficient is typically measured from the peak absorbance. This is in contrast with the bandgap (E_g) of a conjugated polymer, which can be estimated from the extrapolation at high wavelength, as seen in Figure 2.22. Conjugated polymer peak height and position are dependent on the solvent environment, as described in Chapter 8, and therefore these relationships can only be developed between single solvent-polymer pairs.

The absorbance of conjugated polymers is known to change drastically upon crystallization and π-π stacking.[24, 25] The absorbance profile of a semi-crystalline P3AT fiber can be seen in Figure 2.23. The crystalline ordering of P3ATs can be quantitatively evaluated using the exciton bandwidth (W) theory developed by Clark and coworkers.[26] The exciton bandwidth is a ratio that quantifies the inter-chain vs intra-chain π-bond overlap. The inter-chain ordering

within the crystalline structure can be expected to play a significant role in the charge transport properties of the network, where lower W values correspond to a more organized structure.[27] The exciton bandwidth can be calculated using:

$$\frac{A_{0-0}}{A_{0-1}} \approx \left(\frac{1 - 0.24W / E_p}{1 + 0.073W / E_p} \right)^2 \tag{2.22}$$

where $A_{0\text{-}0}$ and $A_{0\text{-}1}$ are the absorbance values defined in Figure 2.23 and E_p is the C=C symmetric stretch (0.18 eV) that dominates the electronic transition.[26]

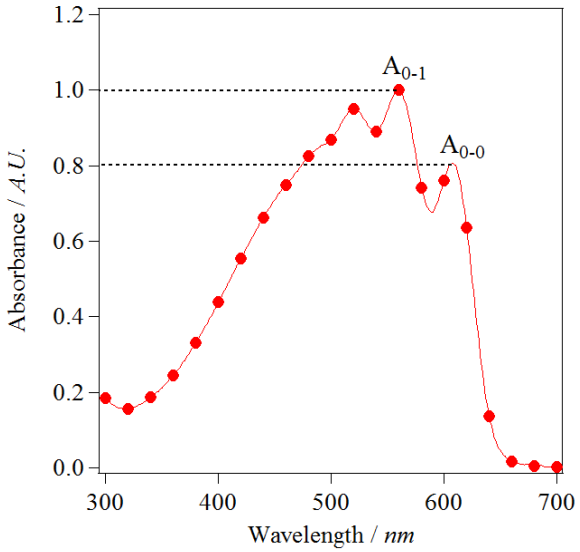

Figure 2.23. Absorbance of 2 mg/mL semi-crystalline P3HT in p-xylene. Dashed lines highlight the $A_{0\text{-}0}$ and $A_{0\text{-}1}$ absorbance peaks.

2.6 References

1. Liberatore, M. W.; Nettesheim, F.; Vasquez, P. A.; Helgeson, M. E.; Wagner, N. J.; Kaler, E. W.; Cook, L. P.; Porcar, L.; Hu, Y. T. *Journal of Rheology* **2009,** 53, (2), 441-458.
2. Millon, L. E.; Nieh, M.-P.; Hutter, J. L.; Wan, W. *Macromolecules* **2007,** 40, (10), 3655-3662.
3. Weigandt, K. M.; Pozzo, D. C.; Porcar, L. *Soft Matter* **2009,** 5, (21), 4321-4330.
4. Lindner, P., *Neutrons, X-Rays and Light: Scattering Methods Applied to Soft Condensed Matter*. Elsevier Science: Amsterdam, 2002.
5. Glinka, C.; Barker, J.; Hammouda, B.; Krueger, S.; Moyer, J.; Orts, W. *Journal of Applied Crystallography* **1998,** 31, 430-445.
6. Barker, J. G.; Glinka, C. J.; Moyer, J. J.; Kim, M. H.; Drews, A. R.; Agamalian, M. *Journal of Applied Crystallography* **2005,** 38, 1004-1011.
7. Kline, S. *Journal of Applied Crystallography* **2006,** 39, 895-900.
8. Guinier, A.; Fournet, G., *Small-Angle Scattering of X-rays*. Wiley: New York, 1955.
9. Sears, V. F. *Neutron News* **1992,** 3, (3), 29-37.
10. Butler, P.; Alina, G.; Hernandez, R. C.; Doucet, M.; Jackson, A.; Kienzle, P.; Kline, S.; Zhou, J. SASView for Small Angle Scattering Analysis. http://www.sasview.org/
11. Yang, X. N.; Loos, J.; Veenstra, S. C.; Verhees, W. J. H.; Wienk, M. M.; Kroon, J. M.; Michels, M. A. J.; Janssen, R. A. J. *Nano Letters* **2005,** 5, (4), 579-583.
12. Mittelbach, P.; Porod, G. *Acta Physica Austriaca* **1961,** 14, 185-211.
13. Chen, C. Y.; Chan, S. H.; Li, J. Y.; Wu, K. H.; Chen, H. L.; Chen, J. H.; Huang, W. Y.; Chen, S. A. *Macromolecules* **2010,** 43, (17), 7305-7311.
14. Liu, J.; Arif, M.; Zou, J.; Khondaker, S. I.; Zhai, L. *Macromolecules* **2009,** 42, (24), 9390-9393.
15. Samitsu, S.; Shimomura, T.; Ito, K. *Thin Solid Films* **2008,** 516, (9), 2478-2486.
16. Yang, X.; Loos, J. *Macromolecules* **2007,** 40, (5), 1353-1362.
17. Hammouda, B. *Advances in Polymer Science* **1993,** 106, 87-133.
18. Newbloom, G. M.; Weigandt, K. M.; Pozzo, D. C. *Soft Matter* **2012,** 8, (34), 8854-8864.
19. Macosko, C. W., *Rheology Principles, Measurements, and Applications*. Wiley-VCH: New York, 1994.
20. Lasia, A., *Modern Aspects of Electrochemistry*. Kluwer Academic/Plenum Publishers: New York, 1999.
21. Porcar, L.; Pozzo, D.; Langenbucher, G.; Moyer, J.; Butler, P. D. *Review of Scientific Instruments* **2011,** 82, (8), 083902-7.
22. Newbloom, G. M.; Weigandt, K. M.; Pozzo, D. C. *Macromolecules* **2012,** 45, (8), 3452-3462.
23. Wohrle, D.; Meissner, D. *Advanced Materials* **1991,** 3, (3), 129-138.

24. Berson, S.; De Bettignies, R.; Bailly, S.; Guillerez, S. *Advanced Functional Materials* **2007,** 17, (8), 1377-1384.
25. Chang, J.-F.; Sun, B.; Breiby, D. W.; Nielsen, M. M.; Sölling, T. I.; Giles, M.; McCulloch, I.; Sirringhaus, H. *Chemistry of Materials* **2004,** 16, (23), 4772-4776.
26. Clark, J.; Chang, J.-F.; Spano, F. C.; Friend, R. H.; Silva, C. *Applied Physics Letters* **2009,** 94, (16), 163306-3.
27. Kim, B.-G.; Jeong, E. J.; Park, H. J.; Bilby, D.; Guo, L. J.; Kim, J. *ACS Applied Materials & Interfaces* **2011,** 3, (3), 674-680.

Chapter 3

Colloidal Networks of Fibrillar Poly(3-hexylthiophene)

3.1 Motivation

Conjugated polymer semiconductors have seen a wide range of applications in the pursuit of low-cost, easy-to-manufacture electronic devices. Poly(3-hexylthiophene) (P3HT) is one of the most studied conjugated polymers due to its high hole mobility, up to 0.1 $cm^2 V^{-1} s^{-1}$, solution processability and capacity for self-assembly.[1, 2] The morphology of conjugated polymers, such as P3HT, is a critical design parameter for high-performance organic field-effect transistors (OFETs) and organic photovoltaics (OPVs).[3, 4] Polymer crystallization induced by π-π stacking, alkyl side-chain interactions and solubility changes allows for an increase of conjugation length and for efficient charge transport.[5] In contrast, frequent conjugation breaks and weak π-orbital overlaps that are seen in the amorphous phase result in a decrease of charge carrier mobility.[6] An interconnected crystal network represents an ideal structure for organic semiconductor layers because it combines the high hole mobility of the crystalline domains with a continuous path for charge transport.[2, 7, 8]

P3HT crystallization can proceed directly in the solution phase through a preparation process that is commonly known as the "whisker method".[9, 10] In this method, P3HT chains have been shown to self-assemble into orthorhombic fibers, with estimated dimensions of 2-10 nm in height, 15-25 nm in width and many micrometers in length, in a process that is driven by changes to the solubility of the polymer.[11, 12] This method has also been applied to develop high efficiency OPVs based on poly(3-butylthiophene).[13, 14] One advantage presented by generating devices using the "whisker method" is that the parameters controlling polymer self-assembly are decoupled from those that control the coating process so that both can be optimized separately. However, fabricating OPV devices from individual fiber dispersions (e.g., whiskers) may have drawbacks because the direction of the shear field applied during coating can lead to a planar orientation of the fibers with respect to the substrates and result in limited charge transport in the vertical direction.

Some researchers have also observed a branching network structure for coated crystalline P3HT dispersions using atomic force microscopy (AFM) and transmission electron microscopy (TEM).[7, 15] However, limitations in resolution of such techniques prevent distinction between overlapping fibers and colloidal fiber networks. Furthermore, the analysis of coated films prevents the investigation of the structures and self-assembly directly in the dispersed state. These proposed networked structures, also obtained from self-assembly in solution, are in contrast with the individual long (> 1 μm) nanofibers that are typically formed in other thin-film coating processes.[2, 16] A network structure of P3HT nanofibers could be ideal for both OFET and OPV devices because the three-dimensional and interconnected fiber structure would significantly enhance charge transport in all directions. Furthermore, polymer self-assembly is

decoupled from the coating process and can be optimized through controlled changes in temperature and solvent quality.

In order to optimize charge transport in these systems it is also critical to fully understand the nature of the fiber junctions and the structure of the network. For example, fibrillar contacts and overlaps, observed in thin film crystallization, are fundamentally different from fibrillar bifurcations (i.e., splitting fibers). The π-π stacking structure of the thiophene ring causes insulating alkyl chains to orient in such a way that they "coat" the outside of the semiconducting fiber.[15] Charge transport between overlapping fibers requires charges to tunnel through the insulating alkyl layers. In contrast, a bifurcating fiber provides a direct, interconnected pathway for charge transport. The overall size and distribution of fibers within the network structure will also impact charge transport between electrodes. So far, these morphological features have not been explicitly considered in the design of organic electronic devices even though differences in these structural parameters could influence the electrical properties.

This chapter focuses on characterizing the nature of the network structures that arise from the colloidal self-assembly of P3HT in various aromatic solvents. Understanding the mesoscopic structure of the network is critical to further optimize charge transport and to improve the performance of OFETs and OPV devices.[4] Because crystallization is a solubility driven process, the use of different aromatic solvents allows for careful control over the intermolecular interactions between P3HT and the solvent.[12] In addition, this chapter evaluates the network structure directly *in situ* using small angle neutron scattering (SANS) and ultra-small angle neutron scattering (USANS). Previous researchers have primarily utilized various *ex situ* microscopy techniques to evaluate these networks even though the coating and drying process could significantly affect the structures observed in microscopy images.[17] In this chapter, the

fibrillar and network structures are directly evaluated by fitting models of the structures to the one-dimensional (1D) SANS/USANS profiles of the dispersed P3HT networks. Scanning TEM (sTEM) and UV-Visible Spectroscopy (UV-Vis) are also utilized to augment and validate the accuracy of the scattering models and to show that solvent choice can have a significant effect on the network structure and affect the resulting electrical properties.

3.2 Experimental Methods

Materials: Sepiolid P200 poly(3-hexylthiophene) (P3HT) was used as purchased from Rieke Metals (Lincoln, NE). The molecular weight (M_w) and polydispersity index (PDI) were characterized using gel permeation chromatography (GPC) and found to be: M_w = 24,060 g/mol, PDI = 2.04 with respect to polystyrene standards. The regioregularity of the material was reported by the manufacturer to be greater than 98%. Hydrogenated solvents: p-xylene, toluene, styrene and benzene were purchased from Sigma-Aldrich (St. Louis, MO) and used as received. Deuterated solvents: D10-pxylene (D > 98%), D8-styrene (D > 98%), D8-toluene (D > 99.5%) and D6-benzene (D > 99.5%) were purchased from Cambridge Isotopes (Andover, MA) and used as received for SANS and USANS experiments to increase the scattering contrast and decrease the incoherent scattering background.

Sample Preparation: Samples were prepared by adding P3HT to an aromatic solvent and heating to 80 ˚C until the polymer was fully dissolved (bright orange solution). The polymer solution was then removed from heat, cooled to room temperature and allowed to crystallize over time. The time required to reach equilibrium varied from 12 hours for p-xylene samples to 1 week for benzene samples. All samples were made at the same concentration of P3HT (0.2 wt%) unless otherwise stated.

Ex Situ Experiments: Samples were loaded into 100 μm quartz cuvettes and the absorbance was measured using a Thermo Evolution 300 UV-Visible Spectrophotometer. Images of the crystallites were taken using scanning TEM on a FEI Tecnai G2 F20 instrument and analyzed using Image J software.[18] Samples were further diluted by a factor of 40 prior to deposition onto a TEM grid in order to analyze the structure of the individual colloidal network particles.

Small Angle Scattering: Small angle neutron scattering (SANS) and ultra-small angle neutron scattering (USANS) were performed at the NIST Center for Neutron Research in Gaithersburg, Maryland. SANS measurements were performed on the NG3 and NG7 instruments using standard configurations to cover a broad q-range ($0.003 < q$ ($Å^{-1}$) < 0.3).[19] SANS experiments were also performed at the ORNL High Flux Isotope Reactor in Oak Ridge, Tennessee. SANS measurements were performed on the CG2 instrument using standard configurations to cover a broad q-range ($0.005 < q < 0.2$ $Å^{-1}$). USANS measurements were performed at NIST on the BT5 perfect crystal diffractometer further extending the q-range to 4×10^{-5} $Å^{-1}$.[20] The scattering length density of P3HT was determined using contrast variation experiments found in Chapter 10.1.

Electrical Characterization: The charge transport properties of P3HT networks were characterized by fabricating and testing organic field-effect transistors (OFETs). OFETs were made on a heavily n-doped silicon substrate with a 200 nm thick thermal oxide. The devices were prepared from the same substrate, at the same time and in the same way to ensure that the calculated mobilities would be comparable. Gold source–drain electrodes with a thin chromium adhesive layer were photolithographically patterned on a substrate to define transistor channels with a width of 800 μm and a length of 20 μm. The surface of silicon dioxide was treated with

octyltrichlorosilane to promote charge transport. P3HT crystallized in different aromatic solvents was drop-cast onto a substrate in an argon-filled glove box to minimize insufficient coverage of charge transport channels and to prevent unintentional doping from ambient air. In addition, a P3HT sample in p-xylene was heated to 110 °C and spin-coated directly in the amorphous state to serve as a control. Deposited thin-films were dried in a vacuum chamber for a few hours. Electrical testing of devices was carried out by using an HP4145B semiconductor parameter analyzer under nitrogen environment. Field-effect mobilities were calculated from the saturation region of the transfer curves.[1, 21, 22] *All OFET measurements in this work were completed with the help of Prof. Felix. S. Kim and Prof. Samson A. Jenekhe.*

3.3 Results and Discussion

3.3.1 Self-Assembly in Various Solvents Affects Structural Features

The structure of crystalline P3HT is strongly dependent on solvent choice and concentration, as seen in Figure 3.1 and Figure 3.2. As described in Chapter 2, the structural fractal dimension (D_f^S) describes the density of fibers in the network whereas the onset of this fractal behavior (d_{onset}) corresponds to the minimum distance at which fibrillar junctions start to occur. Thus, the combination of D_f^S and d_{onset} describe the fibrillar junction density over a given length scale. The fibrillar density of an individual network should play an important role in charge transport since it is related to the overall interconnectivity.

Figure 3.1 shows that the fractal dimension is not strongly dependent on concentration over the range of 0.1 to 1.0 wt%. However, the onset of fractal behavior, d_{onset}, systematically shifts to smaller length scales as concentration increases. This indicates that the fibrillar junctions and the network structure start to affect the scattering data at shorter length scales with

increasing P3HT concentration. This corresponds well with the gel-phase concentration dependence that is reported by Koppe and coworkers.[23, 24] At 1.0 wt%, P3HT exhibits gel-like elastic behavior at room temperature.

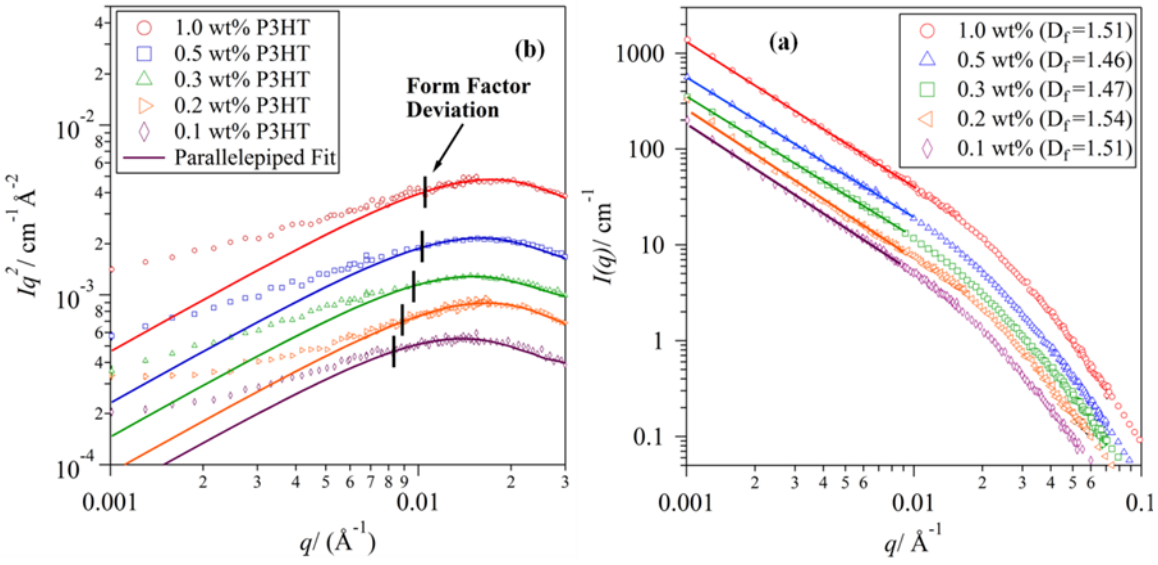

Figure 3.1. (a) I vs. q scattering profile for P3HT crystallized in p-xylene. The power law fit and corresponding fractal dimension are shown for the concentration series. (b) Iq^2 plot of the SANS data, for P3HT crystallized in p-xylene, to highlight the "knee" corresponding to the fibrillar cross-section and the corresponding parallelepiped model fit. The deviation between the model and scattering is determined from this plot and is utilized to delineate the onset of the fractal region.

Figure 3.2 shows that samples prepared in toluene have a high fractal dimension ($D_f^S \sim 3$) and low d_{onset} suggesting the formation of very dense network domains. These network structures are clearly different from those prepared in p-xylene where there is a significantly lower fractal dimension ($D_f^S \sim 1.5$) and high d_{onset}. Unfortunately, the large network features could not be thoroughly evaluated in benzene because USANS data could not be collected fast enough before significant settling would occur.

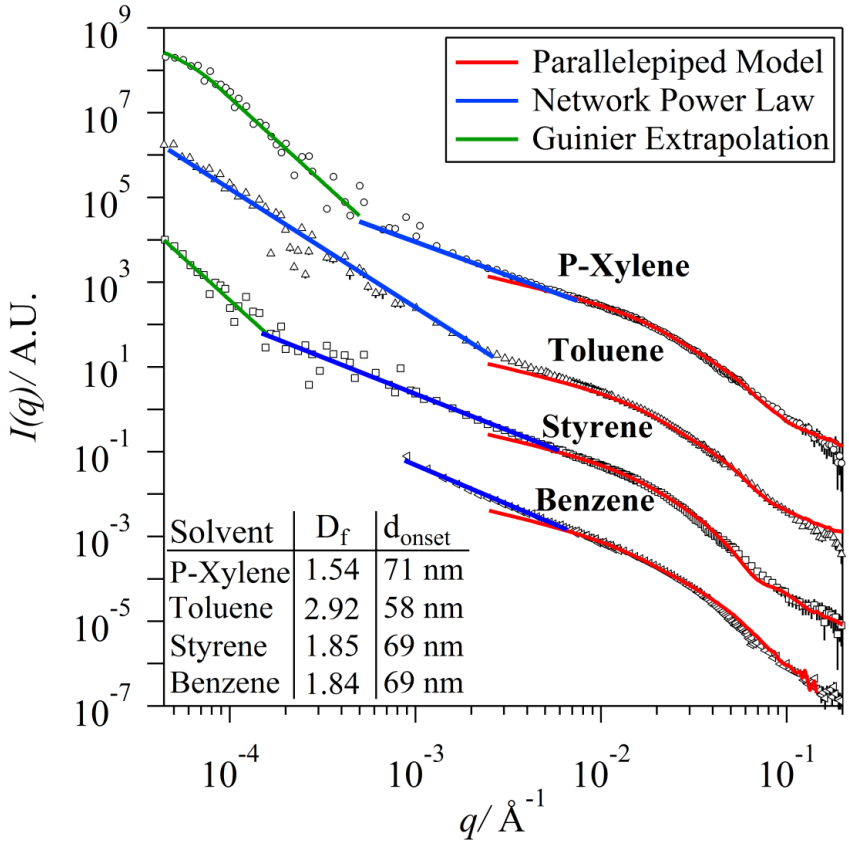

Figure 3.2. SANS and USANS of 0.2 wt% P3HT crystallized in different aromatic solvents. The combined model (Eq 2.6) fit, power-law fit and Guinier extrapolations are shown within their appropriate scattering regions. The fractal dimension and the onset of fractal behavior are listed as an inset. USANS data could not be collected for P3HT crystallized in benzene because of the short time frame over which precipitation occurred.

The persistence of the self-similar behavior towards low-q also has important implications for charge transport because it characterizes the overall size of the colloidal network particles. For p-xylene and styrene, a surface scattering region ($I(q) \sim q^{-4}$) occurs at the lowest q values and for p-xylene a Guinier region is clearly observed in the USANS region. This is ascribed to the scattering from the interface between the colloidal networks and the solvent. In toluene, neither of these features is observed suggesting that the majority of particles are larger than the measurement range of the USANS configuration.

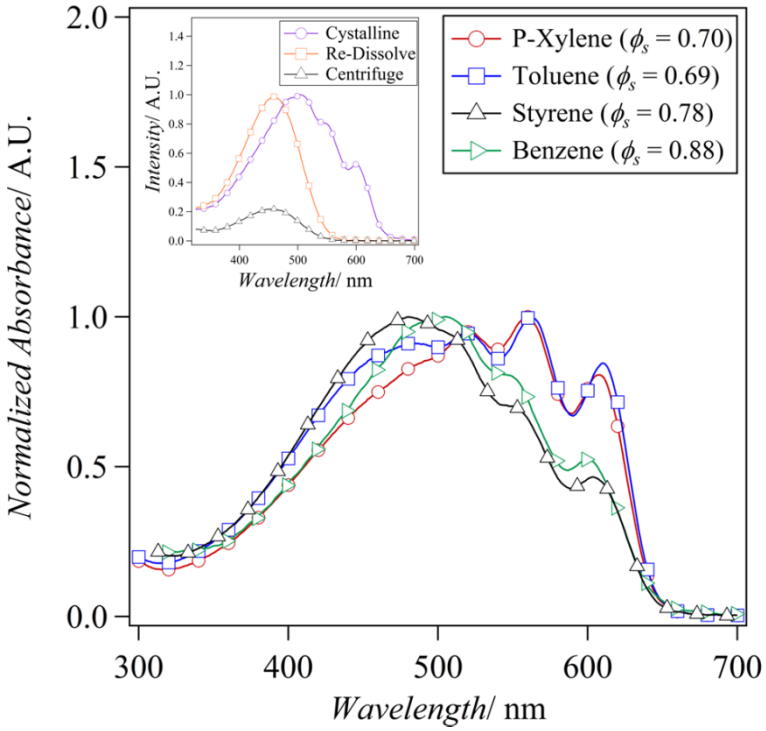

Figure 3.3. Absorption spectrum of 0.2 wt% P3HT dispersed in different aromatic solvents and allowed to crystallize for 1 month. Inset: Absorption spectrum for P3HT crystallized in solution, a crystallized P3HT solution that was re-dissolved at 80 °C and the supernatant of a crystallized P3HT solution with solids removed by centrifugation and filtration.

Fitting of Equation 2.6 to the P3HT scattering profiles, with absolute scaling, allows for the determination of the fraction of P3HT that is found in the parallelepiped fibers, Ψ_f. A similar value can also be obtained independently by removing the solid P3HT network particles from solution, measuring the absorbance of the remaining dissolved P3HT fraction using UV-Vis and calculating the concentration of the dissolved phase as seen in Figure 3.3. The method described by Berson and coworkers for removing solid P3HT from the dispersions, using a combination of centrifugation and filtration, was also utilized here.[25] The samples were also re-dissolved at 80 °C and the P3HT concentration was measured to corroborate that no evaporative losses occur during the crystallization process. The absorbance values of the original (re-dissolved) sample and of the supernatant of the separated sample, at the characteristic absorption peak in the

amorphous state ($\lambda \sim 450$ nm), were used to calculate the solids fraction (ϕ_s). The results of the two independent analyses are included in Table 3.1.

$$\phi_s = 1 - \frac{A_{centrifuged}}{A_{re-dissolved}} \tag{3.1}$$

The optical transitions associated with P3HT crystallization have been previously characterized in the literature.[11, 25] Figure 3.3 shows the normalized absorbance for P3HT crystallized in solution for all solvents. All of the samples show an optical red-shift upon crystallization and confirmation of the presence of inter-chain π-π stacking through the characteristic absorbance peak at ~ 605 nm.[25] However, there is a significant difference in the magnitude of the inter-chain π-stacking peak depending on the solvent choice.

The crystalline ordering can be quantitatively evaluated using the exciton bandwidth theory developed by Clark and coworkers, as described in Chapter 2.[26] The exciton bandwidth (W) was calculated to be 60, 47, 116 and 112 meV for p-xylene, toluene, styrene and benzene, respectively. Lower W values correspond to a more organized structure. P3HT crystallized in p-xylene and toluene forms a well-ordered crystalline structure, whereas styrene and benzene samples show significantly lower ordering. The inter-chain ordering within the crystalline structure can be expected to play a significant role in the charge transport properties of the network.[27] It is important to note that the crystallinity of these samples can only be discussed in the context of the UV-Vis spectroscopy and only refers to the inter-chain π- π stacking. Fitting of Equation 2.6 in SANS provides the fraction of polymer that is in fibrillar form (Ψ_f), but does not provide any quantitative assessment of the P3HT crystallinity within the fibers.

The structures that were proposed through the analysis of the SANS and USANS data are also in good agreement with the scanning transmission electron microscopy (sTEM) images of samples that were dilute 40x and coated over grids. The samples were diluted in order to

evaluate the structure of the individual network particles. TEM experiments were also performed on the original samples without dilution to verify that the structures did not change during this process (Figure 3.4).

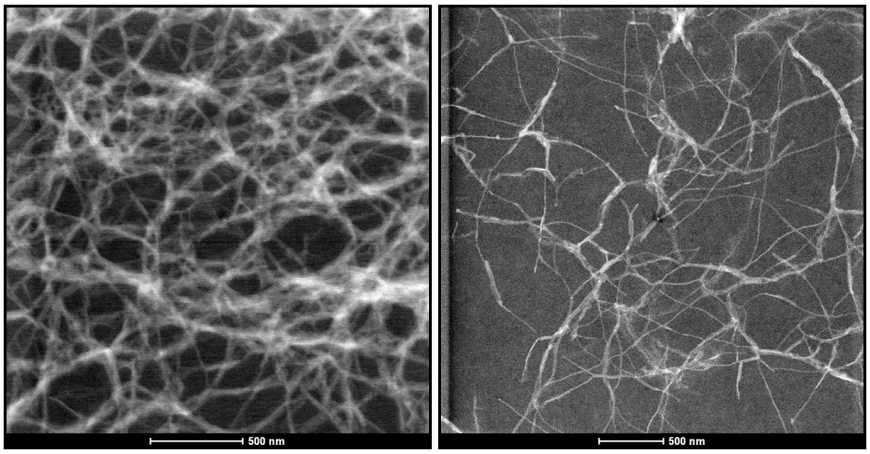

Figure 3.4. TEM micrographs of P3HT crystallized in benzene without dilution (left) and after 40x dilution (right).

Figure 3.5 clearly shows the differences in network densities in the proposed structures. The images also help to illustrate the relationship between the onset of self-similar behavior (d_{onset}) and fibrillar junction density between the networks formed in different solvents. Solvent-polymer interactions lead to a variety of mesoscopic network structures that can be accurately manipulated through small changes in solvent quality. However, these differences could not be correlated exclusively to the solubility of P3HT in the different solvents. On the other hand, the macroscopic phase segregation that exists for benzene samples is most likely related to the limited solubility of P3HT in benzene.

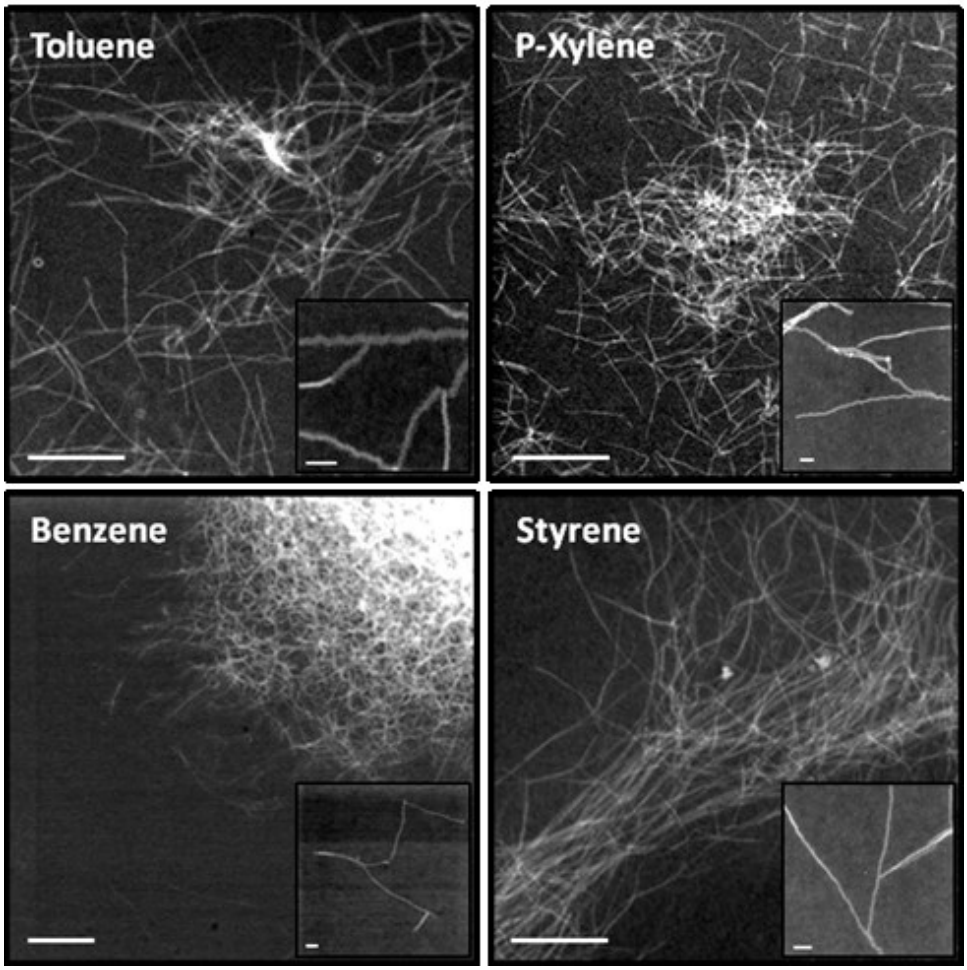

Figure 3.5. sTEM images of coated colloidal P3HT networks, diluted 40x, crystallized in different aromatic solvents. The primary images highlight the network structure with scale bars at 2 μm. The inset images highlight the fibers with scale bars of 100 nm.

The inset images in Figure 3.5 highlight the fact that fibrillar bifurcations form regardless of the solvent choice. However, from sTEM, it was clearly more difficult to find this structural feature in styrene samples than in the other samples. This is presumably a result of the higher solubility of the polymer and of its effect on the kinetics of network growth. Figure 3.6 highlights the three different fibrillar junction types that are present in all samples regardless of the solvent choice. Fibrillar overlap is the most common junction type and this can be easily distinguished in sTEM. At first inspection, the differences between fibrillar contact and bifurcation can be easily mistaken. However, upon close inspection of the images, it is clear that

fibrillar contact is the dominating junction of the two. Bifurcations are desirable because they provide a continuous pathway for charge transport. Recently, Samitsu *et al.* reported a decrease in hole mobility when comparing P3HT networks to isolated nanofibers.[15] This decrease is attributed to fibrillar overlaps, in good agreement with our finding that colloidal networks of P3HT are dominated by fibrillar aggregation rather than bifurcation. Therefore an ideal network structure would minimize fibrillar overlaps while maximizing bifurcating junctions. It may be possible to further optimize this parameter by controlling the kinetics of network growth, as described in Chapter 5.

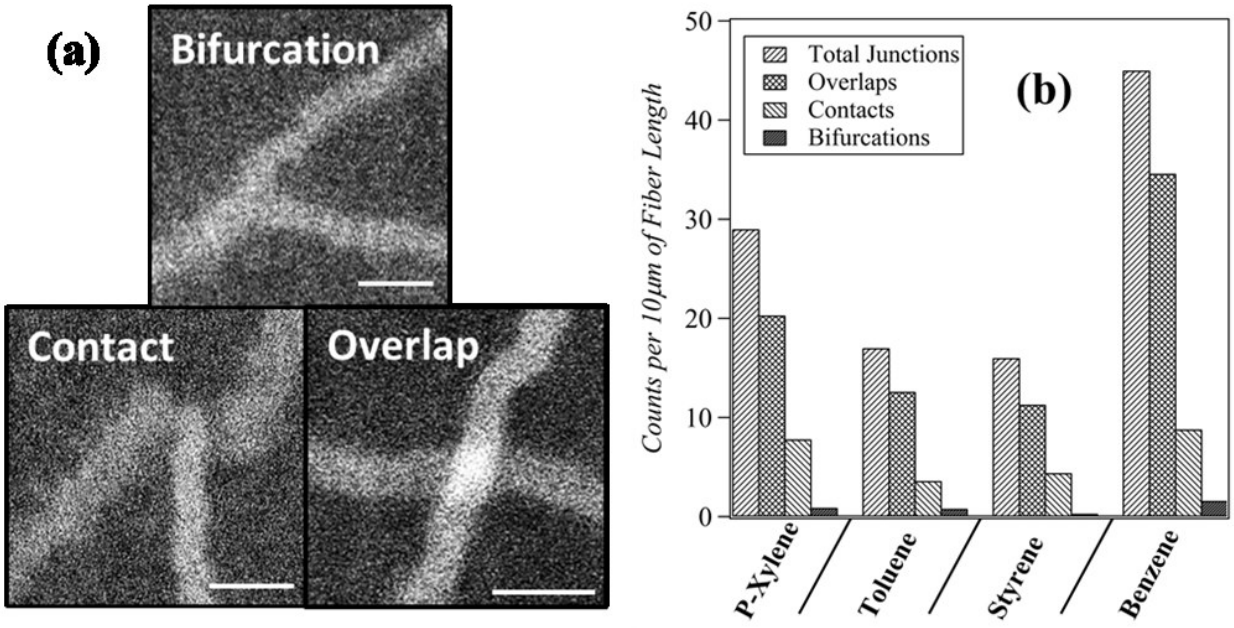

Figure 3.6. (a) sTEM images of different P3HT fibrillar interactions with scale bars at 50 nm. All samples were crystallized in toluene. (b) The fibrillar length, number of junctions and type of junction was evaluated from sTEM images. Between 100-250 μm of fiber length were measured for each solvent.

Optical microscopy was also utilized to better determine the size of individual P3HT networks in each solvent, as seen in Figure 3.7. The samples were diluted 40x prior to deposition and drying on a glass microscopy slide. The drying process did not cause noticeable aggregation

due to the small concentration of P3HT after dilution. The network size is found to be strongly dependent on solvent choice with P3HT crystallized in toluene having the largest network size and P3HT crystallized in p-xylene having the smallest. The order of colloidal network sizes (p-xylene < styrene < toluene) is also well supported by the USANS data even though the resolution was too low to accurately determine the average values for all samples (Figure 3.2). All four solvents show polydispersity in network size, with toluene being the most significant. The size of an individual network is also expected to play an important role in OFET performance as this parameter determines the minimum number of network particles that are required to create a connection between electrodes. Figure 3.8b illustrates how larger particles could result in improved performance for OFET devices. Charge transport within a single network particle is expected to be more effective than transport across different particles. Figure 3.8b is not meant to imply that network particles will form a monolayer structure over the OFET device. This is intentionally drawn in this manner to highlight the finite size of individual network particles. In devices, particles fall on top of each other forming multilayers and they are indistinguishable in TEM.

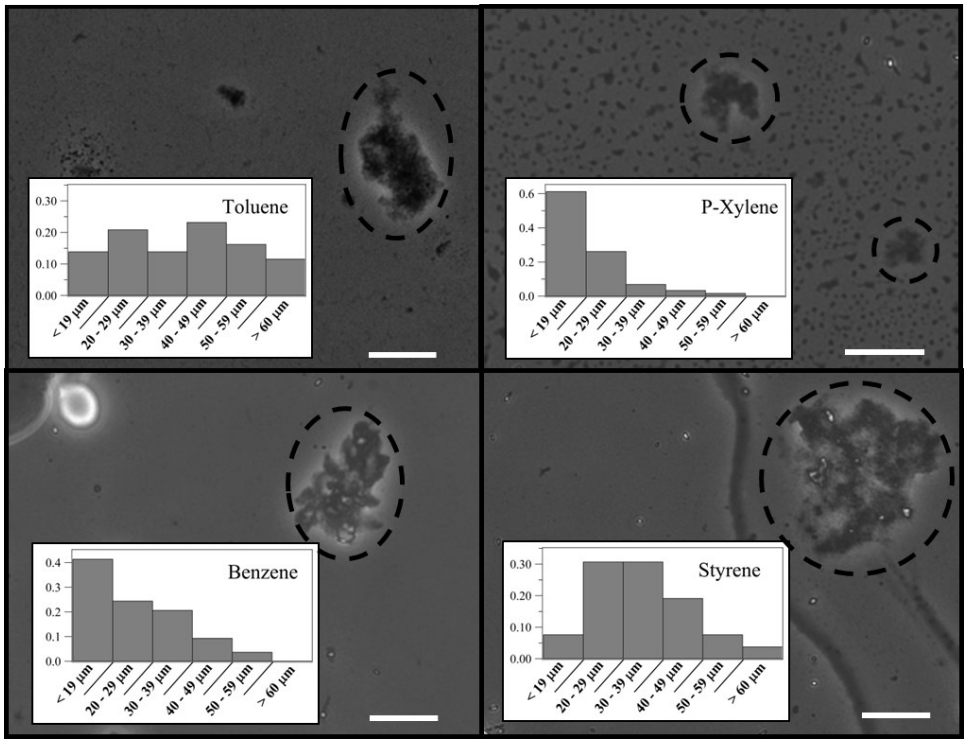

Figure 3.7. Optical micrographs of coated colloidal P3HT networks taken at 20x magnification, with 10 µm scale bars. Inset: Diameter of P3HT networks normalized to the total number of colloidal networks that are counted.

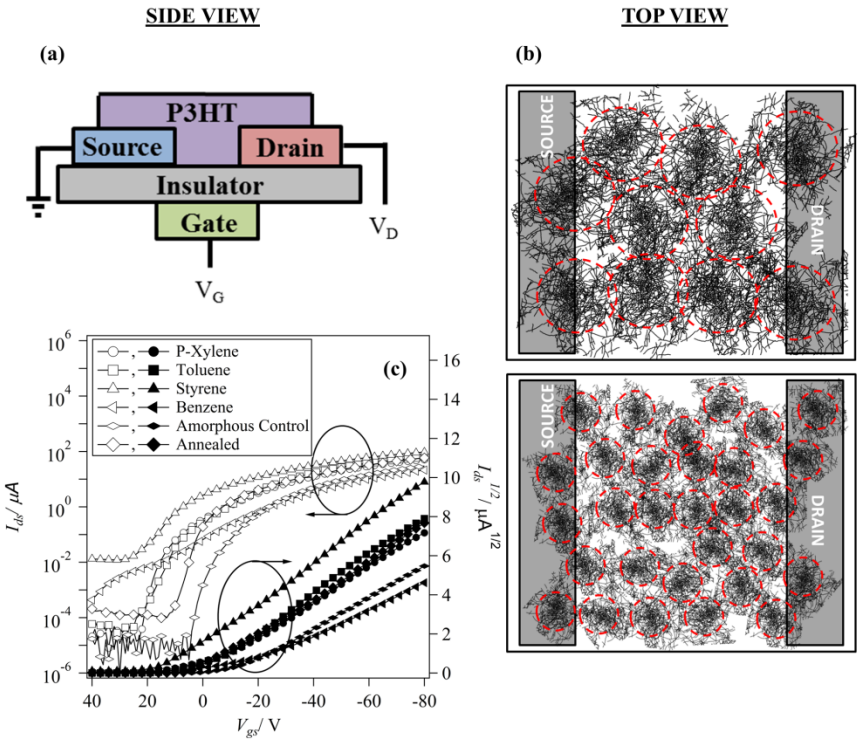

Figure 3.8. (a) Schematic of an OFET (side view). (b) The effect of network size on the number of colloidal particles required to bridge the electrodes (top view of the OFET). (c) Overlay of OFET transfer curves for P3HT crystallized in different aromatic solvents and control thin films.

3.3.2 Multiple Structural Features Correlated to Charge Transport Properties

Ultimately, our goal is to understand how the properties of these networks can be tuned through structural changes. The charge transport of the networks of crystallized P3HT was probed by coating the crystallized network dispersions onto silicon wafers to create organic field effect transistors (OFETs). The OFETs of P3HT crystallized in different solvents showed good current modulation as seen in Figure 3.8c. The output characteristics of these devices showed linear increase of current at low source-drain bias (V_{ds}) and clear current saturation at high V_{ds} (Figure 3.9). The average saturation field-effect mobility of the networks ranged from 1.45×10^{-2} to 3.35×10^{-2} cm^2 V^{-1} s^{-1} with standard deviations of less than 6×10^{-3} cm^2 V^{-1} s^{-1}. The differences in mobility are still evident even when the gate voltages are normalized by the threshold voltages

(Figure 3.10). In addition to the OFETs made from colloidal networks of P3HT, an OFET was also made by spin coating the fully dissolved P3HT (amorphous) onto the substrate and allowing the thin film to crystallize after coating. The electrical performance of this amorphous control sample was characterized before and after annealing at a temperature of 150 °C for 10 min. It has been shown that P3HT forms long, overlapping fibers during thin film crystallization and that the overall crystallinity can be increased through annealing after coating.[2, 16] The charge carrier mobility and threshold voltage were calculated by using the standard equation for the saturation region, and on/off current ratio was derived from the ratio of maximum current to minimum current.[1, 4] All of the relevant electrical and structural parameters are summarized in Table 3.1.

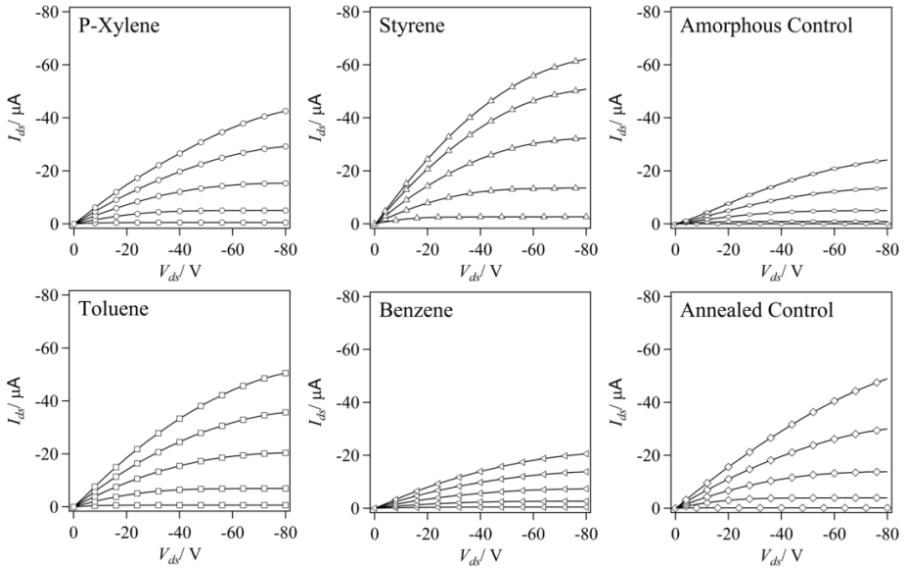

Figure 3.9. Output curves (V_{gs} = 0V to -80V, step -20 V) for transistors of P3HT crystallized in different aromatic solvents as well as control thin-films without and with annealing at 150 °C.

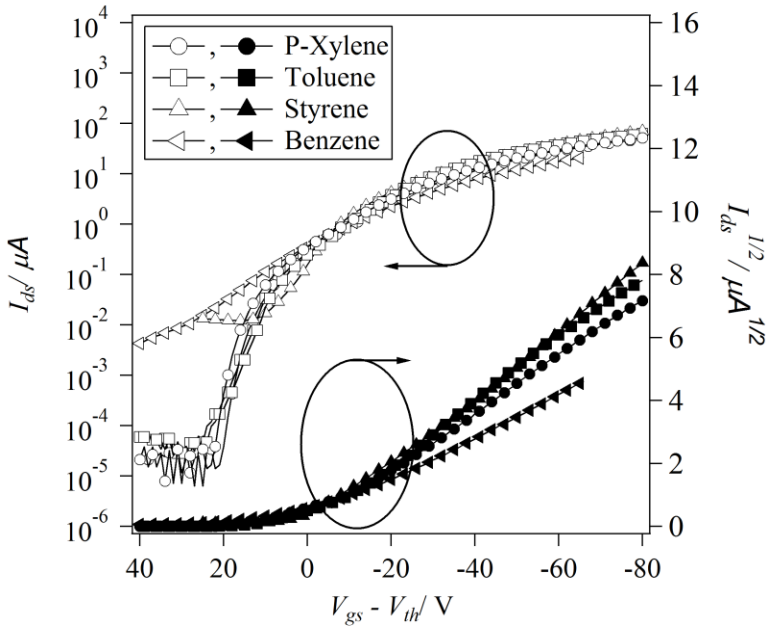

Figure 3.10. Transfer curves for transistors of P3HT crystallized in different aromatic solvents. The gate voltage is "normalized" by the threshold voltage.

The charge-carrier mobility is the parameter that best describes the charge transport through the semiconductor layer. Several of the physical and structural parameters that we have characterized (Table 3.1) can potentially play important roles in influencing charge transport. Some of these include the total solids/fiber fraction (ϕ_s, Ψ_f), the crystalline order characterized by the exciton bandwidth, the branched structure of the network (D_f, d_{onset}), the type and frequency of interfibrillar junctions (bifurcations, contacts or overlaps) and the size of the colloidal network particles. Since all of these can affect charge transport, it is very difficult to distinguish the relative importance of each of these features. One of the primary outcomes of this work is to highlight the need for performing detailed structural characterization spanning over multiple length scales when developing structure-property relationships. Several researchers have reported a strong correlation between P3HT mobility and crystallinity.[2, 6] Although we agree that crystallinity is a very important parameter, our results demonstrate that it is difficult to isolate the importance of a single feature without considering structural changes that occur at other length

scales. Our observations also show a correlation between exciton bandwidth values (i.e., crystalline order) and hole mobility in network particles that are formed in different solvents. However, the scattering and microscopy data also demonstrate that the structures are also changing considerably at other length scales.[26] Without the systematic characterization of all relevant length scales, as performed in this study, it would be inappropriate to conclusively identify the crystalline order of P3HT as the primary parameter contributing to improved charge transport.

P3HT networks were previously reported to have a lower mobility than individual nanofibers and this was attributed to fibrilar overlaps.[15] Through a detailed analysis of sTEM images, we also find an inverse correlation between the number of fibrillar overlaps and the hole mobility. The size of the colloidal network particles also seems to be correlated with charge transport, given that samples prepared in toluene and styrene have the largest sizes and also the largest mobility values. Presumably, this is due to an effective charge transport mechanism within single network particles and to the smaller number of large colloidal particles that is necessary to bridge the source and drain electrodes in the OFET devices. These combined findings demonstrate that the structure of the networks may also play a significant role in determining charge transport.

Table 3.1. Structural and Charge Transport Properties of P3HT Crystallized in Different Aromatic Solvents.

	P-Xylene	Toluene	Styrene	Benzene
Hole Mobility [$cm^2\ V^{-1}\ s^{-1}$]	0.0239 ± 0.0048	0.0305 ± 0.0027	0.0335 ± 0.0049	0.0145 ± 0.0024
Threshold Voltage [V]	2.0 ± 3.4	0.1 ± 2.5	24.0 ± 6.1	-11.8 ± 6.4
On/Off Ratio	1.1×10^6	1.4×10^6	2.9×10^4	5.6×10^4
Solids Fraction (ψ_f[a], ϕ_s[b])	0.70, 0.70	0.62, 0.69	0.81, 0.78	0.81, 0.88

Onset of Fractal Behavior (d_{onset}) [nm] [c]	71	58	69	69
Fractal Dimension (D_f) [c]	1.54	2.92	1.85	1.84
Total fibrillar overlaps per 10μm fiber length [d]	20	12	11	35
Network Size [μm] [e]	19 ± 7	39 ± 17	35 ± 12	25 ± 11
Exciton Bandwidth (meV) [b]	60	47	116	112
Fiber Height [nm] [a]	3.8	5.7	8.0	6.5
Fiber Width [nm] [a, d]	17, 28 ± 15	20, 23 ± 8	24, 21 ± 4	24, 30 ± 10

Electrical parameters are averaged from 6 devices. One standard deviation is also shown for hole mobility and threshold voltage. [a] Obtained from SANS data fitting with parallelepiped model, [b] Obtained from UV-Vis spectroscopy, [c] Obtained from SANS & USANS data fitting with power law dependencies, [d] Obtained from sTEM images, [e] Obtained from optical microscopy images.

It is difficult to draw definitive conclusions from comparison of individual parameters between the networks because of possible interdependencies and competing effects. Still, we expect that the density of fibers in an ideal network, described by D_f and d_{onset}, should be low in order to increase hole mobility. This is due to fibrillar overlaps being the primary junction type and that they could act as effective trap sites. The lowest network density of P3HT particles can be seen in p-xylene, followed by styrene and benzene. Networks formed in toluene have a high fractal dimension but sTEM analysis also shows that they have a larger particle size and a lower concentration of fiber overlaps when compared to other particles. The size of the particles should be maximized as this will allow for the network structure to more easily bridge the device electrodes. Although samples in benzene had the highest solid fractions, UV-Vis spectroscopy shows that the crystalline order of the solid phase is much lower than p-xylene or toluene. The dense junction structure of these samples may also be responsible for the large negative threshold voltage in the OFET measurements by potentially increasing the number of charge transport

barriers through imperfect interconnections between fibers. It should also be noted that networks formed in styrene solutions showed off-current values of 10–100 nA, that are 2–3 orders of magnitude larger compared to other samples (0.01–0.1 nA). This large off-current, in conjunction with a large positive threshold voltage of 24.0 V, might come from unintentional doping and can also lead to an overestimation of the intrinsic field-effect mobility.[5]

These results demonstrate the combined importance of crystalline ordering, network structure, particle size and the dominant type of fiber junctions on charge transport. The hole mobility of solution crystallized samples in toluene and styrene are even higher than those of the thin film crystallized (0.0210 ± 0.0049 cm^2 V^{-1} s^{-1}) and annealed samples (0.0276 ± 0.0057 cm^2 V^{-1} s^{-1}). This suggests that control of crystallinity and network structure of polymer semiconductors crystallized in solution before coating could be an effective means of increasing charge carrier mobility in devices. Furthermore, the formulation of inks based on these colloidal dispersions allows for effective decoupling of the parameters that determine the structure of the networks from those of the coating process. Therefore, the formation of colloidal networks could be an effective and general platform to simplify the fabrication and improve the performance of organic electronic devices.

3.4 Summary

In this chapter, we have measured and quantified the mesoscale network structure for self-assembled colloidal P3HT and have correlated these to charge transport in OFET devices. The morphology of the P3HT networks were evaluated over multiple length scales through *in situ* SANS and USANS experiments. The relevant structural features were identified to be the crystalline order, the network density, the size of network particles, and the frequency and type

of fibrillar junctions. These were all shown to be highly dependent on the choice of solvent that is used to self-assemble the polymer. P3HT fibers were shown to form bifurcating interconnected networks, even though the frequency of actual bifurcations was much lower than the other types of junctions (i.e., contacts and overlaps). OFET measurements were used to compare the structural parameters to performance in real devices. Despite finding clear structure-function correlations, the individual effect of specific parameters cannot be fully established due to non-trivial interdependencies occurring at different length scales. The complexity of the network structures did not allow for the development of simple relationships but did allow us to confirm several design principles. The network density should be low due to the decrease in mobility that results from fibrillar overlaps. However, the size of the individual network particles should be large in order to serve as an effective bridge between the electrode contacts. Intra-network charge transport is expected to be much faster than inter-network transport. Colloidal P3HT networks represent an important pathway towards simple processing of organic electronic materials. This approach is also demonstrated to be a versatile platform to decouple the parameters that affect polymer self-assembly from those that describe the coating process. These results demonstrate the importance of mesoscale morphology over multiple length scales in developing and optimizing organic electronic devices. Work in this chapter was adapted with permission from Newbloom G. M., Kim, F. S., Jenekhe, S. A., Pozzo, D. C., Macromolecules, 2011, 44, 3801-3809. Copyright 2011 American Chemical Society.

3.5 References

1. Bao, Z.; Dodabalapur, A.; Lovinger, A. J. *Applied Physics Letters* **1996,** 69, (26), 4108-4110.
2. Yang, X. N.; Loos, J.; Veenstra, S. C.; Verhees, W. J. H.; Wienk, M. M.; Kroon, J. M.; Michels, M. A. J.; Janssen, R. A. J. *Nano Letters* **2005,** 5, (4), 579-583.

3. Moule, A.; Meerholz, K. *Advanced Functional Materials* **2009,** 20, 3028-3036.
4. Yang, X.; Loos, J. *Macromolecules* **2007,** 40, (5), 1353-1362.
5. Chang, J.-F.; Sun, B.; Breiby, D. W.; Nielsen, M. M.; Sölling, T. I.; Giles, M.; McCulloch, I.; Sirringhaus, H. *Chemistry of Materials* **2004,** 16, (23), 4772-4776.
6. Sirringhaus, H.; Brown, P.; Friend, R.; Nielsen, M.; Bechgaard, K.; Langeveld-Voss, B.; Spiering, A.; Janssen, R.; Meijer, E.; Herwig, P.; de Leeuw, D. *Nature* **1999,** 401, 685-688.
7. Arif, M.; Liu, J.; Zhai, L.; Khondaker, S. I. *Applied Physics Letters* **2010,** 96, (24), -.
8. Merlo, J. A.; Frisbie, C. D. *The Journal of Physical Chemistry B* **2004,** 108, (50), 19169-19179.
9. Samitsu, S.; Shimomura, T.; Ito, K. *Thin Solid Films* **2008,** 516, (9), 2478-2486.
10. Ihn, K. J.; Moulton, J.; Smith, P. *Journal of Polymer Science Part B: Polymer Physics* **1993,** 31, (6), 735-742.
11. Oosterbaan, W. D.; Bolsée, J.-C.; Gadisa, A.; Vrindts, V.; Bertho, S.; D'Haen, J.; Cleij, T. J.; Lutsen, L.; McNeill, C. R.; Thomsen, L.; Manca, J. V.; Vanderzande, D. *Advanced Functional Materials* **2010,** 20, (5), 792-802.
12. Samitsu, S.; Shimomura, T.; Heike, S.; Hashizume, T.; Ito, K. *Macromolecules* **2008,** 41, (21), 8000-8010.
13. Xin, H.; Kim, F. S.; Jenekhe, S. A. *Journal of the American Chemical Society* **2008,** 130, (16), 5424-5425.
14. Xin, H.; Reid, O. G.; Ren, G.; Kim, F. S.; Ginger, D. S.; Jenekhe, S. A. *ACS Nano* **2010,** 4, (4), 1861-1872.
15. Samitsu, S.; Shimomura, T.; Heike, S.; Hashizume, T.; Ito, K. *Macromolecules* **2010,** 43, (19), 7891-7894.
16. Kim, D. H.; Han, J. T.; Park, Y. D.; Jang, Y.; Cho, J. H.; Hwang, M.; Cho, K. *Advanced Materials* **2006,** 18, (6), 719-723.
17. Malik, S.; Jana, T.; Nandi, A. K. *Macromolecules* **2001,** 34, (2), 275-282.
18. Abramoff, M. D.; Magalhaes, P. J.; Ram, S. J. *Biophotonics International* **2004,** 11, (7), 36-41.
19. Glinka, C.; Barker, J.; Hammouda, B.; Krueger, S.; Moyer, J.; Orts, W. *Journal of Applied Crystallography* **1998,** 31, 430-445.
20. Barker, J. G.; Glinka, C. J.; Moyer, J. J.; Kim, M. H.; Drews, A. R.; Agamalian, M. *Journal of Applied Crystallography* **2005,** 38, 1004-1011.
21. Kim, F. S.; Guo, X.; Watson, M. D.; Jenekhe, S. A. *Advanced Materials* **2010,** 22, (4), 478-482.
22. Guo, X.; Kim, F. S.; Jenekhe, S. A.; Watson, M. D. *Journal of the American Chemical Society* **2009,** 131, (21), 7206-7207.
23. Koppe, M.; Brabec, C.; Heiml, S.; Schausberger, A.; Duffy, W.; Heeney, M.; McCulloch, I. *Macromolecules* **2009,** 42, (13), 4661-4666.
24. Malik, S.; Nandi, A. K. *Journal of Physical Chemistry B* **2004,** 108, (2), 597-604.

25. Berson, S.; De Bettignies, R.; Bailly, S.; Guillerez, S. *Advanced Functional Materials* **2007,** 17, (8), 1377-1384.
26. Clark, J.; Chang, J.-F.; Spano, F. C.; Friend, R. H.; Silva, C. *Applied Physics Letters* **2009,** 94, (16), 163306-3.
27. Kim, B.-G.; Jeong, E. J.; Park, H. J.; Bilby, D.; Guo, L. J.; Kim, J. *ACS Applied Materials & Interfaces* **2011,** 3, (3), 674-680.

Chapter 4

Fiber Assembly and Percolation in Poly(3-hexylthiophene) Organogels

4.1 Motivation

To date, polymer gelation and network formation has been largely regarded as a negative attribute for organic electronics, including OPV, fabrication because of difficulties that arise during processing as a result of the increased elasticity.[1, 2] Recent advances in device fabrication have shown that it is still possible to process conjugated polymer organogels while maintaining their structural features.[3-5] These advancements in processing open the door to pursue gelation as a flexible platform to design the photoactive layer of OPVs. Many conjugated polymers (P3ATs, PFO, MEH-PPV, *etc.*) form gels at moderate concentrations (> 10 mg/mL) in organic solvents.[1, 3, 4, 6-17] The gel phase of poly(3-hexylthiophene) (P3HT), in particular, has been shown to have much higher conductivities when compared to films generated using traditional coating processes.[8] Conjugated polymer organogels have also been used to produce functional OPV devices by back-filling the porous network structure with an n-type fullerene.[3, 5] Furthermore, the structure and properties of P3HT organogels can be tuned based on changes to self-assembly conditions.[15, 17] Yet, to further engineer the network structure of organogels there must be a

robust understanding of the self-assembly processes occurring in these systems. Despite recent advances, little is known about how the structure of conjugated polymers evolves during gelation.

Common techniques for evaluating structure in conjugated polymer gels are transmission electron microscopy (TEM), scanning electron microscopy (SEM), atomic force microscopy (AFM), small angle neutron scattering (SANS) and small angle x-ray scattering (SAXS).[3, 4, 11, 12, 14, 15, 17, 18] Small angle scattering has important advantages because the bulk morphology of the gel can be probed *in-situ* during the self-assembly process, over multiple length scales and without any sample manipulation. Still, most SAXS and SANS studies have been limited to probing equilibrium states in these materials. Here we the simultaneous techniques described in Chapter 2.4 to study the intermediate stages of the self-assembly process. This work contributes a detailed understanding of P3HT self-assembly and also demonstrates the great potential to engineer network structures specifically for OPV or other applications involving organic semiconductors.

4.2 Experimental Methods

Materials. Sepiolid P200 poly(3-hexylthiophene) (P3HT, Lot# 22.10.2009) was used as received from Rieke Metals (Lincoln, NE). The weight-averaged molecular weight (M_w) and polydispersity index (PDI) were characterized by gel permeation chromatography (GPC) and determined to be 16,770 g/mol and 1.6, relative to polystyrene standards. The regioregularity of the polymer was reported by the manufacturer to be greater than 98%. Hydrogenated solvents (p-xylene, toluene and benzene) were purchased from Sigma-Aldrich (St. Louis, MO) and used as received. Deuterated solvents were utilized to decrease the incoherent scattering background and

increase the scattering contrast for SANS experiments. D10-p-xylene (D > 98%), D8-toluene (D > 99.5%), and D6-benzene (D > 99.5%) were purchased from Cambridge Isotopes (Andover, MA) and used as received.

Sample Preparation. Samples were prepared by adding 30 ± 0.3 mg/mL P3HT to p-xylene, toluene or benzene and then heating to 80 °C for 10 minutes or more to fully dissolve the polymer prior to loading in various experimental setups. The polymer is considered fully dissolved when the solution is bright orange and there are no visible signs of solid polymer (black).

Scanning Transmission Electron Microscopy. A small quantity of fully-developed (i.e., > 2 days) 10 mg/mL P3HT organogel formed in toluene was transferred to a copper TEM grid with a Formvar support film by briefly placing the grid in contact with the surface of the gel sample without applying pressure. In this way, only a thin-film of organogel was transferred to the TEM grid. Due to the very thin nature of the sample, the toluene evaporated nearly instantaneously under ambient conditions. TEM images were obtained with a FEI Tecnai G2 F20 transmission electron microscope operating at 120 kV in scanning TEM (sTEM) mode.

Dielectric-SANS. Simultaneous AC dielectric spectroscopy and SANS (dielectric-SANS) measurements were performed in the CG2 beam-line at the High Flux Isotope Reactor (HFIR) at Oak Ridge National Lab (Oak Ridge, TN). The AC dielectric spectroscopy, used to measure the AC conductivity, was performed at a frequency of 2 kHz with a perturbation voltage of 200 mV that was determined to be in the linear impedance response region. All dielectric measurements were performed with an Agilent e4980a Precision LCR meter.

SANS measurements were performed at two detector distances to cover a broad q-range ($0.002 < q$ (Å^{-1}) < 0.2) using the dielectric-SANS sample cell with polished aluminum windows.

The hot polymer solution (80 ºC) was loaded into the room temperature sample cell, sealed and then re-heated to 80 ºC to ensure full dissolution of the polymer. The cooling ramp rate was 0.8 °C/min while the heating ramp rate was 1.2 °C/min. The scattering curves were referenced to the incident beam flux and set in an absolute scale. Corrections for transmission, background and empty cell scattering were also applied using standard methods.[19] The scaling procedure was confirmed by measuring the absolute scattering cross-section of D_2O and H_2O and comparing to known values.[20] The 2D scattering profiles were converted to 1D profiles for data fitting and the results were matched point-by-point to the AC conductivity data. The AC conductivity values were normalized because variations in surface resistivity of the polished aluminum windows caused fluctuations in the absolute value of the conductivity. Still, the trends and the shape of the normalized curves were identical between runs and matched dielectric-rheology experiments that were performed with non-corrosive stainless steel electrodes, as seen in Figure 2.21.

Rheology-SANS. Simultaneous oscillatory rheology and SANS (rheology-SANS) experiments were performed in the NG7 beam-line at NIST Center for Neutron Research (NCNR) at the National Institute of Standards and Technology (Gaithersburg, MD).[21] Experiments were performed using an Anton Paar Physica MCR 501 rheometer with a titanium concentric cylinder geometry (gap = 0.5 mm, diameter = 29 mm, height = 36 mm) at a frequency of 1 Hz.[22] The heating and cooling ramp rate for the rheology-SANS experiments was 0.8 °C/min. The applied strain was 1% at high temperature (> 40 ºC), but reduced to 0.25% just prior to the gelation temperature in each respective solvent to avoid breaking the gels.

SANS measurements were performed at two detector distances to provide a wide q-range for fitting ($0.002 < q$ (Å^{-1}) < 0.2), except for samples in benzene that were measured with a smaller q-range ($0.0131 < q$ (Å^{-1}) < 0.2) due to time constraints. The total scattering pathlength

was 1 mm and the scattering was scaled by the empty beam flux and corrected for background and empty cell scattering.[19] This also allowed for direct point-by-point matching of the rheology and SANS data. *All rheo-SANS experiments were performed with the help of Dr. Kathleen Weigandt.*

Dielectric-rheology. Simultaneous AC dielectric spectroscopy and rheology (dielectric-rheology) measurements were performed using an Anton Paar Physica MCR 301 rheometer and an Agilent e4980a Precision LCR meter. Small amplitude oscillatory strain measurements (γ = 0.25% and f = 1 Hz) were used to track changes in mechanical properties during gelation. AC conductivity measurements are made at a frequency of 2 kHz and a perturbation voltage of 600 mV, which is still within the linear response region. The cooling and heating ramp rate utilized for these experiments was 0.8 °C/min.

4.3. Results and Discussion

4.3.1 Structural Evolution during Gelation

Tuning the self-assembly of conjugated polymer gels represents an opportunity to engineer structures with features that are desirable for maximizing the efficiency of organic electronics. It has been established that the morphology of gels made from self-assembling polymers and small molecules can be engineered by adjusting the self-assembly conditions (solvent, temperature, *etc.*).[23-26] Designing specific gel structures requires an understanding of the driving forces behind self-assembly as well as the progression of structural intermediates.[23, 26, 27] The latter can be difficult to probe because studying the progression of self-assembly requires non-invasive techniques that can probe evolving structures over all relevant length-scales. Small

angle scattering is an ideal technique for this and is employed here to probe self-assembling P3HT organogels.

SANS profiles taken during the self-assembly of P3HT are fit using the methods described in Chapter 2.1.5. Equation 2.6 applies a mass balance at each sampling interval to account for the presence of both fibers and dissolved polymer in solution. This equation is bound by the known total volume fraction of P3HT in the original solution (ϕ_v), to determine the cross-sectional dimensions of the fiber (*a* and *b*) and to account for the fraction of P3HT that exists in fiber form (Ψ_f) at any instant. In order to reduce the number of fitting parameters in Equation 2.6, we fit SANS profiles of fully dissolved P3HT chains at elevated temperatures ($40 < T$ (ºC) < 80) using Equation 2.8. The SANS profiles and the fit parameters for the dissolved polymers are found to be constant over a wide temperature range (40-80 ºC) until fiber formation is evident in the data, as seen in Figure 4.1. From the dissolved polymer fits, v was determined to be 0.7 ± 0.04, which is between the value for rod-like chains ($v = 1$) and for Gaussian coils ($v = 0.5$). This result is expected because conjugated polymer chains tend to be rigid in solution.[28, 29] The radius of gyration (R_g) was also calculated, using Equation 4.1, and confirmed with a Guinier fit, to be 53 ± 4 Å across all solvents utilized in the chapter.[28]

$$R_g^{\,2} = \frac{a^2 n^{2\nu}}{(2\nu+1)(2\nu+2)} \tag{4.1}$$

The weight-averaged molecular weight (M_w) of the polymer was also determined from SANS of fully-dissolved P3HT and was determined to be 8500 ± 750 g/mol.[30] The weight-averaged molecular weight (M_w) can be directly calculated from SANS of dissolved polymer chains (Equation 4.2):

$$M_w = \frac{N_A \cdot \left(\rho^m_{P3HT}\right)^2 \cdot I(0)}{c \cdot (\Delta\rho_{PExV})^2} \tag{4.2}$$

where N_A is Avogadro's number, c is the concentration of dissolved P3HT in solution, ρ^m_{P3HT} is the mass density of P3HT chains (1.1 g/cm^3), *I(0)* is the absolute-scaled scattering intensity at q = 0 and $\Delta\rho_{PExV}$ is the scattering contrast between solvent and dissolved polymer chains. This analysis highlights the overestimation of M_w values for rigid conjugated polymers that results from the calibration of GPC measurements with flexible polystyrene standards (M_w = 16,770 g/mol).[31]

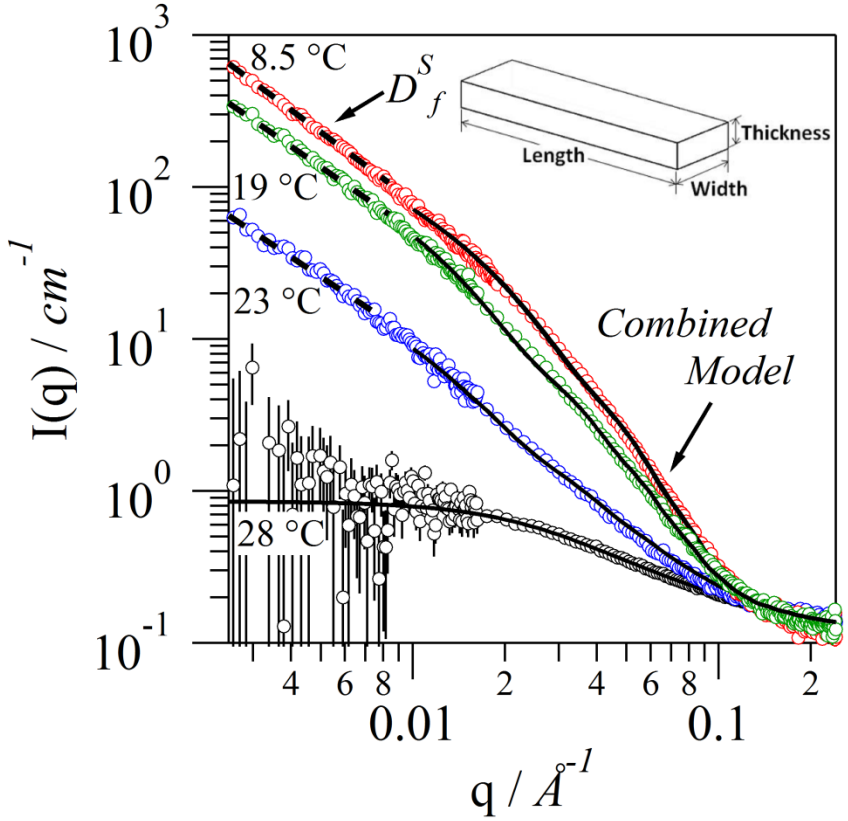

Figure 4.1. SANS profiles collected during the gelation of 30 mg/mL P3HT in toluene fit with the combined model (Equation 2.6). The combined model (▬) is used in the range of 0.01 < q < 0.25 Å^{-1}. At q < 0.007 Å^{-1}, a power law (▬ ▬) is fit to extract the fractal dimension (D^S_f) associated with network formation. Parameters extracted from these fits are found in Table 4.1.

The scattering length density (SLD) is also a critically important physical parameter for fitting of neutron scattering data. A detailed analysis of the P3HT fiber SLD can be found in Chapter 10.1 By fixing most variables in Equation 2.6 to known or independently measured values, only three parameters remain unknown in the model: fiber thickness (*a*), width (*b*) and fraction of P3HT in fiber form (Ψ_f). This leads to rigorous fitting as shown in Figure 4.1 so that detailed structural values can be extracted with high confidence (Table 4.1).

Table 4.1. Fitting results for the data sets of P3HT in toluene presented in Figure 4.1. D_f^S is the fractal dimension of the network and S_v is the specific surface area. Uncertainty values represent the error of individual fits as provided by the data analysis package.[32]

Temperature / *°C*	**28.0**	**23.0**	**19.0**	**8.5**
Fraction of P3HT in fiber form (Ψ_f)	0	0.043 ± 0.001	0.272 ± 0.001	0.439 ± 0.001
Fiber Thickness / *nm*	*N/A*	3.8 ± 0.1	3.9 ± 0.1	4.1 ± 0.1
Fiber Width / *nm*	*N/A*	27.9 ± 0.6	28.5 ± 0.4	20.2 ± 0.2
D_f^S	*N/A*	1.49 ± 0.04	1.42 ± 0.04	1.45 ± 0.03
S_v / *m^2/g*	*N/A*	800 ± 10	780 ± 10	780 ± 10

The scattering in Figure 4.1 provides structural information over a wide range of length scales (~1 nm to 300 nm). The combined model is only valid over a limited *q*-range ($q > 0.01$). At lower-*q* (< 0.01 Å^{-1}), there is an increase in the scattering intensity relative to the expected scattering for discrete fibers. This corresponds to the formation of a branched network structure that is better modeled as a mass fractal. A fractal dimension (D_f^S) characterizing this structure can be extracted from the dependence at low angles ($q < 0.008$ Å^{-1}) using Equation 2.9. The

results are also included in Table 4.1. The specific surface area (S_v) for the fibers was calculated using the Porod equation as described in Chapter 2.1.3. In this case, the scattering invariant (Q) is utilized to determine the volume fraction of fibers in solution at each intermediate structure. A detailed discussion about the specific surface area analysis can be found in Chapter 10.2.

By combining small angle scattering with rheology and conductivity measurements it is possible to simultaneously study the developing structure and properties of the organogels. Rheology-SANS measurements allow for simultaneous monitoring of changes in fiber dimensions (a and b), fraction of P3HT in fiber form (Ψ_f), network fractal dimension (D_f^S), specific surface area (S_v), elastic modulus (G') and viscous modulus (G'') as a function of temperature. These rheological measurements provide critical information about the development of the network structure, such as the gel point ($G' = G''$) and the overall stiffness of the fiber networks.

It has been demonstrated that P3HT undergoes a substantial increase in conductivity with gelation.[8] Here we perform dielectric-SANS measurements that allow structural parameters to be directly correlated with the development of electronic properties in the conductive fiber networks. The rheology-SANS and dielectric-SANS experiments are performed with identical cooling (i.e., gelation) rates of 0.8 ºC/min and with very similar re-heating (i.e., dissolution) rates of 0.8 ºC/min and 1.2 ºC/min for rheology-SANS and dielectric-SANS, respectively. This allows for direct comparison of the evolution of structural, mechanical and electronic properties.

Figure 4.2 shows the development of morphological features in conjunction with the moduli (G' & G'') and electrical conductivity normalized to its maximum value (σ_{Norm}). The structural parameters presented in Figure 4.2 represent point-by-point averages of fitting results from SANS profiles obtained during separate rheology-SANS and dielectric-SANS experiments

on identical samples. Reproducibility and consistency between fitting results is demonstrated by the relatively small standard deviation values (error bars).

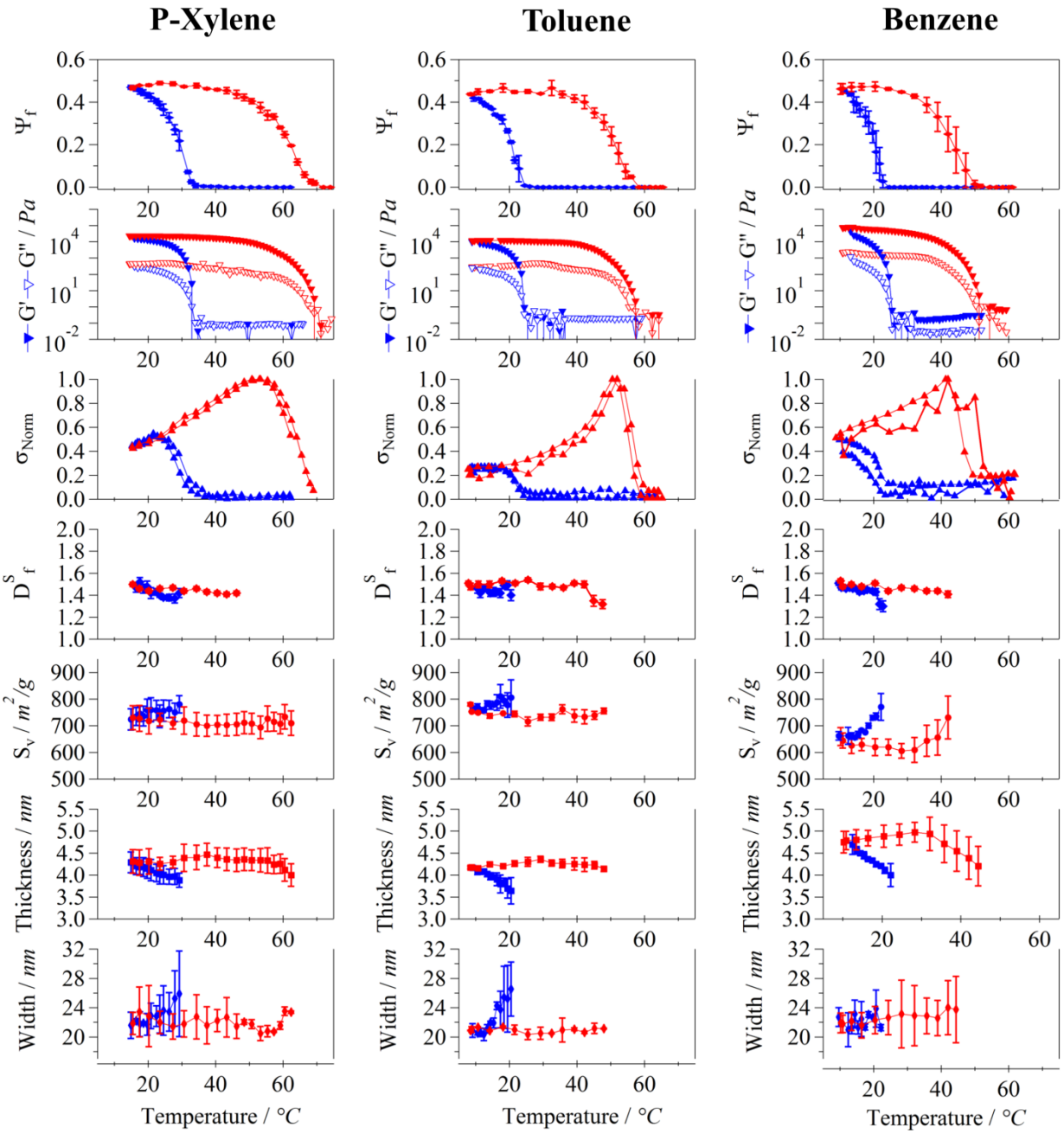

Figure 4.2. Results of dielectric-SANS and rheology-SANS experiments for 30 mg/mL P3HT organogels in aromatic solvents (benzene, toluene and p-xylene). Blue markers represent the cooling ramp (gelation) and red markers represent re-heating (dissolution). Conductivity data (σ_{Norm}) shows two sequential cycles to compare reproducibility. *G'* corresponds to the elastic

modulus, *G"* corresponds to the loss modulus, Ψ_f corresponds to the fraction of P3HT in fiber form, D_f^S corresponds to the network fractal dimension and S_v corresponds to the fiber specific surface area. Error bars represent the standard deviation of the rheology-SANS and dielectric-SANS fitting results.

Complementary dielectric-SANS and rheology-SANS experiments provide a wealth of structure-property information during the intermediate (i.e., non-equilibrium) stages of gelation. The gelation temperature (T_{gel}) is determined from the crossover of the elastic and viscous modulus ($G' = G"$). P3HT shows differences in gelation temperature depending on the solvent: p-xylene (T_{gel} = 34 ºC), toluene (T_{gel} = 26 ºC) and benzene (T_{gel} = 26 ºC). All gels also show differences in their maximum moduli at low temperature. Even toluene and benzene samples, which gel at the same temperature, have different final moduli (G'_{Tol} = 11.8 kPa, G'_{Ben} = 74.4 kPa) suggesting that there are differences in the gel structure. Rheological frequency sweeps of the samples confirm that P3HT is a gel over a wide range of frequencies regardless of the solvent used (Figure 4.3).

Figure 4.2 shows that, after percolation, Ψ_f values increase during the entire cooling cycle. The continued increase in Ψ_f and *G'* indicates that new fibers continue to form over the course of gelation. However, we also find that an increase in the total fraction of P3HT in fiber form does not necessarily contribute to further increases in the conductivity (σ_{Norm}) of the network. A similar result was observed for the isothermal gelation of P3HT in Chapter 5, where an increasing mechanical elasticity did not always correlate with increased conductivity. This was determined to be the result of fibers that form at later stages of gelation but may not contribute to further electrical percolation. These fibers may correspond to dangling ends or "hairs" that could contribute to mechanical elasticity but do not branch or bridge the electrodes to increase the conductivity.

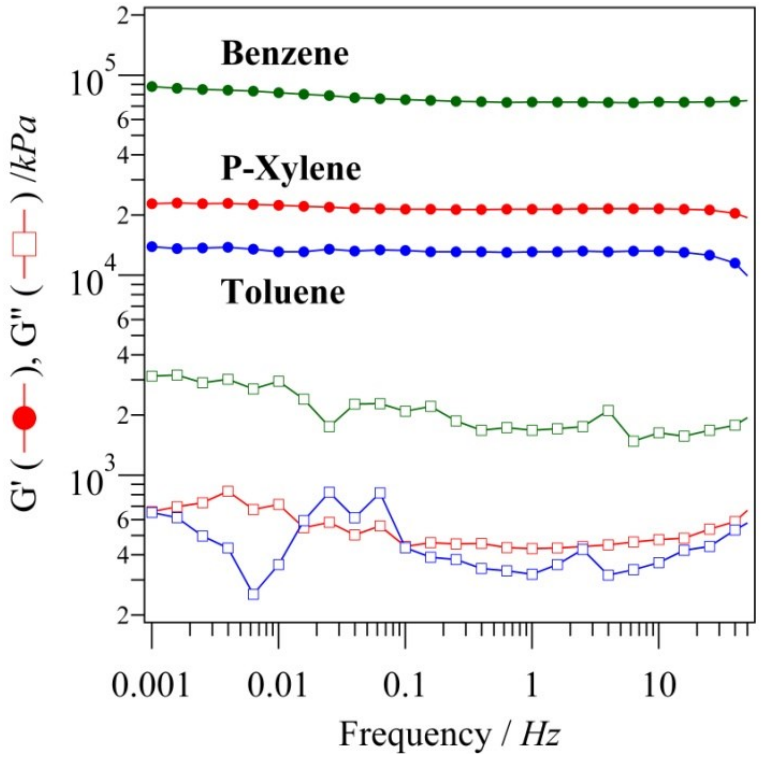

Figure 4.3. Rheological frequency sweep of fully-developed P3HT organogels in different aromatic solvents.

Figure 4.2 also shows that fiber thickness (a) increases for P3HT in all solvents, fiber width (b) decreases for p-xylene and toluene samples, and the specific surface area (S_v) decreases to varying degrees for all solvents during the cooling ramp (gelation). The specific surface area is primarily determined by the cross-sectional dimensions of the growing fibers. The smallest dimension, which in this case is the fiber thickness, is the primary contributor to changes in specific surface area because it is ~ 5 times smaller than the fiber width.

$$S_v \propto \frac{1}{a} + \frac{1}{b} \tag{4.3}$$

The change in S_v during gelation is especially pronounced in benzene because the fiber thickness changes significantly while the width is approximately constant throughout gelation. Additionally, gels formed in benzene have a lower S_v because of the substantially thicker fibers

when compared to those formed in p-xylene or toluene. Regardless of the changes between solvents, all gels show high values of specific surface area that are desirable for efficient charge separation in bulk-heterojunction OPV devices.

The network fractal dimension (D_f^S) characterizes the homogeneity and fiber density of the bulk gel. At fiber fractions just above mechanical and electrical percolation ($\Psi_f > 0.03$) D_f^S is found to be fairly constant. Also, we never observe the $I(q) \propto q^{-1}$ dependence that would indicate rigid isolated fibers forming in dispersion. Instead, all scattering profiles containing fibers show values of $D_f^S \sim 1.5$ that are characteristic of branching networks. These results are consistent with the findings in Chapter 3, where branching was found for P3HT fibers that self-assemble in dilute solutions.[33]

In order to compare the development of properties in different solvents it is informative to compare values at equivalent fractions of P3HT in fiber form ($\Psi_f = 0.20$). The development of *G'* and σ in each solvent, relative to the values for gels at the end of the cooling cycle, is dramatically different. For p-xylene, toluene and benzene gels the conductivity has developed to 80%, 65% and 50% of the value measured at the end of the cooling cycle. In contrast, for p-xylene, toluene and benzene gels *G'* had only developed to 20%, 15% and 5% of the maximum value at the same instant. This suggests that the conductive network structure develops much more rapidly than the mechanical components of the gel. Furthermore, it shows that there are significant differences in the development of gels in different solvents.

4.3.2 Thermoreversible Percolation and Re-Dissolution

Figure 4.4 (left) highlights the fraction of P3HT in fiber form, as well as the mechanical and electrical properties, around the percolation threshold. For all solvents, electrical and the mechanical percolation occur simultaneously and are correlated with the first signs of fiber formation. The percolation threshold is determined to occur at fiber volume fractions ($\phi_{fiber} = \phi_v \cdot \Psi_f$) that are lower than 0.001 in all solvents. Though the intrinsic conductivity of P3HT fibers is lower than many other organic conductive materials, the percolation threshold is still incredibly low. Similar volume fractions are observed for the ultra-low percolation of well-dispersed carbon nanotubes within an epoxy matrix (~ 0.0005).[34, 35]

Unfortunately, the exact value for the percolation volume fraction in each solvent could not be calculated for comparison. The SANS model loses sensitivity at extremely low fiber concentrations (Ψ_f < 0.03) due to the decreasing scattering signal and because of this, the fraction of P3HT in fiber form cannot be determined with the necessary degree of accuracy. We can only conclusively say that percolation in all solvents occurs at very low fractions of P3HT in fiber form (upper bound of Ψ_f ~ 0.03) and that this corresponds to a percolation threshold at fiber volume fractions (ϕ_{fiber}) of less than 0.001. Nevertheless, between 0 < Ψ_f < 0.03 there is a clear increase in scattering intensity at low values of *q* indicating that the fiber fraction is rapidly increasing and the percolation threshold could be even lower.

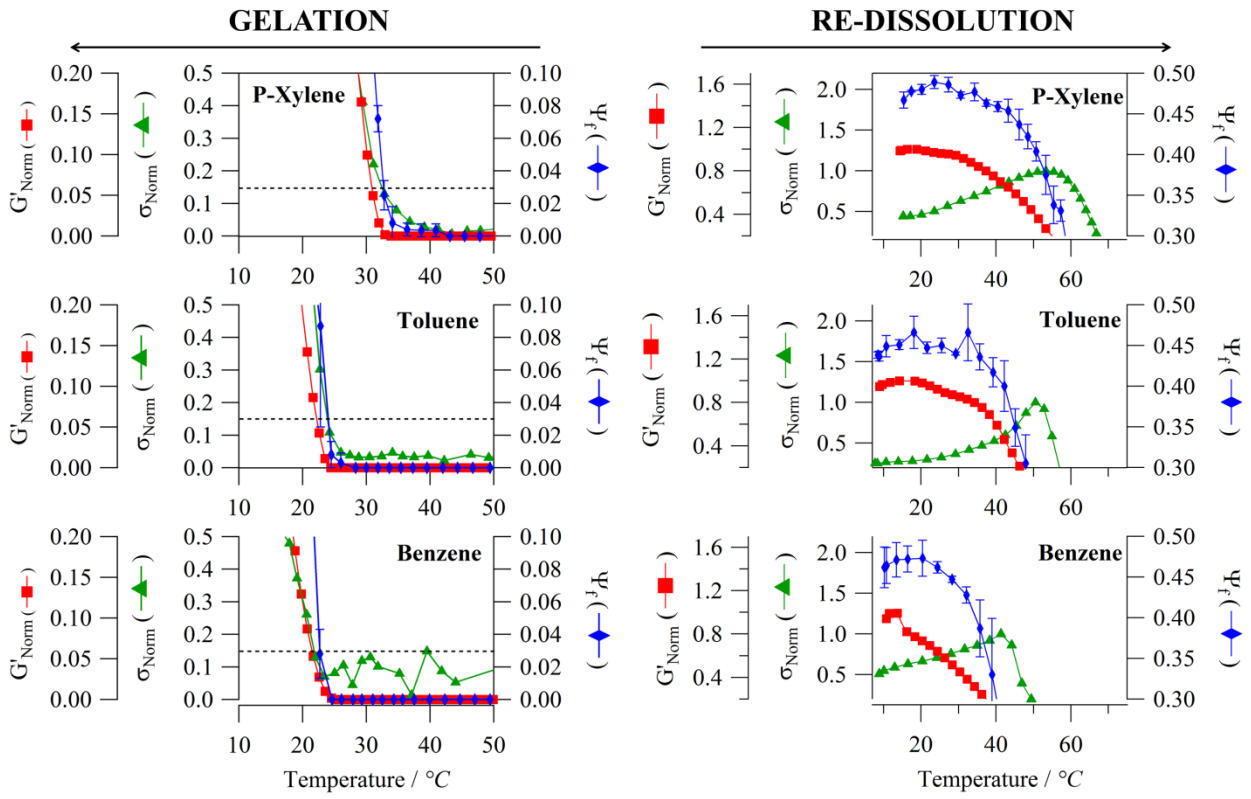

Figure 4.4. Fraction of P3HT in fiber form (Ψ_f), normalized elastic modulus (G'_{Norm}) and normalized conductivity (σ_{Norm}) measured simultaneously during rheology-SANS and dielectric-SANS for 30 mg/mL P3HT organogel right at the point of initial percolation (left) and re-dissolution (right) in different solvents. Dashed horizontal lines (left) indicate the minimum value of Ψ_f that is precisely resolvable from SANS data.

Figure 4.4 (right) also provides a closer look at the mechanical and electrical properties, in conjunction with the fraction of P3HT in fiber form, during re-heating to highlight the organogel dissolution behavior. Upon re-heating, the fraction of P3HT in fiber form slightly increases or remains constant during the initial stages of re-heating. As the temperature continues to increase, eventually Ψ_f decreases until the gels fully dissolve at high temperatures (Figure 4.2). The re-dissolution temperature was determined to be 52 ºC, 58 ºC and 70 ºC, for gels in benzene, toluene and p-xylene, respectively. The elastic modulus decreases simultaneously with the fraction of P3HT in fiber form over most temperatures. In contrast, the conductivity

continues to increase, even after Ψ_f and *G'* have decreased substantially below their maximum values. An increase in conductivity is expected for increasing temperature in semiconductors.[36, 37] However, it is very interesting that, for organogels in all solvents, Ψ_f decreases significantly (30-50%) before the conductivity even begins to decrease.

The changes in conductivity for organic semiconductors with respect to increasing temperature is shown to follow an Arrhenius behavior (Figure 4.5):[38]

$$\sigma = A \cdot e^{-E_A/k_bT} \tag{4.4}$$

where A is a constant, E_A is the activation energy, k_b is Boltzmann's constant and T is the temperature during re-heating. One fundamental assumption for fitting conductivity data with the Arrhenius equation is that the structure should be constant during the measurement. In order to ensure a constant structure, the Arrhenius equation was only used at low re-heating temperatures. We know that, upon re-heating, the structure and the fraction of P3HT in fiber form remains fairly constant (Figure 4.2) up to 25 ºC in benzene, 35 ºC in toluene and 40 ºC in p-xylene. This means that the Arrhenius dependence is expected to break down or change at these higher temperatures.

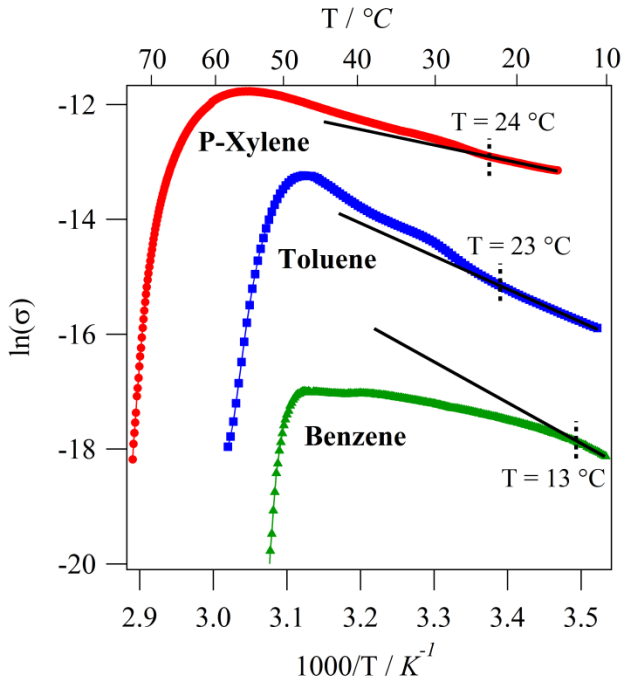

Figure 4.5. Arrhenius plots for 30 mg/mL P3HT organogels in different solvents during re-heating and dissolution. Solid lines correspond to fits to Equation 4.4 at low temperatures that are extended beyond the fit to highlight the deviation. The dashed vertical lines highlight the temperature at which the Arrhenius response deviates from the sample response. The conductivity, σ, has units of units of S/m.

The trend in activation energy is similar to the trend in conductivity. Gels formed in p-xylene, toluene and benzene have activation energy values of 210 meV, 450 meV and 580 meV respectively. Interestingly, the initial Arrhenius behavior of each gel breaks down at 24 ºC, 23 ºC and 13 ºC for p-xylene, toluene and benzene respectively. These temperatures are all significantly lower than those where any structural changes are observed from SANS measurements. This indicates that another process must also be involved in the modification of the initial Arrhenius dependence.

Figure 4.6a highlights the unique interplay between mechanical and electrical properties upon re-heating. As the temperature is raised, the elastic modulus (G') of P3HT gels in all solvents initially increases and then rapidly decreases. In contrast, the conductivity continues to

increase even after the viscous and elastic moduli have reached similar values (i.e., no longer a gel). The initial increase in elastic modulus is likely due to the continued self-assembly of free polymer chains, resulting in increasing fiber thickness or the formation of new fibers altogether. Interestingly, there is a peak in the loss modulus (*G''*), 23 ºC for toluene and 24 ºC for p-xylene, that does not correspond to any specific changes in the elastic modulus (*G'*). For example, *G*' is increasing for p-xylene samples and decreasing for toluene samples. This result is in contrast to P3HT gels formed in benzene, which show a relatively constant loss modulus during re-heating. The peak in loss modulus also occurs near the temperature where the Arrhenius behavior is found to break down for each gel, which indicates that there may be a transition that affects both the mechanical and electronic properties of the material around these temperatures. Physically, this behavior may suggest a transition from a rigid crystalline state to one with increased thermal fluctuation of polymer chains located within the fibers. These fluctuations could decrease the overall stiffness of the fibers and also affect the electronic properties. Eventually, these fluctuations are likely the origin of fiber breakup and dissolution.

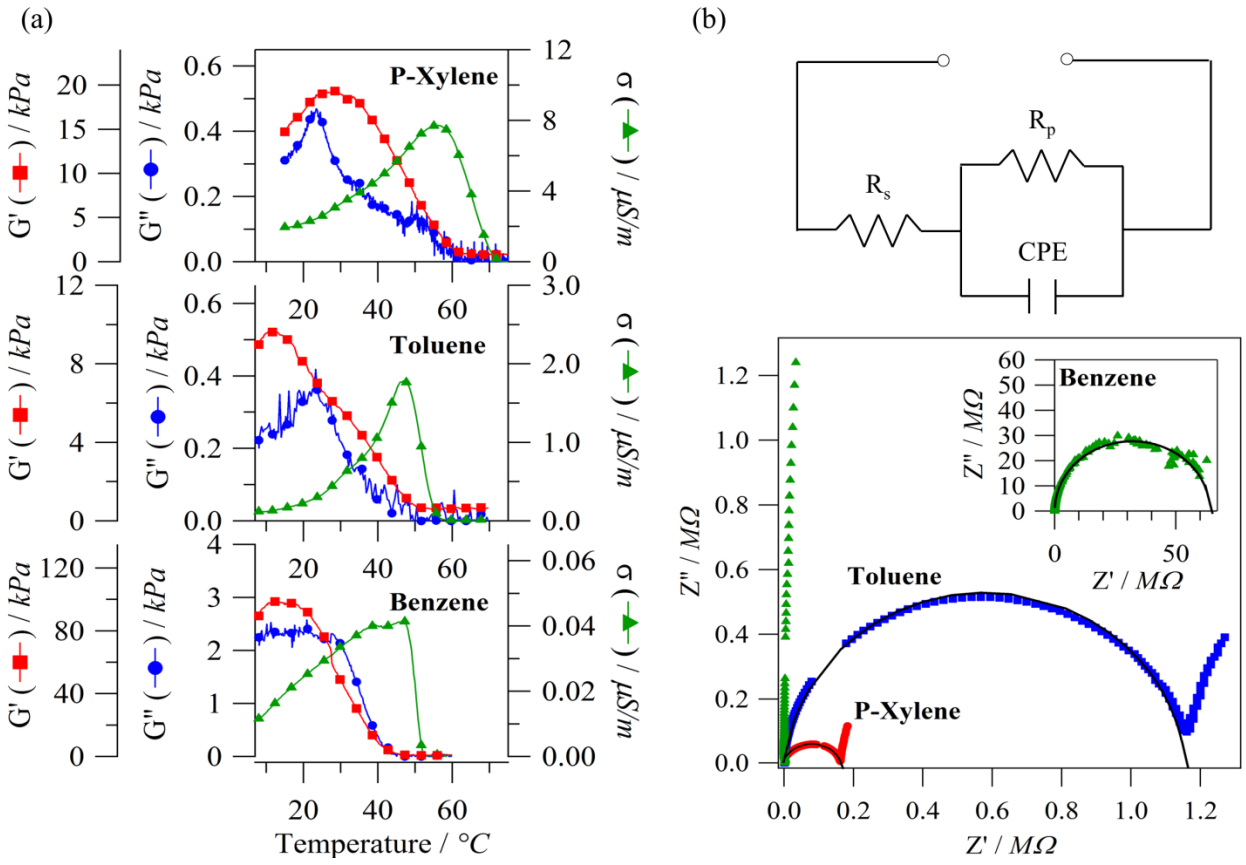

Figure 4.6. (a) Elastic (*G'*) and viscous (*G''*) moduli and AC conductivity (σ) during the re-dissolution of 30 mg/mL P3HT in different aromatic solvents measured using dielectric-rheology. (b) Impedance spectroscopy of fully developed P3HT organogels fit with a simple equivalent circuit.

The trend in conductivity for organogels formed in different solvents is also verified when evaluating the DC conductivity through linear impedance analysis (Figure 4.6b). A frequency sweep, from 20 – 2,000,000 Hz, of the fully developed gel phase was performed between the stainless steel parallel plate electrodes of the dielectric-rheology experimental setup. The linearized impedance spectroscopy is presented in Figure 4.6b. These data sets are fit with a simple equivalent circuit: a resistor (R_s) in series with a parallel resistor (R_p) and constant phase element capacitor (CPE). This equivalent circuit leads to the following equation:

$$Z = R_s + \frac{R_p}{\tau \cdot (j \cdot \omega)^{\alpha}} \tag{4.5}$$

where τ is a constant in units $F\,cm^{-2}s^{\alpha-1}$ and α is the constant phase element.[38, 39] The resistance (R_p) can be converted to dc conductivity (σ) using Equation 4.6, where d is the distance between electrodes and A is the surface area of the electrode. The fitting results are summarized in Table 4.2.

$$\sigma = \frac{1}{R_p} \cdot \frac{d}{A} \tag{4.6}$$

This analysis allows for the direct calculation of the resistance (R_p) associated with the dielectric behavior of the bulk organogel without the potential interference of resistances due to charge injection at the electrodes or due to other interfacial effects. From this analysis, the DC conductivities of the gels are determined to be 5.0 μS/m, 0.7 μS/m and 13 nS/m for p-xylene, toluene and benzene, respectively. These values are within the same order of magnitude as the AC conductivity measurements and also show the same trend as the activation energy. This result further demonstrates that it is possible to tune the electronic properties of organogels by adjusting self-assembly conditions.

Table 4.2. Equivalent circuit fitting results of electrochemical impedance spectroscopy from fully developed 30 mg/mL P3HT organogels formed in different organic solvents. This linearized impedance data is fit with Equation 4.5.

	P-Xylene	**Toluene**	**Benzene**
R_s **(Ω)**	1110	762	47
R_p **(MΩ)**	0.160	1.155	58.89
τ **(** $F\,cm^{-2}s^{\alpha-1}$ **)**	1.00×10^{-10}	3.42×10^{-11}	2.30×10^{-11}
α	0.862	0.944	0.991

4.3.3 Proposed Gelation & Re-Dissolution Mechanism for P3HT

The results in Figure 4.2 suggest that during the gelation of P3HT in p-xylene, toluene and benzene, thin fibers form initially and continue to thicken over time as gelation proceeds. Therefore, increased Ψ_f values likely result from both an increasing cross-sectional size and also from the formation of new fibers. The increase in fiber thickness may provide an explanation for why the development of Ψ_f at lower temperatures does not contribute significantly to further increasing the bulk conductivity. This finding may also explain why Huang and coworkers find that beyond 2 hours, further gelation of P3HT does not contribute to increased OPV device efficiency.[40] New fibers are more likely to increase the percolation between electrodes while thicker fibers may still have similar conductivity values when compared to slightly thinner fibers. A new mechanism for fiber growth is proposed in Figure 4.7 (right) where dissolved polymer chains join fibers at any point and contribute to increasing its thickness.

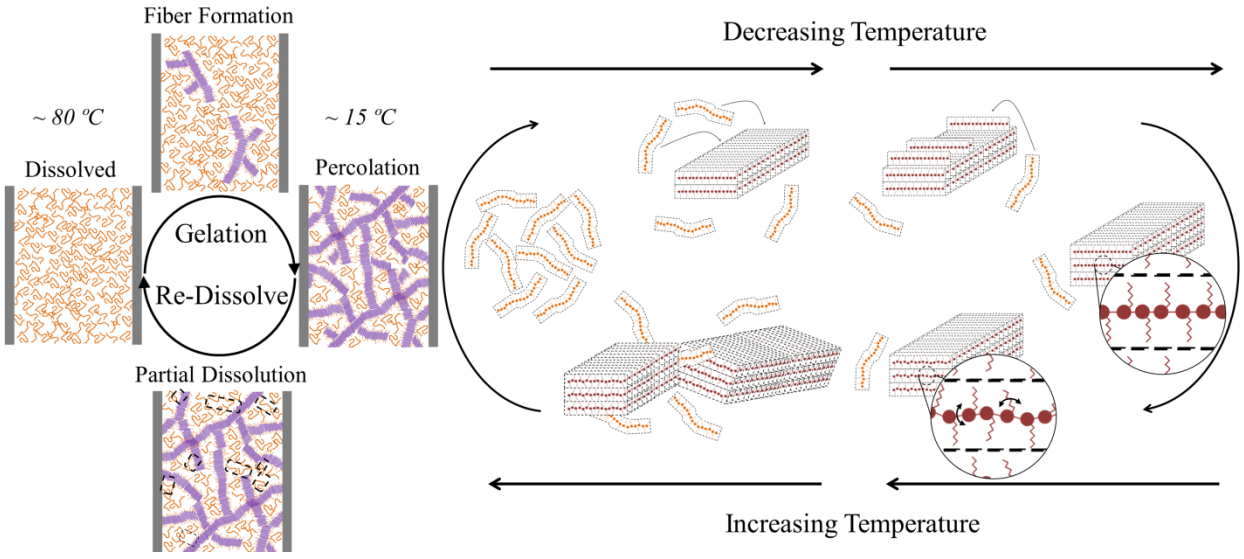

Figure 4.7. The development and re-dissolution of the fibrillar P3HT organogel structure (left). The self-assembly and break-up of individual P3HT fibers that occurs as a function of temperature (right).

Interestingly, the steady state width of the fibers in all solvents is close to 22 ± 3 nm, which is very similar to the contour length (20 ± 2 nm) of the polymer chain as determined from the molecular weight measured by SANS and from the length (3.85 nm) and weight (166.3 g/mol) of the monomer units.[41] This suggests that individual polymer chains could be stacking perpendicular to the fiber axis in an extended conformation and that self-folding of polymer chains within the fiber structure is not necessary.[42] For P3HT samples in p-xylene and toluene, the small but observable change in fiber width during gelation (Figure 4.2) could be due to the biased self-assembly of larger polymer chains first. Yet, this behavior is not seen in samples that gel in benzene. It should be noted that this work was limited to relatively low molecular weight polymer and studies of higher molecular weight polymer fibers have found that the fiber width is insensitive to adjustable parameters including solvent and temperature.[43]

The results from Figure 4.4 show that fiber formation and percolation occur nearly simultaneously during the gelation process. Figure 4.7 (left) shows a representation of how fiber formation leads to P3HT gelation and percolation. For gels formed in p-xylene and toluene, the fiber dimensions (width and thickness) remain constant during the re-heating cycle. Only gels formed in benzene show a decrease in fiber thickness just prior to dissolution. The large thermal hysteresis in the fiber fraction, fiber dimensions, mechanical properties and electrical properties suggest that organogel formation and dissolution differ significantly. The analysis of results in Figure 4.5 and Figure 4.6 suggest that dissolution from within a fiber is likely a cooperative process where multiple chains must loosen their intermolecular interactions in order to break free from the ends of fractured fibers, as seen in Figure 4.7 (right). During gelation, individual

polymer chains can easily crystallize and join growing fibers. In contrast, fiber breakup requires the cooperative dissolution of all the chains within a fiber segment. This dissolution process results in electrical and mechanical contacts being maintained until the fiber cross-section is fully broken. This simple mechanism can explain the large thermal hysteresis observed in the structural, mechanical and electrical properties of conjugated polymer organogels.

It is clear that even with similar fiber fractions and cross-sectional dimensions, drastically different mechanical and electrical properties are achieved during the gelation of P3HT in different solvents. The results presented here demonstrate differences in conductivity of more than two orders of magnitude when comparing p-xylene (most conductive) and benzene (least conductive) gels. Since nanoscale features of individual fibers remain fairly constant between solvents, these property changes may be the result of changes in the branching network structure which is consistent with the results in Chapter 3.3. Understanding the structural and mechanical features that contribute to electronic property enhancements is critical for the engineering of network structures that are designed specifically for OPV and other organic electronic applications. These results show significant promise towards this end.

4.4 Summary

Rheology-SANS, dielectric-SANS and dielectric-rheology measurements provide a robust understanding of the thermoreversible gelation and re-dissolution of P3HT in different solvents. We demonstrate that mechanical and electrical percolation occurs nearly instantaneously with the development of fibers. The percolation threshold for these gels is found to be lower than ~0.001 volume fraction. The large thermal hysteresis and the lack of structural changes in fibers during gel dissolution suggest that there is a very different mechanism for fiber

break-up than for formation. We propose that the breakup mechanism is a thermally activated cooperative process that causes a large hysteresis in the development of properties and structural features during cooling and heating of the samples. We also find that a conductive fiber network structure persists well after a significant fraction of the gel has re-dissolved. Finally, we observe a more than two order of magnitude difference in conductivity values for P3HT organogels formed in different organic solvents. The similarity in nanoscale structural features between these gels suggests that the network structure plays a critical role in the determination of charge transport efficiency within gels. These results further demonstrate that organogels incorporated into OPV photoactive layers would provide an excellent platform for achieving high interfacial area materials with tunable electronic properties.

4.5 References

1. Koppe, M.; Brabec, C.; Heiml, S.; Schausberger, A.; Duffy, W.; Heeney, M.; McCulloch, I. *Macromolecules* **2009,** 42, (13), 4661-4666.
2. Zhao, J.; Swinnen, A.; Van Assche, G.; Manca, J.; Vanderzande, D.; Mele, B. V. *The Journal of Physical Chemistry B* **2009,** 113, (6), 1587-1591.
3. Huang, P.-T.; Chang, Y.-S.; Chou, C.-W. *Journal of Applied Polymer Science* **2011,** 122, 233-240.
4. Kim, B.-G.; Jeong, E. J.; Park, H. J.; Bilby, D.; Guo, L. J.; Kim, J. *ACS Applied Materials & Interfaces* **2011,** 3, (3), 674-680.
5. Richards, J. J.; Weigandt, K. M.; Pozzo, D. C. *Journal of Colloid and Interface Science* **2011,** 364, (2), 341-350.
6. Alcazar, D.; Wang, F.; Swager, T. M.; Thomas, E. L. *Macromolecules* **2008,** 41, (24), 9863-9868.
7. Kitts, C. C.; Vanden Bout, D. A. *Polymer* **2007,** 48, 2322-2330.
8. Malik, S.; Jana, T.; Nandi, A. K. *Macromolecules* **2001,** 34, (2), 275-282.
9. Malik, S.; Nandi, A. K. *Journal of Physical Chemistry B* **2004,** 108, (2), 597-604.
10. Wang, P. S.; Lu, H. H.; Liu, C. Y.; Chen, S. A. *Macromolecules* **2008,** 41, (17), 6500-6504.
11. *Basic Research Needs for Solar Energy Utilization*; U.S. Department of Energy: http://www.sc.doe.gov/bes/reports/files/SEU_rpt.pdf, 2005.

12. Chen, C. Y.; Chan, S. H.; Li, J. Y.; Wu, K. H.; Chen, H. L.; Chen, J. H.; Huang, W. Y.; Chen, S. A. *Macromolecules* **2010,** 43, (17), 7305-7311.
13. Chen, J. H.; Chang, C. S.; Chang, Y. X.; Chen, C. Y.; Chen, H. L.; Chen, S. A. *Macromolecules* **2009,** 42, (4), 1306-1314.
14. Lin, Z.-Q.; Shi, N.-E.; Li, Y.-B.; Qiu, D.; Zhang, L.; Lin, J.-Y.; Zhao, J.-F.; Wang, C.; Xie, L.-H.; Huang, W. *Journal of Physical Chemistry C* **2011,** 115, (11), 4418-4424.
15. Sobkowicz, M. J.; Jones, R. L.; Kline, R. J.; DeLongchamp, D. M. *Macromolecules* **2011,** 45, (2), 1046-1055.
16. Xu, W.; Li, L.; Tang, H.; Li, H.; Zhao, X.; Yang, X. *The Journal of Physical Chemistry B* **2011,** 115, (20), 6412-6420.
17. Xu, W.; Tang, H.; Lv, H.; Li, J.; Zhao, X.; Li, H.; Wang, N.; Yang, X. *Soft Matter* **2012,** 8, (3), 726-733.
18. Yin, W.; Dadmun, M. *ACS Nano* **2011,** 5, (6), 4756-4768.
19. Kline, S. *Journal of Applied Crystallography* **2006,** 39, 895-900.
20. Lindner, P., *Neutrons, X-Rays and Light: Scattering Methods Applied to Soft Condensed Matter*. Elsevier Science: Amsterdam, 2002.
21. Glinka, C.; Barker, J.; Hammouda, B.; Krueger, S.; Moyer, J.; Orts, W. *Journal of Applied Crystallography* **1998,** 31, 430-445.
22. Porcar, L.; Pozzo, D.; Langenbucher, G.; Moyer, J.; Butler, P. D. *Review of Scientific Instruments* **2011,** 82, (8), 083902-7.
23. Li, J. L.; Yuan, B.; Liu, X. Y.; Xu, H. Y. *Crystal Growth & Design* **2010,** 10, (6), 2699-2706.
24. Liu, X. Y.; Sawant, P. D. *Advanced Materials* **2002,** 14, (6), 421-426.
25. Percec, V.; Ahn, C. H.; Ungar, G.; Yeardley, D. J. P.; Moller, M.; Sheiko, S. S. *Nature* **1998,** 391, (6663), 161-164.
26. Terech, P.; Weiss, R. G. *Chemical Reviews* **1997,** 97, (8), 3133-3160.
27. Zhang, S.; Marini, D. M.; Hwang, W.; Santoso, S. *Current Opinion in Chemical Biology* **2002,** 6, (6), 865-871.
28. Benoit, H. *Comptes Rendus Hebd Seances Acad Sci* **1957,** 245, 2244-2247.
29. Hammouda, B. *Advances in Polymer Science* **1993,** 106, 87-133.
30. Plestil, J.; Pospisil, H.; Ostanevich, Y. M.; Degovics, G. *Journal of Applied Crystallography* **1991,** 24, (5), 659-664.
31. Kreyenschmidt, M.; Uckert, F.; Muellen, K. *Macromolecules* **1995,** 28, (13), 4577-4582.
32. Butler, P.; Alina, G.; Hernandez, R. C.; Doucet, M.; Jackson, A.; Kienzle, P.; Kline, S.; Zhou, J. SASView for Small Angle Scattering Analysis. http://www.sasview.org/
33. Samitsu, S.; Shimomura, T.; Heike, S.; Hashizume, T.; Ito, K. *Macromolecules* **2010,** 43, (19), 7891-7894.
34. Ramasubramaniam, R.; Chen, J.; Liu, H. *Applied Physics Letters* **2003,** 83, (14), 2928-2930.

35. Sandler, J. K. W.; Kirk, J. E.; Kinloch, I. A.; Shaffer, M. S. P.; Windle, A. H. *Polymer* **2003,** 44, (19), 5893-5899.
36. Barth, S.; Bässler, H.; Rost, H.; Hörhold, H. H. *Physical Review B* **1997,** 56, (7), 3844-3851.
37. Zuo, F.; Angelopoulos, M.; MacDiarmid, A. G.; Epstein, A. J. *Physical Review B* **1989,** 39, (6), 3570-3578.
38. Lasia, A., *Modern Aspects of Electrochemistry*. Kluwer Academic/Plenum Publishers: New York, 1999.
39. Jorcin, J.-B.; Orazem, M. E.; Pébère, N.; Tribollet, B. *Electrochimica Acta* **2006,** 51, (8–9), 1473-1479.
40. Huang, W. Y.; Huang, P. T.; Han, Y. K.; Lee, C. C.; Hsieh, T. L.; Chang, M. Y. *Macromolecules* **2008,** 41, (20), 7485-7489.
41. Prosa, T. J.; Winokur, M. J.; Moulton, J.; Smith, P.; Heeger, A. J. *Macromolecules* **1992,** 25, (17), 4364-4372.
42. Liu, J.; Arif, M.; Zou, J.; Khondaker, S. I.; Zhai, L. *Macromolecules* **2009,** 42, (24), 9390-9393.
43. Kline, R. J.; McGehee, M. D.; Kadnikova, E. N.; Liu, J.; Fréchet, J. M. J.; Toney, M. F. *Macromolecules* **2005,** 38, (8), 3312-3319.

Chapter 5

Solvent Effects on Isothermal Poly(3-hexylthiophene) Gelation

5.1 Motivation

The diversity of structures required for organic electronics (e.g., OPVs, OFETs and OLEDs) motivates the need for conjugated polymer networks that are highly tunable.[1-11] It is well known that colloidal self-assembly processes are highly dependent on factors such as solvent environment, temperature and concentration.[12-14] In this work we study the effects of both solvent and concentration on the multi-scale structure of P3HT organogels formed at different concentrations and in various aromatic solvents for the purpose of informing the development of percolated networks for organic electronics. We use small-angle neutron scattering (SANS) and ultra small-angle neutron scattering (USANS) to evaluate the structure of P3HT gels over length scales of 1-10,000 nm. Scanning transmission electron microscopy (sTEM) is also utilized to complement the scattering analysis and to directly observe the network structures. Simultaneous rheology and conductivity measurements as well as UV-vis spectroscopy are utilized to further understand the complex self-assembly mechanism and to

develop structure-property relationships. Conductivity measurements confirm that structural variations can significantly impact charge transport characteristics in organogels. These results demonstrate that it is possible to engineer a network structure for specific organic electronic applications using gelation as a general platform.

5.2 Experimental Methods

Materials. Two lots of Sepiolid P200 poly(3-hexylthiophene) (P3HT) were used as received from Rieke Metals (Lincoln, NE). The molecular weight (M_w) and polydispersity index (PDI) of each batch was characterized using gel permeation chromatography (GPC) relative to polystyrene standards. Batch 1 (Lot# 31-10-2008) had M_w = 24,060 g/mol and PDI = 2.0. Batch 2 (Lot# 22.10.2009) had M_w = 16,770 g/mol and PDI = 1.6. The regioregularity of both batches was reported by the manufacturer to be greater than 98%. The results presented in this paper are primarily from Batch 2 samples, unless otherwise indicated. Some results from Batch 1 are also included to illustrate effects originating from batch-to-batch variations. Hydrogenated solvents p-xylene, toluene, and benzene were purchased from Sigma-Aldrich (St. Louis, MO) and used as received. Deuterated solvents were used to increase the scattering contrast and to decrease the incoherent scattering background in SANS and USANS experiments. D10-p-xylene (D > 98%), D8-toluene (D > 99.5%), and D6-benzene (D > 99.5%) were purchased from Cambridge Isotopes (Andover, MA) and were used as received.

Sample Preparation. Samples were prepared by adding 5-50 mg/mL P3HT to p-xylene, benzene or toluene and then heating to 80 °C until the polymer was fully dissolved. The polymer is considered fully dissolved when the solution is bright orange and there are no visible signs of

solid polymer (black). The polymer solution was then removed from heat and allowed to gel at a lower temperature for 24 hours unless otherwise noted.

UV-vis Spectroscopy. The fraction of solids in the gels was determined via UV-vis spectroscopy after allowing gels to self-assemble for a specific length of time. At this point, the gels were fractured through vigorous shaking in the presence of a small controlled amount of extra solvent (~ 2 mL). The fractured P3HT gels were then centrifuged at 21,100 × g for 1 min and the polymer concentration in the supernatant was measured via UV-vis spectroscopy. UV-vis absorbance spectra were obtained using a Thermo Evolution 300 UV-vis spectrophotometer at wavelengths between 350 and 750 nm. The concentration of the dissolved polymer fraction was determined from the maximum absorption at 450 nm using Beer's Law (Equation 2.21) with experimentally determined extinction coefficients of 50.3, 50.2 and 51.6 mL/mg cm for dissolved P3HT in p-xylene, toluene and benzene, respectively. The fraction of polymer in the solid phase was calculated from a simple mass balance.

Rheology and Conductivity. Rheological measurements were made using an Anton Paar Physica MCR301 stress controlled rheometer. Small amplitude oscillatory strain measurements (γ = 0.25% and f = 1Hz) were used to track changes in mechanical properties during gelation using a parallel plate geometry with a 50 mm diameter and 0.4 mm gap. Simultaneous conductivity measurements were also made for some experiments using the setup described in Chapter 2.4. AC conductivity measurements were made using an Agilent e4980a Precision LCR meter at a frequency of 2 kHz and a small perturbation voltage (200 mV) in the linear impedance region.

Scanning Transmission Electron Microscopy. Small quantities of the organogels were transferred to copper TEM grids with Formvar support films by briefly placing the grids in

contact with the surface of the gel samples without applying pressure. In this way, only a thin-film of organogel is transferred to the TEM grid. Due to the very thin nature of the samples, the aromatic solvents evaporate under ambient conditions. TEM images were obtained with a FEI Tecnai G2 F20 transmission electron microscope operating at 120 kV in scanning TEM (sTEM) mode.

Small-Angle Scattering. Ultra small-angle neutron scattering (USANS) and small-angle neutron scattering (SANS) experiments were performed at the NIST Center for Neutron Research in Gaithersburg, MD. SANS measurements were performed on the NG3 and NG7 instruments using standard configurations to cover a broad q-range ($0.001 < q < 0.5$ Å^{-1}).[15] Dissolved polymer solutions were loaded into demountable cells with quartz windows (1 mm path length) and allowed to gel for a minimum of 24 hours prior to measurement. USANS measurements were performed at NIST on the BT5 perfect crystal diffractometer extending the q-range to 4×10^{-5} Å^{-1}.[16] The data was reduced and desmeared using the NIST Igor-based algorithms.[17] Model fitting was performed using the NIST Igor-based analysis algorithms as well as the DANSE SansView software.[17, 18] *Dr. Kathleen Weigandt assisted with the collection and interpretation of this data.*

5.3 Results & Discussion

5.3.1 Structural Features of P3HT Gels in Aromatic Solvents

The self-assembly of an interconnected network of semiconducting fibers makes organogels of P3HT particularly promising for engineering low-cost electronic devices. We have previously shown that P3HT self-assembles into different fiber and network structures under different conditions (different solvent and temperature sweeps). However, isothermal gelation

offers a route towards systematically designing the structure at a fixed self-assembly condition. By doing this we can evaluate structure and property differences that arise from changes in solvent-polymer interactions. The multi-scale structure of these networks must be fully characterized in order to optimize it for relevant applications. Here we use a combination of sTEM and small angle neutron scattering techniques to characterize the bulk structure of P3HT organogels over a wide range of length scales.

Dried P3HT networks were evaluated using sTEM and typical images are shown in Figure 5.1 highlighting important features. Most notable are dense nucleation centers, fibrillar 'ropes' (i.e., lateral fiber bunches) and branching of individual fibers. Dense nucleation centers were primarily observed in samples prepared from Batch 1 of the P3HT. Dense radial growth can originate from impurities or from aggregates that act as nucleation sites for new fibers.[19] We believe that this feature could arise in P3HT samples due to impurities, such as residual polymerization catalyst, or due to high molecular weight fractions that may not fully dissolve and may act as nucleation sites. Batch 1, which shows more nucleation, had a significantly larger molecular weight and polydispersity index when compared to batch 2. Dense nucleation centers are expected to be a potential source of trap-sites for charge carriers in the organogels due to their disordered nature and because they act as junctions to several fibers. Therefore, to improve transmission of charge, it is desirable to minimize the formation of dense nucleation centers.

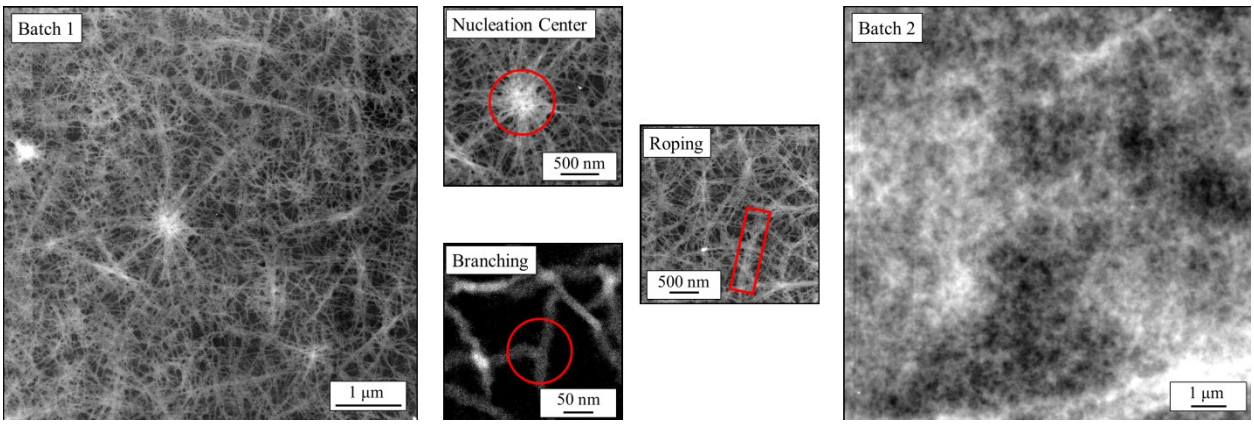

Figure 5.1. P3HT organogel network features can include dense nucleation centers, fibrillar roping and fibrillar branching. The sTEM images are made from 27 mg/mL P3HT (Batch 1) and 30 mg/mL P3HT (Batch 2) in toluene.

The fiber 'ropes' observed in this study are also consistent with reported AFM studies of P3HT gels.[20] Fibrillar roping, which is observed in both P3HT batches, results in the lateral aggregation of fibers often with less than 10 nm of space between fibers. Finally, fibrillar branching (or fiber splitting) is also observed in all sTEM images. Bifurcations are expected to be beneficial for electronic properties as they allow for continuous charge transport along fibers through branch points and reduce the total number of potential charge trap sites, as discussed in Chapter 3.3. Unfortunately, the extent of branching could not be easily quantified in sTEM due to the three-dimensional structure of the gel and the high fiber density.

While sTEM is an effective tool for visualizing the gel structure, it only yields a two-dimensional projection of a three-dimensional structure, it requires a thin sample to resolve the morphology and it is performed on dry films after solvent evaporation. In contrast, small angle neutron scattering (SANS) is a proven non-destructive method for quantifying the average bulk structural properties of solvated P3HT gels over all relevant length scales. Figure 5.2 shows the 1D SANS and USANS profiles for a 30 mg/mL P3HT organogel self-assembled in p-xylene. The scattering provides structural information over multiple length scales (~1 nm to 10,000 nm)

to characterize all features of the gel. The morphology of P3HT organogels is modeled using the approach described in Chapter 2.1.5.

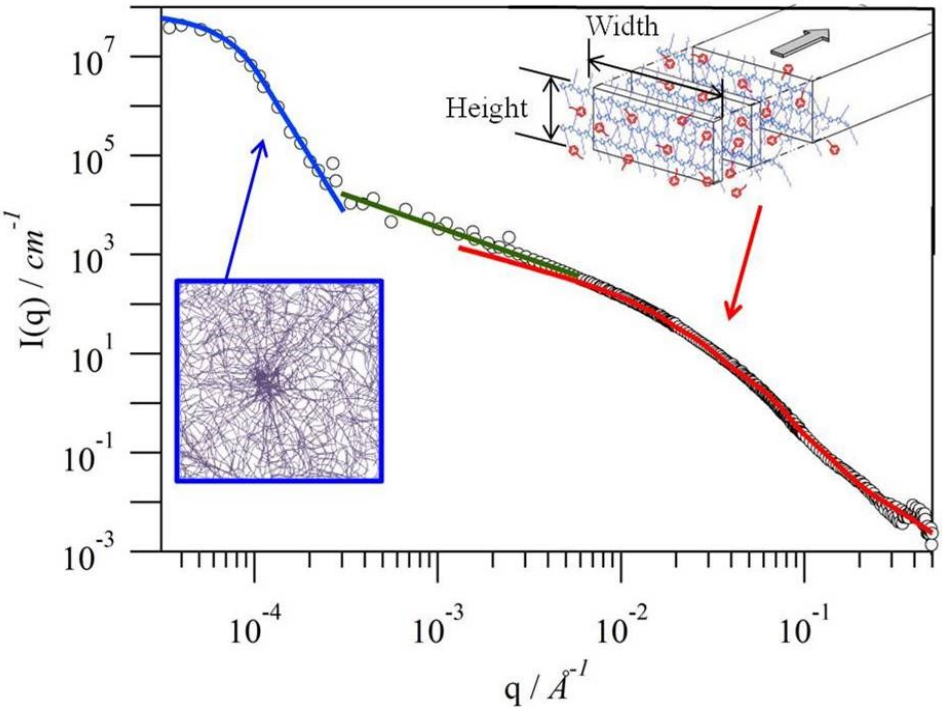

Figure 5.2. SANS & USANS profile for 30 mg/mL P3HT (Batch 1) in p-xylene (○). Fits to different models are shown as colored lines: the combined model (Equation 2.6, ▬), fractal network power law (Equation 2.9, ▬) and Guinier extrapolation (Equation 2.10, ▬). The deviation of the parallelepiped form factor of at q = 0.009 Å^{-1} is due to the increased power-law slope caused by the fractal network structure.

At high-q, the internal structure and semi-crystalline nature of P3HT fibers dominates the scattering intensity. The peak at high-q is characteristic of the lamellar spacing within the P3HT crystal lattice.[9] This region was fit to a Gaussian peak (seen in Figure 5.3) corresponding to a spacing of 15.8 Å, which is within one angstrom of the expected value reported in the literature.[7] A more detailed analysis of the diffraction peak, with respect to concentration, is not possible due to the incoherent background and the resolution limit of the SANS instrument at high-q.

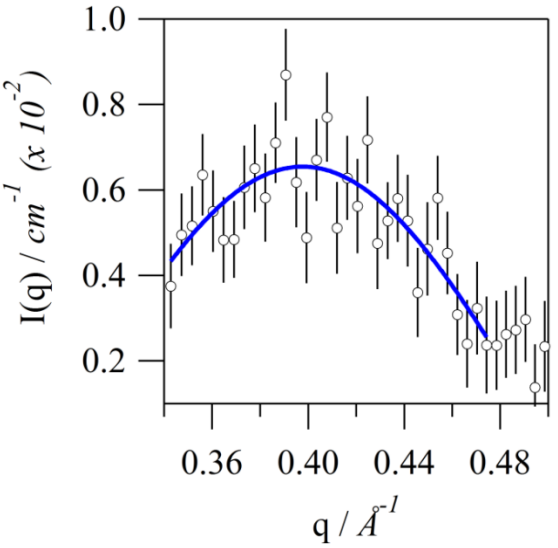

Figure 5.3. The high-*q* region from a 30 mg/mL P3HT organogel (Batch 1) SANS profile shown in Figure 5.2. This high-q diffraction peak is fit with a Gaussian function to extract the peak max at ~ 0.40 $Å^{-1}$.

In the low-*q* region, $7 \times 10^{-5} < q < 2 \times 10^{-4}$ $Å^{-1}$, there is another increase in the scattering intensity that clearly deviates from fractal behavior. Scattering in this region is attributed to the dense nucleation centers in the gels that are also visible in the electron microscopy images. The characteristic size of these dense nucleation centers can be obtained by performing a simple Guinier extrapolation, which results in a radius of gyration of ~10 μm. This low-*q* characteristic is most clearly observed in samples prepared from P3HT in Batch 1. It is still possible that dense nucleation centers also occur in Batch 2 but those domains would need to be larger than the minimum q-range probed by USANS. In contrast, the sTEM images did not show dense nucleation centers in samples prepared from Batch 2 so it is likely that they are not present. Scattering data comparing the two polymer batches can be seen in Figure 5.4.

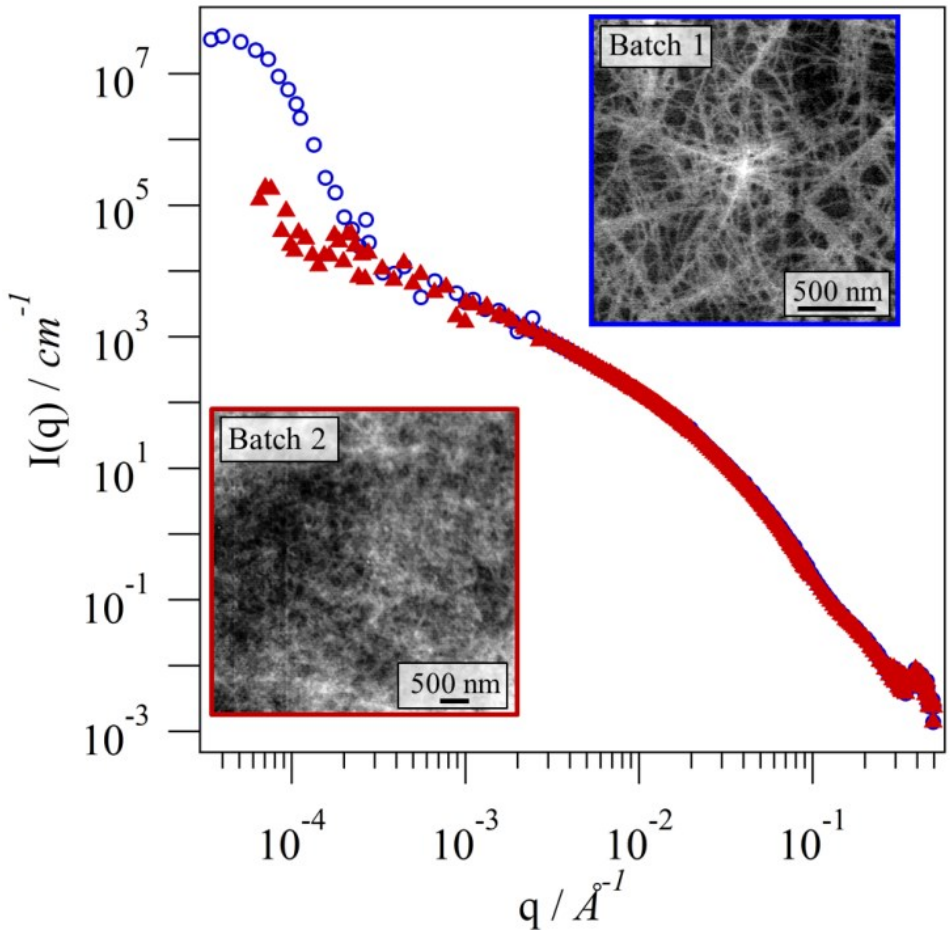

Figure 5.4. SANS and USANS profiles of 30 mg/mL P3HT, from Batch 1 (○) and Batch 2 (▲), self-assembled in p-xylene. Also shown are corresponding sTEM micrographs of the networks with scale bars (500 nm).

SANS probes the multi-scale structure of P3HT organogels without disturbing the gels. Figure 5.5a,b show the results of fitting P3HT scattering data to the combined model (Equation 2.6).[18] Interestingly, the fiber width is relatively constant at about 24 nm regardless of the solvent type or the polymer concentration. The fiber height is also found to be independent of the polymer concentration. However, there is a systematic solvent dependence of the fiber height as P3HT fibers formed in benzene are typically 15% thicker than all other samples.

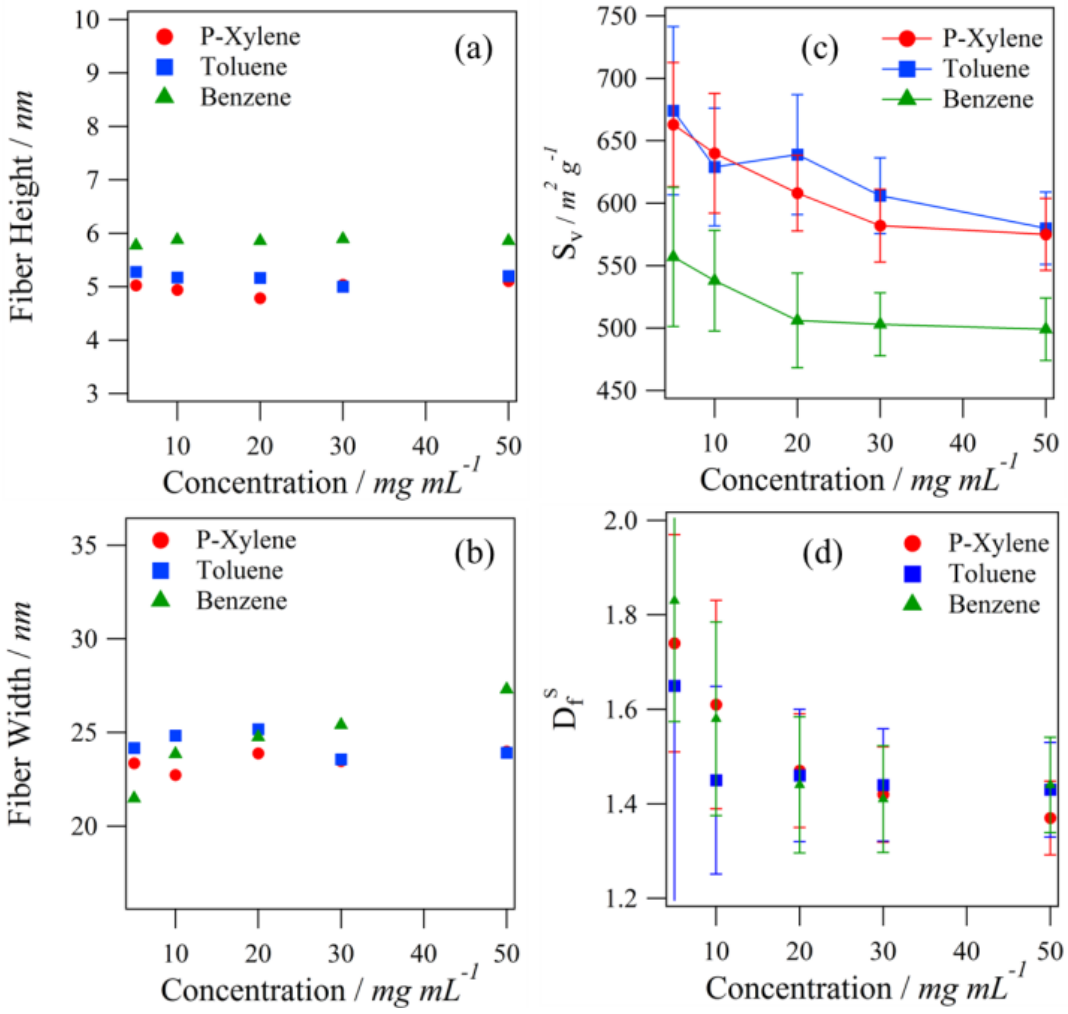

Figure 5.5. P3HT fibrillar (a) height and (b) width as obtained from parallelepiped model, the (c) specific surface area (S_v) of P3HT fibers obtained from a Porod analysis and the (d) network fractal dimension (D_f^S) obtained from power law fitting. The error bars reflect the fitting uncertainty. In (a) and (b) the error bars are smaller than the marker size.

Because exciton dissociation occurs at the interface between donor and acceptor materials, the total interfacial area of the fibers in the gel is an important metric that can significantly affect the overall efficiency of OPV devices. To this end, the specific surface area of the P3HT fibers in each organogel was determined from a standard Porod analysis as described in Chapter 2.1.3. In all samples, an intensity proportional to q^{-4} develops between 0.07

< q < 0.1 Å^{-1} due to the sharp interface between the P3HT fibers and the solvent (as seen in Figure 5.6).[21]

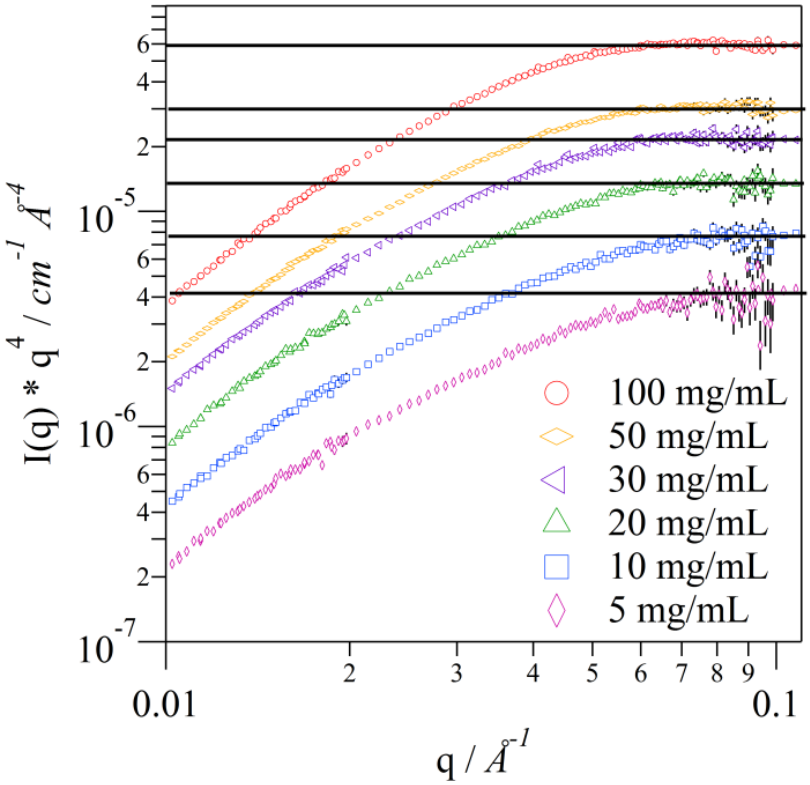

Figure 5.6. Porod plots of a concentration series of P3HT organogels formed in d10-p-xylene highlighting the $I \propto q^{-4}$ dependence at intermediate to high-q. Horizontal black lines indicate the value of the fit for $I(q)*q^4$ as $q \rightarrow \infty$, which is used to calculate S_v.

The specific surface area of the P3HT nanofibers is reported in Figure 5.5c. All of the organogels evaluated have a very high specific surface area that decreases with concentration and that also varies with the solvent type. The slight reduction in the specific surface area with increasing polymer concentration is likely caused by an increase in fiber-fiber contacts leading to lower interfacial area between P3HT and solvent. The reduced specific surface area of P3HT fibers in benzene, relative to the other solvents, can also be fully explained by accounting for the increase in the cross-sectional dimensions of the fibers due to the larger height (Figure 5.5a).

D_f^S is also plotted as a function of concentration and solvent in Figure 5.5d. The P3HT gels characterized in this study are described by fractal dimensions between 1.4 and 1.9. The fractal dimension, like the specific surface area, decreases as a function of concentration. At first look, this could be interpreted as a decrease in the network density with increasing concentration. However, it is also important to note that heterogeneous networks with significant density fluctuations, show higher apparent fractal dimensions than homogeneous networks.[22] At low concentrations, inhomogeneities will occur due to solvent-rich regions that develop between fiber-rich regions of the organogel. These solvent spaces are more abundant at polymer concentrations that are very close to the onset of percolation. When the concentration increases, the organogels effectively fill all free space and become increasingly more homogeneous.

5.3.2 Fractal Branching from Structural, Mechanical and Electrical Measurements

Simultaneous rheology and conductivity measurements allow for direct correlation of the evolution of the mechanical and electrical properties during the gelation process, as described in Chapter 2.4. Figure 5.7 tracks the gelation and dissolution of a sample with 30 mg/mL of P3HT dissolved in p-xylene with simultaneous mechanical and electrical property measurements. For clarity, the mechanical data in Figure 5.7 is shown in terms of the complex modulus (G^*), which is related to the elastic and viscous moduli (G' and G'') by the following equation:

$$G^* = \sqrt{(G')^2 + (G'')^2} \tag{5.1}$$

The complex modulus is effectively equivalent to the elastic modulus for P3HT in the gel phase because $G' >> G''$. However, it is also important to note that the complex modulus prior to gelation (i.e., in the soluble phase) is significantly affected by the friction between the upper geometry shaft and the gold contact that is necessary for the electrical connection, depicted in

Figure 2.19. The data shown in Figure 5.7 suggests that the increase in conductivity develops prior to the increase in G^*. However, this could also be due to the background friction that makes the measurement less sensitive to the initial changes in the elastic modulus. Nevertheless, it is clear that gelation occurs around 26 °C and that it corresponds to an increase of more than two orders of magnitude in the conductivity in addition to the observed increase in elasticity (G^*).

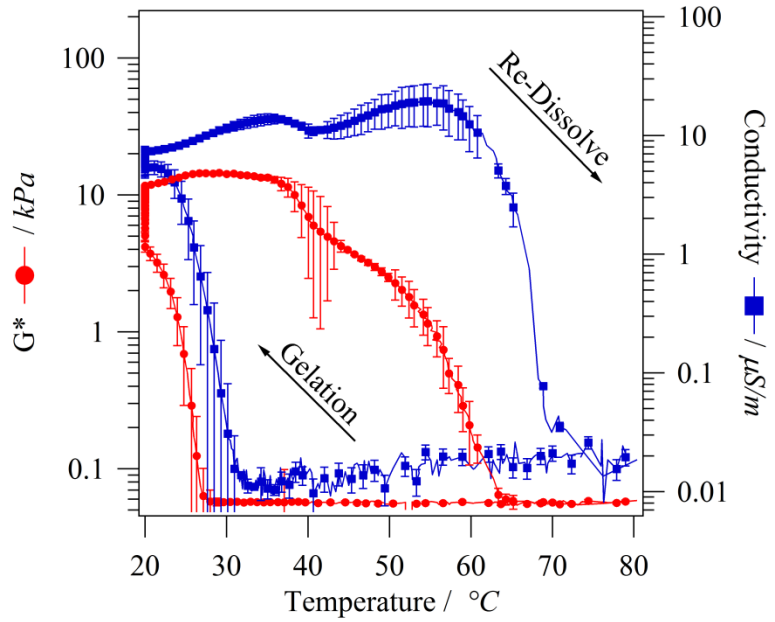

Figure 5.7. Temperature-dependent, simultaneous oscillatory rheology and AC conductivity of a 30 mg/mL P3HT organogel formed and re-dissolved in p-xylene. The temperature sweep rate is 2 °C/min. When the temperature reached 20 °C, gelation was allowed to proceed to completion for 2 hours prior to the heating ramp.

Figure 5.7 also shows that upon re-heating there is significant thermal hysteresis in the mechanical and electronic properties of the gel prior to complete dissolution. This is particularly evident for the conductivity, which shows a significant increase in magnitude upon re-heating. This response is due to the Arrhenius behavior of conductivity that is described by Equation 5.2:

$$\sigma = Ae^{\left(-\frac{E_A}{k_b}\frac{1}{T}\right)} \tag{5.2}$$

Here, σ is the conductivity, A is a proportionality constant, E_A is the activation energy, k_b is Boltzmann's constant and T is the temperature. When the initial increase in conductivity is fit to the Arrhenius equation we find that $E_A = 300 \pm 79$ meV. This value is very similar to what others have reported for solid P3HT films.[23]

Time-dependent simultaneous rheology and conductivity measurements were also performed to probe the development of mechanical and electrical percolation in networks. Rheology is only sensitive to fiber interactions that contribute to the transduction of mechanical stress between the two plates of the rheometer. Meanwhile, conductivity measurements are only sensitive to fiber paths that electronically bridge the electrodes (Figure 5.8a). Thus, a single network can be characterized by two fractal dimensions resulting from these two different macroscopic properties and we will refer to them as D_f^E for electronic percolation and D_f^M for mechanical percolation. Figure 5.8b depicts an example of two different network structures that might have very similar mechanical properties, but would have drastically different electrical properties. Furthermore, the fractal dimension obtained from scattering experiments (D_f^S) may be different from either the fractal dimensions obtained from electrical (D_f^E) or mechanical measurements (D_f^M) as it characterizes yet a different aspect of the network structure.

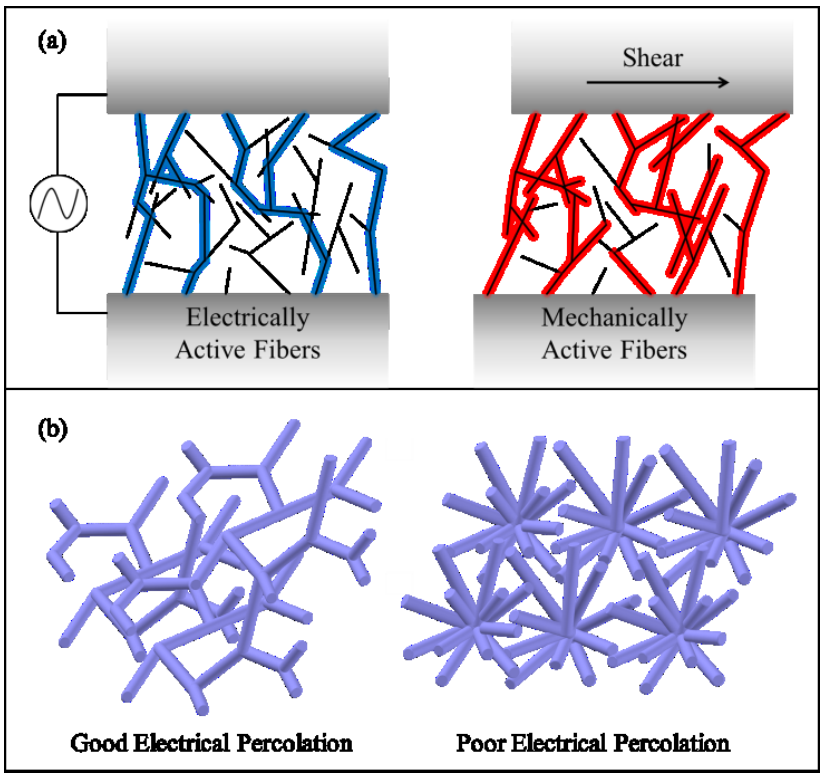

Figure 5.8. a) Sketch to illustrate the sensitivity of rheology and conductivity measurements for characterizing the complex network structures. Fibers can contribute differently to the bulk conductivity (σ) and to the elastic modulus (G') of the network. b) Example of two network structures that could result in similar mechanical properties but different electrical properties.

Liu and coworkers have demonstrated the use of rheology to determine the fractal dimension (D_f) of branching fibrillar organogels by using the Avrami theory to characterize the kinetics of gelation.[24-26] This powerful analysis relies on some basic assumptions including a constant fiber growth rate and branching frequency. Under isothermal conditions, the total extent of gelation is characterized by X_G,

$$X_G(t) = 1 - \exp(-k \cdot (t - t_{gel})^{D_f}) \tag{5.3}$$

where k is a constant proportional to the rate of fiber growth, t is the elapsed time and t_{gel} is the initial gelation time. The extent of gelation (X_G) is related to measurable properties such as the complex modulus (G^*) and the conductivity (σ) using:

$$X_G(t) = \frac{G^*(t) - G^*_{bkg}}{G^*_{\max} - G^*_{bkg}} \; or \; X_G(t) = \frac{\sigma(t) - \sigma_{bkg}}{\sigma_{\max} - \sigma_{bkg}} \tag{5.4}$$

where $G^*(t)$ is the time-dependent complex modulus, G^*_{bkg} is the complex modulus prior to gelation, $G^*_{\max}$ is the maximum complex modulus associated with kinetic equilibrium, *σ(t)* is the time-dependent conductivity, σ_{bkg} is the conductivity of the solution prior to gelation and $\sigma_{\max}$ is the maximum conductivity of the gel. To ensure that gelation was monitored at a constant temperature and from identical initial states, the fully dissolved polymer was rapidly cooled from 80 ºC to 20 ºC at a rate of 22.5 ºC /min. The gelation process was then monitored as a function of time when the test solution reached 20 ºC. The time required to reach the test temperature (< 3 min) was much smaller than the characteristic gelation time.

5.3.3 Impact of Solvent Choice on Branching and Charge Transport

Figure 5.9 shows the isothermal gelation kinetics of P3HT in different organic solvents. Upon close examination, it is evident that the solvent plays an important role in the development of the mechanical and electrical properties. The lower images in Figure 5.9 show the same data, but plotted in a linearized form of Equation 5.5:

$$\ln(-\ln(1 - X_G(t))) = \ln(k) + D_f \ln(t - t_{gel}) \tag{5.5}$$

In this plot, the slope represents the fractal dimension and the intercept is related to the rate of gelation (*k*). In this format it becomes clear that, for all samples, there are two distinct slopes associated with the rheological measurement in the initial growth period and near its end. The slope change occurs near the time when the conductivity is fully developed for p-xylene and toluene organogels. In benzene organogels, there is a slope change associated with both the conductivity and the rheological measurement. This change occurs when the conductivity of the

benzene sample is ~ 50% developed and, unlike the p-xylene and toluene samples, the conductivity of benzene gels continues to increase until gelation is complete. As seen in Figure 5.9, the electrical properties of p-xylene and toluene gels fully develop on a shorter time scale than the mechanical properties. In this work, the mechanical (D_f^M) and electrical (D_f^E) fractal dimensions are extracted from the initial growth region, which corresponds to the largest increase in conductivity for all samples.

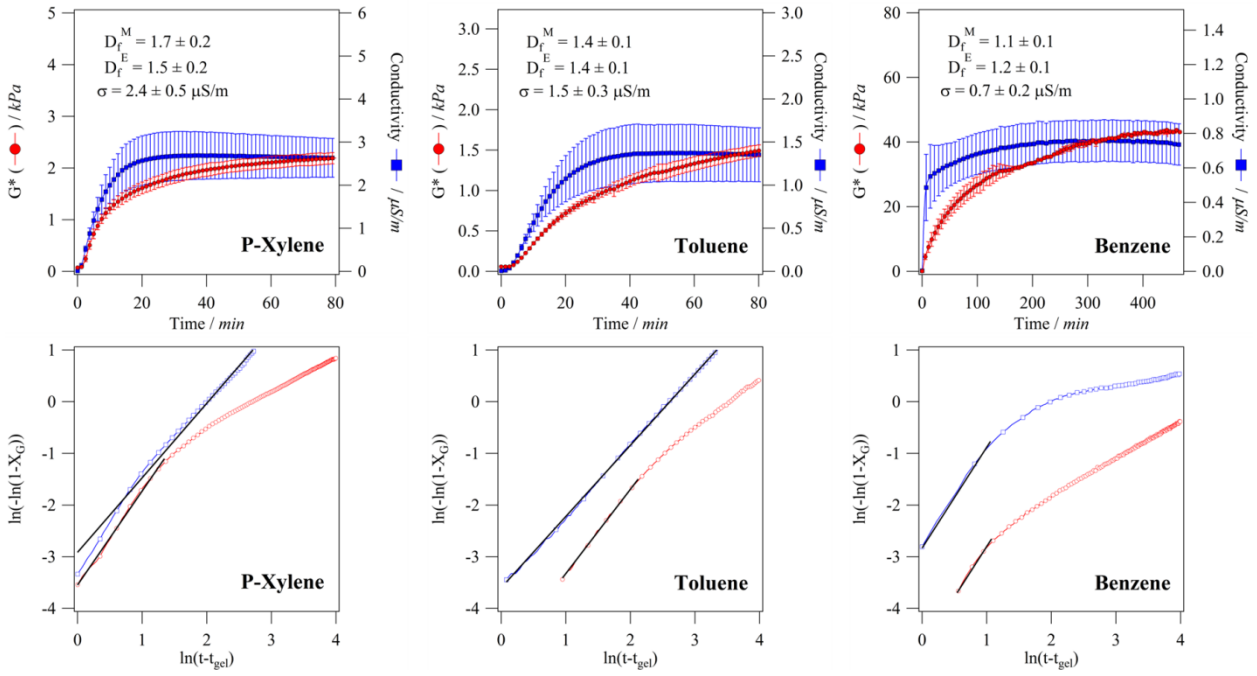

Figure 5.9. Top row: Simultaneous rheology and conductivity collected during the isothermal gelation of 30 mg/mL P3HT in different aromatic solvents at a temperature of T = 20 °C. Bottom row: Data represented in the linearized form (Equation 5.5).

Table 5.1. Summary of fitting results to the kinetic gelation model from isothermal, simultaneous rheology and conductivity experiments for 30 mg/mL P3HT organogels (Batch 2).

	P-Xylene	**Toluene**	**Benzene**
k_E **(min^{-1})**	3.6×10^{-2}	2.4×10^{-2}	1.1×10^{-1}
D_f^E	1.5 ± 0.2	1.4 ± 0.1	1.2 ± 0.1
k_M **(min^{-1})**	3.9×10^{-2}	1.0×10^{-2}	2.5×10^{-2}
D_f^M	1.7 ± 0.2	1.4 ± 0.1	1.1 ± 0.1
$G^*_{\max}$ **(kPa)**	2.3 ± 0.1	1.7 ± 0.1	46.9 ± 5.3
σ_{max} **(μS/m)**	2.4 ± 0.5	1.5 ± 0.3	0.7 ± 0.2

Table 5.1 summarizes the fitting results of the kinetic model as well as the equilibrium mechanical and electrical properties from the experiments shown in Figure 5.9. Benzene gels take significantly longer to reach equilibrium, resulting in a lower fractal dimension and suggesting that fewer fibers are growing simultaneously. According to the fractal dimensions, p-xylene and toluene organogels have denser and more branched network structures than benzene gels. Importantly, all three gels show significantly different maximum elastic moduli and conductivity values indicating that there is potential to tune these properties for specific applications by simply controlling the solvent quality and the kinetics of gelation.

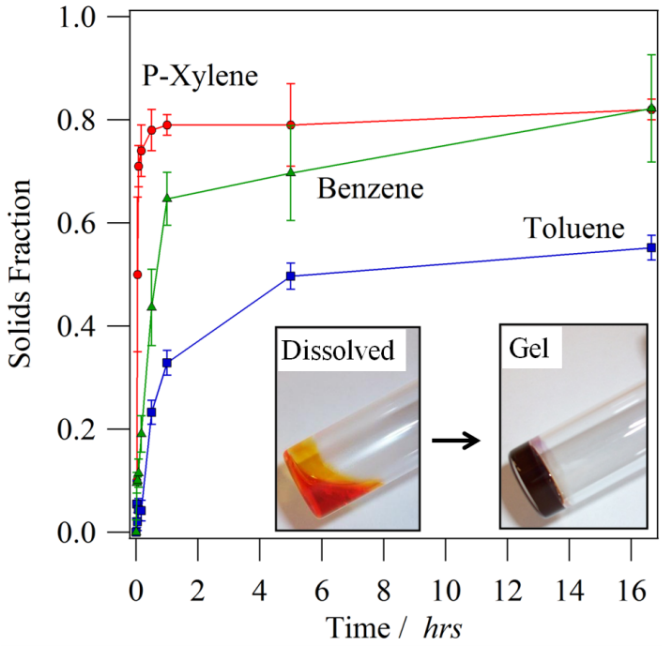

Figure 5.10. Time evolution of the solids content of 30 mg/mL P3HT organogels self-assembled in aromatic solvents at 20 °C.

Conjugated polymers rarely reach a fully self-assembled state due to their finite solubility in aromatic solvents. Therefore, the total amount of polymer in solid form (i.e., solids fraction) is also an important parameter to consider in evaluating the properties of organogels. The total extent of solidification in the gels can be quantified by tracking the concentration of dissolved polymer over time with the following equation:

$$\phi = 1 - \frac{C(t)}{C_i} = 1 - \frac{A(t)/(\varepsilon \cdot l)}{C_i} \cdot d_f \tag{5.6}$$

where ϕ is the solids fraction, $C(t)$ is the dissolved polymer concentration at time t, C_i is the initial concentration of polymer, $A(t)$ is the absorbance due to dissolved polymer at time t, ε is the extinction coefficient of P3HT in the solvent, l is the path length of the cell and d_f is the dilution factor. The development of the solids fraction over time can be seen in Figure 5.10. P-xylene samples take significantly less time to reach the final equilibrium state than organogels formed in toluene and benzene. In contrast, benzene gels form with a slow and continuous

evolution but are still able to reach larger equilibrium solid fractions than toluene gels, which contain the largest amounts of dissolved polymer at long times. After more than 16 hours of gelation, the equilibrium solids fractions of the organogels are 83%, 81% and 56% for benzene, p-xylene and toluene, respectively.

5.4 Discussion

SANS reveals that the fiber structure is nearly identical across solvents and concentrations, with the exception of organogels prepared in benzene that have a slightly larger fiber height. The larger fiber cross-section of gels prepared in benzene (~ 15% increase in fiber thickness) contributes to a lower interfacial area and a larger elastic modulus (46.9 kPa) when compared to gels formed in p-xylene (2.3 kPa) and toluene (1.7 kPa). On the other hand, P3HT gels prepared in benzene also show lower electrical conductivity values when compared to gels formed in other solvents. This suggests that the macroscopic properties in these materials relate differently to specific structural features in the gels. Scanning TEM also demonstrates that gels are bifurcating networks where fibers split and branch to form interconnected networks. The branching observed in P3HT gels allows for effective charge transport through fiber junctions and along the π-π stacking direction of the fiber axis leading to effective and long-range charge propagation (i.e., high conductivity through millimeter thick samples). Charge transport between fibers that are only touching is not expected to be very effective because the exposed alkyl chains of the P3HT act as insulating layers that hinder inter-fiber charge transport.[27]

We have also demonstrated that network structures in P3HT organogels can be evaluated using a variety of complementary techniques (rheology, conductivity and neutron scattering) to characterize different components of the same network (D_f^M, D_f^E and D_f^S). The mechanical

fractal dimension D_f^M is sensitive to fibers that interact and contribute to the transduction of mechanical stress, D_f^E is sensitive to fibers that electrically percolate the electrodes and D_f^S characterizes the total network density and its inhomogeneities. D_f^S was found to be relatively constant across solvents but D_f^M and D_f^E differed significantly for the three solvents. In each of the solvents, D_f^M and D_f^E are found to be very similar during the initial growth region suggesting that both components develop similarly at short time scales. However, unlike the electrical conductivity, the modulus continues to slowly evolve with time during gelation for samples prepared in p-xylene and toluene. The linearized data in Figure 5.9 (bottom plots) shows that the slope corresponding to the mechanical fractal dimension in all samples changes at an intermediate time during the gelation process. In contrast, a single slope characterizes the linearized conductivity data for P3HT gels in toluene and p-xylene over the full time range. Benzene gels show changes in slope for the elastic modulus and the electrical conductivity. These combined rheology and conductivity measurements also demonstrate that increasing elasticity does not always result in increasing electrical conductivity. This is because continued fiber growth may not always improve electrical percolation. For example, at long times newly formed fibers can contribute to the increased transduction of mechanical stress but may not bridge the electrodes in order to contribute to increasing the bulk conductivity.

The structure and property measurements presented in this work provide great insight and allow us to propose a detailed gelation mechanism for P3HT in aromatic solvents (Figure 5.11), which complements the fiber formation mechanism discussed in Chapter 4. In addition, SANS and sTEM both demonstrate that P3HT polymers self-assemble into interconnected fibers in the gels. The isothermal kinetic experiments (Figure 5.9) further show that fibers branch to different

degrees during the gelation process depending on the solvent quality. These branching sites can also be directly observed in the sTEM images shown in Figure 5.1. The detailed gelation mechanism that emerges from these new experiments builds upon those presented in pervious works. Koppe and coworkers proposed that P3HT gelation occurred as a result of polymer aggregation followed by physical cross-linking of aggregates.[28] Xu and coworkers suggested that fibers grew in one dimension and subsequently aggregated to produce a percolated network structure.[29] Our results suggest a mechanism in which discrete branched fiber networks form at short times while the sample remains liquid and continue to grow until percolation and gelation is achieved. This finding is consistent with the work in Chapter 3, where colloidal network structures were formed from P3HT solutions at lower concentrations. Subsequently, significant fiber and network growth continues to occur long after the first signs of gelation are observed. Yet, fibers formed at long times may contribute differently to the development of various macroscopic properties (e.g., electronic or mechanical) depending on whether or not they result in a net increase in the network interconnectivity. Finally, these results also suggest that the solvent quality can be used to alter branching in growing fibers and to modify the final properties of the organogels.

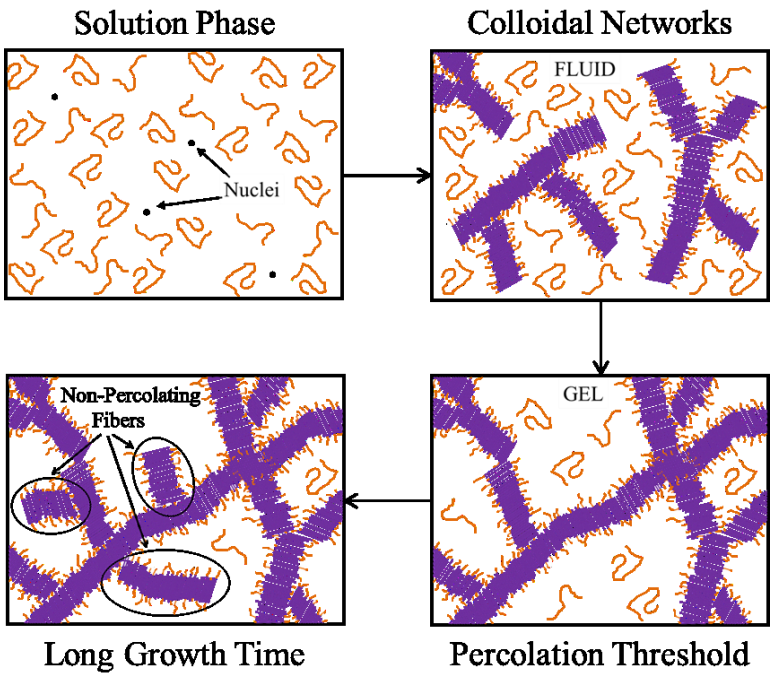

Figure 5.11. Schematic of the proposed gelation mechanism for P3HT in aromatic solvents. Upon cooling, dissolved polymer grows into fibers from nucleation sites. Lattice dislocations lead to branching and the formation of a colloidal dispersion of isolated fiber networks. Eventually, dispersed networks grow and reach the percolation threshold to form a gel. The network structure continues to develop with time as new fibers grow and may contribute differently to the developing gel properties (e.g., conductivity and elasticity).

Simultaneous rheology and conductivity measurements reveal that different mesoscale structures can be achieved by adjusting self-assembly conditions. Solvent quality has been found to be a primary factor controlling the network formation in a variety of small molecule systems.[26] The equilibrium solids fraction (Figure 5.10) in different solvents is an indication of supersaturation and therefore solvent quality.[30] Based on these results, toluene is the best solvent for P3HT. However, our data also suggests that relative solubility is not the only factor contributing to the final structure (i.e., D_f^M and D_f^E) and properties (i.e., elasticity and conductivity) of P3HT networks. For example, the incorporation of solvent molecules within growing fibers may also play a substantial role in controlling growth and the resulting structure.

More work is therefore needed to fully determine all fundamental dependencies between the driving forces for gelation and the resulting network structures.[30, 31]

From our results, it is evident that the network structure of P3HT gels can be manipulated to produce distinctly different mechanical and electrical properties. In fact, there is a direct correlation between increased branching (D_f^M and D_f^E) and the final conductivity of the gels. Branching fibers should increase conductivity more effectively than fibers that only 'touch' each other because the insulating alkane layers will hinder inter-fiber charge transport. Since fibers have a nearly identical nanoscale structure, the changes in mechanical and electrical properties can be primarily attributed to alterations to the mesoscale structure. That being said, the gels formed in benzene have the highest modulus and lowest conductivity. One possible explanation for this is that the increased fiber thickness in benzene results in significantly stiffer fibers compared to p-xylene or toluene. This can easily explain the increased elastic modulus of these gels. On the other hand, both the electrical and mechanical fractal dimensions indicate that fiber growth in benzene is less branched than in any other solvent and this could lead to the reduced bulk conductivity.

Malik and coworkers also found that gelation of P3HT resulted in an order of magnitude increase in conductivity when compared to thin films.[32, 33] Here, we confirm that the conductivity of the gel phase (measured up to 7 μS/m at 20 ºC) is significantly larger when compared to thin solid films reported in literature (0.678 μS/m).[23] Furthermore, organogels are able to effectively transport charges over very large distances due to their percolating network structure. In our experiments, samples as thick as 1 mm were found to maintain excellent conductive properties.

Temperature adjustment could be another way to tune the final network structure. Small molecule organogels have been produced with different network structures through control of

supersaturation by varying the temperature or the thermal history.[31] When comparing identical samples in Figure 5.7 (slow cooling ramp of 2°C/min) and Figure 5.9a (isothermal gelation at 20 °C), it is found that self-assembly associated with slow cooling results in a network structure with a threefold increase in conductivity (measured at 20 °C). Unfortunately, the full Avrami analysis cannot be performed using non-isothermal data such as that presented in Figure 5.7. Still, the results demonstrate that by adjusting self-assembly conditions it is possible to tune the macroscopic properties of P3HT organogels.

Gelation is a nearly universal phenomenon for fiber-forming conjugated polymers, but to this point it has been poorly characterized and largely avoided. The potential to design network structures for organogels of conjugated polymers opens up numerous possibilities within the field of organic electronics, especially when considering OPVs. We have demonstrated that P3HT organogels have a high specific surface area, high conductivity, fibers that are the correct size for exciton diffusion and that there is ample void space for back filling with small molecule n-type semiconductors.[34]

5.5 Summary

Dissolved P3HT at high concentration self-assembles into branching fibrillar organogels with high conductivities and high interfacial areas. Simultaneous rheology and conductivity measurements have been used to systematically probe the gelation mechanism and it was found to be characteristic of classic nucleation and growth for branching fiber systems. Fitting of 1D SANS and USANS profiles has shown that the nanoscale fiber structure of P3HT is relatively constant regardless of solvent or concentration. However, we have also demonstrated that the mesoscale network structure and the resulting mechanical and electrical properties are tunable by

adjusting self-assembly conditions. Furthermore, these results demonstrate that higher conductivities can be achieved by increasing branching in the network structure. This work contributes to developing the fundamental understanding that will be necessary to engineer organogels with optimized properties for target applications. This work was adapted with permission from Newbloom, G. M., Weigandt, K. M., Pozzo, D. C., Macromolecules, 2012, 45, 3452-3462. Copyright 2012 American Chemical Society.

5.6 References

1. Gao, C.-H.; Shi, X.-B.; Zhou, D.-Y.; Zhang, L.; Wang, Z.-K.; Liao, L.-S. *International Jounral of Photoenergy* **2013,** 831765, 1-7.
2. Lee, J.; Lee, J.-I.; Lee, J. Y.; Chu, H. Y. *Applied Physics Letters* **2009,** 94, (19), 193305-3.
3. Krebs, F. C.; Gevorgyan, S. A.; Gholamkhass, B.; Holdcroft, S.; Schlenker, C.; Thompson, M. E.; Thompson, B. C.; Olson, D.; Ginley, D. S.; Shaheen, S. E.; Alshareef, H. N.; Murphy, J. W.; Youngblood, W. J.; Heston, N. C.; Reynolds, J. R.; Jia, S.; Laird, D.; Tuladhar, S. M.; Dane, J. G. A.; Atienzar, P.; Nelson, J.; Kroon, J. M.; Wienk, M. M.; Janssen, R. A. J.; Tvingstedt, K.; Zhang, F.; Andersson, M.; Inganäs, O.; Lira-Cantu, M.; de Bettignies, R.; Guillerez, S.; Aernouts, T.; Cheyns, D.; Lutsen, L.; Zimmermann, B.; Würfel, U.; Niggemann, M.; Schleiermacher, H.-F.; Liska, P.; Grätzel, M.; Lianos, P.; Katz, E. A.; Lohwasser, W.; Jannon, B. *Solar Energy Materials and Solar Cells* **2009,** 93, (11), 1968-1977.
4. Yu, G.; Heeger, A. J. *Journal of Applied Physics* **1995,** 78, (7), 4510-4515.
5. Moule, A.; Meerholz, K. *Advanced Functional Materials* **2009,** 20, 3028-3036.
6. Shaw, P. E.; Ruseckas, A.; Samuel, I. D. W. *Advanced Materials* **2008,** 20, (18), 3516-3520.
7. Sirringhaus, H.; Brown, P.; Friend, R.; Nielsen, M.; Bechgaard, K.; Langeveld-Voss, B.; Spiering, A.; Janssen, R.; Meijer, E.; Herwig, P.; de Leeuw, D. *Nature* **1999,** 401, 685-688.
8. van Bavel, S.; Sourty, E.; de With, G.; Frolic, K.; Loos, J. *Macromolecules* **2009,** 42, (19), 7396-7403.
9. Yin, W.; Dadmun, M. *ACS Nano* **2011,** 5, (6), 4756-4768.
10. Yook, K. S.; Jeon, S. O.; Joo, C. W.; Lee, J. Y. *Journal of Industrial and Engineering Chemistry* **2009,** 15, (3), 420-422.

11. Bao, Z.; Dodabalapur, A.; Lovinger, A. J. *Applied Physics Letters* **1996,** 69, (26), 4108-4110.
12. Svenson, S. *Current Opinion in Colloid & Interface Science* **2004,** 9, (3–4), 201-212.
13. Weigandt, K. M.; Pozzo, D. C.; Porcar, L. *Soft Matter* **2009,** 5, (21), 4321-4330.
14. Jonkheijm, P.; van der Schoot, P.; Schenning, A. P. H. J.; Meijer, E. W. *Science* **2006,** 313, (5783), 80-83.
15. Glinka, C.; Barker, J.; Hammouda, B.; Krueger, S.; Moyer, J.; Orts, W. *Journal of Applied Crystallography* **1998,** 31, 430-445.
16. Barker, J. G.; Glinka, C. J.; Moyer, J. J.; Kim, M. H.; Drews, A. R.; Agamalian, M. *Journal of Applied Crystallography* **2005,** 38, 1004-1011.
17. Kline, S. *Journal of Applied Crystallography* **2006,** 39, 895-900.
18. Butler, P.; Alina, G.; Hernandez, R. C.; Doucet, M.; Jackson, A.; Kienzle, P.; Kline, S.; Zhou, J. SASView for Small Angle Scattering Analysis. http://www.sasview.org/
19. el Maaty, M.; Hosier, I.; Bassett, D. *Macromolecules* **1998**, 153-157.
20. Chen, C. Y.; Chan, S. H.; Li, J. Y.; Wu, K. H.; Chen, H. L.; Chen, J. H.; Huang, W. Y.; Chen, S. A. *Macromolecules* **2010,** 43, (17), 7305-7311.
21. Richards, J. J.; Weigandt, K. M.; Pozzo, D. C. *Journal of Colloid and Interface Science* **2011,** 364, (2), 341-350.
22. Hecht, A.; Duplessix, R.; Geissler, E. *Macromolecules* **1985,** 18, 2167-2173.
23. Obrzut, J.; Page, K. A. *Physical Review B* **2009,** 80, (19).
24. Avrami, M. *Journal of Chemical Physics* **1939,** 7, 1103-1112.
25. Avrami, M. *Journal of Chemical Physics* **1941,** 8, 177-184.
26. Liu, X. Y.; Sawant, P. D. *Advanced Materials* **2002,** 14, (6), 421-426.
27. Samitsu, S.; Shimomura, T.; Heike, S.; Hashizume, T.; Ito, K. *Macromolecules* **2010,** 43, (19), 7891-7894.
28. Koppe, M.; Brabec, C.; Heiml, S.; Schausberger, A.; Duffy, W.; Heeney, M.; McCulloch, I. *Macromolecules* **2009,** 42, (13), 4661-4666.
29. Xu, W.; Tang, H.; Lv, H.; Li, J.; Zhao, X.; Li, H.; Wang, N.; Yang, X. *Soft Matter* **2012,** 8, (3), 726-733.
30. Li, J. L.; Liu, X. Y.; Wang, R. Y.; Xiong, J. Y. *Journal of Physical Chemistry B* **2005,** 109, (51), 24231-24235.
31. Li, J. L.; Yuan, B.; Liu, X. Y.; Xu, H. Y. *Crystal Growth & Design* **2010,** 10, (6), 2699-2706.
32. Malik, S.; Jana, T.; Nandi, A. K. *Macromolecules* **2001,** 34, (2), 275-282.
33. Malik, S.; Nandi, A. K. *Journal of Physical Chemistry B* **2004,** 108, (2), 597-604.
34. Huang, P.-T.; Chang, Y.-S.; Chou, C.-W. *Journal of Applied Polymer Science* **2011,** 122, 233-240.

Chapter 6

Alkyl Chain Effect on Isothermal Poly(3-alkylthiophene) Gelation

6.1 Motivation

The same connectivity that enhances charge transport also increases elasticity, making it difficult to coat uniform films while maintaining an intact structure.[1-3] In fact, gelation and network formation is attributed to poor device performance in spite of conjugated polymer gels having a nearly "ideal" structure for organic electronic active layers.[2, 4] This has led to the development of numerous methodologies to produce uniform coatings from gels. Huang and coworkers designed a freeze-dry coating method for poly(3-hexylthiophene) (P3HT) where a volatile solvent is sublimed under vacuum after gelation is induced by freezing.[1] Kim and coworkers developed a method that involved the sonication of a pre-formed gel prior to coating.[5] Richards and coworkers developed a coating method that involved ultrasound fragmentation in an aqueous dispersion with a stabilizing surfactant (i.e., emulsification).[3] All of these organogel coating methods have yielded promising results for organic electronics but each have issues that can damage the interconnected structure or introduce insulating molecules.

In this chapter, we present a facile route towards controlling poly(3-alkylthiophene) (P3AT) gelation while allowing for the formation of uniform thin-film gels at room temperature. We utilize low volatility solvent/poor-solvent mixtures to control supersaturation (i.e., driving force for gelation) while reducing the influence of solvent evaporation effects. The structure of the gels is characterized using scanning transmission electron microscopy (sTEM) and small angle neutron scattering (SANS). The mechanical and electrical properties of the gels are also measured using oscillatory rheology and dielectric spectroscopy. We demonstrate that changes in both alkyl chain length and supersaturation are effective means for the modification of structure and properties. These results represent a step forward towards controlling the self-assembly of conjugated polymer gels as well as their ultimate application in thin-film electronic devices.

6.2 Experimental Methods

Materials. Two lots of regioregular poly(3-hexylthiophene) (P3HT), one lot of regioregular poly(3-octylthiophene) (P3OT) and one lot of regioregular poly(3-dodecylthiophene) (P3DDT) were used as received from Rieke Metals (Lincoln, NE). The molecular weight (M_w^{chain}), polydispersity index (PDI) and regioregularity (*RR*) for all of these polymers is shown in Table 6.1. The average contour length (L_c) of the polymer is calculated using Equation 1 and listed in Table 6.1.

$$L_c = \frac{M_w^{chain}}{M_w^{monomer}} \cdot L_{monomer} \tag{6.1}$$

The molecular weight of a monomer unit ($M_w^{monomer}$) is 166.3 g/mol for P3HT, 194.3 g/mol for P3OT and 250.4 g/mol for P3DDT while the length of a single monomer unit ($L_{monomer}$) is constant at 1.9 Å.[6, 7]

Table 6.1. Properties of poly(3-alkylthiophene)s including molecular weight (M_w^{chain}), polydispersity index (PDI), regioregularity (*RR*) and contour length (L_c).

	Type	Lot #	M_w^{chain} (g/mol)	PDI	*RR*	L_c (nm)
P3HT (Low M_w)	Sepiolid P200	2010-A6-7	21,000	1.6	95%	24.3 nm
P3HT (High M_w)	4002-E	PTL 12-03	53,000	2.3	92%	61.2 nm
P3OT	4003-E	PTL 11-39	83,000	1.9	91%	82.0 nm
P3DDT	4005-E	BS 14-44	51,000	1.8	92%	39.1 nm

Hydrogenated solvents 1,2-dichlorobenzene (DCB) and n-dodecane were purchased from Sigma-Aldrich (St. Louis, MO) and used as received. Deuterated solvents were used to decrease the incoherent scattering background and increase the scattering contrast in SANS and USANS experiments. D4-1,2-dichlorobenzene (D > 99%) was purchased from Cambridge Isotopes (Tewksbury, MA) and D26-Dodecane (D > 98%) was purchased from Sigma-Aldrich. Both were used as received.

Sample Preparation. All samples were prepared by adding 30 mg/mL P3AT to a mixture of 1,2-dichlorobenzene and dodecane. Samples were then heated above 80 ºC until all visible signs of polymer powder (black) had disappeared and a bright orange solution remained. All solvent mixture percentages in this work are by weight.

Neutron Scattering. Small Angle Neutron Scattering (SANS) and Ultra-Small Angle Neutron Scattering (USANS) experiments were performed at the National Institute of Standards and Technology Center for Neutron Research (NIST CNR) in Gaithersburg, MD. SANS measurements were performed on the NG3 beamline at three detector positions, for equilibrium samples, to obtain the scattering intensity, *I(q)*, over a wide *q*-range ($0.002 < q$ (Å^{-1}) < 0.4), while kinetic measurements (i.e., dielectric-SANS) used only two detector positions for a more limited *q*-range with higher flux ($0.006 < q$ (Å^{-1}) < 0.4).[8]

Equilibrium samples were measured in 1 mm pathlength demountable cells with quartz windows. Kinetic experiments simultaneously measuring AC dielectric properties and SANS (e.g. dielectric-SANS) were performed as described in Chapter 2.4. Sample cells were loaded with a hot polymer solution (~ 80 °C) before being rapidly quenched (> 10 °C/min) in the beamline to experimental temperatures. Experiments were started when samples reached experimental temperatures as judged by an identical cell that was filled with ethylene glycol that was in the same temperature control block. USANS measurements were performed on the BT5 perfect crystal diffractometer extending the q-range to 5×10^{-5} $Å^{-1}$ for equilibrium organogel samples. The data was reduced and desmeared using Igor-based macros developed by NIST.[9] All model fitting was performed using DANSE SASView software.[10]

Dielectric Spectroscopy. AC dielectric spectroscopy measurements were performed using an Agilent e4980a LCR Meter. A perturbation voltage of 600 mV, within the linear impedance response range, and a frequency range of 20 Hz – 2 MHz were used for all samples. Reported conductivities were calculated at a frequency of 2 kHz and all measurements were performed between stainless steel plates.

Rheology. Oscillatory rheology measurements were performed on an Anton Paar MCR 301 stress controlled rheometer using a 25 mm parallel plate geometry. Unless otherwise stated, a frequency of 1 Hz, 0.4 mm gap and 0.25% perturbation strain (in the linear viscoelastic regime for P3HT gels), were used for all measurements. Temperature sweeps were performed using a cooling rate of 1 °C/min while kinetic experiments were performed by rapidly quenching (> 40 °C/min) the sample.

Scanning Transmission Electron Microscopy. Small quantities of organogels formed at 20 °C were transferred to copper grids with Formvar supports by gently touching the grid to the

surface of the gel without applying pressure. Because of the thin nature of the transferred sample, the solvent evaporates rapidly under ambient conditions. Scanning transmission electron microscopy (sTEM) images were obtained with a FEI Technai G2 F20 transmission electron microscope operating at 200 kV.

Pablo de la Iglesia helped with the collection and analysis of the data presented in this chapter.

6.3 Results & Discussion

6.3.1 Solvent Mixtures to Control Gelation Kinetics

Self-assembly in solution for conjugated polymers is driven by a reduction in solubility induced through changes in temperature or the addition of a miscible poor-solvent.[11-13] Variability in shape and structure are common for different conjugated polymers assembled in solution.[14-21] This is largely dependent on the specific chemistry of the backbone and side chains, the regioregularity, molecular weight and the solvent environment during crystallization. Self-assembled regioregular poly(3-alkylthiophene)s (RR-P3ATs) have been shown to form long fibers (a.k.a. whiskers, nanowires or ribbons) with high aspect ratio and rectangular cross-section.[11, 16, 22] When assembled at moderately high concentrations (> 5 mg/mL) these fibers will percolate to form weak interconnected organogels, as discussed in Chapters 4-5.[1, 4, 15, 18, 20, 23-31] Figure 6.1 shows the evolution of mechanical properties with decreasing temperature and solubility for a 30 mg/mL P3OT solution.

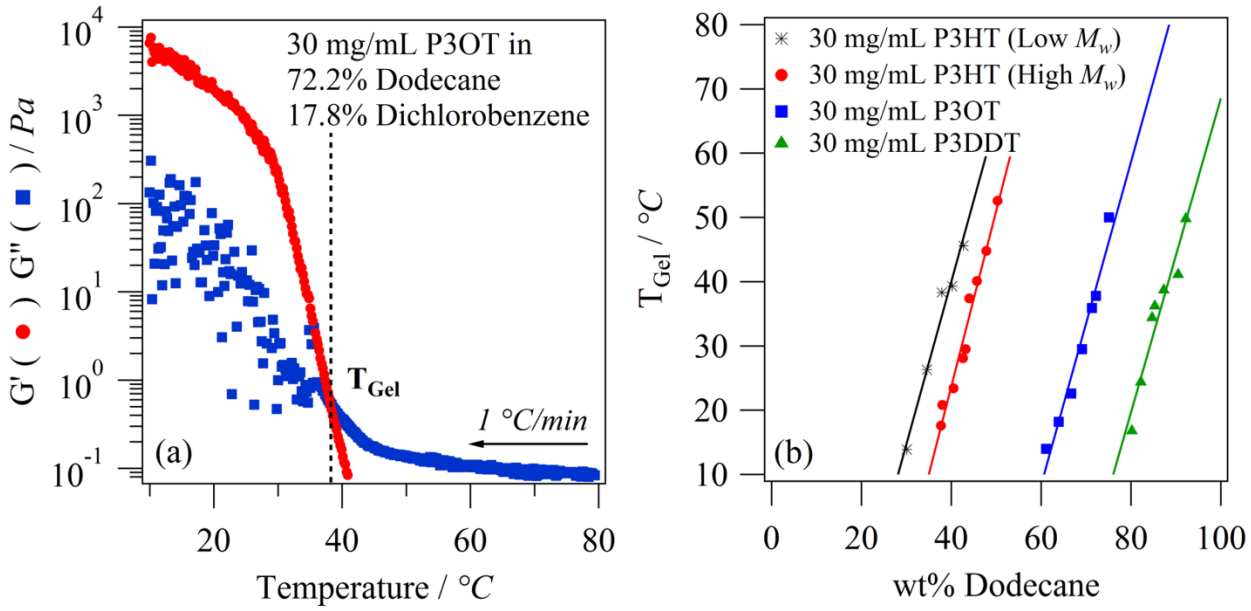

Figure 6.1. a) Oscillatory rheology of 30 mg/mL P3OT in a mixed solvent of dodecane/1,2-dichlorobenzene that is cooled at a rate of 1 °C/min. The gelation temperature (T_{Gel}) is defined as the crossover between the storage (G') and loss (G'') moduli. b) Gelation temperature is plotted against dodecane content in the solvent mixture for different P3ATs (all measured at a cooling rate of 1 °C/min). Linear fits are also shown with nearly identical slopes.

Figure 6.1a shows the rheological response of a typical P3AT in solution during a slow cooling ramp (1 °C/min). At high temperatures the solution is liquid-like ($G' = 0$). When the temperature is reduced crystallization is eventually triggered and an elastic response is measured ($0 < G' < G''$) due to the growth of polymer fibers in solution, as discussed in Chapter 4.3.1. Further cooling results in an increasing storage modulus (elastic) that eventually surpasses the loss modulus (viscous) at the crossover point ($G' = G''$). This is commonly known as the gel point because it corresponds well with mechanical percolation and gelation. The temperature corresponding to the crossover point is herein referred to as the gelation temperature (T_{Gel}). P3AT self-assembly is both a kinetic and thermodynamic process and therefore T_{Gel} will be dependent on experimental conditions such as the cooling rate, as seen in Figure 6.2. As expected, faster cooling rates lead lower gelation temperatures and slower cooling rates lead to

higher gelation temperatures. However in this work, the cooling rate was held constant for all samples.

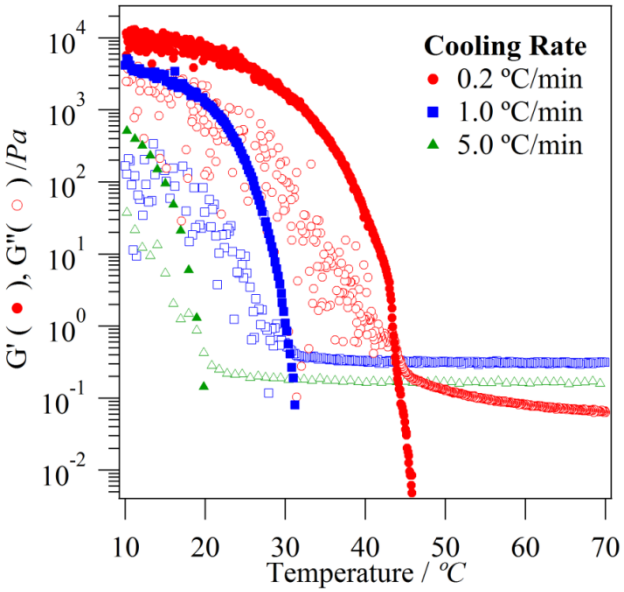

Figure 6.2. Rheology of 30 mg/mL High M_w P3HT in 43.9 wt% dodecane/ 56.1 wt% DCB measured during a cooling ramp from 80 °C to 10 °C.

Figure 6.1b shows that T_{Gel} varies linearly as a function of dodecane content for each alkyl chain length when all experimental conditions are held constant. Dodecane acts as a poor-solvent for P3ATs while 1,2-dichlorobenzene (DCB) acts as a "good" solvent. Therefore, it is expected that an increasing dodecane ratio would result in reduced solubility, higher gelation temperatures and faster self-assembly. The trend with alkyl chain length is also as expected. Alkyl side chains are considered detrimental to device performance because they act as electrical insulators and because they can prevent crystalline packing due to steric effects.[32, 33] Yet, they are necessary to entropically facilitate the dissolution of the typically rigid polymer backbones of conjugated polymers.[34, 35] Longer alkyl chains (i.e., P3DDT) add more entropy and result in higher polymer solubility than short alkyl chain lengths (i.e., P3HT).

Figure 6.1b also shows a difference in solubility between P3HT batches. In this case, it is as a result of differences in molecular weight. It is well known that polymers with higher M_w are generally less soluble and in this study there is a difference of 250% between these two batches (Table 6.1). The difference in solubility could also be the results of small differences in regioregularity. However, this would be expected to produce the opposite trend where higher regioregularity leads to reduced solubility and larger gelation temperatures. There is also an unexpected, but distinctly linear, trend between dodecane content and gelation temperature for all P3ATs. The slopes are similar: low M_w P3HT (253 ± 24 °C/dodecane wt%), high M_w P3HT (274 ± 19 °C/dodecane wt%), P3OT (251 ± 22 °C/dodecane wt%) and P3DDT (244 ± 31 °C/dodecane wt%) suggesting that dodecane content may influence the solubility of the thiophene backbone by changing the solvent's polarizability. This suggests that solvent mixtures and variable alkyl chain structures may help to probe for specific solvent-polymer interactions.

Solvent ratios can also be chosen to achieve similar self-assembly conditions. By using T_{Gel} as a surrogate for solubility, a solvent ratio can be chosen for each polymer to provide similar gelation conditions. In Chapter 5, we have shown that the network structure and properties of P3HT organogels can be modified by changes in gelation kinetics under isothermal conditions. Engineering similar gelation kinetics through tunable solvent ratios allows for the study of developing structure-property relationships as a function of alkyl chain length. The nanoscale structure and electronic properties at intermediate stages of self-assembly can be studied using a combination of small angle neutron scattering (SANS) and AC dielectric spectroscopy, as seen in Chapter 4. Figure 6.3 shows SANS profiles and fit results, using the parallelepiped model to account for fibers and a polymer model to account for dissolved chains,

for a P3HT organogel assembled isothermally at a temperature ($T_{Experiment}$) that is 5 °C lower than T_{Gel}.

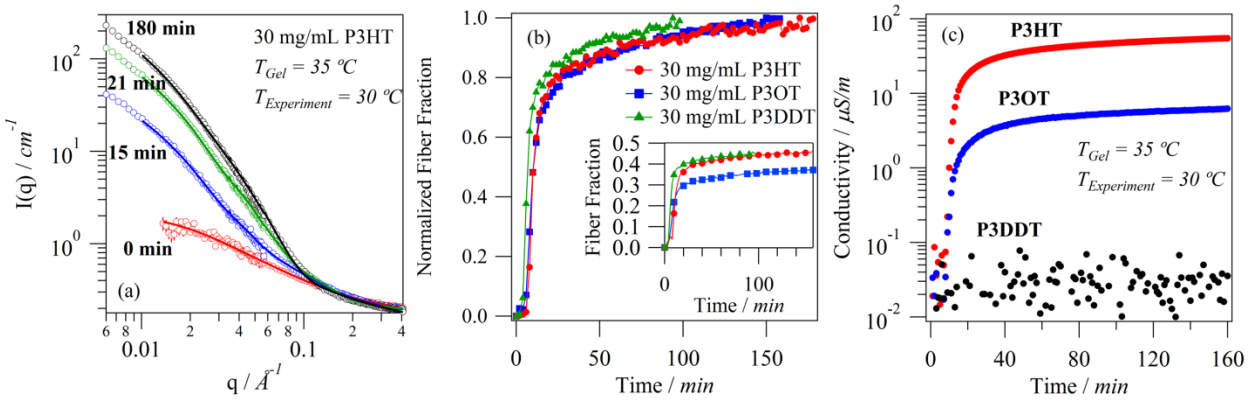

Figure 6.3. a) 1D SANS profiles of 30 mg/mL high M_w P3HT in 43.9% dodecane/56.1% DCB isothermally gelled at 30 °C shown at incremental times. Solid lines represent fits with a mass balanced parallelepiped model and polymer model with excluded volume effects.[11, 12] b) Fraction of P3AT in fiber extracted from a SANS model fit for 30 mg/mL high M_w P3HT in 43.9 wt% dodecane/56.1 wt% DCB, 30 mg/mL P3OT in 71.3 wt% dodecane/28.7 wt% DCB and 30 mg/mL P3DDT in 84.7 wt% dodecane/15.3 wt% DCB, normalized to the maximum fiber fraction. The inset image shows the non-normalized fiber fraction as a function of time. c) Conductivity from simultaneous dielectric-SANS experiments for 30 mg/mL P3ATs in the same solvent mixtures as listed above.

Figure 6.3 shows dielectric-SANS results for 30 mg/mL P3AT organogels self-assembled in solvent mixtures. Solvent mixtures were selected for each polymer to achieve a T_{Gel} of 35 °C. This corresponded to 43.9 wt% dodecane/56.1 wt% DCB for P3HT (high M_w), 71.3 wt% dodecane/28.7 wt% DCB for P3OT and 84.7 wt% dodecane/15.3 wt% DCB for P3DDT based on Figure 6.1. A lower temperature ($T_{Experiment}$) of 30 °C was selected for isothermal gelation to drive the self-assembly. The measurements follow the structural evolution of samples from fully dissolved polymer to fully formed organogels.

Figure 6.3a shows SANS profiles fit with a mass balanced model (Equation 2.6) to account for all scattering objects in solution at any point in time, as discussed in Chapter 2.1.5.

Dissolved P3AT conformations were determined from SANS profiles (Equation 2.8) at time zero and are listed in Table 6.2. The results of the fits are in agreement with expectations based on the polymer properties (Table 6.1). The radius of gyration scales with the length of the polymer chain and the spatial distribution of the polymer chain (v) scales with the alkyl chain length. Schweizer predicted that increasing entropy from longer alkyl chains would result in increased backbone torsion and therefore less rigid conjugated polymer chains which is also in agreement with our findings.[35]

Table 6.2. The conformation of dissolved polymers at 30 °C as determined from SANS for 30 mg/mL high M_w P3HT in 43.9% dodecane/56.1% DCB, 30 mg/mL P3OT in 71.3% dodecane/28.7% DCB and 30 mg/mL P3DDT in 84.7% dodecane/15.3% DCB. R_g is the radius of gyration and v is related to the spatial distribution of the chain.

	R_g (Å)	v
High M_w P3HT	54	0.78
P3OT	70	0.66
P3DDT	49	0.56

By fixing most variables in the model to known or independently measured values, only three unknown parameters remain: fraction of polymer in fiber from (Ψ_f), fiber thickness (a) and fiber width (b). Each profile is fit with this model enabling the accurate extraction of these parameters as a function of time. Chapters 3-5 have shown that the parallelepiped model is only valid over a limited q-range ($q > 0.009$ Å^{-1}) because the branched network starts to dominate the scattering at low-q ($q < 0.009$ Å^{-1}). Surprisingly, the dimensions of the near-equilibrium P3AT fibers are similar. SANS shows high M_w P3HT fibers with an average width of 23.4 nm and thickness of 4.4 nm, P3OT fibers with an average width of 26.1 nm and thickness of 4.6 nm, and P3DDT fiber with an average width of 22.2 nm and thickness of 4.9 nm. The lattice parameters

of non-intercalating P3AT fibers can be used to estimate that high *Mw* P3HT and P3OT fibers are on average between 2 – 3 chains thick, while P3DDT fibers are on average 2 chains thick.[7]

Figure 6.3b shows the kinetics of self-assembly for P3AT gels by plotting the normalized fiber fraction (Ψ_f) over time. It shows that kinetically, the gels form in a very similar fashion where almost 80% of self-assembly occurs within the first 30 minutes and then reduces to a much slower rate. The similar self-assembly kinetics for variable alkyl chain lengths indicates that the driving force is also similar. Even though the driving force for self-assembly is similar, the final conductivity of the gels varies by orders of magnitude (Figure 6.3c). Furthermore, the conductivity of the P3DDT sample does not change during self-assembly. The simultaneous nature of the dielectric-SANS measurement allows for direct comparison of variations in conductivity and fiber fraction, as seen in Figure 6.4.

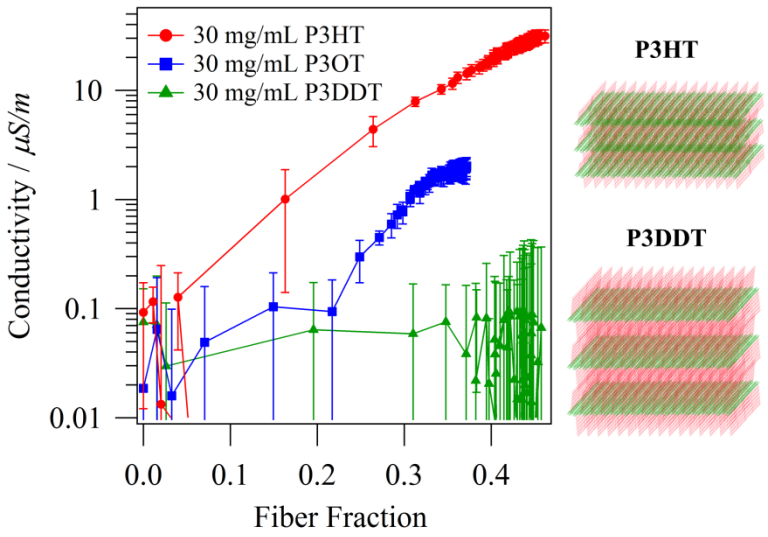

Figure 6.4. Variation of conductivity with fiber fraction from isothermal dielectric-SANS at 30 °C for high M_w P3HT in 43.9% dodecane/56.1% DCB, P3OT in 71.3% dodecane/28.7% DCB and P3DDT in 84.7% dodecane/15.3% DCB. The right-set images depict the non-intercalated packing of P3HT and P3DDT fibers with the alkyl chains colored red and thiophene backbones colored green. All samples are at 30 mg/mL.

Figure 6.4 shows a time-based point-by-point matching of conductivity and fiber fraction. Even though self-assembly kinetics are nearly identical, variations in fiber-conductivity are drastically different. P3HT gelation shows an exponential dependence between fiber fraction and conductivity for $\Psi_f > 0.04$, where increasing fibers result in a consistent increase in conductivity. P3OT self-assembly shows no significant increase in conductivity for $\Psi_f < 0.21$ at which point there is a rapid increase in conductivity with new fiber formation ($0.21 < \Psi_f < 0.34$) followed by a plateau in conductivity ($\Psi_f > 0.34$). In contrast, P3DDDT shows no increase in conductivity upon the formation of new fibers. The differences in magnitude of the conductivity at similar fiber fractions are likely due, in part, to the difference in alkyl chain length. The right-set image in Figure 6.4 contrasts three chain stacks of fiber cross-sections for P3HT and P3DDT. The conjugated thiophene backbone is colored green while the insulating alkyl chains are colored red. It is obvious that charge hoping between thiophene layers, a transport mechanism in conjugated polymer networks, will be less likely for longer alkyl chains.[36] This may also explain the shift in fiber percolation threshold for these gels where P3HT is $\Psi_f \sim 0.04$, P3OT is $\Psi_f \sim 0.21$. For P3DDT the changes in conductivity are either below the resolution of the measurement or even more fibers would be needed to achieve percolation (i.e., $\Psi_f > 0.48$).

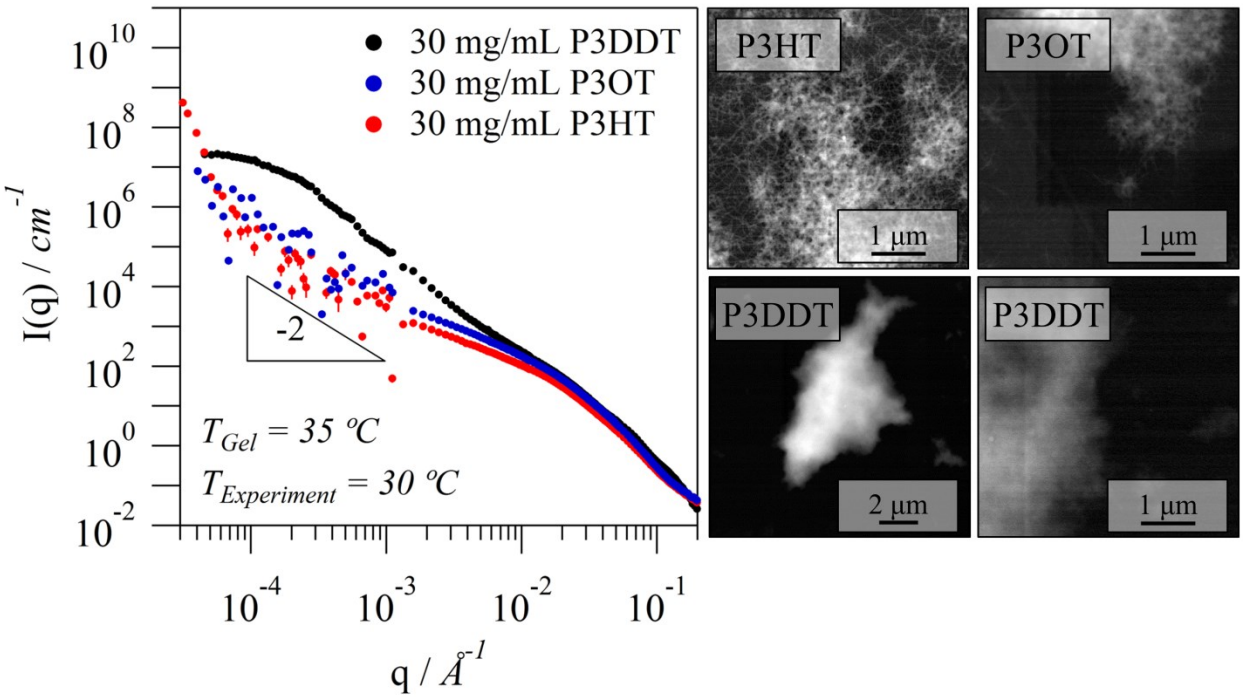

Figure 6.5. Left: Combined SANS and USANS (desmeared) profiles of high M_w P3HT in 43.9% dodecane/56.1% DCB, P3OT in 71.3% dodecane/28.7% DCB and P3DDT in 84.7% dodecane/15.3% DCB self-assembled for 24 hours at 30 °C. Right: Corresponding sTEM images of dried P3AT organogels self-assembled at the same solvent ratios. All samples are at 30 mg/mL.

Figure 6.5 shows that scattering profiles at high-q (q > 0.009 Å^{-1}) are similar in the region where the model is used to determine the fiber cross-sectional dimensions. In contrast, the scattering at q < 0.009 Å^{-1} is quite different between samples. As discussed in Chapters 3-5, this is attributed to differences in inter-fiber correlations (i.e., network structure) leading to a power law dependence that is generally larger than expected for isolated fibers (q^{-1}).[17, 37] Figure 6.5 shows that P3HT and P3OT have similar network structures over 10^{-4} < q (Å^{-1}) < 10^{-2}, corresponding to a region of real space dimensions of 63 nm – 6.3 µm. This is confirmed with sTEM (Figure 6.5), which shows that the network structure is very similar for P3HT and P3OT gels and both have regions of high and low fiber density. In contrast, the scattering profile of the P3DDT gel at low q (USANS range) has a larger slope suggestive of a denser network structure.

It also shows a turnover characteristic of finite domains with a radius of gyration of approximately 1.2 μm based a Guinier fit (Equation 2.10). P3DDT sTEM images also indicate a very dense and smaller fibrillar network structure. The small size and high density of the P3DDT network domains, in combination with the long insulating alkyl chains can help explain the low conductivity (Figure 6.4). At $q < 10^{-4}$ Å^{-1}, the scattering of P3HT and P3OT also start to differ. The profile of the P3OT organogel has a fairly constant slope at low q but there is a turn-over to a larger slope for the P3HT organogel. This is suggestive of a slightly more heterogeneous network structure for P3HT organogels when compared to P3OT for the largest length scales (> 10 μm). The similarity between P3HT and P3OT at all other length scales suggests that the dependence of conductivity (Figure 6.4) is most likely dominated by the length of the insulating alkyl chains.

6.3.2 Structure-Property Engineering through Solvent Mixtures

It is possible to engineer the structure and properties of organogels through changes in the content of poor-solvent in the mixture for any polymer. The theory that links gelation kinetics to supersaturation and branching fibrillar network structure has been established by Li *et al*.[38] De la Iglesia and coworkers recently reported that, for organogels of poly(9,9-dioctylfluorine) (PFO), increased supersaturation resulted in denser, branched networks.[17] Figure 6.6 shows that a similar trend exists for low M_w P3HT organogels.

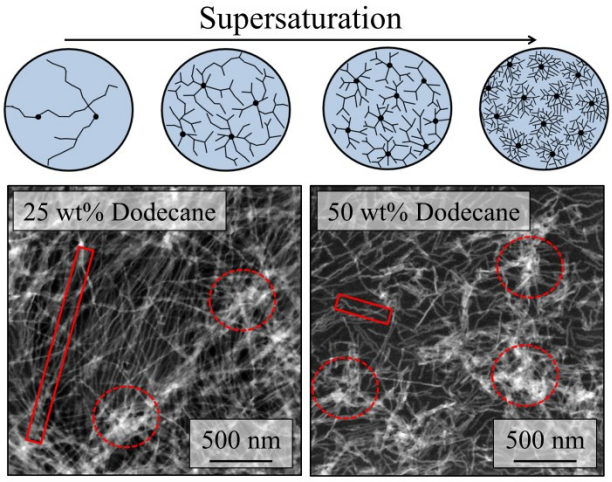

Figure 6.6. Top: Schematics showing the correlation between solvent-quality and fiber branching as proposed by Li *et al*.[38] Bottom: Scanning transmission electron microscopy (sTEM) images of 30 mg/mL low M_w P3HT organogels isothermally self-assembled to equilibrium in 1,2-dichlorobenzene/dodecane solvent mixtures at 20 °C. Samples were allowed to evaporate prior to imaging. Fiber length is highlighted with a solid box and dense fiber regions are highlighted with a dashed circle.

sTEM images of low M_w P3HT organogel networks formed in different solvent/poor-solvent mixture ratios as shown in Figure 6.6. As the ratio of dodecane increases so does the driving force for polymer self-assembly. The SANS results in Figure 6.7 show that more fibers are formed as a result of increasing dodecane ratio. However, Figure 5 shows that the structure of the fiber network also changes. At a dodecane ratio of 25 wt%, sTEM images show predominantly long, overlapping fibers (> 3 μm). This is in contrast to gels formed in a 50 wt% dodecane ratio which show shorter, more branched fiber networks often with less than 1 μm fiber length before branching or splitting occurs. Furthermore, low M_w P3HT fiber networks formed at high dodecane ratios also show an increased frequency of dense heterogeneous regions. The structural trends seen in these sTEM images are well described by the theory for supersaturation of organogelators where a higher driving force for self-assembly results in more nucleation centers and lattice mismatches that lead to higher branching frequency.[38]

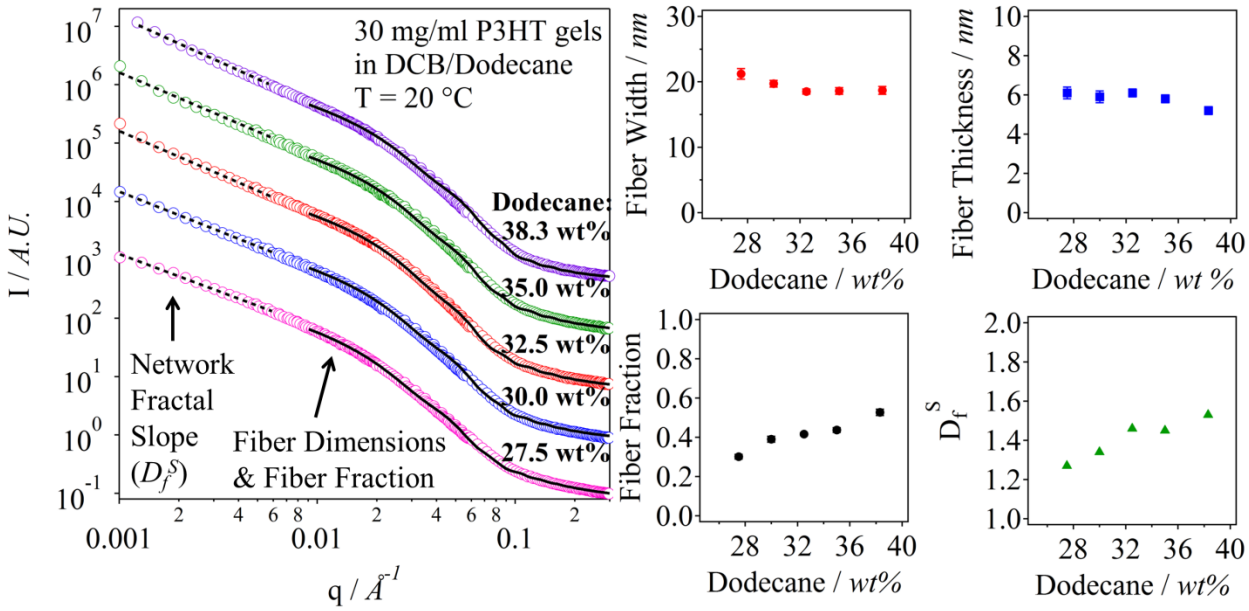

Figure 6.7. SANS profiles and corresponding fits, both shifted for clarity, of 30 mg/mL low M_w P3HT in dodecane/1,2-dichlorobenzene solvent mixtures self-assembled for at least 24 hours at 20 °C. Fiber width, fiber thickness and fiber fraction are extracted from SANS using Equation 2. The network fractal dimension (D_f^S) is extracted using a power law fit of the SANS profiles from $0.001 < q$ (Å^{-1}) < 0.006 shown as a dashed black line.

Figure 6.7 shows the SANS profiles, fit with Equation 2.6, of fully formed low M_w P3HT organogels in different solvent ratios. As previously demonstrated in Chapter 5, changes in driving force for P3HT organogel self-assembly has little impact on the cross-sectional shape of the fibers. In this case, the fiber thickness and width are nearly identical with an average width of ~ 20 nm and an average thickness of ~6 nm, which corresponds to three polymer chains without interdigitation.[7] At low-q ($q < 0.006$ Å^{-1}), SANS profiles are also fit with a power law equation (Equation 2.9) to extract a fractal dimension for this length scale (D_f^S). The fractal dimension arises from inter-fiber correlations that develop over a size range of 100 – 600 nm. The D_f^S results in Figure 6 show a similar trend to the sTEM images, where increasing dodecane ratio results in more dense fiber network structures with $D_f^S = 1.27$ for low M_w P3HT in 27.5 wt% dodecane and $D_f^S = 1.53$ for low M_w P3HT in 38.3 wt% dodecane.

Figure 6.8 shows the USANS profiles corresponding to some of the SANS profiles in Figure 6.7. This measurement characterizes a size range of 250 nm to 20 μm that is primarily influenced by the network structure. All of the USANS profiles, except for the low M_w P3HT gel in 27.5 wt% dodecane, show a turnover at low-q that is similar to the P3DDT gel in Figure 6.5. This indicates the formation of a more heterogeneous structure at these length scales as illustrated in the inset diagram in Figure 6.8. The turnover can be fit with the Guinier equation to determine a radius of gyration of these domains. The radius of gyration was found to be 5.1 μm, 1.3 μm, 1.1 μm for 30 mg/mL low M_w P3HT in 30 wt%, 32.5 wt% and 38.3 wt% dodecane. This is in agreement with the trend in Figure 6.6 that shows that gels formed in solvents with higher dodecane content have more nucleation centers and smaller network domains.

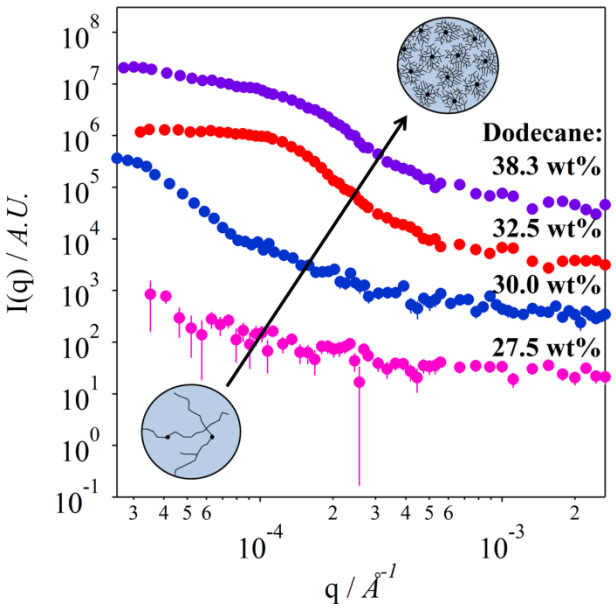

Figure 6.8. Smeared USANS profiles of 30 mg/mL low M_w P3HT in 1,2-dichlorobenzene/dodecane solvent mixtures self-assembled for at least 24 hours at 20 °C.

The properties and self-assembly kinetics are also affected by the solvent ratio. Figure 6.9 shows the isothermal rheology kinetics of P3HT gels formed in different solvent mixture ratios.

The complex modulus (G^*), where $G^* = \sqrt{(G')^2 + (G'')^2}$, is plotted as a function of time after the temperature reaches 20 °C. As expected, all samples start as viscous polymer solutions before the modulus rapidly increases, indicating gelation. The initial gelation time decreases as the fraction of dodecane increases. Furthermore, the final modulus of the gel increases with increasing dodecane fraction for samples with dodecane fractions of 25 – 30 wt%. However, the final modulus for samples with more than 30 wt% dodecane decreases again. This same trend is observed in the final conductivity of the P3AT organogels (Figure 6.10). A maximum in conductivity was also observed by Zhu and coworkers who studied P3HT solution phase self-assembly with solvent mixtures (chlorobenzene/anisole), but did not ascribe this behavior to structural features.[21] The structural data from SANS, USANS and sTEM indicate that this peak in modulus and conductivity is a result of competing factors between increasing fiber fraction and increasing network heterogeneity or branching. Gels formed at low dodecane fractions form fewer fibers (Figure 6.7) but these fibers tend to be longer (Figure 6.6) and a more homogeneous network structure is formed (Figure 6.8). In contrast, with very high dodecane fractions, gels contain more fibers (Figure 6.7) but these tend to be highly branched (Figure 6.6) and more heterogeneous which is detrimental to conductivity (Figure 6.8). This leads to a maximum conductivity when there is a relatively large number of fibers but where these also form homogeneous interconnected networks. Finally, difference in conductivities (Figure 6.10) of more than order of magnitude demonstrate that solvent/poor-solvent ratios are important engineering parameters to optimize the performance and structure of networks in organic electronic devices.

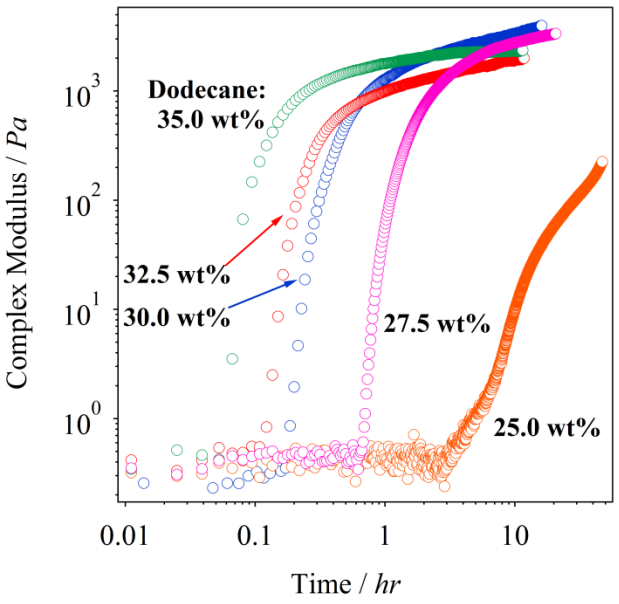

Figure 6.9. Oscillatory rheology of 30 mg/mL low M_w P3HT in 1,2-dichlorobenzene/dodecane solvent mixtures during isothermal gelation at 20 °C.

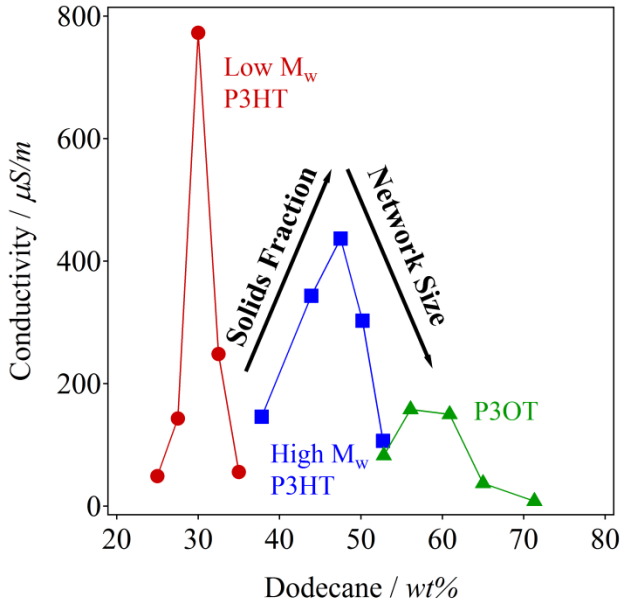

Figure 6.10. Conductivity of 30 mg/mL low M_w P3HT, high M_w P3HT and P3OT organogels self-assembled to equilibrium at 20 °C in 1,2-dichlorobenzene/dodecane solvent mixtures.

6.3.3 Low Volatility Solvents Enable Thin Film Gels

The potential for forming interconnected networks in thin-film organic electronics has long been suggested but the elastic mechanical nature of organogels is incompatible with traditional coating processes (e.g., spin-coating).[2] Figure 6.11 demonstrates a novel approach for forming organogels in thin-films using solvent/poor-solvent mixtures with low vapor pressures. The pictures demonstrate thermoreversible gelation in bulk and in thin-films for P3HT. Gelation in thin-films that are deposited as liquids is only possible because the vapor pressures of the two solvents are low enough to slow down evaporation while gelation proceeds. 1,2-dichlorobenzene (DCB) has a vapor pressure of 1.4 mm Hg at 20 °C, while n-dodecane has a vapor pressure of 0.1 mm Hg at 20 °C.[39] These thin-films can be dried under vacuum in approximately 24 hours or they can be rinsed with a miscible poor-solvent of higher volatility (e.g., hexane) after the gel is fully formed. Figure 6.11 shows films formed using drop-casting from the dissolved liquid state. We have also used this method to produce thin-films with blade coating, screen printing and spin coating.

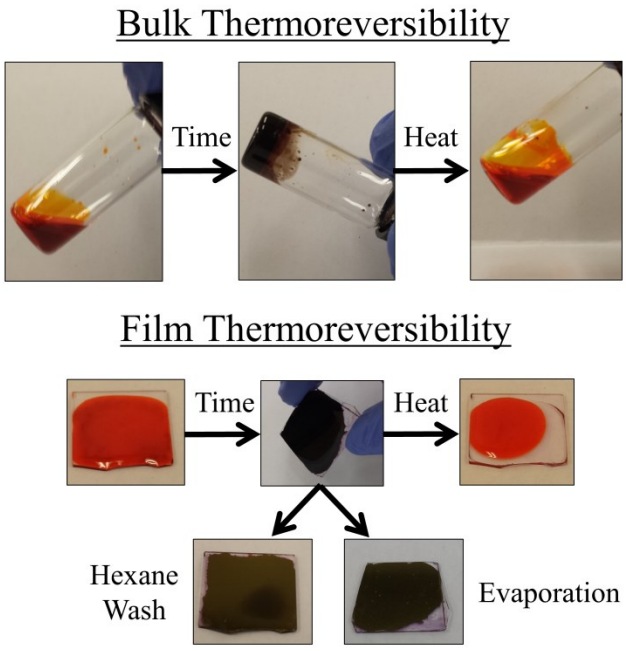

Figure 6.11. Pictures of 30 mg/mL low M_w P3HT in a solvent mixture of 70 wt% 1,2-dichlorobenzene and 30 wt% dodecane. Top images represent bulk gelation while bottom images represent gels formed in a film. The left image on top and bottom is a fully dissolved P3HT solution after heating. Over time the solutions, in bulk or coated, self-assemble into P3HT organogels that can be re-heated again to re-dissolve the gel and form orange solutions. The two lower images are of organogel films that were dried by evaporation and through a hexane rinse.

6.4 Summary

We have demonstrated that low volatility solvent/poor-solvent mixtures can be used to engineer the structure and properties of poly(3-alkylthiophene) (P3AT) organogels. Furthermore, we showed that the low volatility of the solvent mixture could be utilized to achieve thermoreversible gelation in a thin-film environment and at room temperature. These findings enable the facile design and application of organogels of conjugated polymers with desired structure and properties for use in organic electronics. We demonstrated that the use of dodecane and 1,2-dichlorobenzene allowed for gelation over of a wide range of alkyl chain lengths. We determined that differences in insulating alkyl chain length led to drastically different properties even when self-assembly kinetics were very similar. We also showed that increasing dodecane

fraction leads to faster self-assembly kinetics for P3HT organogels. The resultant organogel structures could be described by invoking a well-known nucleation and growth theory. sTEM, SANS and USANS all showed that higher dodecane ratios led to more branching and smaller network sizes. A peak in the conductivity of fully formed low M_w P3HT gels was found to be the result of a competition between the number of fibers and the network size and it is likely these same parameters that lead to the conductivity peaks in the high M_w P3HT and P3OT gels. These results demonstrate that simple and tunable parameters, such as alkyl chain structure and solvent ratio, can have drastic effects on the properties of conjugated polymer organogels. Moreover, this work presents a novel way to incorporate this range of engineering control into the final application of thin-film electronic devices.

6.5 References

1. Huang, P.-T.; Chang, Y.-S.; Chou, C.-W. *Journal of Applied Polymer Science* **2011,** 122, 233-240.
2. Koppe, M.; Brabec, C.; Heiml, S.; Schausberger, A.; Duffy, W.; Heeney, M.; McCulloch, I. *Macromolecules* **2009,** 42, (13), 4661-4666.
3. Richards, J. J.; Weigandt, K. M.; Pozzo, D. C. *Journal of Colloid and Interface Science* **2011,** 364, (2), 341-350.
4. Malik, S.; Jana, T.; Nandi, A. K. *Macromolecules* **2001,** 34, (2), 275-282.
5. Kim, B.-G.; Jeong, E. J.; Park, H. J.; Bilby, D.; Guo, L. J.; Kim, J. *ACS Applied Materials & Interfaces* **2011,** 3, (3), 674-680.
6. Brinkmann, M.; Wittmann, J. C. *Advanced Materials* **2006,** 18, (7), 860-863.
7. Prosa, T. J.; Winokur, M. J.; Moulton, J.; Smith, P.; Heeger, A. J. *Macromolecules* **1992,** 25, (17), 4364-4372.
8. Glinka, C.; Barker, J.; Hammouda, B.; Krueger, S.; Moyer, J.; Orts, W. *Journal of Applied Crystallography* **1998,** 31, 430-445.
9. Barker, J. G.; Glinka, C. J.; Moyer, J. J.; Kim, M. H.; Drews, A. R.; Agamalian, M. *Journal of Applied Crystallography* **2005,** 38, 1004-1011.
10. Butler, P.; Alina, G.; Hernandez, R. C.; Doucet, M.; Jackson, A.; Kienzle, P.; Kline, S.; Zhou, J. SASView for Small Angle Scattering Analysis. http://www.sasview.org/

11. Oosterbaan, W. D.; Bolsée, J.-C.; Gadisa, A.; Vrindts, V.; Bertho, S.; D'Haen, J.; Cleij, T. J.; Lutsen, L.; McNeill, C. R.; Thomsen, L.; Manca, J. V.; Vanderzande, D. *Advanced Functional Materials* **2010,** 20, (5), 792-802.
12. Samitsu, S.; Shimomura, T.; Heike, S.; Hashizume, T.; Ito, K. *Macromolecules* **2008,** 41, (21), 8000-8010.
13. Samitsu, S.; Shimomura, T.; Ito, K. *Thin Solid Films* **2008,** 516, (9), 2478-2486.
14. Alcazar, D.; Wang, F.; Swager, T. M.; Thomas, E. L. *Macromolecules* **2008,** 41, (24), 9863-9868.
15. Berson, S.; De Bettignies, R.; Bailly, S.; Guillerez, S. *Advanced Functional Materials* **2007,** 17, (8), 1377-1384.
16. Liu, J.; Arif, M.; Zou, J.; Khondaker, S. I.; Zhai, L. *Macromolecules* **2009,** 42, (24), 9390-9393.
17. de la Iglesia, P.; Pozzo, D. C. *Soft Matter* **2013,** 9, (47), 11214-11224.
18. Kim, F. S.; Jenekhe, S. A. *Macromolecules* **2012,** 45, (18), 7514-7519.
19. Szymanski, C.; Wu, C.; Hooper, J.; Salazar, M. A.; Perdomo, A.; Dukes, A.; McNeill, J. *The Journal of Physical Chemistry B* **2005,** 109, (18), 8543-8546.
20. Yu, Z.; Fang, J.; Yan, H.; Zhang, Y.; Lu, K.; Wei, Z. *The Journal of Physical Chemistry C* **2012,** 116, (45), 23858-23863.
21. Zhu, Z.; Wei, B.; Wang, J. *physica status solidi (RRL) – Rapid Research Letters* **2013,** 8, (3), 252-255.
22. Samitsu, S.; Shimomura, T.; Heike, S.; Hashizume, T.; Ito, K. *Macromolecules* **2010,** 43, (19), 7891-7894.
23. Chen, J.-Y.; Hsu, F.-C.; Sung, Y.-M.; Chen, Y.-F. *Journal of Materials Chemistry* **2012,** 22, (31), 15726-15731.
24. Huang, W. Y.; Huang, P. T.; Han, Y. K.; Lee, C. C.; Hsieh, T. L.; Chang, M. Y. *Macromolecules* **2008,** 41, (20), 7485-7489.
25. Malik, S.; Nandi, A. K. *Journal of Physical Chemistry B* **2004,** 108, (2), 597-604.
26. Sobkowicz, M. J.; Jones, R. L.; Kline, R. J.; DeLongchamp, D. M. *Macromolecules* **2011,** 45, (2), 1046-1055.
27. Xu, W.; Li, L.; Tang, H.; Li, H.; Zhao, X.; Yang, X. *The Journal of Physical Chemistry B* **2011,** 115, (20), 6412-6420.
28. Xu, W.; Tang, H.; Lv, H.; Li, J.; Zhao, X.; Li, H.; Wang, N.; Yang, X. *Soft Matter* **2012,** 8, (3), 726-733.
29. Chang, M.-Y.; Huang, Y.-H.; Han, Y.-K. *Organic Electronics* **2014,** 15, (1), 251-259.
30. Keum, J. K.; Xiao, K.; Ivanov, I. N.; Hong, K.; Browning, J. F.; Smith, G. S.; Shao, M.; Littrell, K. C.; Rondinone, A. J.; Andrew Payzant, E.; Chen, J.; Hensley, D. K. *CrystEngComm* **2013,** 15, (6), 1114-1124.
31. Seidler, N.; Lazzerini, G. M.; Destri, G. L.; Marletta, G.; Cacialli, F. *Journal of Materials Chemistry C* **2013,** 1, 7748-7757.

32. Sirringhaus, H.; Brown, P.; Friend, R.; Nielsen, M.; Bechgaard, K.; Langeveld-Voss, B.; Spiering, A.; Janssen, R.; Meijer, E.; Herwig, P.; de Leeuw, D. *Nature* **1999,** 401, 685-688.
33. Yao, Y.; Dong, H.; Hu, W. *Polymer Chemistry* **2013,** 4, (20), 5197-5205.
34. Ballauff, M. *Macromolecules* **1986,** 19, (5), 1366-1374.
35. Schweizer, K. S. *The Journal of Chemical Physics* **1986,** 85, (2), 1156-1175.
36. Lan, Y.-K.; Huang, C.-I. *The Journal of Physical Chemistry B* **2008,** 112, (47), 14857-14862.
37. Abboud, J.-L. M.; Notario, R. *Pure and Applied Chemistry* **1999,** 71, (4), 645-718.
38. Li, J. L.; Yuan, B.; Liu, X. Y.; Xu, H. Y. *Crystal Growth & Design* **2010,** 10, (6), 2699-2706.
39. *Handbook of Chemistry and Physics: 83rd Edition*. CRC Press LLC: Davers, MA, 2002.

Chapter 7

Porous Poly(3-hexylthiophene) Networks for Hybrid Photovoltaics

7.1 Motivation

Organic-inorganic hybrid photovoltaic (HPV) devices show potential advantages over purely organic photovoltaic (OPV) devices. Both HPV and OPV devices usually rely on p-type conjugated polymers to perform as the primary solar energy absorber.[1, 2] However, HPVs use inorganic n-type semiconductor materials (e.g., metal oxides and metal sulfides) while most OPV devices use fullerene or fullerene derivatives (e.g., PCBM) to complete the heterojunction. Although OPVs are usually more efficient than HPVs, the structural evolution of the polymer and fullerene domains eventually leads to performance deterioration and premature device failure.[3] In contrast, the rigid structure of metal oxides in HPVs could prevent degradation and address these stability issues. In addition, HPV devices can also provide many of the benefits of OPV devices including the use of inexpensive raw materials, tunable optical absorption, environmental stability and potential for preparing flexible devices.[1, 4, 5]

Substantial progress has been made recently towards improving efficiency of HPV devices based on p-type poly(3-hexythiophene) (P3HT) and n-type zinc oxide (ZnO). Two different approaches have emerged as favorites for generating these devices. Takanezawa et al. created P3HT/ZnO HPVs by templated growth of ZnO nanowires followed by backfilling of dissolved P3HT to complete the heterojunction and generate devices with power conversion efficiency (PCE) as high as 2.7%.[1] This is just one example of the inorganic template approach to HPVs. In one example of the mixing approach, Beek et al. fabricated P3HT/ZnO devices by directly mixing of crystalline ZnO nanoparticles with dissolved P3HT followed by coating the solution to generate active layers and devices with PCE of 0.9%.[6]

Though both of these methods have been extensively optimized to maximize PCE, there are some fundamental limitations that will be difficult to overcome.[5, 7] Devices prepared by backfilling nanowire templates are limited by the large size of the space between metal oxide domains and also by the incomplete penetration of the polymer phase.[7] On the other hand, devices prepared by mixing dispersed metal oxide nanoparticles with conjugated polymers usually suffer from poor percolation of the inorganic phase. Here we present, for the first time, a third approach that could help overcome these fundamental issues. We will demonstrate that HPV devices could also be generated by backfilling a metal oxide material over an exisitng porous conjugated polymer network as shown in Figure 7.1. In this work, we specifically explore the use of magnetron sputtering to deposit and intercalate an inorganic material around the organic semiconductor network but note that other deposition methods could also be used.

The proposed new process takes advantage of the large specific surface area and intrinsic interconnectivity of dried organogel networks as the primary structural platform for the formation of the HPV active layer. The metal oxide components can then be delivered using

sputtering, atomic layer deposition, plasma-assisted deposition, vapor-phase deposition or even liquid-phase infiltration. Ideally, process conditions are chosen such that the inorganic components will conformally coat the polymer fibers to generate a bicontinuous structure without compromising the underlying organic material. In addition to all the potential advantages of HPVs, this new approach is ideally suited to fabricate tandem solar cells because it eliminates the need for orthogonal solvents that are necessary to avoid re-dissolution of underlying layers.[8, 9] To demonstrate feasibility of this approach, we use the organogel phase of poly(3-hexylthiophene) (P3HT) and magnetron sputtered zinc oxide (ZnO) to form HPV devices. We also characterize the structural and optical properties of the organogel phase, the material properties of the metal oxide phase and the performance of devices prepared with these composite films. Although a low performance is achieved, these results demonstrate a completely new approach that can be used towards fabricating hybrid organic-inorganic photovoltaic devices.

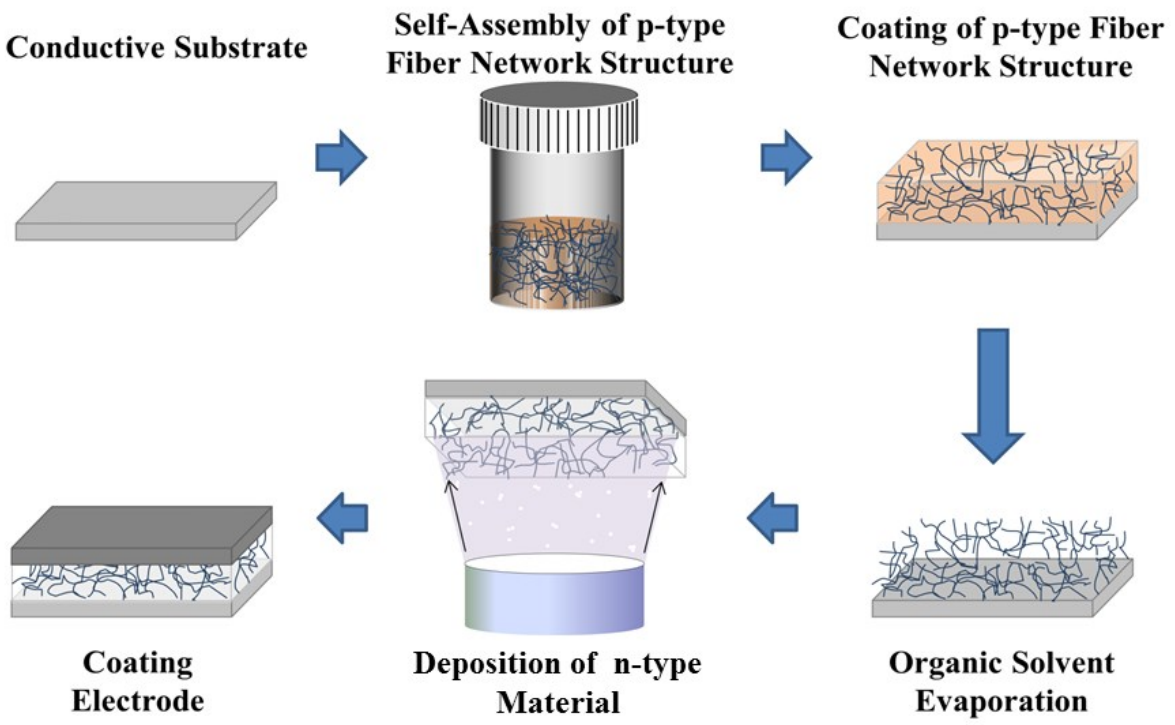

Figure 7.1. Schematic of fabrication process for the deposition of a metal oxide within the porous network structure of dried conjugated polymer organogels.

7.2 Experimental Methods

Financial support for this work was provided by the Boeing Company. We would like to acknowledge experimental assistance and helpful discussions provided by Dr. Alpana N. Ranade, Dr. Marvi A. Matos, Dr. Eric Black, Jeannie Nielson, Mark Chisa, Valerie Loebs, Dr. Carlton (Skip) Christy and Rex Smith who are all employees of the Boeing Company.

Materials. Regioregular poly(3-hexylthiophene) (Lot# BS20-80) with an average molecular weight (M_w) of 41,000 g/mol, polydispersity index (*PDI*) of 2.0 and regioregularity of 93% was utilized as received from Rieke Metals (Lincoln, NE). Toluene was utilized as received from Sigma-Aldrich (St. Louis, MO). Poly(3,4-ethylenedioxythiophene):poly(styrenesulfonate) (PEDOT:PSS) was purchased from Clevios (Leverkusen, Germany), stored in a refrigerator (~ 5 ºC) and filtered (450 μm pore size) prior to use. Zinc oxide and aluminum targets were purchased

from Plasmaterials Inc. (Livermore, CA) and Materials Research Corporation (Austin, TX), respectively.

Solar Cell Fabrication. P3HT was dissolved in toluene (30 mg/mL) at elevated temperatures (~ 80 ºC) and rapidly cooled to 5 ºC to induce self-assembly and gelation. After gelation reached equilibrium (~ 1 day), fresh toluene (cooled to 5 ºC) was added to the gel sample in a 1:3 ratio to remove any remaining non-crystallized polymer. Results in Chapter 4 have shown that P3HT organogels in toluene are stable upon the addition of fresh solvent. The toluene-capped organogels were then vigorously shaken to fracture the weak gels and to form an organogel-particle dispersion. The dispersion was centrifuged at 4,000 RPM for 30 minutes to separate the dissolved polymer from the fractured organogel particles. The dissolved polymer fraction was removed and replaced with fresh toluene to generate a pure organogel particle dispersion with a final concentration of 5 mg/mL. The organogel dispersion was vigorously shaken before spin coating to ensure the particles were well dispersed.

Glass substrates with indium-doped tin oxide (ITO), purchased from Delta Technologies (Loveland, CO), were cleaned prior to deposition by sequential sonication (15 min) in: soapy water, DI water, acetone and ethanol. The substrates were further cleaned by exposure to air plasma using a Plasmod from March Instruments Inc. (Concord, CA) at 150 W and 0.2 Torr for five minutes. Subsequently, substrates were coated with 1 mL of PEDOT:PSS at 1500 RPM for 1 minute and baked at 150 ºC for 5 minutes. The P3HT organogel dispersion was then deposited via spin-coating over the PEDOT:PSS film at 1500 RPM for 1 minute. P3HT coating steps were repeated up to four times to increase the thickness of the P3HT layer, with approximately 50 nm deposited after each coating cycle. All solution coating steps were performed in air.

Varying thicknesses of zinc oxide were deposited over porous P3HT or glass slides using RF magnetron sputtering in a CVC SC-4000 system from Myers Vacuum (Kittanning, PA). The vacuum pressure was 10 mtorr, the sputtering power was 50 W and the deposition rate was 2 Å/s. Film thicknesses ranged from 50 to 250 nm, as measured by contact profilometry.

Aluminum top contacts were deposited over the ZnO layer under vacuum (base pressure = 5.7×10^{-7} torr) using a deposition rate of 1 nm/sec with a CHA Thermal Metal Evaporator (Fremont, CA). A shadow mask was used to define the size of the top contact (5 mm diameter), and therefore the size of the photovoltaic device. The thickness of the aluminum contact layer was 250 nm.

UV-Visible Spectroscopy (UV-vis). UV-vis was utilized to measure the absorbance of the hybrid materials over a wavelength range of 200 – 800 nm using a Cary 5000 from Agilent Technologies (Santa Clara, CA). The instrument was configured for both transmittance (*%T*) and reflectance (*%R*) modes to calculate the true absorbance (*%A*) of the thin films using $100 = \%T + \%R + \%A$.

Profilometry. Contact profilometry was utilized to measure film thickness using a Taylor Hobson (Leicester, United Kingdom) Form Talysurf 60 instrument.

Small Angle X-ray Scattering (SAXS). The organogel structure was determined from SAXS using an Anton Paar (Graz, Austria) SAXSess instrument. Experiments were performed using line-collimated CuKα x-rays with a wavelength of 1.54 Å. Experiments were performed for dispersed organogel networks and for drop cast films on ultra-thin Mylar substrates (thickness = 2.5 μm). Scattering from the empty cell and substrate were subtracted prior to desmearing using the Anton Paar SAXquant software. DANSE SASView is utilized for all SAXS data fitting with a parallelepiped fiber model (Equation 2.7).

X-ray Photoelectron Spectroscopy (XPS). XPS was utilized to measure the valence band energy level using a high resolution scan (0.1 eV) over low energy levels (0 - 10eV). This was performed under vacuum using an M-Probe from Surface Science Instruments (Mountain View, CA).

Scanning Electron Microscopy (SEM). SEM was utilized to image the cross-sectional morphology of composite P3HT/ZnO films. Films were fractured and coated with a 10 nm of Pd/Au mixture to enhance contrast. Imaging was performed at 10.0 kV using a Tescan (Kohoutovice, Czech Republic) Mira 3XMU.

Solar Cell Testing. The *I-V* curves were collected at an illumination of 100 mW/cm^2 (AM 1.5 filter) by a Keithley (Cleveland, OH) Series 2400 Source Measure Unit (SMU). The light source was calibrated using a standard silicon reference cell to AM1.5G 1 sun test conditions (100 mW/cm^2). All devices were tested at room temperature in air.

7.3 Results & Discussion

7.3.1 Structural Characterization of Porous P3HT Networks

Small angle x-ray scattering (SAXS) was utilized to characterize the cross-sectional dimensions of the P3HT nanofibers within the organogel solution prior to coating, as discussed in Chapter 2.1.5. Figure 7.2a shows the 1D scattering intensity profile of the final, fractured organogel solution (5 mg/mL P3HT in toluene) and the corresponding Equation 2.7 fit, which was used to determine an average fiber thickness (5 ± 0.5 nm) and width (17 ± 2 nm). These dimensions, which are typical for P3HT nanofibers, could be ideally suited for effectively harvesting charge because of the short exciton diffusion length scale (< 20 nm) of P3HT.[10] By

introducing an inorganic semiconductor phase into the empty pore space of the P3HT nanofibers, excitons that are generated in the polymer will be efficiently dissociated.

After coating and drying, the scattering of the P3HT organogel film was compared to that of the solution phase (Figure 7.2b). Solvated P3HT organogels are known to form an interconnected network of fibers (Chapters 4-6). The scattering profiles shown in Figure 7.2b are nearly identical, indicating that there are only minimal changes to the network and fiber structures occurring at the nanoscale (< 100 nm). A network structure is required in order to maintain a high interfacial contact area between the p-type organogel and the n-type metal oxide.

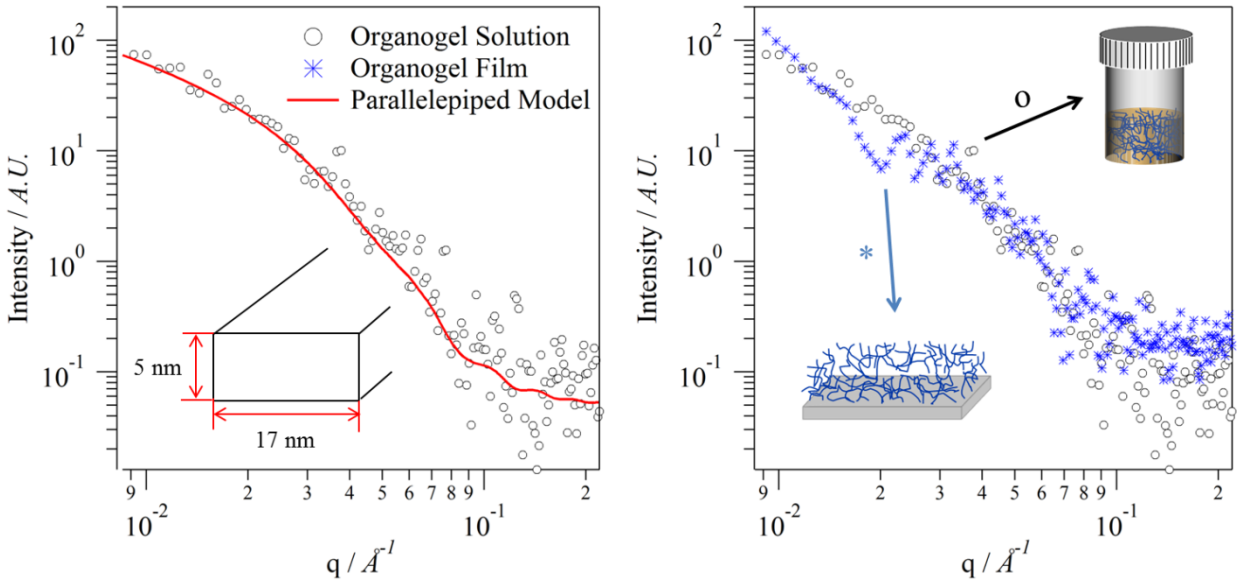

Figure 7.2. Small angle x-ray scattering (SAXS) of a 5 mg/mL toluene-based P3HT organogel dispersion before (left) and after (right) coating. The red line shows the parallelepiped model (Equation 2.7) fit.

7.3.2 Zinc Oxide Coating Properties

X-ray photoelectron spectroscopy (XPS) was performed on a 100 nm ZnO thin film to determine the position of the valence band (HOMO). This can be accomplished by finding the peak intensity at low binding energies (Figure 3 inset). The HOMO was found to be E_v = 6.0 eV

for the ZnO films that were being generated via magnetron sputtering.[11] This value is lower than expected, given that most crystalline ZnO has a HOMO level near 7.1 eV.[12] This difference is likely arising from the amorphous nature of the ZnO phase that is produced at the temperatures that are used in these experiments (< 100 °C).[13] The band gap of ZnO is also determined using the low energy band-edge extrapolation from UV-Vis absorption spectroscopy, as seen in Figure 7.3. The band gap (E_g = 3.2 eV) matches the values commonly reported for ZnO.[12] The deviation in valence band energy causes issues with the alignment of conduction bands (LUMO), as seen in Figure 7.3. Typically, the conduction band of ZnO is E_c = 4.2 eV, which allows for exciton dissociation at the P3HT/ZnO interface and an ohmic contact between ZnO/Al.[1, 6] In this study, there is an energetic barrier to exciton dissociation that will reduce the overall device efficiency.

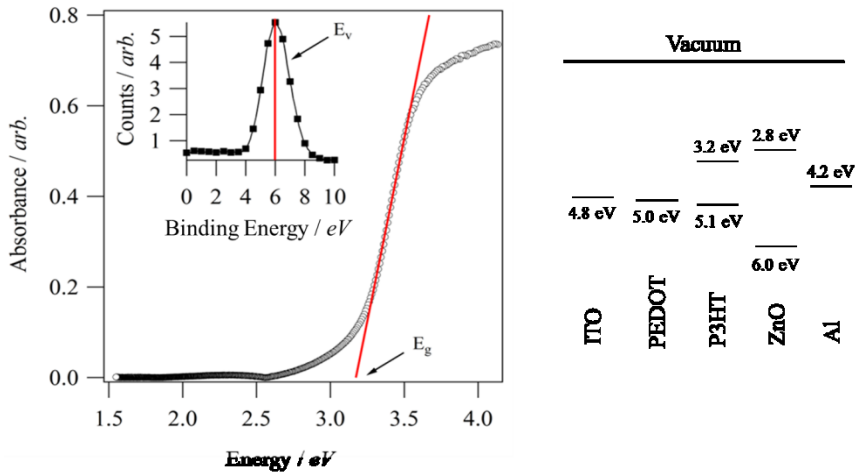

Figure 7.3. Left: UV-vis absorption spectroscopy of a 100 nm ZnO thin film produced using magnetron sputtering. Inset figure shows x-ray photoelectron spectroscopy (XPS) results of the same thin film. Right: HOMO-LUMO band alignment for devices generated in this study.

7.3.3 P3HT/ZnO Composite Thin Films

Figure 7.4 shows a cross-sectional SEM image of the composite film structure of ZnO coated on top of a porous P3HT organogel, as depicted in Figure 7.1. Figure 7.4 shows that magnetron sputtering results in limited penetration of the ZnO phase into the P3HT organogel. This is likely the result of the fact that magnetron sputtering is a line-of-sight deposition method and this organogel network may be too dense for effective penetration. High concentration organogels provide good interconnectivity and effective charge transport properties, as described in Chapters 4-6. However, lower concentration organogels are more porous (i.e., lower fiber concentration) and ZnO is more likely to effectively infiltrate the network structure during sputter deposition. A slower and more diffuse deposition method, such as atmospheric plasma deposition or atomic layer deposition, could also allow for better network interpenetration. Alternatively, a solvent-based approach to deposit precursors or ZnO nanoparticles could be explored as long as the solvent wets the organogel but it does not re-dissolve it. Improving the infiltration of metal oxides in the organogel network structure is critical to optimizing device performance because increasing interfacial contacts between materials will result in higher exciton dissociation.[2] Therefore, the use of more open networks and/or different deposition methods will be the focus of future studies.

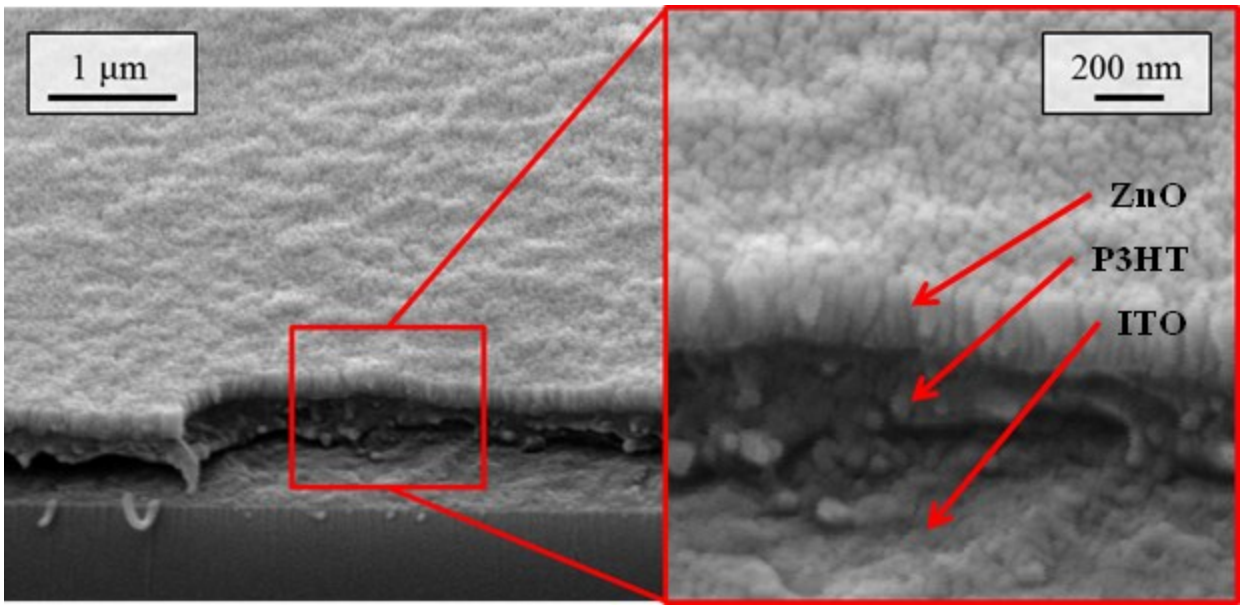

Figure 7.4. SEM image of a composite glass:ITO:P3HT:ZnO film structure coated with 10 nm of Pd/Au to enhance contrast. The enlarged view shows a 30 mg/mL P3HT organogel layer (lower) and a magnetron sputtered ZnO layer (top).

Figure 7.5 shows the optical absorption profile of the composite P3HT/ZnO film. The large wavelength absorption spectrum (500 – 700 nm) of P3HT remains nearly unchanged after ZnO deposition. Only a slight increase in intensity is observed that is likely the result of variations in film thickness of the regions that were evaluated. Figure 7.5 demonstrates that the electronic properties of the underlying P3HT network structure are not damaged by the magnetron sputtering process that is used to deposit ZnO. Rather, the optical properties of both components are additive such that the absorption of P3HT and ZnO can be clearly distinguished.

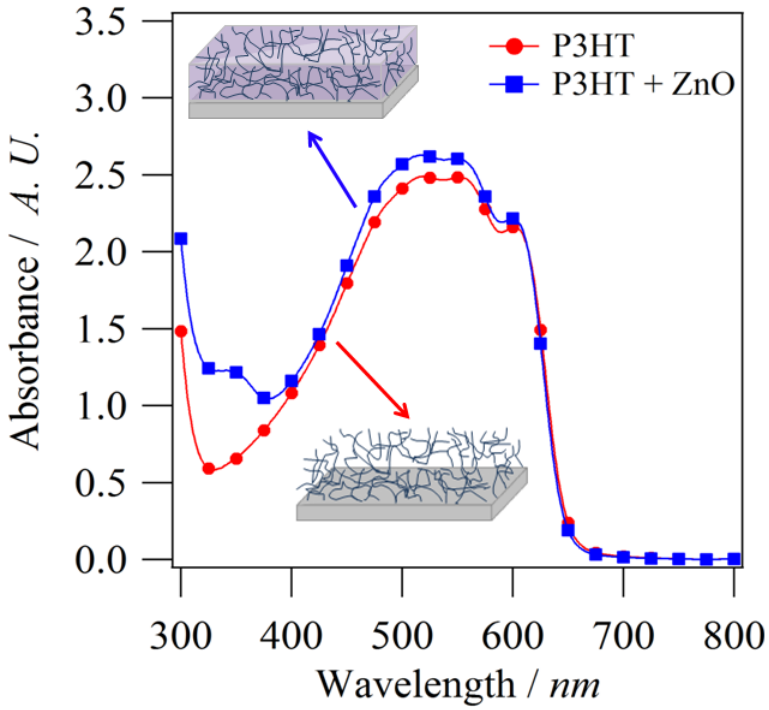

Figure 7.5. UV-vis absorption spectrum of a P3HT organogel layer (~500 nm) before and after deposition of 100 nm magnetron sputtered ZnO.

7.3.4 Hybrid Photovoltaic Device Performance

Hybrid organic/inorganic photovoltaic devices were generated by depositing PEDOT:PSS on ITO coated glass. A P3HT organogel solution was then spin-coated before magnetron sputtering the ZnO layer. The device geometry was defined to 0.2 cm^2 by masking and evaporating aluminum to act as the anode. Figure 7.6 shows the current-voltage behavior for P3HT-ZnO solar cells under no illumination and under 1-sun conditions. The hybrid device has an open circuit voltage (V_{oc}) of 0.33 V, short circuit current density (I_{sc}) of 0.017 mA/cm^2 and fill factor (*FF*) of 0.29. The V_{oc} is similar to what has been reported by other researchers for P3HT/ZnO devices: V_{oc} = 0.44 - 0.57 V.[1, 4, 14] However, the short circuit current is three orders of magnitude smaller than other HPV devices and this leads to the poor device performance. The

cause of the low PCE is investigated further by varying the thickness of both the magnetron sputtered ZnO and the P3HT organogel layers, as shown in Figure 7.7.

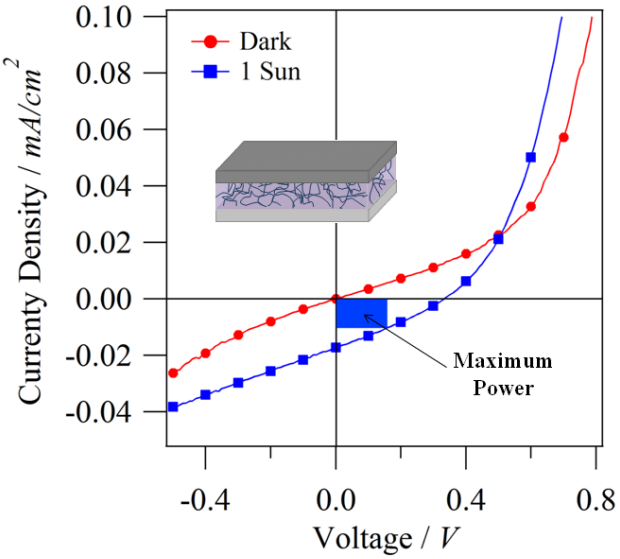

Figure 7.6. I-V curve for a hybrid P3HT/ZnO-based photovoltaic device (800 nm and 250 nm respective thicknesses) under no illumination and under 1-sun conditions. The maximum operating power of this device is also highlighted.

The data in Figure 7.7 does not show significant differences in PCE with changes in layer thickness. This indicates both positive and negative attributes of this preparation procedure. The lack of a significant difference in PCE shows that the device efficiency is not negatively impacted by coating relatively thick P3HT or ZnO layers. This suggests that once charges are separated, the interconnectivity of each phase leads to efficient charge transport. These attributes are expected for devices prepared from P3HT networks because they have been shown to lead to superior charge transport when compared to other polymer processing methods, as demonstrated in Chapter 3.3.2.

On the other hand, results in Figure 7.7 also indicate that changes in thickness do not have any positive impact on device performance. This suggests that the interpenetration of the magnetron sputtered ZnO into the porous P3HT organogel is limited to $\leq$ 50 nm and this is likely

the dominant problem with these devices. Shallow penetration leads to low interfacial contact area and low exciton dissociation causing low PCE values. Further work is needed to overcome this limitation by tuning the deposition parameters so that, ideally, ZnO will conformably coat all of the conjugated polymer fibers in the network. Other metal oxide deposition techniques, such as atmospheric plasma deposition, atomic layer deposition (ALD) or solvent-based deposition may be better suited to achieve this. ALD is known to produce conformal coatings of porous structures, but would need to be optimized for low temperature conditions to avoid melting the organogel.[15, 16] It has been hypothesized that atmospheric plasma deposition can also be utilized to conformally coat porous structures using sequential deposition steps.[8] Reductions in fiber density and increases in porosity of the polymer network are other potential routes to improving penetration and device efficiency.

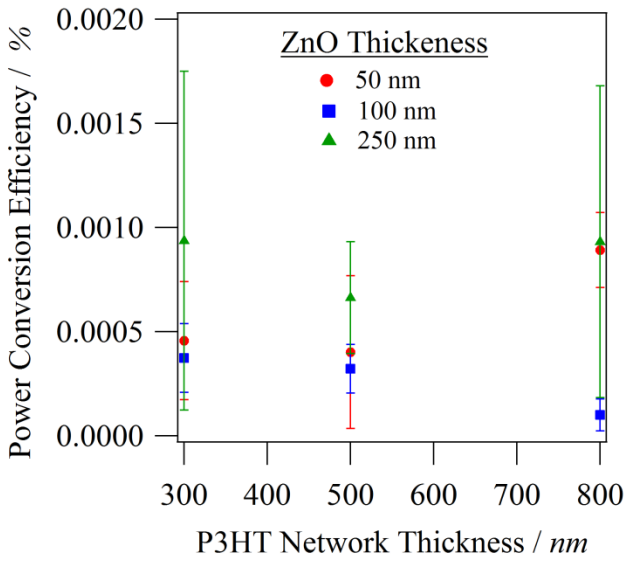

Figure 7.7. Power conversion efficiency values for hybrid P3HT/ZnO photovoltaic devices with variable layer thickness.

7.4 Summary

We have demonstrated the feasibility of fabricating hybrid organic/inorganic devices through the deposition of a metal oxide coating over a porous conjugated polymer network. This methodology aims to take advantage of the high surface area and intrinsic connectivity of self-assembled conjugated polymer networks to form bulk heterojunctions through backfilling with metal oxides via magnetron sputter deposition. These proof-of-concept experiments have notably low efficiencies (PCE ~ 0.001%) that result from poor impregnation of the ZnO phase in the P3HT porous matrix and from poor electronic band structure matching. Additional studies are proposed to fully understand the role of network porosity and deposition conditions on the penetration depth of the metal oxide and to improve performance. Enhancing crystallinity of the metal oxide phase or using other semiconductors could also lead to better electronic structure matching and to higher efficiencies. This work demonstrates a fundamentally new approach towards the fabrication of hybrid organic/inorganic photovoltaic devices.

7.5 References

1. Takanezawa, K.; Hirota, K.; Wei, Q.-S.; Tajima, K.; Hashimoto, K. *The Journal of Physical Chemistry C* **2007,** 111, (19), 7218-7223.
2. Vanlaeke, P.; Swinnen, A.; Haeldermans, I.; Vanhoyland, G.; Aernouts, T.; Cheyns, D.; Deibel, C.; D'Haen, J.; Heremans, P.; Poortmans, J.; Manca, J. V. *Solar Energy Materials and Solar Cells* **2006,** 90, (14), 2150-2158.
3. Richards, J. J.; Weigandt, K. M.; Pozzo, D. C. *Journal of Colloid and Interface Science* **2011,** 364, (2), 341-350.
4. Olson, D. C.; Piris, J.; Collins, R. T.; Shaheen, S. E.; Ginley, D. S. *Thin Solid Films* **2006,** 496, (1), 26-29.
5. Gonzalez-Valls, I.; Lira-Cantu, M. *Energy & Environmental Science* **2009,** 2, (1), 19-34.
6. Beek, W. J. E.; Wienk, M. M.; Janssen, R. A. J. *Advanced Functional Materials* **2006,** 16, (8), 1112-1116.

7. Boucle, J.; Ravirajan, P.; Nelson, J. *Journal of Materials Chemistry* **2007,** 17, (30), 3141-3153.
8. Kim, J. Y.; Lee, K.; Coates, N. E.; Moses, D.; Nguyen, T.-Q.; Dante, M.; Heeger, A. J. *Science* **2007,** 317, (5835), 222-225.
9. Cai, W.; Gong, X.; Cao, Y. *Solar Energy Materials and Solar Cells* **2010,** 94, (2), 114-127.
10. Lunt, R. R.; Giebink, N. C.; Belak, A. A.; Benziger, J. B.; Forrest, S. R. *Journal of Applied Physics* **2009,** 105, (5), 053711-7.
11. Xing, K. Z.; Fahlman, M.; Chen, X. W.; Inganäs, O.; Salaneck, W. R. *Synthetic Metals* **1997,** 89, (3), 161-165.
12. Preston, A. R. H.; Ruck, B. J.; Piper, L. F. J.; DeMasi, A.; Smith, K. E.; Schleife, A.; Fuchs, F.; Bechstedt, F.; Chai, J.; Durbin, S. M. *Physical Review B* **2008,** 78, (15), 155114.
13. Tan, S. T.; Chen, B. J.; Sun, X. W.; Fan, W. J.; Kwok, H. S.; Zhang, X. H.; Chua, S. J. *Journal of Applied Physics* **2005,** 98, (1), 013505-5.
14. Olson, D. C.; Shaheen, S. E.; Collins, R. T.; Ginley, D. S. *The Journal of Physical Chemistry C* **2007,** 111, (44), 16670-16678.
15. Carcia, P. F.; McLean, R. S.; Reilly, M. H. *Applied Physics Letters* **2006,** 88, (12), 123509-3.
16. Elam, J. W.; Routkevitch, D.; Mardilovich, P. P.; George, S. M. *Chemistry of Materials* **2003,** 15, (18), 3507-3517.

Chapter 8

Solution Phase Conformation and Properties of Poly(3-alkyltiophenes)

8.1 Motivation

Advances in the synthesis of a variety of conjugated polymer backbones and side-chain architectures have resulted in highly tunable polymer properties (e.g., mobility, band gap and solubility).[1-4] In Chapters 3-6, we have demonstrated that conjugated polymer aggregation and/or crystallization can be induced in solution to modify optical and electronic properties and to optimize materials for specific applications.[5] It is often hypothesized that the conformation of individual polymer chains in solution is key to determine the likelihood of aggregation and/or crystallization.[6-8] McCulloch and coworkers carefully explored changes in polymer chain shape as a function of the synthesis method, solvent and alkyl chain structure for poly(3-alkylthiophenes) (P3ATs) in solution.[9] These results provided conclusive evidence of morphological changes for a variety of P3ATs in different solvent conditions. Despite these advances, there is still a need to directly relate changes in polymer conformation to changes in properties, such as optical absorption, that are relevant to device applications.

Conjugated polymers are known to have unique optical properties, such as thermochromism and solvatochromism.[6, 8-12] Solvatochromism is broadly defined as a change in the photophysical properties (i.e., absorption, fluorescence, stokes shift) of a solute as a function of changes in the solvent condition.[13] Solvatochromic effects in conjugated polymers are often attributed to either inter-chain mechanisms, such as aggregation and crystallization, or to intra-chain mechanisms that can affect conjugation.[6, 8, 10, 11, 14]

Intra-chain solvatochromic shifts are often explained as changes in the conjugation length due to variations in stiffness when the polymer is assumed to be a fully dissolved chain.[6, 11] This hypothesis stems from the combined results of studies performed on oligomeric species and from conformon studies.[8, 11, 15-18] Studies on oligomers of conjugated polymers show that there is a red-shift in the primary absorption peak as the chain length increases indicating increased number of π-bond overlaps along the oligomer backbone.[15-18] Conformon studies have hypothesized that twists and rotations of a conjugated polymer backbone result in "subdivisions" of the polymer chain that can be described as effectively planar and therefore conjugated polymers have a "conjugation length" that is smaller than the length of the chain.[6, 11, 14] Until recently it was assumed that the persistence length of the chain was the upper limit for the conjugation length, however McCulloch and coworkers postulated that for P3HT in 1,2-dichlorobenzene (DCB) the conjugation length can be greater than the persistence length.[9]

For many small molecule dyes, solvatochromic shifts are fully described by changes in the solvent dipolarity, polarizability, acidity and/or basicity without any necessary change in molecular conformation of the dye.[13, 19] This solvent effect has also been observed in conjugated polymers and solvatochromic shifts were correlated to solvent polarity.[2-4] Yet, for commonly used polymers, such as poly(3-alkylthiophenes) (P3ATs) and poly[2-methoxy-5-(20-ethyl-

hexyloxy)-p-phenylenevinylene] (MEH-PPV), optical absorption shifts in the dilute dissolved phase are, in the literature, consistently attributed to changes in steric intramolecular interactions, backbone planarity and conjugation length frequently without also accounting for changes occurring in solvent environment during photoexcitation.[7, 11, 18, 20]

In this work, we utilize experiments and molecular dynamics simulations to demonstrate that solvatochromic optical shifts in monodisperse poly(3-alkylthiophenes) can be described by changes in general solvent properties (e.g. acidity, basicity, polarizability and dipolarity) as well as specific solvent-polymer interactions. The peak position from UV-vis absorption profiles of P3ATs in different solvents are fit and normalized by accounting for the photophysical solvent effect using the method developed by Catalán.[19] Small angle neutron scattering (SANS) experiments are also used to directly determine the conformation of the dissolved polymer chains in these solvents. SANS reveals that there are conformational changes occurring as a function of solvent environment and alkyl chain structure for P3ATs and molecular simulations provide insights into the underlying physics behind these conformational changes. However, the combination of UV-vis and SANS shows that there is no direct correlation between polymer conformation and shifts in optical absorption. These experiments demonstrate that changes in solvent-polymer interactions must also be accounted for in order to develop accurate physical descriptions of conjugated polymer solutions and to describe solvatochromic changes.

8.2 Experimental Methods

Polymer Synthesis. Monodispersed poly(3-alkylthiophenes) (P3ATs) with four different alkyl chain moieties: poly(3-hexylthiophene) (P3HT), poly(3-octylthiophene) (P3OT), poly(3-dodecylthiophene (P3DDT) and poly(3-(2-ethylhexyl)thiophene) (P3EHT) were synthesized and characterized to determine their molecular weight (M_w), polydispersity index (*PDI*) and

regioregularity, which are reported in Table 8.1.[1] This synthesis was performed by Prakash Sista, Hoi-Ki Cheung and Christine Luscombe at the University of Washington and the details of the polymer synthesis and characterization procedures can be found in the Chapter 10.3. The contour length (L_c) of the polymer chain can be calculated using Equation 8.1:

$$L_c = \frac{M_w}{m_{m,monomer}} \cdot L_{monomer} \tag{8.1}$$

where M_w is the molecular weight of the polymer chain and $m_{m,monomer}$ is the molecular mass of monomer unit which is 166.2, 194.3, 250.4 and 194.3 g/mol for P3HT, P3OT, P3DDT and P3EHT, respectively. The length of the monomer ($L_{monomer}$) is defined as the distance between sulfur atoms along the polymer backbone and is constant at 3.85 Å regardless of alkyl chain structure.[21]

Table 8.1. The molecular weight (M_w) and polydispersity index (*PDI*) of the P3ATs were measured using GPC. Regioregularity (*RR*) was determined using H-NMR and the contour length (L_c) of the polymer was calculated using Equation 8.1.

Polymer	*M_w (g/mol)*	*PDI*	*RR*	*L_c (nm)*
P3HT	47,500	1.26	96.4%	110
P3OT	52,500	1.23	96.7%	104
P3DDT	48,800	1.27	94.2%	75
P3EHT	44,300	1.26	97.4%	88

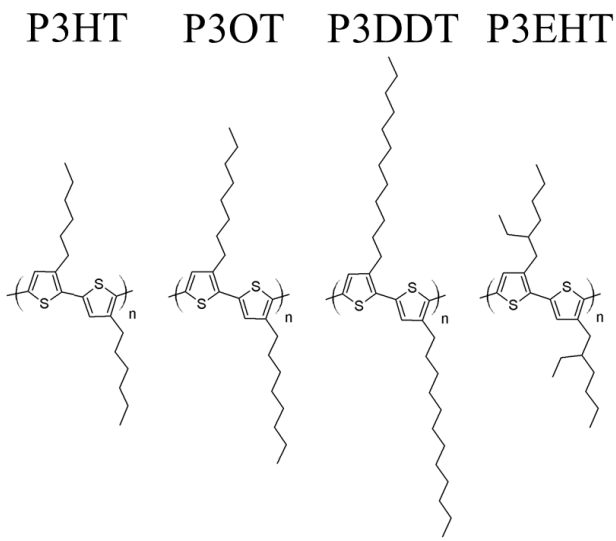

Figure 8.1. Molecular structure of poly(3-hexylthiophene) (P3HT), poly(3-octylthiophene) (P3OT), poly(3-dodecylthiophene) (P3DDT) and poly(3-(2-ethylhexyl)thiophene) (P3EHT)

Sample Preparation. A concentration range of 0.01 – 10 mg/mL was prepared by adding conjugated polymer directly into organic solvents. The solutions were heated (> 60 °C) until the solid black polymer powder was fully dissolved and the sample turned bright orange. Hydrogenated solvents were purchased from Sigma Aldrich (St. Louis, MO) and used as received. Deuterated solvents toluene-d8 (D > 99.5%), benzene-d6 (D > 99.5%), cyclohexane-d12 (D > 99.5%), 1,2-dichlorobenzene-d4 (D > 99%), chlorobenzene-d5 (D > 99%) and chloroform-d (D > 99.8%) were purchased from Cambridge Isotopes (Tewksbury, MA) and used as received.

UV-vis Absorption Spectroscopy. These experiments were performed using a Thermo-Fischer Evolution 300 UV-visible spectrophotometer. Samples prepared to a concentration of < 0.03 mg/mL were loaded into 10 mm quartz cuvettes and temperature was controlled with a Peltier cell holder (10 °C to 90 °C range, ± 0.5 °C). Results in Chapter 3 shows that P3ATs self-assemble and crystallize in certain solvents, resulting in the formation of characteristic red-shifted absorption peaks. For the experiments presented herein, no spectra exhibiting

characteristic P3AT crystalline peaks were observed. These experiments are designed to probe the fully dissolved state at very low polymer concentrations in order to investigate solvent effects for isolated polymer chains.

Small Angle Neutron Scattering. SANS experiments were performed on the D22 beamline at the Institut Laue-Langevin (ILL) in Grenoble, France. Samples were prepared in deuterated solvents to decrease the incoherent scattering background and increase the coherent scattering contrast. Pristine 2 mm path length Hellma cells were utilized to minimize scattering from cell defects. Standards instrument configurations were utilized to cover a broad q-range ($0.3 < q\ (\mathring{A}^{-1}) < 0.004$). Temperature control (± 1 ºC variance) was achieved using a water-circulation bath and monitored using a blank ethylene glycol sample in the same sample environment. Standard data processing and model fitting was performed according to the procedure in Chapter 2.1.

Simulations. Density functional theory (DFT) calculations were completed for 3-hexylthiophene (3HT), 3-octylthiophene (3OT), 3-dodecylthiophene (3DDT) and 3-(2-ethylhexyl)thiophene (3EHT) monomers in vacuum to determine their permanent dipole moment. This was accomplished using Gaussian 09.[22] Becke's three parameter hybrid functional (B3LYP), with a 6-311G(d,p) basis set, was utilized in conjunction with geometry optimization to a minimum energy stationary point and frequency calculations.[23] This method and basis set combination were selected by comparing a series of several functional and basis sets against experimental data for thiophene and alkylthiophene monomers. Ogata and coworkers determined the dipole moment of a thiophene and 3-methylthiophene monomer to be 0.55 D and 0.95 D, respectively.[24] DFT calculations at the B3LYP/6-311G(d,p) level yielded the best agreement with

experiment with dipole moments of 0.56 D and 0.94 D for a thiophene and 3-methylthiophene monomer, respectively. *These calculations were performed by Melissa Gile and Jim Pfaendtner.*

Molecular dynamics (MD) simulations were performed using the GROMACS 4.5.5 package.[25] The force field parameters used for the P3HT chain were taken from the model proposed and validated by Moulé and coworkers.[26, 27] Solvents benzene, toluene, chloroform and 1,2-dichlorobenzene were modeled using the OPLS-AA force field, which has been shown to accurately predict behavior in liquid simulations.[28]

Packmol was used to generate initial solvation structures for simulation.[29] A single regioregular 60-monomer P3HT chain was positioned with the center of mass at the center of the simulation box. The number of solvent molecules in each simulation was selected to approximate the bulk density of the solvent with a folded polymer chain inside of a cubic simulation box of 15 nm length. We found that this value was sufficiently large to allow for rotation and unfolding of the polymer chain with only minimal self-interaction (at highly extended, entropically unfavorable states) through the periodic boundary. The systems for solvent benzene, toluene, chloroform and o-dichlorobenzene contain 222302, 307502, 103502, and 205502 atoms respectively.

Each system was subject to steepest decent energy minimization until the maximum force reached a tolerance of 10 kJ mol^{-1} nm^{-1}. The minimized system was simulated for 1 ns in the NVT ensemble in order to allow the bonds to relax. Next 4 ns of NPT simulation allowed the box dimensions to adjust to equilibrate the density of the solvent. Following this, production runs of length 150 ns were performed in the NVT ensemble. Two repeat simulations were completed for each solvent. Temperature was held constant in all simulations at 300 K using a stochastic global thermostat.[30] Simulations in the NPT ensemble used the Berendsen barostat.[31] All MD

simulations used a time step of 2 fs and LINCS constraints on all bonds.[32] Radial distribution functions were calculated using the g_rdf tool from GROMACS from an additional 5 ns of NVT simulation started from the end of each production run. This was done for both repeat simulations for each solvent, and the difference between repeat simulations was negligible. *These simulations were performed by Stephanie Hoffmann and Jim Pfaendtner.*

8.3 Results

8.3.1 Dissolved Phase Absorption Spectroscopy

Non-aggregated and non-crystalline conjugated polymers in solution exhibit a single, broad absorption peak in the optical spectrum.[8] This peak position is determined by the molecular structure of the monomer unit, the average number of overlapping π-bonds along the polymer backbone and the local solvent environment upon excitation.[12] P3ATs show a characteristic absorption peak in the dissolved phase that generally falls in the 400 – 500 nm range.[8, 12] Figure 8.2 shows the normalized UV-vis absorbance profile for non-aggregated and non-crystalline P3DDT in different aromatic and halogenated solvents.

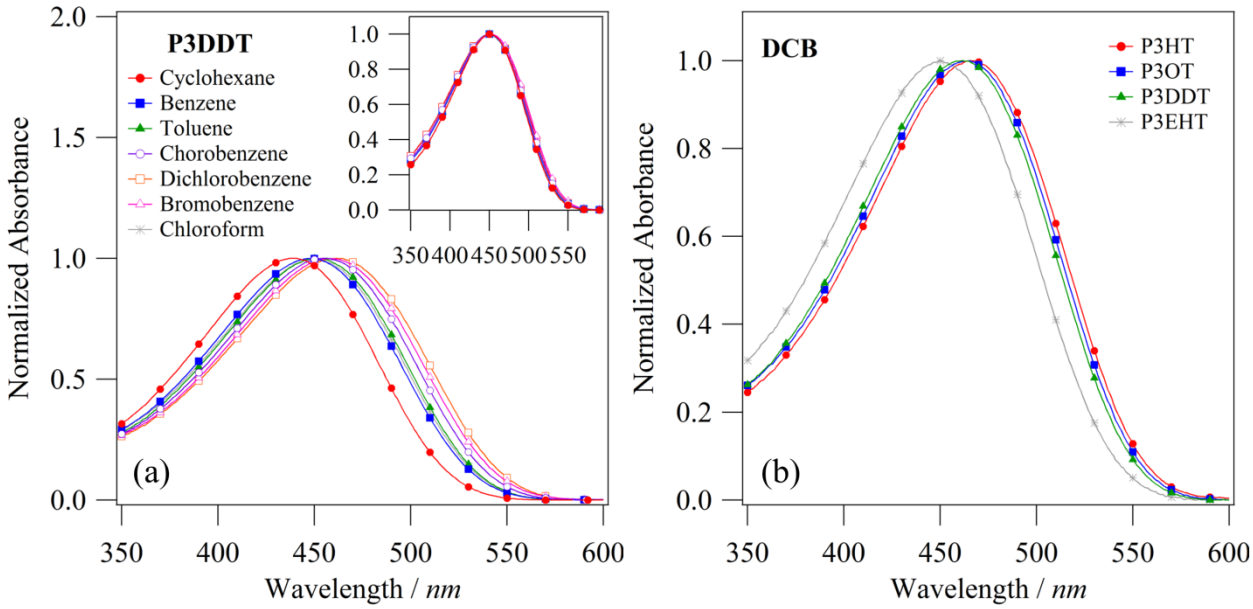

Figure 8.2. a) Normalized UV-visible absorption profiles for dilute P3DDT (< 0.03 mg/mL) in cyclohexane, benzene, toluene, chlorobenzene, 1,2-dichlorobenzene, bromobenzene and chloroform at 25 °C. Inset: Shows the absorption profiles shifted to a peak max of 450 nm. b) Normalized UV-visible absorption profiles for dilute P3HT, P3OT, P3DDT and P3EHT (< 0.03 mg/mL) in 1,2-dichlorobenzene (DCB) at 25 °C.

The spectrum peak position shifts as a function of solvent, however the shape of the absorbance profile is nearly identical, as seen in the normalized Figure 8.2a inset. Figure 8.2b highlights the difference in absorption spectrum for different P3ATs in the same solvent. There are small (~ 4 nm) but systematic spectrum shifts with respect to increasing alkyl chain length (i.e., P3HT > P3OT > P3DDT). The shift in peak position for each P3AT in all solvents can be found in Figure 8.3. The wavelength at maximum absorption (peak max) for P3HT > P3OT > P3DDT > P3EHT for almost all solvents utilized.

In general, P3EHT has a substantially blue-shifted absorbance peak maximum (~ 15 nm) when compared to the other P3ATs. Other researchers have attributed this behavior to conformational changes in P3EHT that result from the steric hindrance of the branched alkyl chain.[9, 12] However, it may also be the result of an intrinsically lower dipole moment (μ). The gas

phase dipole moment of 3-hexylthiophene (3HT), 3-octylthiophene (3OT), 3-dodecylthiophene (3DDT) and 3-(2-ethylhexyl)thiophene (3EHT) was calculated to be 0.99 D, 1.00 D, 1.01 D and 0.80 D. A dipole moment difference of 0.2 D is substantial, considering that μ for 3-methylthiophene (MT) and thiophene (T) were calculated to be 0.95 D and 0.56 D.

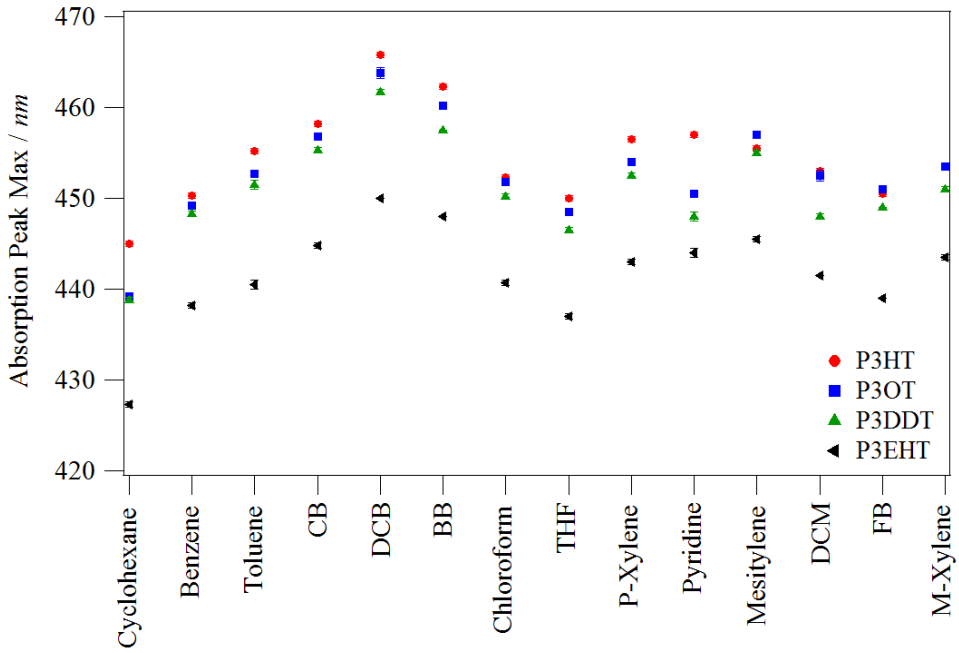

Figure 8.3. UV-vis absorption peak max for fully dissolved and dilute (< 0.03 mg/mL) P3HT, P3OT, P3DDT and P3EHT in cyclohexane, benzene, toluene, chlorobenzene (CB), 1,2-dichlorobenzene (DCB), bromobenzene (BB), chloroform, tetrahydrofuran (THF), p-xylene, pyridine, mesitylene, dichloromethane (DCM), fluorobenzene (FB) and m-xylene at 25 °C. P3HT and P3OT in m-xylene have identical absorption peak maximums.

Solvatochromism has been well characterized for numerous molecular dyes.[13, 19] In these cases, solvatochromic shifts can be associated to the interaction of the ground state solvent molecules with the excited state of the solute. Hypsochromic and bathochromic shifts can be attributed to the dampening or the heightening of the excitation process by the surrounding solvent according to the Frank-Condon principle.[33] Even though these principles have been well established in absorption spectroscopy for many decades, researchers rarely account for these

when studying absorption spectrum shifts in conjugated polymers in solution. Here we utilize the Catalán solvent scale for characterizing solvent effects in fully dissolved P3ATs.[19]

Catalán considers four empirically derived parameters to model the solvent effect: solvent acidity (SA), basicity (SB), dipolarity (SdP) and polarizability (SP). Solvent acidity (SA) and basicity (SB) are related to the propensity of a solvent to donate or accept charges, respectively. Solvent dipolarity (SdP) is related to the strength of the dipole moment of the solvent molecule. Solvent polarizability (SP) is related to the capacity of the solvent molecule to become polarized. Table 8.2 lists the solvent parameters used to study the P3ATs in this work.[19]

Table 8.2. Empirically derived solvent polarizability (SP), dipolarity (SdP), acidity (SA) and basicity (SB) as reported by Catalán.[19]

Solvent	**SP**	**SdP**	**SA**	**SB**
Cyclohexane	0.683	0.000	0.000	0.073
Benzene	0.793	0.270	0.000	0.124
Toluene	0.782	0.284	0.000	0.128
Chlorobenzene	0.833	0.537	0.000	0.182
1,2-Dichlorobenzene	0.869	0.676	0.033	0.144
Bromobenzene	0.875	0.497	0.000	0.192
Chloroform	0.783	0.614	0.047	0.071
Tetrahydrofuran	0.714	0.634	0.000	0.591
P-Xylene	0.778	0.175	0.000	0.160
Pyridine	0.842	0.761	0.033	0.581
Mesitylene	0.775	0.155	0.000	0.190
Dichloromethane	0.761	0.769	0.040	0.178
Fluorobenzene	0.761	0.511	0.000	0.113
M-Xylene	0.771	0.205	0.000	0.162

According to Catalán, the solvent effect can be modeled using the following multi-linear equation:

$$A = A_0 + b \cdot SP + c \cdot SdP + d \cdot SA + e \cdot SB \tag{8.2}$$

where A is the solvent dependent physicochemical property of a given solute, in this case the peak absorbance wavelength, A_0 corresponds to the value of the property in the gas phase and *SP*, *SdP*, *SA* and *SB* are the solvent parameters characterizing various solvent-solute interactions and are listed in Table 8.2. The fitting coefficients: *b*, *c*, *d* and *e* describe the sensitivity of the peak absorbance to the respective solvent-solute interaction. Simultaneous multi-linear fitting is performed using Equation 8.2, the constants in Table 8.2 and the absorption peak position of each P3AT polymer in the corresponding solvents, to determine the susceptibility of monodisperse P3ATs to different solvent-solute interactions.

Table 8.3. The magnitude of solvatochromic wavelength shifts based on the product of the multi-linear regression coefficients (*b*, *c*, *d* and *e*) from Equation 8.2 and the solvent constants (SP, SdP, SA and SB), for P3ATs in two sample solvents: toluene and 1,2-dichlorobenzene (DCB). The absorbance of the polymer in the gas phase is denoted by A_0. The bracketed value in each column refers to the relevant fitting coefficient (i.e., *b*, *c*, *d* or *e*) utilized to calculate the product. All values have units of nanometers.

Polymer	***A_0 (nm)***	***Solvent***	***b×SP (b)***	***c×SdP (c)***	***d×SA (d)***	***e×SB (e)***
P3HT	378 ± 14	Toluene	76.7 (98.1)	-0.2 (0.3)	0.0 (-8.8)	0.1 (-1.2)
		DCB	85.2 (98.1)	-0.2 (0.3)	-0.3 (-8.8)	0.2 (-1.2)
P3OT	387 ± 18	Toluene	65.0 (83.2)	-0.9 (5.1)	0.0 (-56.9)	1.4 (-6.7)
		DCB	72.3 (83.2)	-1.0 (5.1)	-1.9 (-56.9)	3.4 (-6.7)
P3DDT	387 ± 17	Toluene	64.6 (82.7)	-0.9 (3.2)	0.0 (-57.1)	0.9 (-7.4)
		DCB	71.8 (82.7)	-1.1 (3.2)	-1.9 (-57.1)	2.1 (-7.4)
P3EHT	373 ± 16	Toluene	68.0 (87.0)	0.2 (0.7)	0.0 (-6.0)	0.2 (1.3)
		DCB	75.6 (87.0)	0.2 (0.7)	-0.2 (-6.0)	0.5 (1.3)

Table 8.3 shows the magnitude of the influence of each term in the Catalán solvation model on the P3AT peak position, for two sample solvents. These values for all solvents can be found in Chapter 10.4. The gas phase absorbance (A_0) is similar across all P3ATs which indicates that the conjugation length of the polymer chains is also similar. However, this is difficult to say with confidence due to the high uncertainty A_0. Solvent-polymer interactions give rise to a range of spectral shifts as a function of alkyl chain length. This is likely due to molecular packing and the steric shielding by different alkyl moieties. The dependence of the dominant term ($b \times SP$) with respect to alkyl chain size can be observed in Table 8.3. The fits conclusively demonstrate that solvent polarizability is the dominant factor altering solvatochromic shifts for P3ATs. The magnitude of the interaction is also affected by the solvent properties with the results suggesting that DCB more readily polarizes P3ATs than toluene.

After determination of the fit coefficient values (found in Chapter 10.4) using several solvents, the Catalán model can also be utilized to predict the peak absorbance wavelength of P3ATs in other unknown solvents. Figure 8.4 highlights the fit quality by comparing the calculated absorption peak (y-axis) and the measured absorption peak (x-axis) for P3ATs in the library of organic solvents that were used to evaluate the model coefficients.

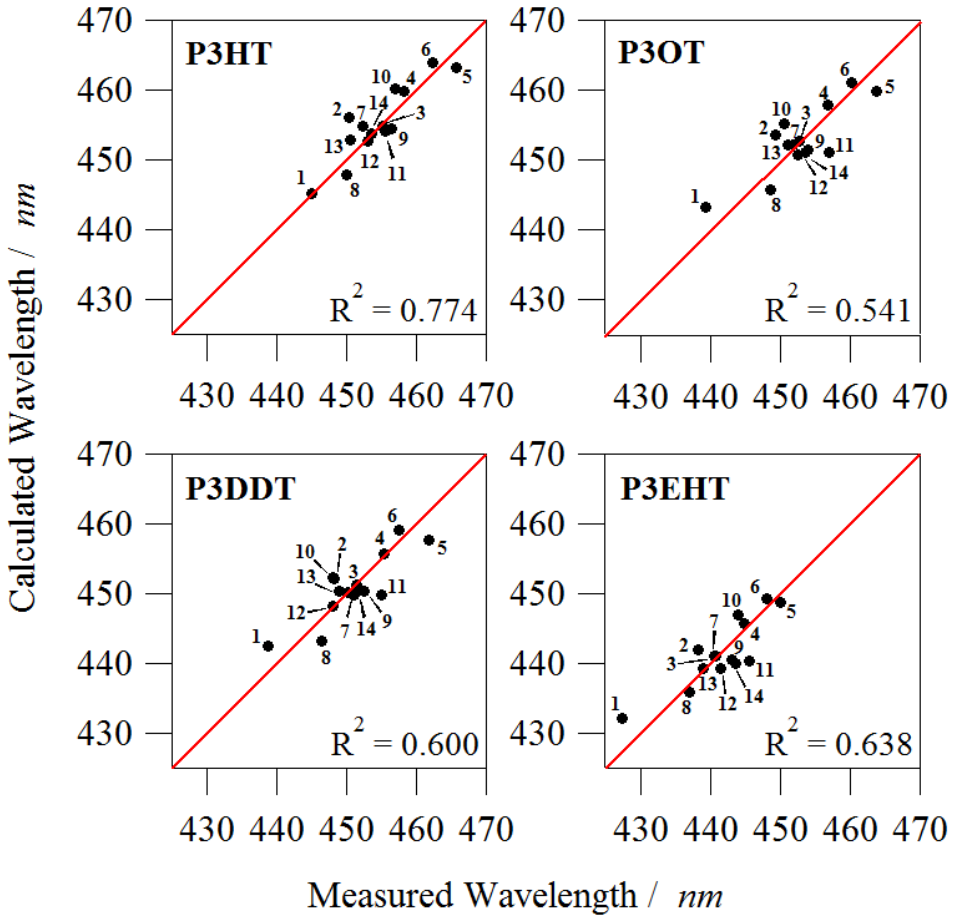

Figure 8.4. The calculated peak absorbance versus the measured peak absorbance for P3ATs in (1) - cyclohexane, (2) - benzene, (3) - toluene, (4) - chlorobenzene, (5) - 1,2-dichlorobenzene, (6) – bromobenzene, (7) – chloroform, (8) – tetrahydrofuran, (9) – p-xylene, (10) – pyridine, (11) – mesitylene, (12) – dichloromethane, (13) – fluorobenzene and (14) – m-xylene at 25 °C. Error bars for measured wavelength are smaller than the marker size.

The line of slope = 1 indicates the goodness of the Catalán solvatochromic model when applied to P3ATs, with $R^2 = 1$ indicating perfect correlation. P3HT, P3OT, P3DDT and P3EHT have R^2 values of 0.774, 0.541, 0.600 and 0.638, respectively. The fit quality suggests that deviations in peak position could perhaps also be caused by solvent-polymer interactions that are unaccounted for in the Catalán model or by differences in conjugation length that may arise from changes in polymer conformation. Yoshino and coworkers suggest that deviations from generalized solvatochromic theory, the Taft parameter (π^*) in their analysis, may be the result of

acid-base interactions between the solvent and the polymer chain.[12] However, the results in Table 8.3 clearly demonstrate that solvent acidity/basicity have a minimal influence on peak absorption maximum. Instead, it is likely that these deviations arise from specific solvent-polymer interactions that cannot be accounted for in any generalized solvatochromic theory. For example, there are likely differences in the orientation and packing of solvent molecules that could control the solvent-backbone separation distances and therefore the optical properties of the conjugated polymer.

8.3.2 Molecular Packing of Solvent Molecules

The simulations in this section were performed by Stephanie M. Hoffmann and Jim Pfaendtner for the University of Washington and have been included with their permission.

The Catalán model has been shown to be very effective at describing solvatochromic shifts of small molecule dyes.[13, 19] These small molecules are free to rotate, can translate efficiently and typically have smaller topological constraints. In contrast, the steric constraints imposed by polymeric materials, with bulky side groups, can lead to shape-dependent solvent-polymer interactions that eventually cause deviations from simple solvatochromic models. Molecular dynamics simulations were performed for a single P3HT chain in different organic solvents to investigate the spatial packing of different solvent molecules around the polymer chain. All-atom (AA) molecular dynamics has been used in a number of simulation studies of the structural properties of conjugated polymers.[26, 27, 34] However, most existing simulations consider smaller length scales than explored here, or do not include explicit solvents. While coarse-grained (CG) simulations could be a more computationally efficient approach, we chose to use AA simulations in this study due to our desire to quantitatively connect the atomistic features of the solvent with the polymer structure and dynamics.

Figure 8.5 shows the pairwise distribution function for the solvent carbon with respect to specific P3HT ring atoms. All solvents are found to generally pack closer with to the sulfur atom and the C2-carbon compared with the other thiophene carbon atoms. This is the result of steric hindrance for solvent packing around the C1-carbon and C4-carbon (due to polymerization) and the C3-carbon (due to the aliphatic hexyl side chain). Figure 8.6 shows that there is also preferential orientation of the solvent molecules. Toluene is more likely to pack around the P3HT backbone with the methyl group (electron donating group) closer to the polymer chain. On the other hand, DCB is more likely to pack around the P3HT backbone with the chlorine atoms (electron withdrawing group) shielded from the polymer chain. These preferential interactions show a propensity for polar solvent molecules to pack with the partial positive charge (δ^+) closest to the polymer chain. This specific solvent-polymer interaction could be expected given that P3HT is more likely to experience p-type (i.e., positive) doping.[35] Ultimately, the steric packing barriers, preferential molecular orientation and solvent effect on chain structure and dynamics cannot be completely accounted for with generalized solvatochromic models, such as the Catalán model.[19] These interactions between solvent and polymer chain could be the cause for the solvatochromic deviations seen in Figure 8.4.

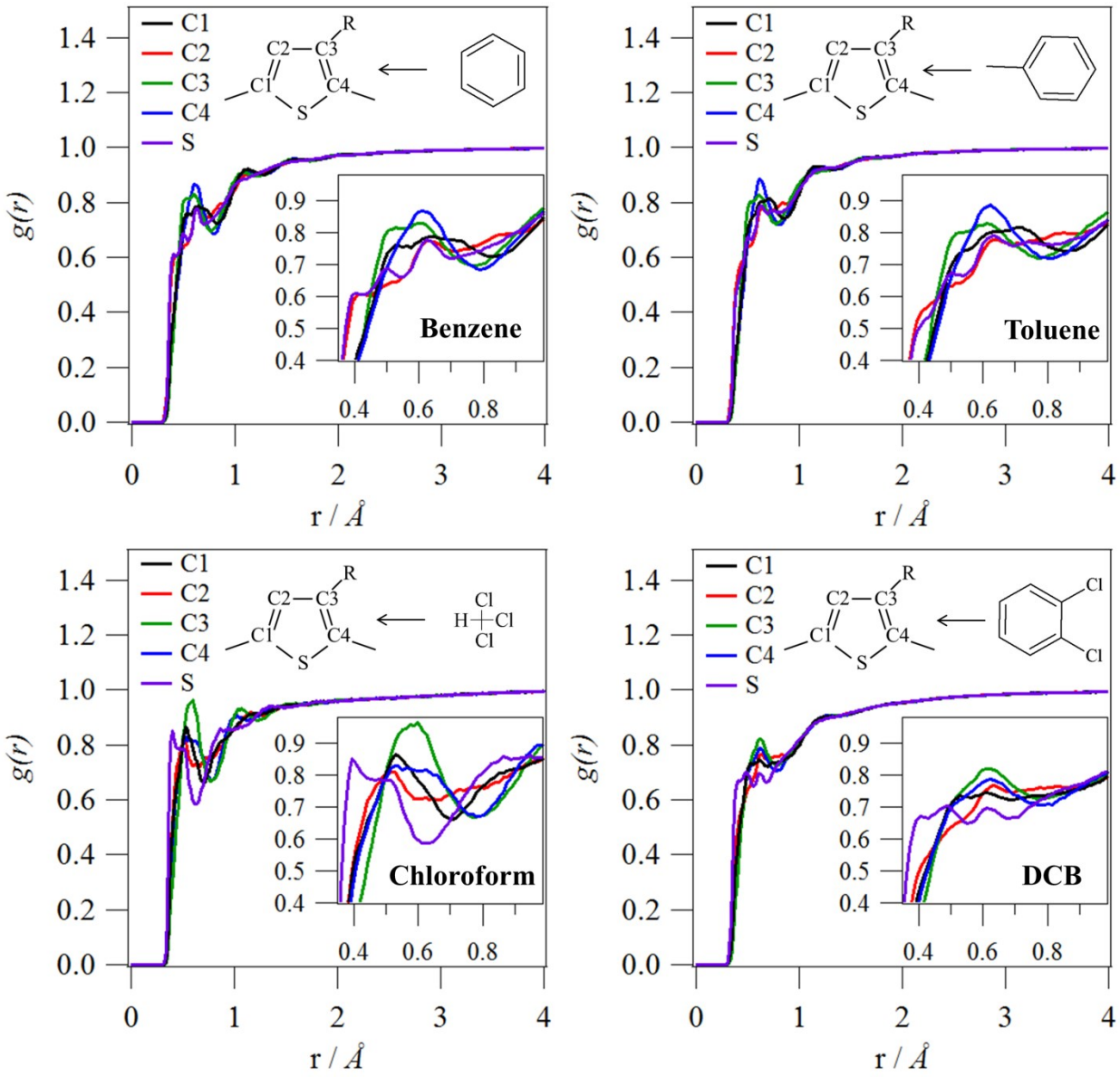

Figure 8.5. Pairwise distribution functions relating the specific sites along the P3HT backbone to the carbon atoms in the four different solvent molecules. In this plot, the specific backbone sites are decomposed into different curves, whereas the sites in the solvent molecules are averaged out.

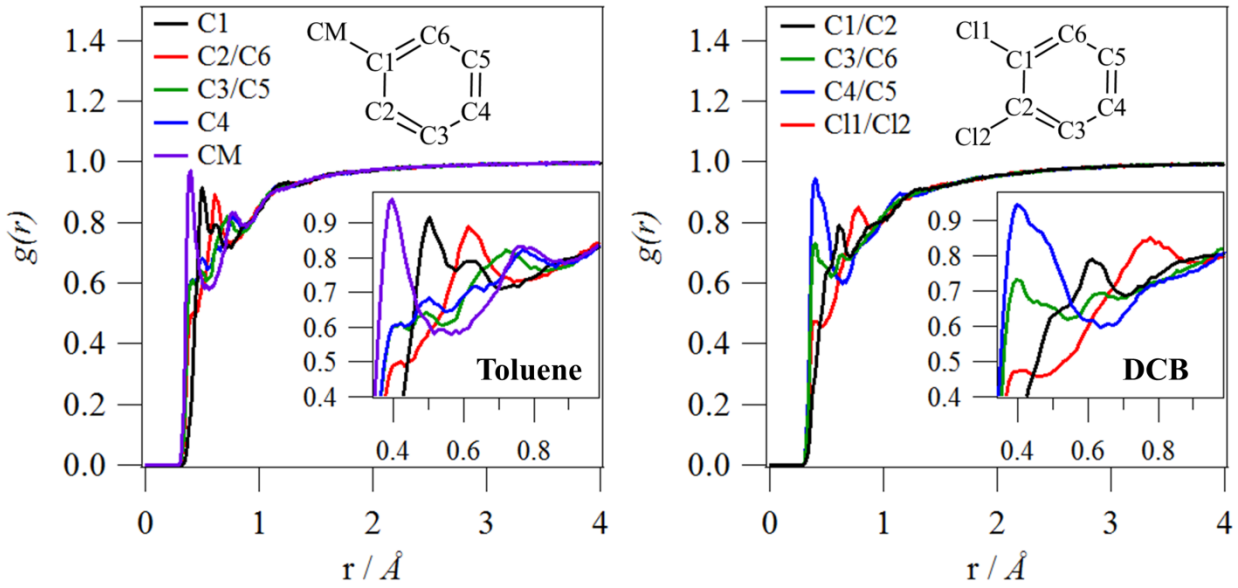

Figure 8.6. Pairwise distribution functions relating the carbon atoms along the P3HT backbone to specific atoms in a toluene molecule (left) and a DCB molecule (right). In this plot, the specific solvent atom sites are decomposed into different curves.

Molecular simulations can also be utilized to investigate the conformation of polymer chains in different solvent environments. Snapshots of the polymer backbone from the AA-MD simulations were first coarse-grained into a linear polymer by averaging the coordinates of the sulfur atoms from monomers i-1, i, and i+1 so that the contribution of each to the average were respectively ¼, ½, and ¼. This procedure is functionally identical to previous work studying the mechanical properties of actin filaments from AA-MD simulations.[36, 37] The following equation is used to calculate persistence length (L_p):

$$\langle \cos(\theta(L_c)) \rangle = \exp\left(-\frac{L_c}{L_p} \right) \tag{8.3}$$

where L_c is the contour length and $\theta(L_c)$ is the angle between the tangent vector at L_c and the tangent vector at a reference point on the polymer chain. The persistence length was averaged from calculations starting from six equally spaced points along the polymer backbone spaced such that each calculation was independent. The Kuhn length (b) is twice as large as the

persistence length (L_p) and the simulated Kuhn length of P3HT in benzene, toluene, chloroform and DCB were determined to be 6.7 ± 0.3 nm, 6.7 ± 0.4 nm, 6.4 ± 0.1 nm and 6.0 ± 0.1 nm, respectively. The reported uncertainty is the standard deviation arising from averaging the Kuhn length from two unique simulations.

The increased flexibility of the polymer backbone could be a result of the closer packing of DCB and chloroform, compared to toluene and benzene, to the thiophene repeat unit as seen in Figure 8.5. However, we hypothesize instead that the difference in flexibility is a result of the solvent interaction with the alkyl chain. Figure 8.7 shows the extension of the alkyl chain (i.e., end-to-end distance) as a function of solvent. This behavior can largely be described by the cis/trans conformation of the chain, where 2 cis-segments results in a peak at 5.9 Å, one cis-segment results in a peak at 7.0 Å and all trans-segments results in a peak at 7.6 Å.

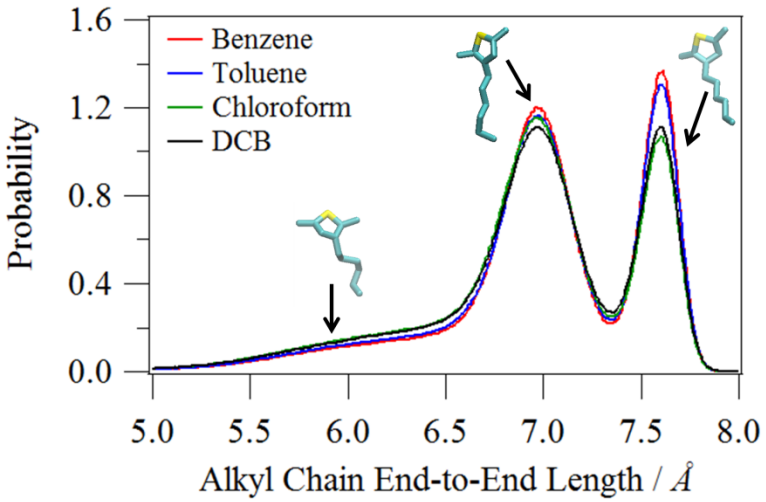

Figure 8.7. Histogram of the average end-to-end distance of the P3HT alkyl chain in different organic solvents using bin width of 0.009 Å. Inset images highlight the conformational differences.

Figure 8.7 shows that P3HT chains in benzene and toluene are more likely to have fully extended hexyl chains than P3HT in chloroform and DCB. Furthermore, P3HT in DCB and chloroform are more likely have two cis-segments in the hexyl chain than P3HT in benzene or

toluene. As described later, the hexyl-chain conformational differences may be the reason for the differences in the Kuhn length.

8.3.3 Dissolved Phase Conformation of P3ATs

In order to properly probe the conformation of isolated polymer chains, the sample must be at a sufficiently dilute concentration so that chains do not overlap or interact. Small angle neutron scattering (SANS) can be used to determine the critical overlap concentration (c^*), above which inter-chain interactions are significant. Once the value of c^* is established, the structure of individual polymers can be characterized at a concentration slightly below c^* in order to maximize signal-to-noise while still ensuring that the data is representative of isolated chains. Scattering intensities that are normalized by concentration (i.e., from a dilution series) are used to determine when substantial deviations emerge, as shown in Figure 8.8a. In addition to showing the same general shape, in the dilute limit, the curves must also be flat at low-q in order to be consistent with the form-factor of single isolated chains.[38] Aggregated polymers or samples above c^*, will usually show increasing intensity at low-q that is related to a developing structure factor (i.e., inter-chain scattering correlations).

Figure 8.8a shows a dilution series for fully dissolved P3DDT in chloroform using SANS normalized to the polymer volume fraction. Figure 8.8 shows that there are no conformational changes as a function of concentration in the range of 1-5 mg/mL. The flat low-q behavior indicates that the scattering is characteristic of single, fully dispersed chains. In contrast, the 10 mg/mL P3DDT sample shows significant deviation upon normalization indicating that polymer chains are increasingly in close proximity to one another and that the critical overlap concentration has been reached.

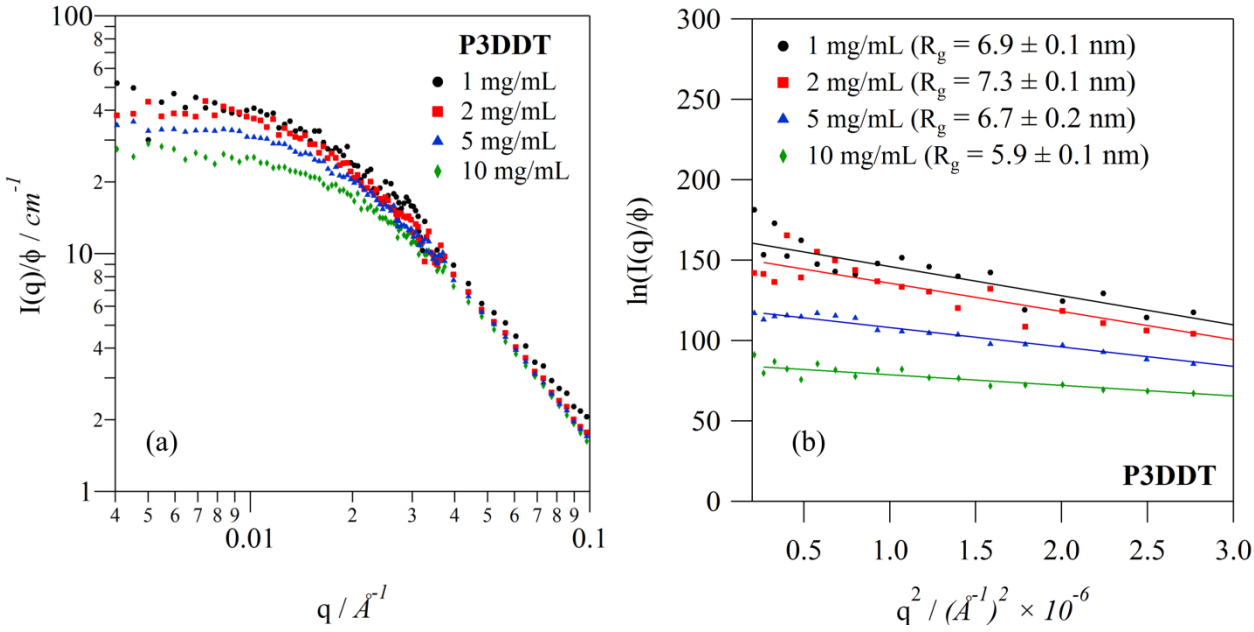

Figure 8.8. a) SANS of 1, 2, 5 and 10 mg/mL P3DDT in chloroform at 25 °C. b) Guinier plot of P3DDT in the same conditions.

According to Doi, c^* can also be determined using a calculation based on the radius of gyration (R_g), as seen in Equation 8.4:[39]

$$c^* \cong \frac{N \cdot M_{w,monomer}}{N_A \cdot R_g^{\,3}} \tag{8.4}$$

where $M_{w,monomer}$ is the molecular weight of the monomer, N_A is Avogadro's number and N is the number of statistical segments, defined as $N = L_c / b$ where L_c is the contour length (Table 8.1) and b is the Kuhn statistical segment length (Kuhn length). The radius of gyration can be determined from the slope of a Guinier plot, as shown in Figure 8.8b, using Equation 2.10. The Guinier plot shows that there is little change in the radius of gyration for samples with concentrations between 1 – 5 mg/mL. 10 mg/mL P3DDT has a slightly lower R_g, which is likely due to the close proximity of polymer chains in solution.

The polymer conformation, which encompasses the Kuhn Length (b), can be determined by fitting of 1-D SANS profiles (as seen in Figure 8.9). A model for polymers with excluded

volume interactions (Equation 2.8) can be used to represent a wide range of polymer conformations. Moreover it is also sensitive to changes in the radius of gyration (R_g) and in the Flory parameter (v), which describes the stiffness of the polymer chain (v = 0.5 for Gaussian coils and v = 1 for rod-like chains).[38, 40] Equation 8.5 can also be utilized to determine the Kuhn length.

$$R_g^{\,2} = \frac{b^2 N^{2\upsilon}}{(1+2\upsilon)(2+2\upsilon)} \tag{8.5}$$

From values for R_g and Equation 8.4 for 1, 2, 5 mg/mL P3DDT in chloroform we can determine that c^* is 12.2 ± 0.4 mg/mL. Similar experiments were also performed for all P3ATs in chloroform. The resultant c^* for P3HT, P3OT and P3EHT are 5.9 ± 2.7 mg/mL, 6.8 ± 1.3 mg/mL and 9.0 ± 1.4 mg/mL, respectively. As expected, these c^* values are directly correlated with polymer chain length (Table 8.1) because longer chains will overlap sooner when values for persistence lengths are similar. In order to maximize data quality, we evaluate conformational changes at 5 mg/mL which is still smaller than the calculated c^* of all samples.

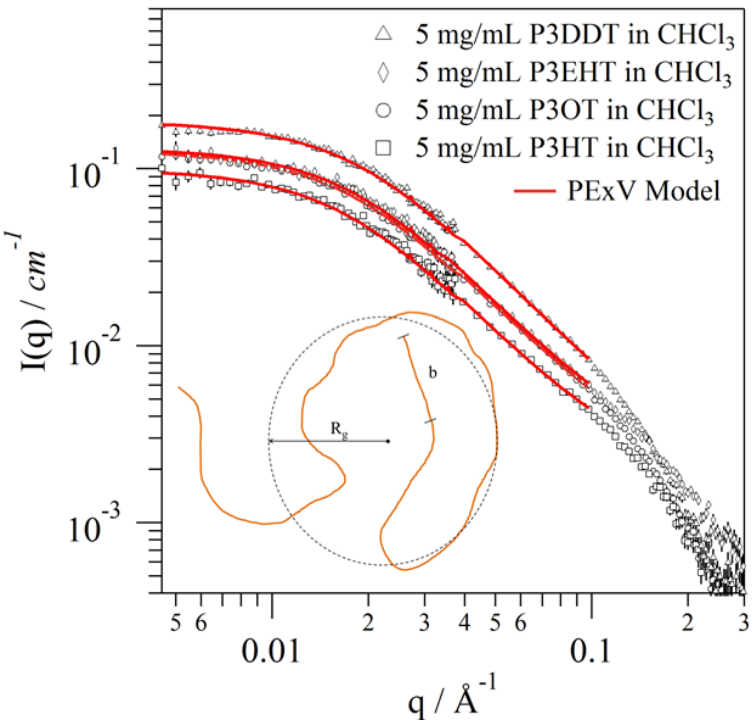

Figure 8.9. SANS profile of 5 mg/mL P3ATs in chloroform at 25 ºC fit with the model for polymers with excluded volume interactions (Equation 2.8). Inset image depicts the relevant physical properties obtained from the model.

Figure 8.9 shows SANS profiles for P3ATs in chloroform fit with the polymer excluded volume model. The polymer excluded volume model fits these scattering profiles, and all other scattering profiles, very well. Figure 8.10 shows fit parameters for fully dissolved P3ATs in different solvents at 25 °C. As expected, the R_g of the polymers scales directly with contour length such that P3HT > P3OT > P3EHT > P3DDT. However, for any given P3AT there are also evident changes in R_g as a function of solvent. For example, R_g is systematically higher for all P3ATs in benzene and toluene than it is for the same P3ATs in chlorinated solvents. The Kuhn length (b) also shows changes as a function of solvent and polymer alkyl chain structure. Some data sets (P3HT in benzene and toluene) were run at lower concentrations (2 mg/mL) to avoid crystallization occurring on the time scale of the SANS experiment. Other data sets (P3HT and P3OT in cyclohexane) could not be obtained by SANS on a time scale prior to the onset of

polymer self-assembly and crystallization because of the higher concentrations (> 1 mg/mL) required for SANS experiments.

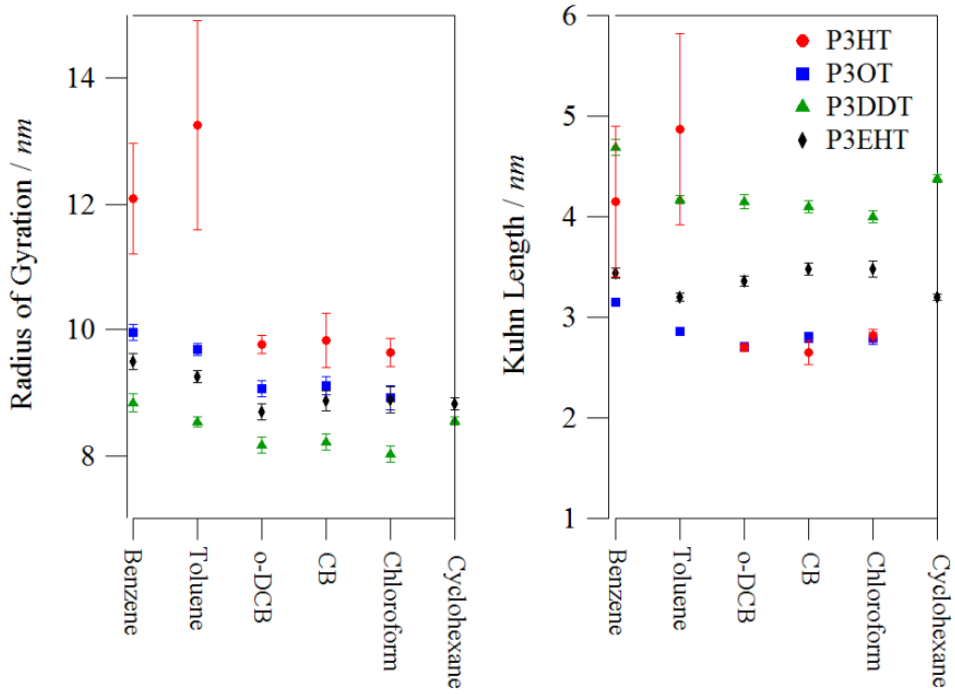

Figure 8.10. SANS profile fit results for 5 mg/mL P3OT, P3DDT and P3EHT in benzene, toluene, o-dichlorobenzene (o-DCB), chlorobenzene (CB), chloroform and cyclohexane at 25 °C. SANS profile fit results are at 2 mg/mL for P3HT in benzene and toluene and 5 mg/mL for P3HT in o-DCB, CB and chloroform at 25 °C.

8.4 Discussion

Stiffer conjugated polymers are expected to have higher conjugation lengths and red-shifted absorption profiles.[7, 11, 18, 20] This is not what our data shows. Figure 8.11a shows the Kuhn length (related to the stiffness of the polymer chain) plotted against the peak absorbance value of the polymer in the same solvent. This figure demonstrates the lack of a direct correlation between the position of the absorption peak and the polymer stiffness. It is reasonable to assume that this correlation cannot be made because the effect of the local solvent environment has not been explicitly accounted for and therefore the absorption response in Figure 8.11a is a

combination of multiple effects (e.g., possible changes in conjugation length and also changes in solvent-polymer interactions).

Traiphol and coworkers suggested that for MEH-PPV, deviations from solvatochromic models are the results of changes in polymer conformation.[10] Figure 8.11b shows the Kuhn length plotted against the deviation from the fits obtained with the Catalán method (Figure 8.4). This plot also highlights the fact that deviations from a model accounting for solvent specific effects, such as the Catalán method, cannot be automatically explained by changes in polymer stiffness. Instead, deviations from solvatochromic models are more likely due to specific polymer-solvent interactions. These interactions can arise from steric constraints (Figure 8.5) or from orientation effects (Figure 8.6). Figure 8.11 clearly demonstrates that, as an experimental technique, UV-vis absorption spectroscopy cannot be utilized independently to probe for changes in stiffness resulting from RR-P3ATs in different solvents. Though the scope of this study only includes RR-P3ATs, we expect that many of these finding can also apply to other conjugated polymers (e.g., MEH-PPV and PFO).

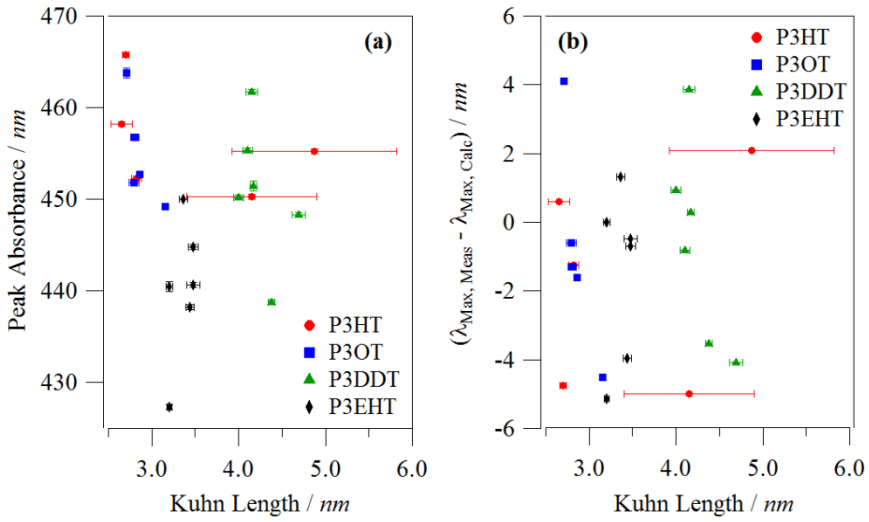

Figure 8.11. a) The peak absorbance, extracted from UV-vis, plotted against the Kuhn length, extracted from SANS model fitting, for P3ATs in benzene, toluene, chloroform, o-

dichlorobenzene, chlorobenzene and cyclohexane at 25 ºC. b) The difference between the calculated peak absorbance (Catalán method) and the measured peak absorbance for P3ATs also plotted against the Kuhn length.

Many groups have used absorption spectroscopy to probe for polymer conformational changes without explicitly accounting for effects due to changing the solvent properties (e.g., acidity, basicity, polarizability, dipolarity or size/shape).[7, 11, 18, 20] Only a few groups have accounted for and used solvent-solute interactions to explain changes in spectroscopy of conjugated polymers. Traiphol and coworkers correlate the optical shifts of MEH-PPV in various solvents to changes in solvent dielectric constant.[41] Yoshino and coworkers also correlate solvent dependent changes in P3AT peak position to the Taft parameter (π^*), which is related to solvation energy.[12] These studies accurately attribute major changes in optical properties to solvent-polymer interactions through the use of a single solvent parameter, which encompasses the solvent polarizability. However, we find that the Catalán method results in more accurate representation of the spectroscopy data. This is confirmed by fitting the Taft parameter and the dielectric constant to the absorption peak position measured in this work, which results in R^2 values of less than 0.5 (Taft parameter) and 0.2 (dielectric constant) for all P3ATs. Even though solvent polarizability accounts for the majority of the solvatochromic shift, other parameters such as basicity can play a significant role for certain solvents (as seen in Chapter 10.4).

This work also highlights the complexity of extracting the conjugation length of a polymer chain using UV-Vis spectroscopy. It is important to note that conjugation length could still perhaps be extracted from spectroscopic data by comparing to peak positions found in oligomer studies.[16, 17] However, to do this correctly it is necessary that the solvents that are used for both datasets match, or that appropriate corrections are applied for differences that arise from changing solvents. This is an important distinction because, frequently, optical studies of

oligomer are performed in chloroform and devices (e.g., OFETs and OPVs) are most often fabricated from polymer solutions in 1,2-dichlorobenzene.[16, 17] The solvent effect alone could explain the surprising result of McCulloch and coworkers where P3HT in DCB showed larger conjugation lengths than persistence lengths.[9] If one accounts for the solvent effect between the oligomer study (chloroform) and the McCulloch study (DCB) prior to calculating the conjugation length one would arrive at an estimated conjugation length that is 11% smaller than the reported value and that is also very close to the reported persistence lengths.[16, 17] This suggests that the persistence length of a conjugated polymer can still be considered an adequate upper limit for the conjugation length.

Our SANS data also shows evidence of changes in conformation and stiffness as a function of alky chain structure, even though these are poorly correlated to optical properties. The stiffness of the chain is also related to steric hindrance, the torsional energy landscape, the electronic structure of the polymer backbone and the regioregularity (RR). Because P3HT and P3OT are very similar both in RR and alkyl chain size it is not surprising that they have similar Kuhn lengths in many solvents, as seen in Figure 8.10. Figure 8.10 also shows that P3EHT has a slightly higher Kuhn length compared to P3OT and P3HT, which is likely the result of the branched side chain which leads to steric hindrance and therefore less torsional freedom for the polymer backbone. P3DDT has an even higher chain stiffness which is likely due to the large steric hindrance of the 12-carbon alkyl chain, as reported by McCulloch and coworkers.[9]

Both SANS and simulations find P3HT in toluene and benzene to have a higher Kuhn length (i.e., more stiff) than P3HT in chloroform and DCB. This result could be due to the combination of the higher solvent polarity, as suggested by Traiphol, and closer proximity of DCB and chloroform to polymer backbone (Figure 8.5).[10] However, it may also be the result of

differences in hexyl side chain flexibility (Figure 8.7). Alkyl side chains are utilized to provide entropy to an otherwise stiff and insoluble conjugated polymer backbone. Further simulations are required to determine whether the solvent interaction or the alkyl chain conformation contribute more significantly to the flexible polymer conformation. Either way, the increased rigidity of P3HT in toluene and benzene may explain why colloidal self-assembly, or crystallization, is possible in these solvents, but does not occur in chloroform and DCB. This would support the hypothesis of Rughooputh and coworkers that a rod-like polymer chain is required for self-assembly to occur.[8]

8.5 Summary

Wavelength shifts observed in absorption profiles of fully dissolved conjugated P3AT polymers can be described by changes in general solvent properties as well as specific solvent-polymer interactions and do not necessarily correlate with changes in polymer conformation. SANS shows that fully dissolved P3ATs do undergo some conformational changes as a function of solvent environment and alkyl chain structure. Molecular simulations were utilized to show that these conformational differences correlate with changes in solvent proximity to the polymer backbone as well as the flexibility of the alkyl chain. However, these conformational changes cannot be directly correlated to the observed changes in optical properties**.** Though our results do not eliminate the possibility of using absorption spectroscopy to assess changes in conjugation length, they do raise the standards necessary to unequivocally prove that conformational changes are indeed occurring. The results also motivate the need for additional studies that utilize both experiments and molecular simulations of conjugated polymers in the dissolved state to help

explain the connection between optical properties, solvent-chain interactions and chain conformation for this important class of materials.

8.5 References

1. Bronstein, H. A.; Luscombe, C. K. *Journal of the American Chemical Society* **2009,** 131, (36), 12894-12895.
2. Ren, S.; Zeng, D.; Zhong, H.; Wang, Y.; Qian, S.; Fang, Q. *The Journal of Physical Chemistry B* **2010,** 114, (32), 10374-10383.
3. Siram, R. B. K.; Stephen, M.; Ali, F.; Patil, S. *The Journal of Physical Chemistry C* **2013,** 117, (18), 9129-9136.
4. Steyrleuthner, R.; Schubert, M.; Howard, I.; Klaumünzer, B.; Schilling, K.; Chen, Z.; Saalfrank, P.; Laquai, F.; Facchetti, A.; Neher, D. *Journal of the American Chemical Society* **2012,** 134, (44), 18303-18317.
5. Berson, S.; De Bettignies, R.; Bailly, S.; Guillerez, S. *Advanced Functional Materials* **2007,** 17, (8), 1377-1384.
6. Dufresne, G.; Bouchard, J.; Belletête, M.; Durocher, G.; Leclerc, M. *Macromolecules* **2000,** 33, (22), 8252-8257.
7. Potai, R.; Kamphan, A.; Traiphol, R. *Journal of Polymer Science Part B: Polymer Physics* **2013,** 51, (17), 1288-1297.
8. Rughooputh, S. D. D. V.; Hotta, S.; Heeger, A. J.; Wudl, F. *Journal of Polymer Science Part B: Polymer Physics* **1987,** 25, (5), 1071-1078.
9. McCulloch, B.; Ho, V.; Hoarfrost, M.; Stanley, C.; Do, C.; Heller, W. T.; Segalman, R. A. *Macromolecules* **2013,** 46, (5), 1899-1907.
10. Traiphol, R.; Sanguansat, P.; Srikhirin, T.; Kerdcharoen, T.; Osotchan, T. *Macromolecules* **2006,** 39, (3), 1165-1172.
11. Salaneck, W. R.; Inganäs, O.; Thémans, B.; Nilsson, J. O.; Sjögren, B.; Österholm, J. E.; Brédas, J. L.; Svensson, S. *The Journal of Chemical Physics* **1988,** 89, (8), 4613-4619.
12. Yoshino, K.; Love, P.; Onoda, M.; Sugimoto, R.-i. *Japanese Journal of Applied Physics* **1988,** 27, (12), L2388-L2391.
13. Abboud, J.-L. M.; Notario, R. *Pure and Applied Chemistry* **1999,** 71, (4), 645-718.
14. Schwartz, B. J. *Annual Reviews of Physical Chemistry* **2003,** 54, 141-172.
15. Meier, H.; Stalmach, U.; Kolshorn, H. *Acta Polymerica* **1997,** 48, (9), 379-384.
16. Ten Hoeve, W.; Wynberg, H.; Havinga, E. E.; Meijer, E. W. *Journal of the American Chemical Society* **1991,** 113, (15), 5887-5889.
17. Thienpont, H.; Rikken, G. L. J. A.; Meijer, E. W.; ten Hoeve, W.; Wynberg, H. *Physical Review Letters* **1990,** 65, (17), 2141-2144.
18. Padmanaban, G.; Ramakrishnan, S. *Pramana - J Phys* **2003,** 61, (2), 425-434.

19. Catalán, J. *The Journal of Physical Chemistry B* **2009,** 113, (17), 5951-5960.
20. Nguyen, T.-Q.; Doan, V.; Schwartz, B. J. *The Journal of Chemical Physics* **1999,** 110, (8), 4068-4078.
21. Brinkmann, M.; Wittmann, J. C. *Advanced Materials* **2006,** 18, (7), 860-863.
22. Frisch, M. J. T., G. W.; Schlegel, H. B.; Scuseria, G. E.; Robb, M. A.; Cheeseman, J. R.; Scalmani, G.; Barone, V.; Mennucci, B.; Petersson, G. A. Gaussian 09, Revision A.1.
23. Becke, A. D. *The Journal of Chemical Physics* **1993,** 98, (7), 5648-5652.
24. Ogata, T.; Kozima, K. *Journal of Molecular Spectroscopy* **1972,** 42, (1), 38-46.
25. Hess, B.; Kutzner, C.; van der Spoel, D.; Lindahl, E. *Journal of Chemical Theory and Computation* **2008,** 4, (3), 435-447.
26. Do, K.; Huang, D. M.; Faller, R.; Moule, A. J. *Physical Chemistry Chemical Physics* **2010,** 12, (44), 14735-14739.
27. Huang, D. M.; Faller, R.; Do, K.; Moulé, A. J. *Journal of Chemical Theory and Computation* **2009,** 6, (2), 526-537.
28. Jorgensen, W. L.; Maxwell, D. S.; Tirado-Rives, J. *Journal of the American Chemical Society* **1996,** 118, (45), 11225-11236.
29. Martínez, L.; Andrade, R.; Birgin, E. G.; Martínez, J. M. *Journal of Computational Chemistry* **2009,** 30, (13), 2157-2164.
30. Bussi, G.; Donadio, D.; Parrinello, M. *The Journal of Chemical Physics* **2007,** 126, (1), 014101-7.
31. Berendsen, H. J. C.; Postma, J. P. M.; van Gunsteren, W. F.; DiNola, A.; Haak, J. R. *The Journal of Chemical Physics* **1984,** 81, (8), 3684-3690.
32. Hess, B. *Journal of Chemical Theory and Computation* **2007,** 4, (1), 116-122.
33. Bayliss, N. S.; McRae, E. G. *The Journal of Physical Chemistry* **1954,** 58, (11), 1002-1006.
34. Schwarz, K. N.; Kee, T. W.; Huang, D. M. *Nanoscale* **2013,** 5, (5), 2017-2027.
35. Duong, D. T.; Wang, C.; Antono, E.; Toney, M. F.; Salleo, A. *Organic Electronics* **2013,** 14, (5), 1330-1336.
36. Chu, J.-W.; Voth, G. A. *Proceedings of the National Academy of Sciences of the United States of America* **2005,** 102, (37), 13111-13116.
37. Pfaendtner, J.; Lyman, E.; Pollard, T. D.; Voth, G. A. *Journal of Molecular Biology* **2010,** 396, (2), 252-263.
38. Hammouda, B. *Advances in Polymer Science* **1993,** 106, 87-133.
39. Doi, M., *Introduction to Polymer Physics*. Oxford University Press: 2004.
40. Benoit, H. *Comptes Rendus Hebd Seances Acad Sci* **1957,** 245, 2244-2247.
41. Traiphol, R.; Charoenthai, N.; Srikhirin, T.; Kerdcharoen, T.; Osotchan, T.; Maturos, T. *Polymer* **2007,** 48, (3), 813-826.

Chapter 9

Conclusions and Outlook

9.1 Key Results

The active layer network structure is a crucial design parameter in the optimization of organic electronic devices (e.g., light emitting diodes, photovoltaics and field effect transistors).[1-4] In this research, we demonstrate that colloidal self-assembly and network formation is an effective means for controlling the multi-length scale structure of poly(3-alkythiophene) (P3AT) independently of the deposition method. Intermediate-stage and equilibrium-stage structure-property relationships were developed by investigating changes in self-assembly conditions (e.g., concentration, temperature and solvent environment). These results provide engineering control guidelines for the use of colloidal self-assembly and network formation as a platform for the optimization of organic electronics.

In Chapter 3, we demonstrated that multi-length scale structural differences are possible through changes in P3HT concentration and solvent environment. Colloidal self-assembly and fibrillar network formation was demonstrated for low concentrations (< 2 mg/mL) of P3HT in

aromatic solvents. Structural parameters occurring on multiple length scales (e.g., crystalline ordering, type of fibrillar junction and size of the network particles) were found to change for self-assembly in different solvents. OFET measurements were performed in order to generate structure-electrical mobility relationships. Clear structure-function correlations were observed but non-trivial structural interdependencies that exist on multiple length scales prevent the development of simple structure-property relationships. Instead, we find two specific design principles for these networks: 1) The fibrillar density of the network should be low and 2) The size of individual network particles should be large. Furthermore, we demonstrated that a multi-length scale (1 nm – 100 μm) approach to structural characterization is crucial for the development of accurate structure-property relationships. These results were published in Macromolecules in 2011.[5]

The mechanism for thermoreversible fiber formation in concentrated P3HT networks (30 mg/mL) is examined in Chapter 4. The intermediate stages of self-assembly and re-dissolution were studied using simultaneous combinations of SANS, dielectric spectroscopy and rheology. A cooling ramp was utilized to induce self-assembly and P3HT fibers in aromatic solvents were found to start thinner and grow thicker, but have a constant width during the assembly process. Conductivity and mechanical property measurements show that fiber percolation occurs almost instantaneously upon self-assembly. This was in contrast with fiber re-dissolution, during a heating ramp, where the P3HT fiber size and network properties were found to remain constant before spontaneous re-dissolution. P3HT fiber break-up was found to be the result of a thermally-activated, cooperative dissolution process. Furthermore, fibers were determined to be the favorable thermodynamic state for P3HT in aromatic solvents near room temperature. Fibrillar networks with similar nano-scale structural features were found to have a more than two

order-of-magnitude difference in conductivity when at structural equilibrium which motivates the need to better understand the network structure. These results were published in Soft Matter in 2012.[6]

In Chapter 5, we investigate the impact of the network structure on the electrical and mechanical properties of P3HT gels formed isothermally at various concentrations in aromatic solvents. The fibrillar cross-section and specific surface area of isothermal P3HT gels were found be relatively constant as a function of concentration and solvent environment. It should be noted that all gels investigated have the high surface area (i.e., 500 – 650 m^2/g) required for efficient charge separation in organic photovoltaics. Avrami theory was utilized to model the self-assembly kinetics and determine the fiber branching structure for mechanical and electrical percolation.[7] This analysis was utilized to reveal another network design parameter: increased P3HT fibrillar branching leads to better conductivities. Furthermore, these results were utilized to propose a new gelation mechanism for P3HT. We find that P3HT obeys a classic nucleation and growth process, where crystalline lattice dislocations lead branching and the formation of colloidal dispersions of isolated fiber networks. Eventually, dispersed networks grow and reach the percolation threshold to form a gel. The network structure continues to develop as new fibers grow, however these new fibers do not necessarily enhance the mechanical or electrical properties of the final gel structure. These results were published in Macromolecules in 2012.[8]

The network structure was further investigated using low volatility solvent/poor-solvent mixtures for P3AT gels in Chapter 6. We demonstrate the use of dodecane and 1,2-dichlorobenzene (DCB) allow for the gelation of a range of alkyl chain lengths and shows that increasing dodecane content leads to faster gelation kinetics. The conductive properties of P3HT, P3OT and P3DDT gels were drastically different, even though the self-assembly kinetics were

almost identical, due to insulating nature of the alkyl chain. For P3HTs and P3OT, higher non-solvent ratios could be utilized to produce more fibers which led to higher conductivities. In contrast, higher non-solvent ratios also led to more nucleation centers and therefore smaller network sizes. This competing relationship resulted in an effective maximum conductivity for the P3AT network structures. Furthermore, the low volatility of the solvent mixture allowed for thin film formation prior to gelation, which enables the interconnected network structure of P3AT gels to be utilized for organic electronic applications.

In Chapter 7, we demonstrate the feasibility to utilize P3HT networks in hybrid organic/inorganic photovoltaic (HPV) devices. A novel fabrication method was proposed, where the porous network structure of fibrillar P3HT was utilized as a template in which an n-type component can be backfilled. We shows that coating and film formation of colloidal P3HT networks does not result in aggregation and collapse upon drying. Rather, the porous fiber structure remains intact after solvent removal. In this work, zinc oxide was sputter coated over the porous P3HT structure but other backfilling methodologies were also discussed. High fiber density and line-of-sight sputtering led to poor ZnO impregnation, low interfacial organic/inorganic contact and therefore poor HPV device performance. Methods to overcome these challenges were also discussed.

The dissolved phase (i.e., prior to self-assembly and fiber formation) conformation and optical properties of P3ATs were investigated in Chapter 8. Experiments and molecular dynamics simulations show polymer conformational differences for P3HT in different solvents. P3HT in benzene and toluene (where self-assembly was observed) was found to be more rigid and extended, whereas P3HT in chloroform and DCB (where self-assembly was not observed) remain more coiled. This was due to differences in the alkyl chain conformation as well as the

molecular packing of the solvent around the polymer chain. These results show that molecular packing of solvent molecules may play a key role in controlling the self-assembly of P3ATs. Furthermore, P3AT absorption changes as a function solvent environment were investigated and modeled using the Catalán parameters.[9] Unfortunately, after a systematic investigation we determined that absorption spectrum shifts cannot be correlated to polymer conformation. These results motivate the need for additional molecular information to further understand the driving force behind conjugated polymer self-assembly in order to better control the formation of network structures.

These collective results contribute to a detailed understanding of P3AT self-assembly and network formation. We have studied each stage of the assembly process: from dissolved polymer conformation, to fiber formation, to branching and to percolation and gelation. We have demonstrated multi-length scale engineering control of the self-assembly process and shown that network design can result in multiple order of magnitude differences in mechanical and electrical properties. Furthermore, we have proposed a way to incorporate these structures directly into thin films for use in organic electronics. These results demonstrate that colloidal self-assembly and network formation is an effective platform to engineering the multi-scale structure of conjugated polymers.

9.2 Future Work

This research has laid the groundwork to demonstrate the promise of engineering specific structures of conjugated polymers. However, there are many natural follow-on projects to be pursued as a result of this work. Some of these are briefly discussed in this section.

9.2.1 Self-Assembly of Other Conjugated Polymer Chemistries

Though P3ATs are an excellent example of the potential to tune the multi-scale structure, it is crucial to expand this approach to new conjugated polymers that have better solar spectrum overlap for higher efficiencies.[1] Preliminary data towards this end has been collected in collaboration with Prof. Sam Jenekhe and Dr. Selvam Subramaniyan at the UW to utilize a new donor-acceptor (D-A) polymer that they have synthesized.[10] D-A polymers are attractive for photovoltaic work because of their facile tunability of band structure. Herein we utilize poly[(4,4'-bis(3-(2-ethyl-hexyl)dithieno[3,2-b:'',3'-d]silole)-2,6-diyl-alt-(2,5-bis(3-(2-ethyl-hexyl)thiophen-2yl)thiazolo[5,4-d]thiazole)] (PSEHTT) whose molecular structure can be seen in Figure 9.1.

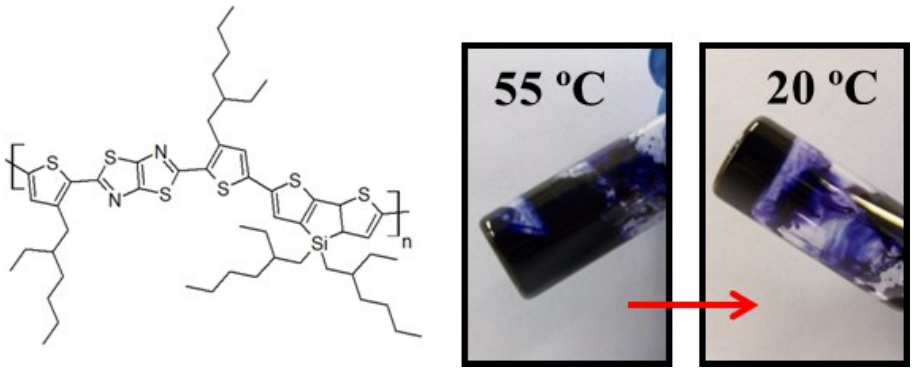

Figure 9.1. Molecular structure of donor-acceptor conjugated polymer PSEHTT and an image of a PSEHTT solution and gel formed via cooling.

Using the same solvent/poor-solvent (dodecane/o-DCB) system demonstrated for the study of P3ATs in Chapter 6, we have found that PSEHTT will self-assemble into an elastic organogel structure. Using a combination of SANS and USANS we find that the form factor of the gel is very similar to that of P3HT, as seen in Figure 9.2. Given the slopes and the apparent "knee" in the scattering profile it is expected that the form factor is a rod-like shape as opposed

to a dissolved polymer chain and therefore the profile was fit with Equation 2.6. The constant slope > -1 at low-*q* also indicates the presence of a large-scale network structure.

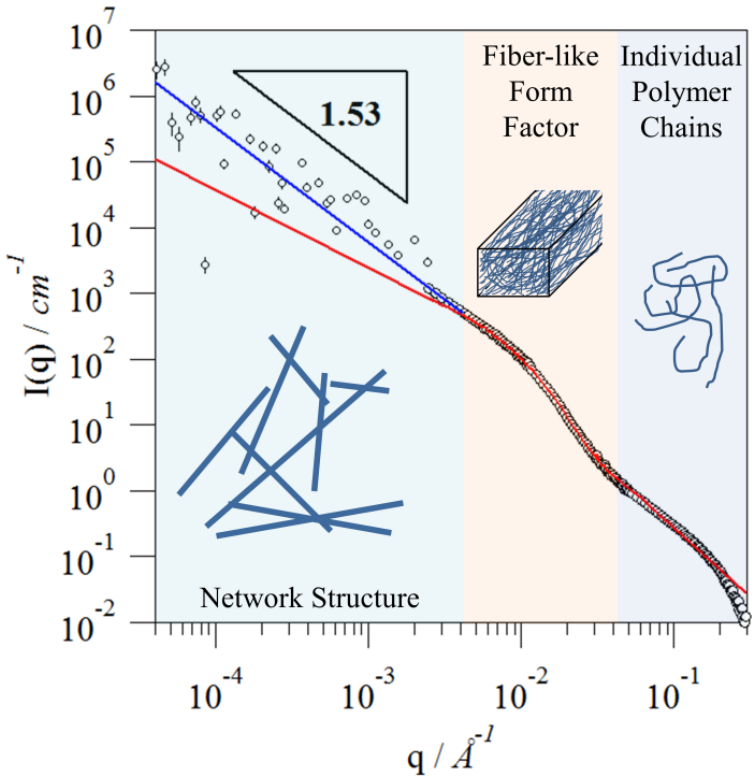

Figure 9.2. SANS and USANS profile of a 30 mg/mL PSEHTT organogel self-assembled in a 25% dodecane/75% DCB solution at 30 ºC. The red line represents an Equation 2.6 fit to the SANS data over 0.007 < *q* (Å^{-1}) < 0.3 and also extrapolated to low-q to highlight the fitting deviation. Blue line represents a power law fit (Equation 2.9) of the low-q data.

Scanning transmission electron microscopy (sTEM) images of the gel support the findings within the scattering, as seen in Figure 9.3. There appears to be fiber-like structures on the order of 50-100 nm as well as a larger network structure that spans > 1 μm.

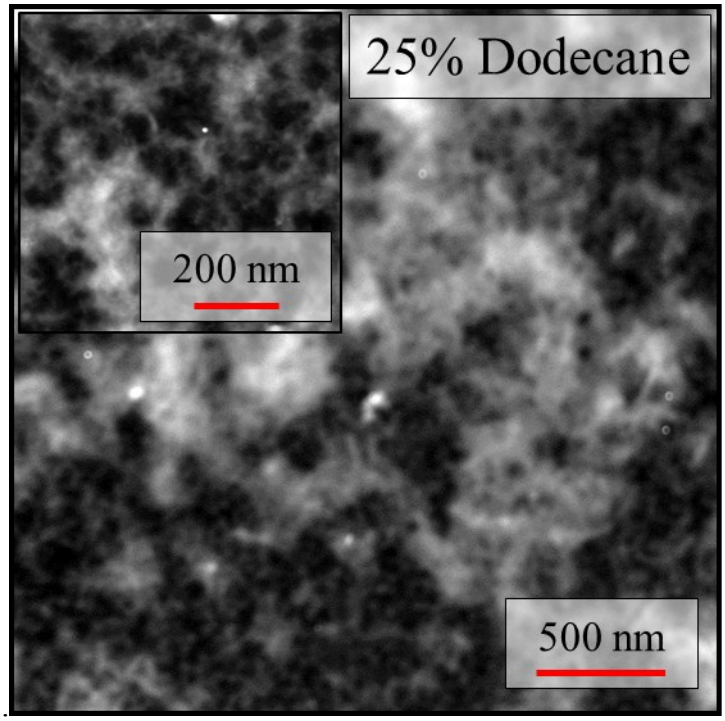

Figure 9.3. Scanning transmission electron microscope image of 30 mg/mL PSEHTT in a DCB/dodecane that were aged at room temperature for 24 hours prior to deposition on Formvar-coated grids and subsequent solvent evaporation.

This preliminary data demonstrates that it is possible to form fibrillar organogels out of more complex backbone chemistries (i.e., PSEHTT) using solvent/poor-solvent mixtures. Furthermore, the multi-length scale structural analysis developed in Chapter 2.1 also holds promise for these networks with new chemistries. Unfortunately, the conductivity of PSEHTT is reduced upon self-assembly and therefore it is not an ideal candidate for incorporation into organic electronics. Therefore, there is still a need to find other low band-gap conjugated polymers that will benefit from designed gelation and can be utilized to enhance the properties organic photovoltaic devices.

9.2.2 Self-Assembly during the Application of External Fields

Chapters 3-6 describe the self-assembly of fibrillar P3AT organogels under different conditions (i.e., concentration, temperature and solvent environment). Small changes in self-assembly conditions were shown to have a substantial effect on the multi-length scale structure and properties. Another route to control the multi-scale structure is through the application of an external field (e.g., magnetic, electrical or shear) during the self-assembly process. This could be an effective means to control fibrillar branching and network size, both of which were key design parameters for performance.

To this end, preliminary Rheo-SANS data has been collected for the self-assembly of a colloidal P3OT network in a dodecane/DCB mixture with and without shear, as seen in Figure 9.4. The plot on the right shows the intensity as a function of the azimuthal angle (ϕ) for a P3OT network. The q-range (0.008 to 0.011 $Å^{-1}$) over which the intensity is averaged corresponds to a real space length scale of 55 to 80 nm, which is larger than the fiber cross-section. The sinusoidal behavior of the P3OT network under shear indicates the partial alignment of the fibers in the direction of the shear field. Further analysis and experiments are required to understand the extent of alignment as a function of shear as well as the influence of shear on the multi-length scale structure and properties of the fiber networks.

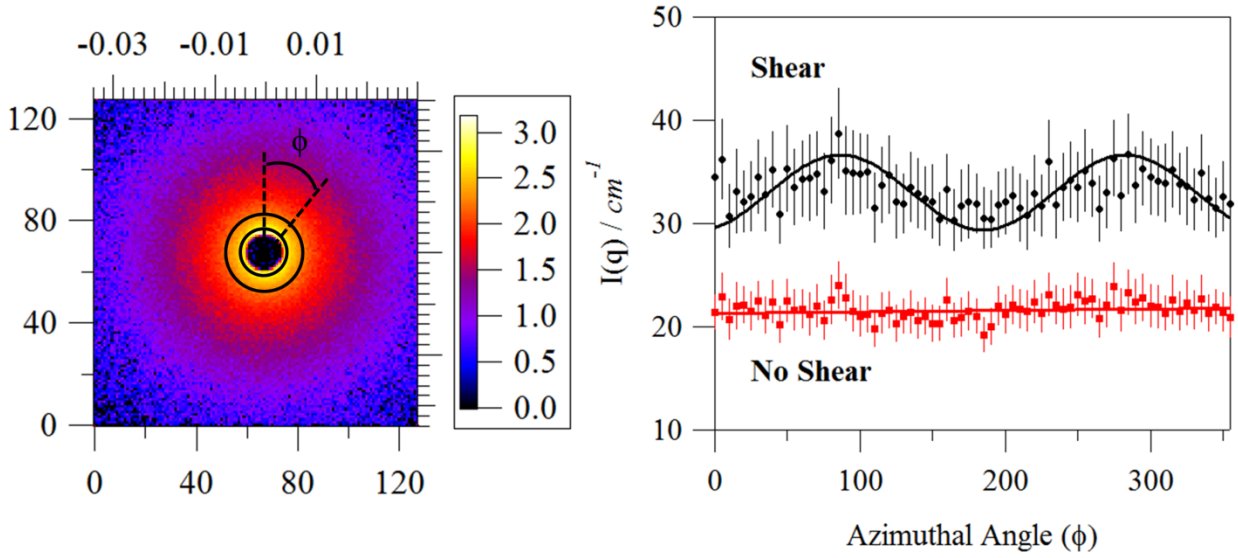

Figure 9.4. Left: 2-dimensional SANS profile for a 2 mg/mL P3OT gel during isothermal self-assembly at 20 °C. The two solid black circles indicate the q-range over which the intensity is binned as a function of the azimuthal angle (ϕ). Right: The intensity as a function of azimuthal angle during isothermal self-assembly of P3OT under shear (1000 s^{-1}) and at rest. The solid lines are data fits used to highlight the shape of the curve.

9.2.3 Self-Assembly and Doping of Network Structures

The molecular doping of conjugated polymers has been shown to increase polymer conductivity by up to 3-4 orders of magnitude compared to the un-doped state.[11, 12] This allows for similar conductive properties as doped metal oxides (e.g., ITO) and has led some researchers to utilize doped conjugated polymer thin films as charge transport layers in OLEDs.[13] Typical conjugated polymer doping is performed after thin film formation, where an ionizing gas or liquid dopant is exposed to the film to increase the conductivity.[11-13] Here we present preliminary data to demonstrate that molecular doping of P3HT is also possible in the solution phase after colloidal self-assembly and network formation. In this case, doping is made possible through the addition of $AuCl_3$ to isopropanol, which is then added to a pure nanofibers solution. However, it should be noted that there are many solution phase dopants (e.g., metal ions and sulfonic acids) that could be utilized towards a similar end.

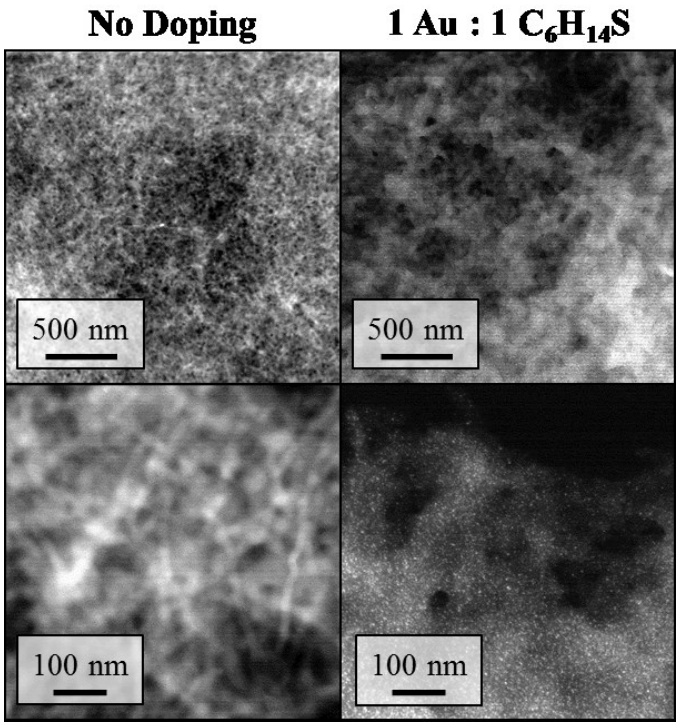

Figure 9.5. Scanning TEM images of 0.12 mg/mL P3HT nanofibers networks formed in p-xylene with (right) and without (left) solution phase doping (1:1 molar ratio) with $AuCl_3$.

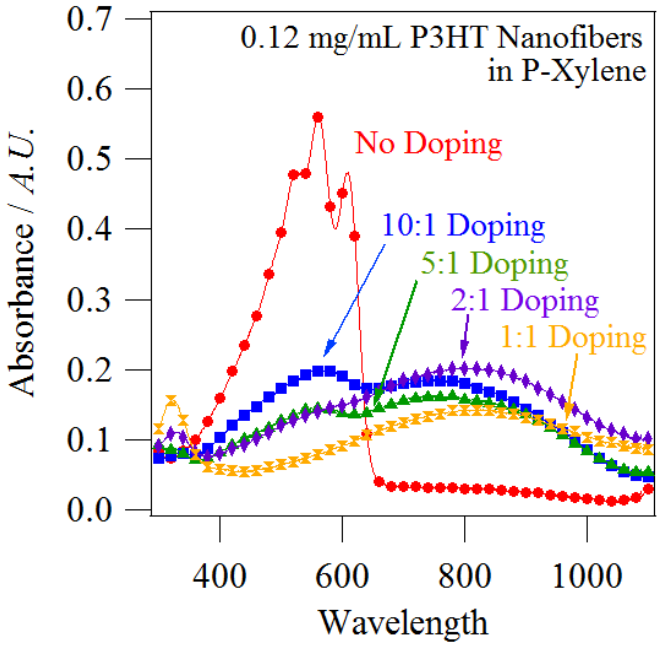

Figure 9.6. UV-vis absorption profiles of 0.12 mg/mL P3HT nanofibers networks in p-xylene at different $AuCl_3$ molar doping ratios.

Figure 9.5 shows TEM images of a P3HT nanofiber solution before and after doping with $AuCl_3$. In this case, solution phase doping results in the aggregation of fibrillar domains as insoluble (in p-xylene) $AuCl_3$ attaches to dispersed P3HT fibers. It may be possible to reduce fiber aggregation by doping with sparingly soluble ions instead of $AuCl_3$. At high magnification, discrete metal nanoparticles can be seen attached to the fibrillar P3HT network indicating that large scale phase segregation does not occur. Furthermore, $AuCl_3$ doping results in an optical transition seen in Figure 9.6. This figure shows a decrease in the absorbance of the classic P3HT nanofiber peaks with increase $AuCl_3$ molar ratio. There is also the rise of a new absorbance band near 800 nm. This "leveling" effect in the absorbance profile enables the application of these materials as translucent conductors. Future work should include conductivity measurements as a function of doping concentration as well as the exploration of different dopant molecules. Furthermore, these materials should be incorporated into composite coatings for semi-transparent, anti-static applications.

9.2.4 Conjugated Polymer Networks in Organic Electronic Devices

Chapters 3 & 7 focused on the application of dilute conjugated polymer networks in organic field effect transistors and photovoltaic devices, respectively. In Chapter 6, we developed a new method for the fabrication of thin film organogels. However, the structure-property relationships discussed in this thesis have not been systematically applied to the optimization of organic electronic devices. Moving forward, there is a substantial need to demonstrate that these new methods for designing network structures can enhance or compete with the current performance of P3HT-based organic electronic devices. For OFETs, the highest reported mobility is near 0.1 V/cm^2 s and the highest reported P3HT-PCBM OPV device has a power conversion efficiency near 5%.[14, 15] The primary hurdle towards OPV device fabrication

utilizing the methods described in Chapter 6 is the incorporation of PCBM into the interstitial space of the network structure. One strategy to overcome this would be the back-diffusion of PCBM into the porous fiber structure as performed by Huang and coworkers.[16] Another option would be the self-assembly of P3AT gels in the presence of PCBM, as demonstrated Sobkowicz and coworkers, towards the fabrication of thin film OPVs.[17] Ultimately, this work will need to utilize the structure-property relationships developed for bulk gels as well as develop new relationships specific for the self-assembly in confined thin-film environments.

9.3 References

1. Yang, X. N.; Loos, J.; Veenstra, S. C.; Verhees, W. J. H.; Wienk, M. M.; Kroon, J. M.; Michels, M. A. J.; Janssen, R. A. J. *Nano Letters* **2005,** 5, (4), 579-583.
2. Halls, J., Walsh, CA, Greenham, NC, Marseglia, EA, Friend, RH, Moratti, SC, Holmes, AB. *Nature* **1995,** 376, 498-500.
3. Yu, G.; Gao, J.; Hummelen, J. C.; Wudl, F.; Heeger, A. J. *Science* **1995,** 270, (5243), 1789-1791.
4. Yu, G.; Heeger, A. J. *Journal of Applied Physics* **1995,** 78, (7), 4510-4515.
5. Newbloom, G. M.; Kim, F. S.; Jenekhe, S. A.; Pozzo, D. C. *Macromolecules* **2011,** 44, (10), 3801-3809.
6. Newbloom, G. M.; Weigandt, K. M.; Pozzo, D. C. *Soft Matter* **2012,** 8, (34), 8854-8864.
7. Avrami, M. *Journal of Chemical Physics* **1939,** 7, 1103-1112.
8. Newbloom, G. M.; Weigandt, K. M.; Pozzo, D. C. *Macromolecules* **2012,** 45, (8), 3452-3462.
9. Catalán, J. *The Journal of Physical Chemistry B* **2009,** 113, (17), 5951-5960.
10. Subramaniyan, S.; Xin, H.; Kim, F. S.; Shoaee, S.; Durrant, J. R.; Jenekhe, S. A. *Advanced Energy Materials* **2011,** 1, (5), 854-860.
11. Pingel, P.; Neher, D. *Physical Review B* **2013,** 87, (11), 115209-9.
12. Tashiro, K.; Kobayashi, M.; Kawai, T.; Yoshino, K. *Polymer* **1997,** 38, (12), 2867-2879.
13. Gross, M.; Muller, D. C.; Nothofer, H.-G.; Scherf, U.; Neher, D.; Brauchle, C.; Meerholz, K. *Nature* **2000,** 405, (6787), 661-665.
14. Yang, H.; LeFevre, S. W.; Ryu, C. Y.; Bao, Z. *Applied Physics Letters* **2007,** 90, (17), 661-665.
15. Ma, W.; Yang, C.; Gong, X.; Lee, K.; Heeger, A. J. *Advanced Functional Materials* **2005,** 15, (10), 1617-1622.

16. Huang, P.-T.; Chang, Y.-S.; Chou, C.-W. *Journal of Applied Polymer Science* **2011,** 122, 233-240.
17. Sobkowicz, M. J.; Jones, R. L.; Kline, R. J.; DeLongchamp, D. M. *Macromolecules* **2011,** 45, (2), 1046-1055.

Chapter 10

Supporting Information

10.1 Scattering Length Density Calculations

The scattering length density (SLD) is a critically important physical parameter for fitting of neutron scattering data. The SLD contrast ($\Delta\rho$) between different phases (e.g., fibrillar P3HT vs. solvent) is directly related to the scattering intensity as described in Chapter 2.1.4. The SLD can be easily calculated if the density and molecular formula of each material are precisely known (Equation 2.5). This is simple for fully dissolved P3ATs, as seen in Table 10.1.

Table 10.1. Molecular formula, density (ρ_m) and scattering length density (ρ_{SLD}) for poly(3-hexylthiophene) (P3HT), poly(3-octylthiophene) (P3OT), poly(3-(2-ethylhexyl)thiophene) (P3EHT) and poly(3-dodecylthiophene) (P3DDT). The mass density of P3HT, P3OT and P3DDT were determined by Prosa et al. and P3EHT was estimated to be similar to P3OT.[1]

	Molecular Formula	ρ_m **(g/cm^3)**	ρ_{SLD} **(Å^{-2})**
P3HT	$C_{10}H_{14}S$	1.10	6.76×10^{-7}
P3OT	$C_{12}H_{18}S$	1.02	4.83×10^{-7}
P3EHT	$C_{12}H_{18}S$	1.02	4.83×10^{-7}
P3DDT	$C_{16}H_{26}S$	1.01	2.90×10^{-7}

Unfortunately, there are too many discrepancies between the reported densities of fibrillar P3HT in the literature with values ranging between 1.1 and 1.3 g/cm^3.[1-4] Therefore, we performed a careful contrast variation experiment to determine the SLD of P3AT gels in all of our solvent systems. In all experiments, the isotopic composition of the solvent was changed in order to vary the SLD contrast between the two phases. The SLD of fibrillar P3ATs were determined from a linear fit of the square-root of the intensity, at low-*q*, as a function of the SLD of the solvent phase.

For the data presented in Chapter 3-5, the SLD of P3HT fibers was determined to be 1.1 ± 0.2 × 10^{-6} Å^{-2} with little variability between solvents (i.e., benzene, toluene and p-xylene) as seen in Figure 10.1. Given the known atomic composition of P3HT, the corresponding mass density for a P3HT fiber to yield this SLD would have to be 1.75 g/cm^3. This value is much larger than any published report. Therefore, it is likely that another factor must be causing the SLD of the fibers to be much larger than expected. With an Anton Paar DMA 35 density meter, we measured the mass density of extracted fibers and obtained a value of 1.1 g/cm^3 that is nearly identical to other published values.[4] This suggests that there is likely a considerable amount of deuterated solvent incorporated within the volume of the P3HT fibers. If one assumes the density of solid P3HT to be 1.1 g/cm^3, then the fibers in the organogel would contain approximately 11 wt% of entrained solvent. This correctly accounts for the higher SLD value of P3HT fibers in the gel when compared reports from neutron reflectivity for solid thin films of P3HT or from density and atomic composition (be 0.676 × 10^{-6} Å^{-2}).[3, 5, 6] This contrast variation experiment verifies that P3HT fibers within solvated gels contain semi-crystalline domains as well as entrained solvent. [7-10]

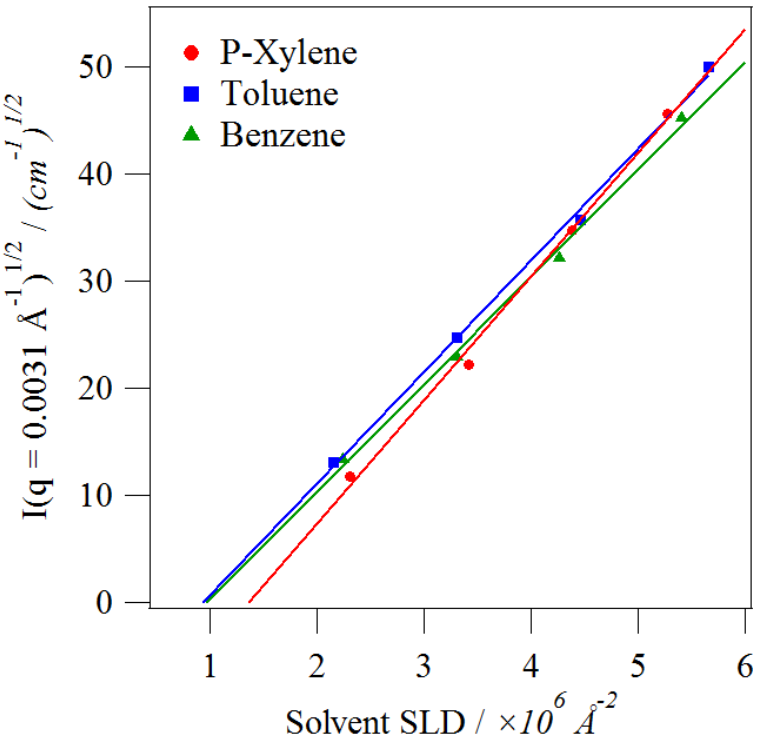

Figure 10.1. Square-root SANS intensity plotted against the scattering length density of solvents for a 30 mg/mL P3HT gel.

The scattering length density (SLD) of P3AT fibers was also determined by doing a contrast variation experiment for the polymers used in Chapter 6. Figure 10.2 shows the SANS contrast variation experiment of P3AT organogels self-assembled in different dodecane/1,2-dichlorobenzene solvent mixtures where d4-1,2-dichlorobenzene was utilized while the ratio of deuterated/hydrogenated dodecane was varied before self-assembly. The SLD of each solvent mixture was determined from predicted densities and the molecular composition. The square-root intensity ($I^{1/2}$) at a q-value (0.0031 Å^{-1}) is plotted against the SLD and fit to find the zero-contrast point, which is equivalent to the SLD of the organogel.[11] The SLD of high M_w P3HT gels in different solvent mixtures can also be seen in Figure 10.2 and show little difference in the zero-contrast point.

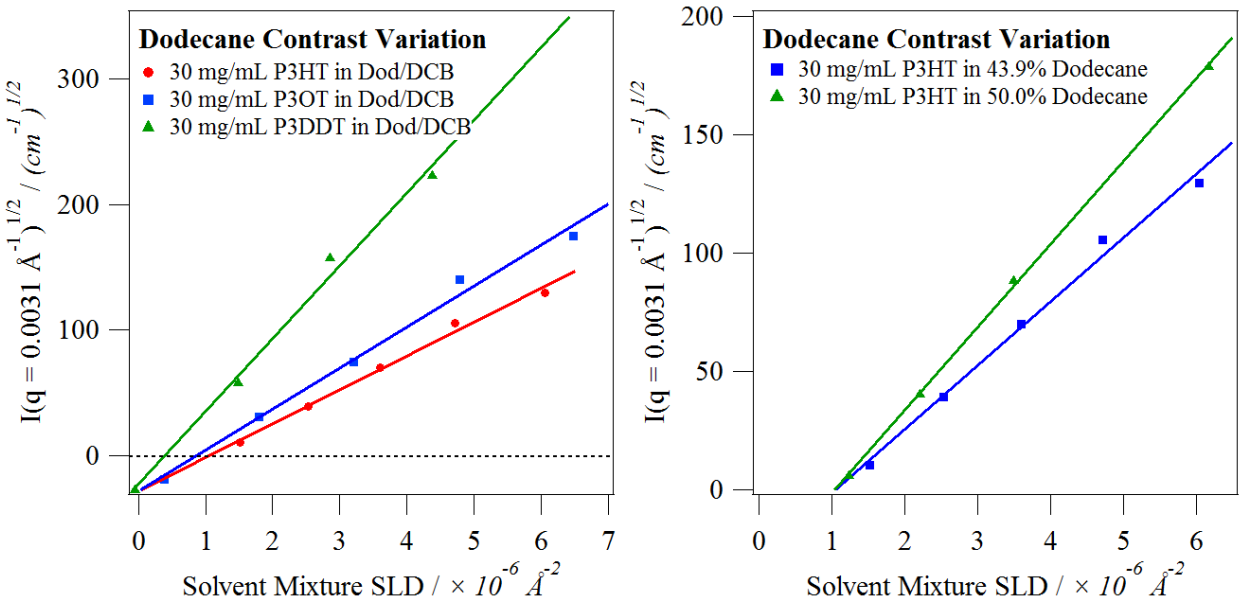

Figure 10.2. Square-root SANS intensity plotted against the scattering length density of a d26-dodecane/d4-1,2-dichlorobenzene solvent mixture for a 30 mg/mL high M_w P3HT gel in 43.9 wt% dodecane/56.1 wt% DCB, 30 mg/mL P3OT gel in 71.3 wt% dodecane/28.7 wt% DCB and 30 mg/mL P3DDT gel in 84.7 wt% dodecane/15.3 wt% DCB (left) and for a 30 mg/mL high M_w P3HT gel in two solvent mixtures: 50.0 wt% dodecane/50.0 wt% DCB and 43.9 wt% dodecane/56.1 wt% DCB (right). All measurements were taken at 20 °C.

The measured SLD values for solvated P3HT, P3OT and P3DDT fibers were 1.1 × 10^{-6} Å^{-2}, 0.9 × 10^{-6} Å^{-2} and 0.4 × 10^{-6} Å^{-2}, respectively. The SLD values correspond to fibers that contain ~14 wt% dichlorobenzene (High M_w P3HT and P3OT) or 5 wt% (P3DDT). Furthermore, there is no correlation between fiber SLD and solvent ratio, suggesting that solvent incorporation is limited by steric packing interactions as proposed by Zuo and coworkers.[10] Figure 10.2 also shows similar zero contrast points for P3HT in different dodecane/DCB ratios. This suggests that the amount of DCB in the fibers is identical, even though the solvent ratios differ. Furthermore, the SLD of P3HT fibers in aromatic solvents (e.g., benzene) is similar to that of P3HT fibers in mixed solvents.

The mass density ($\rho^{m}_{Solvent}$) is directly related to molecular volume and therefore the temperature dependence of mass density will play a role in the scattering length density for the

experiments in Chapter 4. The mass density of d10-pxylene, d8-toluene and d6-benzene was measured as a function of temperature using an Anton Paar DMA 5000 Density Meter and then converted to scattering length density, seen in Figure 10.3. This temperature dependence was accounted for during SANS data fitting to ensure the accuracy of other fitting parameters. The mass density of the hydrogenated dodecane/DCB solvent mixtures is also shown in Figure 10.4.

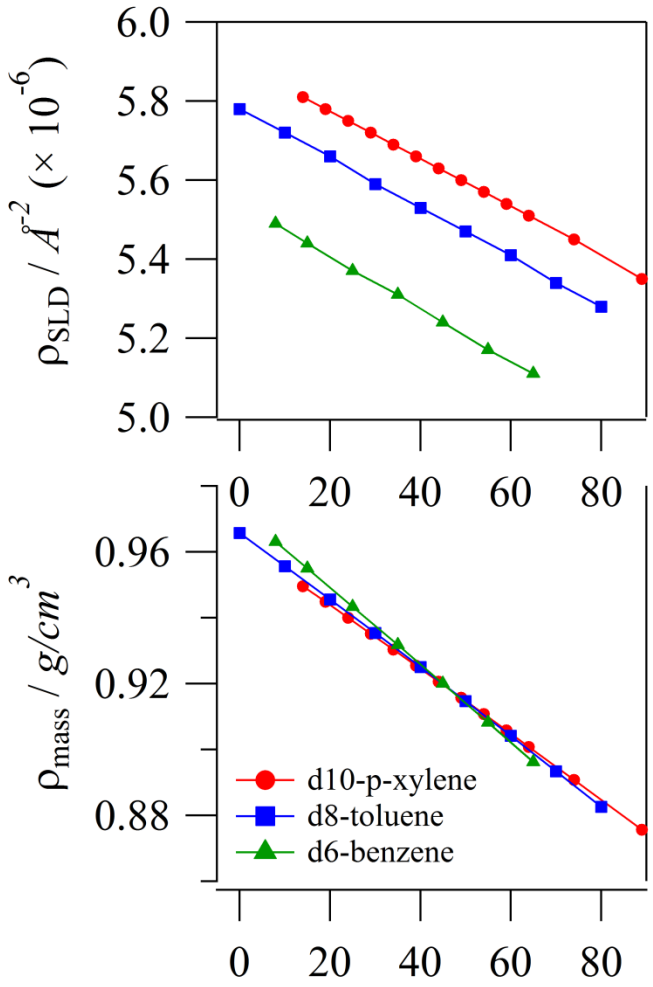

Figure 10.3. The temperature dependence on the measured mass density and subsequently calculated scattering length density of d10-p-xylene (d > 98%), d8-toluene (d > 99.5%) and d6-benzene (d > 99.5%).

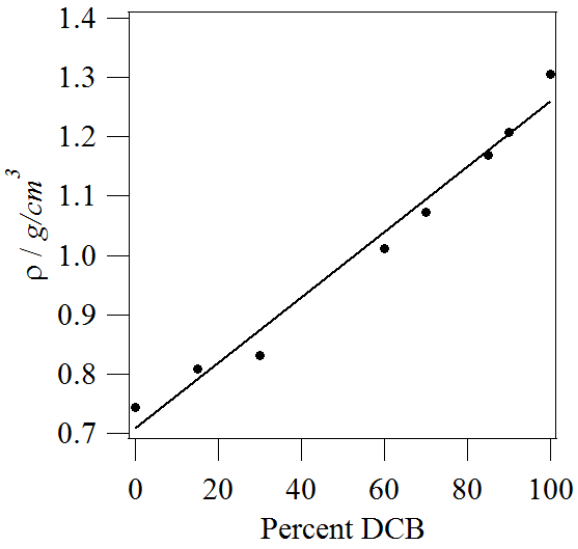

Figure 10.4. The measured mass density of hydrogenated mixtures of dodecane and 1,2-dichlorobenzene at 20 ºC.

10.2 Porod Analysis for Chapter 4

The specific surface area (S_v) for the fibers was calculated using the Porod equation as described in Chapter 2.1.3. The scattering invariant (Q) can be utilized to determine fiber volume fractions (ϕ_{fiber}) when calculating the specific surface area.[9] The volume fraction of fibers can also be determined from model fitting, where $\phi_{fiber} = \phi_v \cdot \Psi_f$, and the difference between these independent methods is less than 10%. Herein, the scattering invariant is utilized for all S_v calculations.

The Porod analysis requires that the system is composed of two phases (i.e. solvent and fibers) with a sharp interface that results in an intensity dependence of $I(q) \propto q^{-4}$ at high-q. At the intermediate stages of gelation, the amount of dissolved polymer is not negligible and it contributes significantly to the scattering intensity at high-q. This occurs because the evolving P3HT gel is effectively a three-component system containing solvent, P3HT fibers and dissolved P3HT chains. In order to find the specific surface area (S_v) of the P3HT fiber, the scattering due

to the dissolved polymer must first be subtracted. The scattering of the fully dissolved polymer, at elevated temperatures (40 ºC to 80 ºC), was fit with a model for polymers with excluded volume interactions to determine the molecular weight and conformation in solution (Equation 2.8). The mass balance presented in Equation 2.6 can then be utilized to determine the fraction of P3HT in dissolved form $(1-\Psi_f)$. The model for polymers with excluded volume interactions can be scaled by this factor and subtracted from the combined SANS profile to yield the scattering corresponding only to P3HT fibers.

Figure 10.5 shows the SANS profile for 30 mg/mL P3HT in toluene at a specific temperature (10.6 ºC) during the gelation of P3HT. The fraction of P3HT in fiber from (Ψ_f) was determined to be 0.419 by fitting Equation 2.6 to the SANS profile. This leads to a dissolved fraction $(1-\Psi_f)$ of 0.581 at the same temperature. The total scattering as a function of q due to the dissolved polymer alone can be determined by scaling the model for polymers with excluded volume interactions (Equation 2.8) by the dissolved fraction. The result can be seen in Figure 10.5a. The 1D SANS profile is a linear combination of the dissolved polymer phase and the fiber phase, so we can directly subtract the scaled dissolved polymer model from the "fiber + dissolved" polymer scattering to generate the scattering due to P3HT fibers alone. This subtraction is shown to generate the expected $I(q) \propto q^{-4}$ dependence for P3HT fibers, as seen in Figure 10.5a. We find this same result to be true at earlier stages in gelation, to Ψ_f as low as 0.03. This behavior is shown as a function of gelation progress (i.e. temperature) in Figure 10.5b which highlights the $I(q) \alpha q^{-4}$ dependence.

After the dissolved polymer is subtracted, the scattering invariant (Q) can be utilized to directly calculate the fiber volume fraction (ϕ_{fiber}). The invariant can be utilized with minimal

assumptions and regardless of the shape of the scattering object. At low-q, the slope associated with the network structure of P3HT gels (seen in Figure 10.5a) has to be extrapolated to $q = 0$ but the extrapolation only accounts for < 0.5% of the total scattering invariant (Q). At high-q, the $I \propto q^{-4}$ dependence associated with the Porod slope (seen in Figure 3.6) is also extrapolated to $q \rightarrow \infty$ and this accounts for ~ 7% of the total invariant. This means that ~ 93% of the scattering invariant (Q) is directly accounted for in the SANS profile, leading to low error in the calculation of the volume fraction of fibers (ϕ_{fiber}).

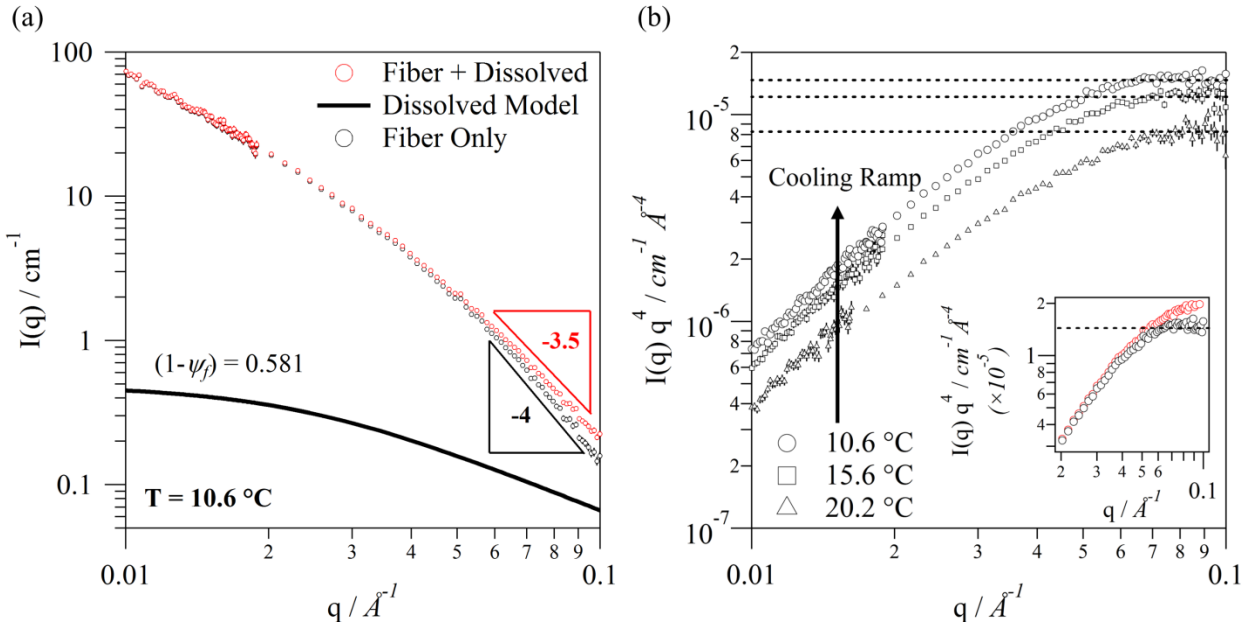

Figure 10.5. (a) SANS profiles from the cooling ramp and gelation of 30 mg/mL P3HT in d8-toluene at 10.6 ºC. "Fiber + dissolved" (i.e. unmodified scattering) is represented by ○, the polymer excluded volume model scaled by $(1-\Psi_f)$ is represented by —, and the "fiber only" is represented by ○. At high-q, the difference between the "fiber + dissolved" scattering slope and the "fiber only" slope is compared. (b) The $I(q) \sim q^{-4}$ is evaluated for multiple "fiber only" SANS profiles at differing temperatures from the same cooling ramp. The horizontal dashed lines represent the values extracted for the Porod analysis. The inset figure highlights the differences at high-q for 10.6 ºC scattering for "fiber + dissolved" and "fiber only" scattering.

10.3 P3AT Polymer Synthesis for Chapter 8

All materials were purchased from Sigma Aldrich and were used without further purification unless specified otherwise. Tetrahydrofuran (THF) was dried using a solvent drying system from Innovative Technologies. 2-Bromo-5-iodo-3-hexylthiophene, 2-Bromo-5-iodo-3-octylthiophene, 2-Bromo-5-iodo-3-dodecylthiophene and 2-Bromo-5-iodo-3-(2-ethylhexyl)thiophene were all synthesized according to previously established procedures.[12] The synthesis of the four polymers, used in Chapter 8, was performed according to previously reported procedure by Prakash Sista and Hoi-Ki Cheung from Christine Luscombe's lab.[13] A typical synthetic procedure for the four polymers is described below and was written by Prakash Sista.

Synthesis of Poly(3-hexylthiophene) (P3HT). 2-Bromo-5-iodo-3-hexylthiophene (1.123 g, 3.011 mmol) was added to a schlenk flask maintained in N_2 atmosphere. 30 mL of anhydrous THF was added to the flask and the flask was immersed into an ice bath to cool the contents to 0 °C. Isopropyl magnesium chloride (1.50 mL, 3.01 mmol) was added drop-wise and the contents of the flask were stirred for an hour. At this time, the synthesized initiator cis-chloro(tolyl)(dppp)nickel(II) solution (0.0199 mmol) was added quickly to the reaction flask under rapid stirring and subsequently the ice bath was removed. The reaction flask was warmed slightly to keep the growing polymer in solution. The polymer starts precipitating out after 30 minutes, when the reaction was quenched by the addition of 6 M HCl and the polymer was precipitated out in methanol. The polymer was purified by consecutive soxhlet extractions in methanol, hexanes and chloroform. The chloroform fraction was concentrated by solvent evaporation under reduced pressure to obtain a reddish brown solid. (Yield 80 %). M_n = 37.6

kg/mol, *PDI* = 1.26; ^{1}H NMR ($CDCl_3$, 300 MHz) δ 7.61 (m, 2H), 6.98 (s, 1H), 6.91(m, 2H), 2.80 (t, 2H), 2.49 (s, 3H), 1.71 (m, 2H), 1.44(m, 2H), 1.35(m, 4H), 0.91 (t, 3H)

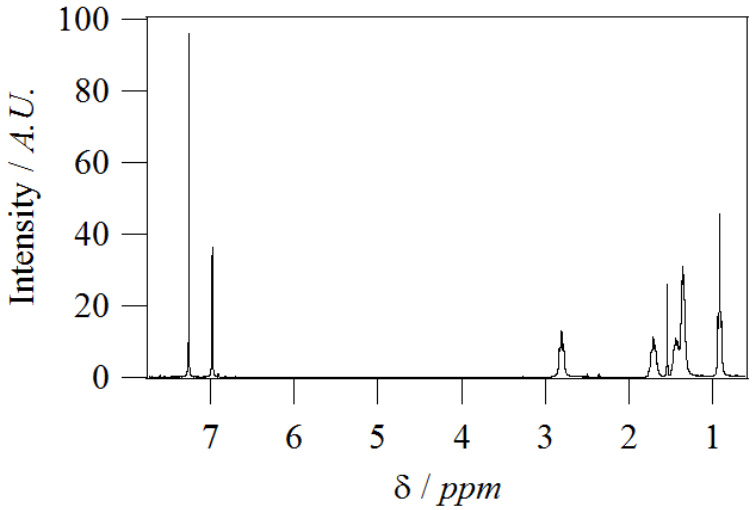

Figure 10.6. ^{1}H NMR spectrum of poly(3-hexylthiophene) (P3HT)

Synthesis of Poly(3-octylthiophene) (P3OT). The synthetic procedure adopted for the synthesis of poly(3-octylthiophene) was similar to that of poly(3-hexylthiophene). After the addition of the initiator cis-chloro(tolyl)(dppp)nickel(II) to a solution of 5-chloromagnesio-2-bromo-3-octylthiophene, the reaction was allowed to proceed at room temperature for three hours under nitrogen atmosphere. The reaction was then quenched by the addition of 6 M HCl and the polymer was precipitated out in methanol. The polymer was purified by consecutive soxhlet extractions in methanol, hexanes and chloroform. The chloroform fraction was concentrated by solvent evaporation under reduced pressure to obtain a reddish brown solid. (Yield 79.7 %). M_n = 42.5 kg/mol, *PDI* = 1.23; ^{1}H NMR ($CDCl_3$, 300 MHz) δ 7.61 (m, 2H), 6.98 (s, 1H), 6.91(m, 2H), 2.80 (t, 2H), 2.49 (s, 3H), 1.71 (m, 2H), 1.43(m, 2H), 1.29(m, 4H), 0.88 (t, 3H)

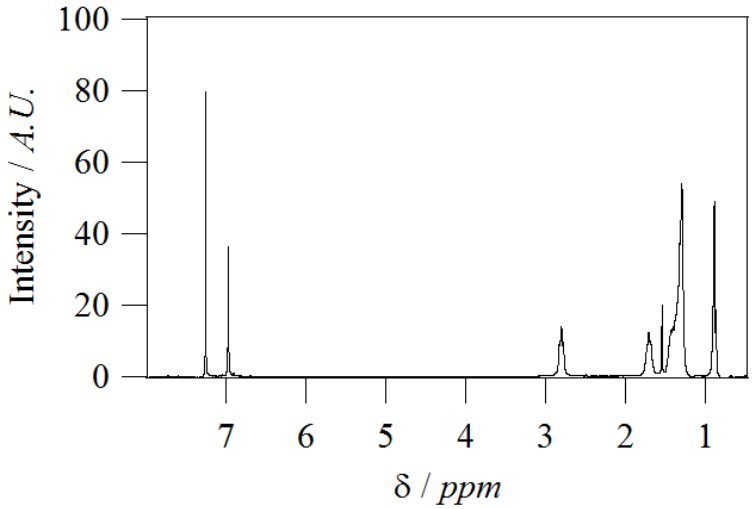

Figure 10.7. ^{1}H NMR of poly(3-octylthiophene) (P3OT)

Synthesis of Poly(3-dodecylthiophene) (P3DDT). The synthetic procedure adopted for the synthesis of poly(3-dodecylthiophene) was similar to that of poly(3-hexylthiophene). After the addition of the initiator cis-chloro(tolyl)(dppp)nickel(II) to a solution of 5-chloromagnesio-2-bromo-3-dodecylthiophene, the reaction was allowed to proceed overnight at room temperature under nitrogen atmosphere. The reaction was then quenched by the addition of 6 M HCl and the polymer was precipitated out in methanol. The polymer was purified by consecutive soxhlet extractions in methanol, hexanes and chloroform. The chloroform fraction was concentrated by solvent evaporation under reduced pressure to obtain a reddish brown solid. (Yield 63.7%). M_n = 38.7 kg/mol, *PDI* = 1.27; ^{1}H NMR ($CDCl_3$, 300 MHz) δ 7.61 (m, 2H), 6.98 (s, 1H), 6.91(m, 2H), 2.80 (t, 2H), 2.49 (s, 3H), 1.70 (m, 2H), 1.26 (m, 6H), 0.87 (t, 3H)

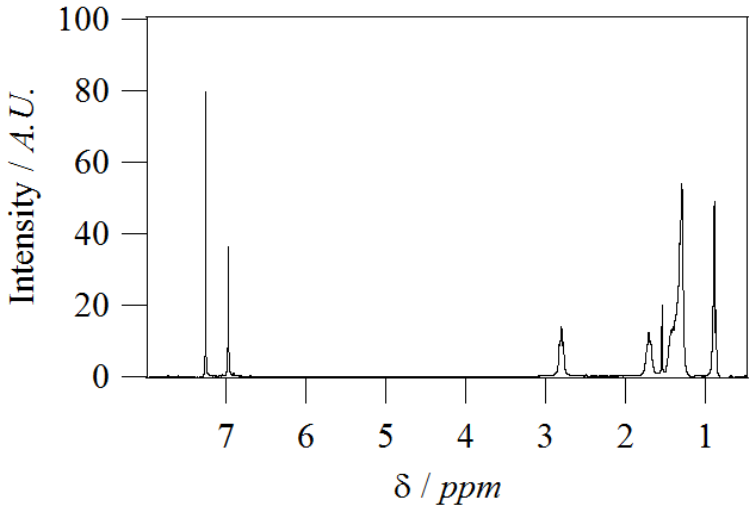

Figure 10.8. ^{1}H NMR of poly(3-dodecylthiophene) (P3DDT)

Synthesis of Poly(3-(2-ethylhexyl)thiophene) (P3EHT). The synthetic procedure adopted for the synthesis of poly(3-(2-ethylhexyl)thiophene) was similar to that of poly(3-hexylthiophene). After the addition of the initiator cis-chloro(tolyl)(dppp)nickel(II) to a solution of 5-chloromagnesio-2-bromo-3-(2-ethylhexyl)thiophene, the reaction was allowed to react at 1.5 hours at room temperature. The reaction was then performed at 35 °C overnight under nitrogen atmosphere. The reaction was quenched by the addition of 6 M HCl and the polymer was precipitated out in methanol. The polymer was purified by consecutive soxhlet extractions in methanol, hexanes and chloroform. The chloroform fraction was concentrated by solvent evaporation under reduced pressure to obtain a reddish solid. (Yield 53.1%). M_n = 35.3 kg/mol, *PDI* = 1.26; ^{1}H NMR ($CDCl_3$, 300 MHz) δ 7.61 (m, 2H), 6.94 (s, 1H), 6.88 (m, 2H), 2.73 (d, 2H), 2.49 (s, 3H), 1.70 (m, 1H), 1.29 (m, 8H), 0.88 (t, 6H).

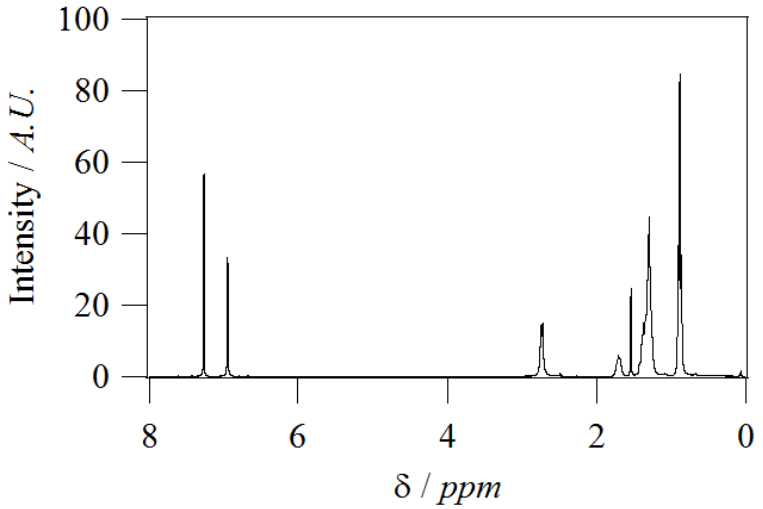

Figure 10.9. [1]H NMR of poly(3-(2-ethylhexyl)thiophene) (P3EHT)

[1]H NMR spectra were recorded on Bruker Avance AV-300 spectrometer using CDCl3 as a solvent. Molecular weights of the polymers were determined using a Viscotek TDA 305 with polystyrene standards at room temperature with THF as the eluent and at a flow rate of 1.0 mg/mL.

10.4 Catalán Fitting Parameters for Chapter 8

Table 10.2 shows the multi-linear regression coefficients for the Catalán solvent parameters based on P3ATs in 14 different solvents. Table 10.3 shows the magnitude of the solvatochromic shifts for P3ATs in different organic solvents.

Table 10.2. Fitting values to characterize the solvent effect on P3ATs where A_0 is the absorbance of the polymer in the gas phase and *b*, *c*, *d* and *e* are the multi-linear regression coefficients related to SA, SB, SP and SdP, respectively. All values have units in nanometers.

Polymer	***A₀***	***b (SP)***	***c (SdP)***	***d (SA)***	***e (SB)***
P3HT	378 ± 14	98.1 ± 18.0	0.3 ± 6.3	-8.8 ± 70.0	-1.2 ± 6.5
P3OT	387 ± 18	83.2 ± 23.5	5.1 ± 8.3	-56.9 ± 90.3	-6.7 ± 8.4
P3DDT	387 ± 17	82.7 ± 22.2	3.2 ± 8.0	-57.1 ± 85.7	-7.4 ± 8.0
P3EHT	373 ± 16	87.0 ± 13.0	0.7 ± 7.2	-6.0 ± 78.9	1.3 ± 7.3

Table 10.3. The magnitude of solvatochromic wavelength shifts based on the product of the multi-linear regression coefficients (*b*, *c*, *d* and *e*) from Equation 2 and the solvent constants (SP, SdP, SA and SB), for P3ATs in different solvents. The following solvents are abbreviated: Chlorobenzene (CB), 1,2-Dichlorobenzene (DCB), Tetrahydrofuran (THF), Dichloromethane (DCM) and Fluorobenzene (FB).

Polymer	*Solvent*	*b×SP (nm)*	*c×SdP (nm)*	*d×SA (nm)*	*e×SB (nm)*
P3HT	**Cyclohexane**	67.0	0.0	0.0	-0.1
	Benzene	77.8	0.1	0.0	-0.2
	Toluene	76.7	0.1	0.0	-0.2
	CB	81.7	0.1	0.0	-0.2
	DCB	85.2	0.2	-0.3	-0.2
	Bromobenzene	85.8	0.1	0.0	-0.2
	Chloroform	77.1	0.2	-0.4	-0.1
	THF	70.0	0.2	0.0	-0.7
	P-Xylene	76.3	0.0	0.0	-0.2
	Pyridine	82.6	0.2	-0.3	-0.7
	Mesitylene	76.0	0.0	0.0	-0.2
	DCM	74.6	0.2	-0.4	-0.2
	FB	74.6	0.1	0.0	-0.1
	M-Xylene	75.6	0.1	0.0	-0.2
P3OT	**Cyclohexane**	56.8	0.0	0.0	-0.5
	Benzene	66.0	1.4	0.0	-0.8
	Toluene	65.0	1.4	0.0	-0.9
	CB	69.3	2.7	0.0	-1.2
	DCB	72.3	3.4	-1.9	-1.0
	Bromobenzene	72.8	2.5	0.0	-1.3
	Chloroform	65.4	3.1	-2.7	-0.5
	THF	59.4	3.2	0.0	-4.0
	P-Xylene	64.7	0.9	0.0	-1.1
	Pyridine	70.0	3.9	-1.9	-3.9
	Mesitylene	64.5	0.8	0.0	-1.3

	DCM	63.3	3.9	-2.3	-1.2
	FB	63.3	2.6	0.0	-0.8
	M-Xylene	64.1	1.0	0.0	-1.1
P3DDT	**Cyclohexane**	56.5	0.0	0.0	-0.5
	Benzene	65.6	0.9	0.0	-0.9
	Toluene	64.6	0.9	0.0	-0.9
	CB	68.9	1.7	0.0	-1.3
	DCB	71.8	2.1	-1.9	-1.1
	Bromobenzene	72.3	1.6	0.0	-1.4
	Chloroform	65.0	1.9	-2.7	-0.5
	THF	59.0	2.0	0.0	-4.4
	P-Xylene	64.3	0.6	0.0	-1.2
	Pyridine	69.6	2.4	-1.9	-4.3
	Mesitylene	64.1	0.5	0.0	-1.4
	DCM	62.9	2.4	-2.3	-1.3
	FB	62.9	1.6	0.0	-0.8
	M-Xylene	63.7	0.6	0.0	-1.2
P3EHT	**Cyclohexane**	59.4	0.0	0.0	0.1
	Benzene	69.0	0.2	0.0	0.2
	Toluene	68.0	0.2	0.0	0.2
	CB	72.5	0.4	0.0	0.2
	DCB	75.6	0.5	-0.2	0.2
	Bromobenzene	76.1	0.3	0.0	0.3
	Chloroform	68.4	0.4	-0.3	0.1
	THF	62.1	0.4	0.0	0.8
	P-Xylene	67.7	0.1	0.0	0.2
	Pyridine	73.2	0.5	-0.2	0.8
	Mesitylene	67.4	0.1	0.0	0.2
	DCM	66.2	0.5	-0.2	0.2
	FB	66.2	0.3	0.0	0.2

	M-Xylene	67.1	0.1	0.0	0.2

10.5 References

1. Prosa, T. J.; Winokur, M. J.; Moulton, J.; Smith, P.; Heeger, A. J. *Macromolecules* **1992,** 25, (17), 4364-4372.
2. Erwin, M.; McBride, J.; Kadavanich, A.; Rosenthal, S. *Thin Solid Films* **2002**, 198-205.
3. Kiel, J. W.; Kirby, B. J.; Majkrzak, C. F.; Maranville, B. B.; Mackay, M. E. *Soft Matter* **2010,** 6, (3), 641-646.
4. Yin, W.; Dadmun, M. *ACS Nano* **2011,** 5, (6), 4756-4768.
5. Kiel, J. W.; Eberle, A. P. R.; Mackay, M. E. *Physical Review Letters* **2010,** 105, (16), 168701-4.
6. Lee, K. H.; Schwenn, P. E.; Smith, A. R. G.; Cavaye, H.; Shaw, P. E.; James, M.; Krueger, K. B.; Gentle, I. R.; Meredith, P.; Burn, P. L. *Advanced Materials* **2011,** 23, (6), 766-770.
7. Abboud, J.-L. M.; Notario, R. *Pure and Applied Chemistry* **1999,** 71, (4), 645-718.
8. de la Iglesia, P.; Pozzo, D. C. *Soft Matter* **2013,** 9, (47), 11214-11224.
9. Richards, J. J.; Weigandt, K. M.; Pozzo, D. C. *Journal of Colloid and Interface Science* **2011,** 364, (2), 341-350.
10. Zuo, L.-J.; Hu, X.-L.; Ye, T.; Andersen, T. R.; Li, H.-Y.; Shi, M.-M.; Xu, M.; Ling, J.; Zheng, Q.; Xu, J.-T.; Bundgaard, E.; Krebs, F. C.; Chen, H.-Z. *The Journal of Physical Chemistry C* **2012,** 116, (32), 16893-16900.
11. Dingenouts, N.; Bolze, J.; Pötschke, D.; Ballauff, M., Analysis of Polymer Latexes by Small-Angle X-Ray Scattering. In *Polymer Latexes - Epoxide Resins - Polyampholytes*, Springer Berlin Heidelberg: 1999; Vol. 144, pp 1-47.
12. Yokoyama, A.; Miyakoshi, R.; Yokozawa, T. *Macromolecules* **2004,** 37, (4), 1169-1171.
13. Bronstein, H. A.; Luscombe, C. K. *Journal of the American Chemical Society* **2009,** 131, (36), 12894-12895.

Bibliography

Abboud, J.-L. M.; Notario, R., Critical Compilation of Scales of Solvent Parameters. Part I. Pure, Non-Hydrogen Bond Donor Solvents. *Pure and Applied Chemistry* **1999,** *71* (4), 645-718.

Abramoff, M. D.; Magalhaes, P. J.; Ram, S. J., Image Processing with ImageJ. *Biophotonics International* **2004,** *11* (7), 36-41.

Alcazar, D.; Wang, F.; Swager, T. M.; Thomas, E. L., Gel Processing for Highly Oriented Conjugated Polymer Films. *Macromolecules* **2008,** *41* (24), 9863-9868.

Arif, M.; Liu, J.; Zhai, L.; Khondaker, S. I., Poly(3-hexylthiophene) crystalline nanoribbon network for organic field effect transistors. *Applied Physics Letters* **2010,** *96* (24), 243304-3.

Avrami, M., Granulation, Phase Change, and Microstructure - Kinetics of Phase Change. III. *Journal of Chemical Physics* **1941,** *8*, 177-184.

Avrami, M., Kinetics of Phase Change I - General Theory. *Journal of Chemical Physics* **1939,** *7*, 1103-1112.

Ballauff, M., Phase Equilibria in Rodlike Systems with Flexible Side Chains. *Macromolecules* **1986,** *19* (5), 1366-1374.

Bao, Z.; Dodabalapur, A.; Lovinger, A. J., Soluble and Processable Regioregular Poly(3-hexylthiophene) for Thin Film Field-effect Transistor Applications with High Mobility. *Applied Physics Letters* **1996,** *69* (26), 4108-4110.

Barker, J. G.; Glinka, C. J.; Moyer, J. J.; Kim, M. H.; Drews, A. R.; Agamalian, M., Design and Performance of a Thermal-Neutron Double-Crystal Diffractometer for USANS at NIST. *Journal of Applied Crystallography* **2005,** *38*, 1004-1011.

Barth, S.; Bässler, H.; Rost, H.; Hörhold, H. H., Extrinsic and Intrinsic DC Photoconductivity in a Conjugated Polymer. *Physical Review B* **1997,** *56* (7), 3844-3851.

Basic Research Needs for Solar Energy Utilization; U.S. Department of Energy: http://www.sc.doe.gov/bes/reports/files/SEU_rpt.pdf, **2005**.

Bayliss, N. S.; McRae, E. G., Solvent Effects in Organic Spectra: Dipole Forces and the Franck–Condon Principle. *The Journal of Physical Chemistry* **1954,** *58* (11), 1002-1006.

Becke, A. D., Density-functional thermochemistry. III. The role of exact exchange. *The Journal of Chemical Physics* **1993,** *98* (7), 5648-5652.

Beek, W. J. E.; Wienk, M. M.; Janssen, R. A. J., Hybrid Solar Cells from Regioregular Polythiophene and ZnO Nanoparticles. *Advanced Functional Materials* **2006,** *16* (8), 1112-1116.

Benoit, H., La Diffusion de la Lumière Par Des Macromolécules en Chaînes en Solution Das un Bon Solvant. *Comptes Rendus Hebd Seances Acad Sci* **1957,** *245*, 2244-2247.

Berendsen, H. J. C.; Postma, J. P. M.; van Gunsteren, W. F.; DiNola, A.; Haak, J. R., Molecular dynamics with coupling to an external bath. *The Journal of Chemical Physics* **1984,** *81* (8), 3684-3690.

Berson, S.; De Bettignies, R.; Bailly, S.; Guillerez, S., Poly(3-hexylthiophene) Fibers for Photovoltaic Applications. *Advanced Functional Materials* **2007,** *17* (8), 1377-1384.

Boal, A. K.; Ilhan, F.; DeRouchey, J. E.; Thurn-Albrecht, T.; Russell, T. P.; Rotello, V. M., Self-Assembly of Nanoparticles into Structured Spherical and Network Aggregates. *Nature* **2000,** *404* (6779), 746-748.

Boucle, J.; Ravirajan, P.; Nelson, J., Hybrid Polymer-Metal Oxide Thin Films for Photovoltaic Applications. *Journal of Materials Chemistry* **2007,** *17* (30), 3141-3153.

Brinkmann, M.; Wittmann, J. C., Orientation of Regioregular Poly(3-hexylthiophene) by Directional Solidification: A Simple Method to Reveal the Semicrystalline Structure of a Conjugated Polymer. *Advanced Materials* **2006,** *18* (7), 860-863.

Bronstein, H. A.; Luscombe, C. K., Externally Initiated Regioregular P3HT with Controlled Molecular Weight and Narrow Polydispersity. *Journal of the American Chemical Society* **2009,** *131* (36), 12894-12895.

Bussi, G.; Donadio, D.; Parrinello, M., Canonical sampling through velocity rescaling. *The Journal of Chemical Physics* **2007,** *126* (1), 014101-7.

Butler, P.; Alina, G.; Hernandez, R. C.; Doucet, M.; Jackson, A.; Kienzle, P.; Kline, S.; Zhou, J. SASView for Small Angle Scattering Analysis. http://www.sasview.org/., **2005**.

Cai, W.; Gong, X.; Cao, Y., Polymer Solar Cells: Recent Development and Possible Routes for Improvement in the Performance. *Solar Energy Materials and Solar Cells* **2010,** *94* (2), 114-127.

Carcia, P. F.; McLean, R. S.; Reilly, M. H., High-Performance ZnO Thin-Film Transistors on Gate Dielectrics Grown by Atomic Layer Deposition. *Applied Physics Letters* **2006,** *88* (12), 123509-3.

Catalán, J., Toward a Generalized Treatment of the Solvent Effect Based on Four Empirical Scales: Dipolarity (SdP, a New Scale), Polarizability (SP), Acidity (SA), and Basicity (SB) of the Medium. *The Journal of Physical Chemistry B* **2009,** *113* (17), 5951-5960.

Chang, J.-F.; Sun, B.; Breiby, D. W.; Nielsen, M. M.; Sölling, T. I.; Giles, M.; McCulloch, I.; Sirringhaus, H., Enhanced Mobility of Poly(3-hexylthiophene) Transistors by Spin-Coating from High-Boiling-Point Solvents. *Chemistry of Materials* **2004,** *16* (23), 4772-4776.

Chang, M.-Y.; Huang, Y.-H.; Han, Y.-K., Aggregation, crystallization, and resistance properties of poly(3-hexylthiophene-2,5-diyl) solid films gel-cast from CHCl3/p-xylene mixed solvents. *Organic Electronics* **2014,** *15* (1), 251-259.

Chen, B.; Wu, K.; Yao, W., Conductivity of carbon fiber reinforced cement-based composites. *Cement and Concrete Composites* **2004,** *26* (4), 291-297.

Chen, C. Y.; Chan, S. H.; Li, J. Y.; Wu, K. H.; Chen, H. L.; Chen, J. H.; Huang, W. Y.; Chen, S. A., Formation and Thermally-Induced Disruption of Nanowhiskers in Poly(3-hexylthiophene)/Xylene Gel Studied by Small-Angle X-ray Scattering. *Macromolecules* **2010,** *43* (17), 7305-7311.

Chen, J. H.; Chang, C. S.; Chang, Y. X.; Chen, C. Y.; Chen, H. L.; Chen, S. A., Gelation and Its Effect on the Photophysical Behavior of Poly(9,9-dioctylfluorene-2,7-diyl) in Toluene. *Macromolecules* **2009,** *42* (4), 1306-1314.

Chen, J.-Y.; Hsu, F.-C.; Sung, Y.-M.; Chen, Y.-F., Enhanced charge transport in hybrid polymer/ZnO-nanorod solar cells assisted by conductive small molecules. *Journal of Materials Chemistry* **2012,** *22* (31), 15726-15731.

Choi, H.; Stathatos, E.; Dionysiou, D. D., Photocatalytic TiO2 films and membranes for the development of efficient wastewater treatment and reuse systems. *Desalination* **2007,** *202* (1–3), 199-206.

Chu, J.-W.; Voth, G. A., Allostery of actin filaments: Molecular dynamics simulations and coarse-grained analysis. *Proceedings of the National Academy of Sciences of the United States of America* **2005,** *102* (37), 13111-13116.

Clark, J.; Chang, J.-F.; Spano, F. C.; Friend, R. H.; Silva, C., Determining exciton bandwidth and film microstructure in polythiophene films using linear absorption spectroscopy. *Applied Physics Letters* **2009,** *94* (16), 163306-3.

Coakley, K.; McGehee, M., Conjugated polymer photovoltaic cells. *Chemistry of Materials* **2004,** *16* (23), 4533-4542.

Coffey, D. C.; Reid, O. G.; Rodovsky, D. B.; Bartholomew, G. P.; Ginger, D. S., Mapping local photocurrents in polymer/fullerene solar cells with photoconductive atomic force microscopy. *Nano Letters* **2007,** *7* (3), 738-744.

Cravino, A.; Sariciftci, N. S., Double-cable polymers for fullerene based organic optoelectronic applications. *Journal of Materials Chemistry* **2002,** *12*, 1931-1943.

Cui, J.; Lackey, M. A.; Madkour, A. E.; Saffer, E. M.; Griffin, D. M.; Bhatia, S. R.; Crosby, A. J.; Tew, G. N., Synthetically Simple, Highly Resilient Hydrogels. *Biomacromolecules* **2012,** *13* (3), 584-588.

de la Iglesia, P.; Pozzo, D. C., Effects of supersaturation on the structure and properties of poly(9,9-dioctyl fluorene) organogels. *Soft Matter* **2013,** *9* (47), 11214-11224.

Dingenouts, N.; Bolze, J.; Pötschke, D.; Ballauff, M., Analysis of Polymer Latexes by Small-Angle X-Ray Scattering. In *Polymer Latexes - Epoxide Resins - Polyampholytes*, Springer Berlin Heidelberg: 1999; Vol. 144, pp 1-47.

Do, K.; Huang, D. M.; Faller, R.; Moule, A. J., A comparative MD study of the local structure of polymer semiconductors P3HT and PBTTT. *Physical Chemistry Chemical Physics* **2010,** *12* (44), 14735-14739.

Doi, M., *Introduction to Polymer Physics*. Oxford University Press: 2004.

Dufresne, G.; Bouchard, J.; Belletête, M.; Durocher, G.; Leclerc, M., Thermochromic and Solvatochromic Conjugated Polymers by Design. *Macromolecules* **2000,** *33* (22), 8252-8257.

Duong, D. T.; Wang, C.; Antono, E.; Toney, M. F.; Salleo, A., The chemical and structural origin of efficient p-type doping in P3HT. *Organic Electronics* **2013,** *14* (5), 1330-1336.

el Maaty, M.; Hosier, I.; Bassett, D., A unified context for spherulitic growth in polymers. *Macromolecules* **1998**, 153-157.

Elam, J. W.; Routkevitch, D.; Mardilovich, P. P.; George, S. M., Conformal Coating on Ultrahigh-Aspect-Ratio Nanopores of Anodic Alumina by Atomic Layer Deposition. *Chemistry of Materials* **2003,** *15* (18), 3507-3517.

Erwin, M.; McBride, J.; Kadavanich, A.; Rosenthal, S., Effects of impurities on the optical properties of poly-3-hexylthiophene thin films. *Thin Solid Films* **2002**, 198-205.

Friend, R. H.; Gymer, R. W.; Holmes, A. B.; Burroughes, J. H.; Marks, R. N.; Taliani, C.; Bradley, D. D. C.; Santos, D. A. D.; Bredas, J. L.; Logdlund, M.; Salaneck, W. R., Electroluminescence in conjugated polymers. *Nature* **1999,** *397* (6715), 121-128.

Frisch, M. J. T., G. W.; Schlegel, H. B.; Scuseria, G. E.; Robb, M. A.; Cheeseman, J. R.; Scalmani, G.; Barone, V.; Mennucci, B.; Petersson, G. A. Gaussian 09, Revision A.1.

Gao, C.-H.; Shi, X.-B.; Zhou, D.-Y.; Zhang, L.; Wang, Z.-K.; Liao, L.-S., Highly Efficient White Organic Light-Emitting Diodes with Controllable Excitons Behavior by Mixed Interlayer between Fluorescence Blue and Phosphorescence Yellow-Emitting Layers. *International Jounral of Photoenergy* **2013,** *831765*, 1-7.

Glinka, C.; Barker, J.; Hammouda, B.; Krueger, S.; Moyer, J.; Orts, W., The 30 m small-angle neutron scattering instruments at the National Institute of Standards and Technology. *Journal of Applied Crystallography* **1998,** *31*, 430-445.

Gong, J. P.; Katsuyama, Y.; Kurokawa, T.; Osada, Y., Double-Network Hydrogels with Extremely High Mechanical Strength. *Advanced Materials* **2003,** *15* (14), 1155-1158.

Gonzalez-Valls, I.; Lira-Cantu, M., Vertically-aligned nanostructures of ZnO for excitonic solar cells: a review. *Energy & Environmental Science* **2009,** *2* (1), 19-34.

Gross, M.; Muller, D. C.; Nothofer, H.-G.; Scherf, U.; Neher, D.; Brauchle, C.; Meerholz, K., Improving the performance of doped [pi]-conjugated polymers for use in organic light-emitting diodes. *Nature* **2000,** *405* (6787), 661-665.

Guinier, A.; Fournet, G., *Small-Angle Scattering of X-rays*. Wiley: New York, 1955.

Guo, X.; Kim, F. S.; Jenekhe, S. A.; Watson, M. D., Phthalimide-Based Polymers for High Performance Organic Thin-Film Transistors. *Journal of the American Chemical Society* **2009,** *131* (21), 7206-7207.

Halls, J., Walsh, CA, Greenham, NC, Marseglia, EA, Friend, RH, Moratti, SC, Holmes, AB, Efficient Photodiodes from Interpenetrating Polymer Networks. *Nature* **1995,** *376*, 498-500.

Hammouda, B., SANS from Heterogeneous Polymer Mixtures - A Unified Overview. *Advances in Polymer Science* **1993,** *106*, 87-133.

Handbook of Chemistry and Physics: 83rd Edition. CRC Press LLC: Davers, MA, **2002**.

Hecht, A.; Duplessix, R.; Geissler, E., Structural Inhomogeneities in the Range 2.5-2500 A in Polyacrylamide Gels. *Macromolecules* **1985,** *18*, 2167-2173.

Hess, B., P-LINCS: A Parallel Linear Constraint Solver for Molecular Simulation. *Journal of Chemical Theory and Computation* **2007,** *4* (1), 116-122.

Hess, B.; Kutzner, C.; van der Spoel, D.; Lindahl, E., GROMACS 4: Algorithms for Highly Efficient, Load-Balanced, and Scalable Molecular Simulation. *Journal of Chemical Theory and Computation* **2008,** *4* (3), 435-447.

Hoppe, H.; Sariciftci, N. S., Morphology of polymer/fullerene bulk heterojunction solar cells. *Journal of Materials Chemistry* **2006,** *16* (1), 45-61.

Hoppe, H.; Sariciftci, N., Organic solar cells: An overview. *Journal of Materials Research* **2004,** *19* (7), 1924-1945.

Hoyle, C. E.; Lee, T. Y.; Roper, T., Thiol–enes: Chemistry of the past with promise for the future. *Journal of Polymer Science Part A: Polymer Chemistry* **2004,** *42* (21), 5301-5338.

Huang, D. M.; Faller, R.; Do, K.; Moulé, A. J., Coarse-Grained Computer Simulations of Polymer/Fullerene Bulk Heterojunctions for Organic Photovoltaic Applications. *Journal of Chemical Theory and Computation* **2009,** *6* (2), 526-537.

Huang, P.-T.; Chang, Y.-S.; Chou, C.-W., Preparation of porous poly(3-hexylthiophene) by freeze-dry method and its application to organic photovoltaics. *Journal of Applied Polymer Science* **2011,** *122*, 233-240.

Huang, W. Y.; Huang, P. T.; Han, Y. K.; Lee, C. C.; Hsieh, T. L.; Chang, M. Y., Aggregation and Gelation Effects on the Performance of Poly(3-hexylthiophene)/Fullerene Solar Cells. *Macromolecules* **2008,** *41* (20), 7485-7489.

Ihn, K. J.; Moulton, J.; Smith, P., Whiskers of poly(3-alkylthiophene)s. *Journal of Polymer Science Part B: Polymer Physics* **1993,** *31* (6), 735-742.

James, S. L., Metal-Organic Frameworks. *Chemical Society Reviews* **2003,** *32* (5), 276-288.

Jiang, S.; Cao, Z., Ultralow-Fouling, Functionalizable, and Hydrolyzable Zwitterionic Materials and Their Derivatives for Biological Applications. *Advanced Materials* **2010,** *22* (9), 920-932.

Jonkheijm, P.; van der Schoot, P.; Schenning, A. P. H. J.; Meijer, E. W., Probing the Solvent-Assisted Nucleation Pathway in Chemical Self-Assembly. *Science* **2006,** *313* (5783), 80-83.

Jorcin, J.-B.; Orazem, M. E.; Pébère, N.; Tribollet, B., CPE Analysis by Local Electrochemical Impedance Spectroscopy. *Electrochimica Acta* **2006,** *51* (8–9), 1473-1479.

Jorgensen, W. L.; Maxwell, D. S.; Tirado-Rives, J., Development and Testing of the OPLS All-Atom Force Field on Conformational Energetics and Properties of Organic Liquids. *Journal of the American Chemical Society* **1996,** *118* (45), 11225-11236.

Keum, J. K.; Xiao, K.; Ivanov, I. N.; Hong, K.; Browning, J. F.; Smith, G. S.; Shao, M.; Littrell, K. C.; Rondinone, A. J.; Andrew Payzant, E.; Chen, J.; Hensley, D. K., Solvent Quality-Induced Nucleation and Growth of Parallelepiped Nanorods in Dilute Poly(3-hexylthiophene) (P3HT) Solution and the Impact on the Crystalline Morphology of Solution-cast Thin Film. *CrystEngComm* **2013,** *15* (6), 1114-1124.

Kiel, J. W.; Eberle, A. P. R.; Mackay, M. E., Nanoparticle Agglomeration in Polymer-Based Solar Cells. *Physical Review Letters* **2010,** *105* (16), 168701-4.

Kiel, J. W.; Kirby, B. J.; Majkrzak, C. F.; Maranville, B. B.; Mackay, M. E., Nanoparticle Concentration Profile in Polymer-based Solar Cells. *Soft Matter* **2010,** *6* (3), 641-646.

Kim, B.-G.; Jeong, E. J.; Park, H. J.; Bilby, D.; Guo, L. J.; Kim, J., Effect of Polymer Aggregation on the Open Circuit Voltage in Organic Photovoltaic Cells: Aggregation-Induced Conjugated Polymer Gel and its Application for Preventing Open Circuit Voltage Drop. *ACS Applied Materials & Interfaces* **2011,** *3* (3), 674-680.

Kim, D. H.; Han, J. T.; Park, Y. D.; Jang, Y.; Cho, J. H.; Hwang, M.; Cho, K., Single-Crystal Polythiophene Microwires Grown by Self-Assembly. *Advanced Materials* **2006,** *18* (6), 719-723.

Kim, F. S.; Guo, X.; Watson, M. D.; Jenekhe, S. A., High-mobility Ambipolar Transistors and High-gain Inverters from a Donor–Acceptor Copolymer Semiconductor. *Advanced Materials* **2010,** *22* (4), 478-482.

Kim, F. S.; Jenekhe, S. A., Charge Transport in Poly(3-butylthiophene) Nanowires and Their Nanocomposites with an Insulating Polymer. *Macromolecules* **2012,** *45* (18), 7514-7519.

Kim, J. Y.; Lee, K.; Coates, N. E.; Moses, D.; Nguyen, T.-Q.; Dante, M.; Heeger, A. J., Efficient Tandem Polymer Solar Cells Fabricated by All-Solution Processing. *Science* **2007,** *317* (5835), 222-225.

Kitts, C. C.; Vanden Bout, D. A., The Effect of Solvent Quality on the Chain Morphology in Solutions of Poly(9,9 '-dioctylfluorene). *Polymer* **2007,** *48*, 2322-2330.

Kline, R. J.; McGehee, M. D.; Kadnikova, E. N.; Liu, J.; Fréchet, J. M. J.; Toney, M. F., Dependence of Regioregular Poly(3-hexylthiophene) Film Morphology and Field-Effect Mobility on Molecular Weight. *Macromolecules* **2005,** *38* (8), 3312-3319.

Kline, S., Reduction and Analysis of SANS and USANS Data using IGOR Pro. *Journal of Applied Crystallography* **2006,** *39*, 895-900.

Koehler, R. D.; Raghavan, S. R.; Kaler, E. W., Microstructure and Dynamics of Wormlike Micellar Solutions Formed by Mixing Cationic and Anionic Surfactants. *The Journal of Physical Chemistry B* **2000,** *104* (47), 11035-11044.

Koppe, M.; Brabec, C.; Heiml, S.; Schausberger, A.; Duffy, W.; Heeney, M.; McCulloch, I., Influence of Molecular Weight Distribution on the Gelation of P3HT and Its Impact on the Photovoltaic Performance. *Macromolecules* **2009,** *42* (13), 4661-4666.

Krebs, F. C., Fabrication and Processing of Polymer Solar Cells: A review of Printing and Coating Techniques. *Solar Energy Materials and Solar Cells* **2009,** *93* (4), 394-412.

Krebs, F. C.; Gevorgyan, S. A.; Gholamkhass, B.; Holdcroft, S.; Schlenker, C.; Thompson, M. E.; Thompson, B. C.; Olson, D.; Ginley, D. S.; Shaheen, S. E.; Alshareef, H. N.; Murphy, J. W.; Youngblood, W. J.; Heston, N. C.; Reynolds, J. R.; Jia, S.; Laird, D.; Tuladhar, S. M.; Dane, J. G. A.; Atienzar, P.; Nelson, J.; Kroon, J. M.; Wienk, M. M.; Janssen, R. A. J.; Tvingstedt, K.; Zhang, F.; Andersson, M.; Inganäs, O.; Lira-Cantu, M.; de Bettignies, R.; Guillerez, S.; Aernouts, T.; Cheyns, D.; Lutsen, L.; Zimmermann, B.; Würfel, U.; Niggemann, M.; Schleiermacher, H.-F.; Liska, P.; Grätzel, M.; Lianos, P.; Katz, E. A.; Lohwasser, W.; Jannon, B., A Round Robin Study of Flexible Large-area Roll-to-Roll Processed Polymer Solar Cell Modules. *Solar Energy Materials and Solar Cells* **2009,** *93* (11), 1968-1977.

Kreyenschmidt, M.; Uckert, F.; Muellen, K., A New Soluble Poly(p-phenylene) with Tetrahydropyrene Repeating Units. *Macromolecules* **1995,** *28* (13), 4577-4582.

Lan, Y.-K.; Huang, C.-I., A Theoretical Study of the Charge Transfer Behavior of the Highly Regioregular Poly-3-hexylthiophene in the Ordered State. *The Journal of Physical Chemistry B* **2008,** *112* (47), 14857-14862.

Lasia, A., *Modern Aspects of Electrochemistry*. Kluwer Academic/Plenum Publishers: New York, 1999.

Lee, J.; Lee, J.-I.; Lee, J. Y.; Chu, H. Y., Enhanced Efficiency and Reduced Roll-off in Blue and White Phosphorescent Organic Light-Emitting Diodes with a Mixed Host Structure. *Applied Physics Letters* **2009,** *94* (19), 193305-3.

Lee, K. H.; Schwenn, P. E.; Smith, A. R. G.; Cavaye, H.; Shaw, P. E.; James, M.; Krueger, K. B.; Gentle, I. R.; Meredith, P.; Burn, P. L., Morphology of All-Solution-Processed "Bilayer" Organic Solar Cells. *Advanced Materials* **2011,** *23* (6), 766-770.

Li, J. L.; Liu, X. Y.; Wang, R. Y.; Xiong, J. Y., Architecture of a Biocompatible Supramolecular Material by Supersaturation-Driven Fabrication of its Fiber Network. *Journal of Physical Chemistry B* **2005,** *109* (51), 24231-24235.

Li, J. L.; Yuan, B.; Liu, X. Y.; Xu, H. Y., Microengineering of Supramolecular Soft Materials by Design of the Crystalline Fiber Networks. *Crystal Growth & Design* **2010,** *10* (6), 2699-2706.

Liao, H.; Munoz-Pinto, D.; Qu, X.; Hou, Y.; Grunlan, M. A.; Hahn, M. S., Influence of hydrogel mechanical properties and mesh size on vocal fold fibroblast extracellular matrix production and phenotype. *Acta Biomaterialia* **2008,** *4* (5), 1161-1171.

Liberatore, M. W.; Nettesheim, F.; Vasquez, P. A.; Helgeson, M. E.; Wagner, N. J.; Kaler, E. W.; Cook, L. P.; Porcar, L.; Hu, Y. T., Microstructure and shear rheology of entangled wormlike micelles in solution. *Journal of Rheology* **2009,** *53* (2), 441-458.

Lin, Z.-Q.; Shi, N.-E.; Li, Y.-B.; Qiu, D.; Zhang, L.; Lin, J.-Y.; Zhao, J.-F.; Wang, C.; Xie, L.-H.; Huang, W., Preparation and Characterization of Polyfluorene-Based Supramolecular pi-Conjugated Polymer Gels. *Journal of Physical Chemistry C* **2011,** *115* (11), 4418-4424.

Lindner, P., *Neutrons, X-Rays and Light: Scattering Methods Applied to Soft Condensed Matter*. Elsevier Science: Amsterdam, 2002.

Liu, J.; Arif, M.; Zou, J.; Khondaker, S. I.; Zhai, L., Controlling Poly(3-hexylthiophene) Crystal Dimension: Nanowhiskers and Nanoribbons. *Macromolecules* **2009,** *42* (24), 9390-9393.

Liu, X. Y.; Sawant, P. D., Mechanism of the formation of self-organized microstructures in soft functional materials. *Advanced Materials* **2002,** *14* (6), 421-426.

Lunt, R. R.; Giebink, N. C.; Belak, A. A.; Benziger, J. B.; Forrest, S. R., Exciton diffusion lengths of organic semiconductor thin films measured by spectrally resolved photoluminescence quenching. *Journal of Applied Physics* **2009,** *105* (5), 053711-7.

Ma, W.; Yang, C.; Gong, X.; Lee, K.; Heeger, A. J., Thermally Stable, Efficient Polymer Solar Cells with Nanoscale Control of the Interpenetrating Network Morphology. *Advanced Functional Materials* **2005,** *15* (10), 1617-1622.

Macosko, C. W., *Rheology Principles, Measurements, and Applications*. Wiley-VCH: New York, 1994.

Malik, S.; Jana, T.; Nandi, A. K., Thermoreversible gelation of regioregular poly(3-hexylthiophene) in xylene. *Macromolecules* **2001,** *34* (2), 275-282.

Malik, S.; Nandi, A. K., Influence of alkyl chain length on the gelation mechanism of thermoreversible gels of regioregular poly(3-alkyl thiophenes) in xylene. *Journal of Applied Polymer Science* **2007,** *103* (4), 2528-2537.

Malik, S.; Nandi, A. K., Thermodynamic and structural investigation of thermoreversible poly(3-dodecyl thiophene) gels in the three isomers of xylene. *Journal of Physical Chemistry B* **2004,** *108* (2), 597-604.

Martínez, L.; Andrade, R.; Birgin, E. G.; Martínez, J. M., PACKMOL: A package for building initial configurations for molecular dynamics simulations. *Journal of Computational Chemistry* **2009,** *30* (13), 2157-2164.

Matsuura, T., Progress in membrane science and technology for seawater desalination — a review. *Desalination* **2001,** *134* (1–3), 47-54.

McCulloch, B.; Ho, V.; Hoarfrost, M.; Stanley, C.; Do, C.; Heller, W. T.; Segalman, R. A., Polymer Chain Shape of Poly(3-alkylthiophenes) in Solution Using Small-Angle Neutron Scattering. *Macromolecules* **2013,** *46* (5), 1899-1907.

Meier, H.; Stalmach, U.; Kolshorn, H., Effective conjugation length and UV/vis spectra of oligomers. *Acta Polymerica* **1997,** *48* (9), 379-384.

Merlo, J. A.; Frisbie, C. D., Field Effect Transport and Trapping in Regioregular Polythiophene Nanofibers. *The Journal of Physical Chemistry B* **2004,** *108* (50), 19169-19179.

Millon, L. E.; Nieh, M.-P.; Hutter, J. L.; Wan, W., SANS Characterization of an Anisotropic Poly(vinyl alcohol) Hydrogel with Vascular Applications. *Macromolecules* **2007,** *40* (10), 3655-3662.

Mittelbach, P.; Porod, G., Small-Angle X-Ray Scattering by Dilute Colloid Systems: The Calculation of Scattering Curves for Parallelepipeds. *Acta Physica Austriaca* **1961,** *14*, 185-211.

Moule, A.; Meerholz, K., Morphology Control in Solution-Processed Bulk-Heterojunction Solar Cell Mixtures. *Advanced Functional Materials* **2009,** *20*, 3028-3036.

Na, Y.-H.; Kurokawa, T.; Katsuyama, Y.; Tsukeshiba, H.; Gong, J. P.; Osada, Y.; Okabe, S.; Karino, T.; Shibayama, M., Structural Characteristics of Double Network Gels with Extremely High Mechanical Strength. *Macromolecules* **2004,** *37* (14), 5370-5374.

Nam, S.; Cho, H. W.; Kim, T.; Kim, D.; Sung, B. J.; Lim, S.; Kim, H., Effects of silica particles on the electrical percolation threshold and thermomechanical properties of epoxy/silver nanocomposites. *Applied Physics Letters* **2011,** *99* (4), 043104-3.

Newbloom, G. M.; Kim, F. S.; Jenekhe, S. A.; Pozzo, D. C., Mesoscale Morphology and Charge Transport in Colloidal Networks of Poly(3-hexylthiophene). *Macromolecules* **2011,** *44* (10), 3801-3809.

Newbloom, G. M.; Weigandt, K. M.; Pozzo, D. C., Electrical, Mechanical, and Structural Characterization of Self-Assembly in Poly(3-hexylthiophene) Organogel Networks. *Macromolecules* **2012,** *45* (8), 3452-3462.

Newbloom, G. M.; Weigandt, K. M.; Pozzo, D. C., Structure and property development of poly(3-hexylthiophene) organogels probed with combined rheology, conductivity and small angle neutron scattering. *Soft Matter* **2012,** *8* (34), 8854-8864.

Nguyen, T.-Q.; Doan, V.; Schwartz, B. J., Conjugated polymer aggregates in solution: Control of interchain interactions. *The Journal of Chemical Physics* **1999,** *110* (8), 4068-4078.

Obrzut, J.; Page, K. A., Electrical conductivity and relaxation in poly(3-hexylthiophene). *Physical Review B* **2009,** *80* (19).

Ogata, T.; Kozima, K., Microwave spectrum, barrier height to internal rotation of methyl group of 3-methylthiophene, and dipole moments of 3-methylthiophene and thiophene. *Journal of Molecular Spectroscopy* **1972,** *42* (1), 38-46.

Olson, D. C.; Piris, J.; Collins, R. T.; Shaheen, S. E.; Ginley, D. S., Hybrid photovoltaic devices of polymer and ZnO nanofiber composites. *Thin Solid Films* **2006,** *496* (1), 26-29.

Olson, D. C.; Shaheen, S. E.; Collins, R. T.; Ginley, D. S., The Effect of Atmosphere and ZnO Morphology on the Performance of Hybrid Poly(3-hexylthiophene)/ZnO Nanofiber Photovoltaic Devices. *The Journal of Physical Chemistry C* **2007,** *111* (44), 16670-16678.

Oosterbaan, W. D.; Bolsée, J.-C.; Gadisa, A.; Vrindts, V.; Bertho, S.; D'Haen, J.; Cleij, T. J.; Lutsen, L.; McNeill, C. R.; Thomsen, L.; Manca, J. V.; Vanderzande, D., Alkyl-Chain-Length-Independent Hole Mobility via Morphological Control with Poly(3-alkylthiophene) Nanofibers. *Advanced Functional Materials* **2010,** *20* (5), 792-802.

Padmanaban, G.; Ramakrishnan, S., Segmented conjugated polymers. *Pramana - J Phys* **2003,** *61* (2), 425-434.

Percec, V.; Ahn, C. H.; Ungar, G.; Yeardley, D. J. P.; Moller, M.; Sheiko, S. S., Controlling polymer shape through the self-assembly of dendritic side-groups. *Nature* **1998,** *391* (6663), 161-164.

Pfaendtner, J.; Lyman, E.; Pollard, T. D.; Voth, G. A., Structure and Dynamics of the Actin Filament. *Journal of Molecular Biology* **2010,** *396* (2), 252-263.

Pileni, M.-P., The role of soft colloidal templates in controlling the size and shape of inorganic nanocrystals. *Nat Mater* **2003,** *2* (3), 145-150.

Pingel, P.; Neher, D., Comprehensive picture of p-type doping of P3HT with the molecular acceptor FTCNQ. *Physical Review B* **2013,** *87* (11), 115209-9.

Pingree, L.; MacLeod, B.; Ginger, D., The changing face of PEDOT : PSS films: Substrate, bias, and processing effects on vertical charge transport. *Journal of Physical Chemistry C* **2008,** *112* (21), 7922-7927.

Plestil, J.; Pospisil, H.; Ostanevich, Y. M.; Degovics, G., Molecular-weight determination from small-angle scattering without absolute intensities: advantages and limitations. *Journal of Applied Crystallography* **1991,** *24* (5), 659-664.

Porcar, L.; Pozzo, D.; Langenbucher, G.; Moyer, J.; Butler, P. D., Rheo--small-angle neutron scattering at the National Institute of Standards and Technology Center for Neutron Research. *Review of Scientific Instruments* **2011,** *82* (8), 083902-7.

Potai, R.; Kamphan, A.; Traiphol, R., Conformational change, intrachain aggregation and photophysical properties of regioregular poly(3-octylthiophene) in alkanes. *Journal of Polymer Science Part B: Polymer Physics* **2013,** *51* (17), 1288-1297.

Preston, A. R. H.; Ruck, B. J.; Piper, L. F. J.; DeMasi, A.; Smith, K. E.; Schleife, A.; Fuchs, F.; Bechstedt, F.; Chai, J.; Durbin, S. M., Band structure of ZnO from resonant x-ray emission spectroscopy. *Physical Review B* **2008,** *78* (15), 155114-4.

Prosa, T. J.; Winokur, M. J.; Moulton, J.; Smith, P.; Heeger, A. J., X-Ray Structural Studies of Poly(3-alkylthiophenes) - An Example of an Inverse Comb. *Macromolecules* **1992,** *25* (17), 4364-4372.

Ramasubramaniam, R.; Chen, J.; Liu, H., Homogeneous carbon nanotube/polymer composites for electrical applications. *Applied Physics Letters* **2003,** *83* (14), 2928-2930.

Ren, S.; Zeng, D.; Zhong, H.; Wang, Y.; Qian, S.; Fang, Q., Star-Shaped Donor-π-Acceptor Conjugated Oligomers with 1,3,5-Triazine Cores: Convergent Synthesis and Multifunctional Properties. *The Journal of Physical Chemistry B* **2010,** *114* (32), 10374-10383.

Rice, A. H.; Giridharagopal, R.; Zheng, S. X.; Ohuchi, F. S.; Ginger, D. S.; Luscombe, C. K., Controlling Vertical Morphology within the Active Layer of Organic Photovoltaics Using Poly(3-hexylthiophene) Nanowires and Phenyl-C(61)-butyric Acid Methyl Ester. *ACS Nano* **2011,** *5* (4), 3132-3140.

Richards, J. J.; Weigandt, K. M.; Pozzo, D. C., Aqueous dispersions of colloidal poly(3-hexylthiophene) gel particles with high internal porosity. *Journal of Colloid and Interface Science* **2011,** *364* (2), 341-350.

Rughooputh, S. D. D. V.; Hotta, S.; Heeger, A. J.; Wudl, F., Chromism of soluble polythienylenes. *Journal of Polymer Science Part B: Polymer Physics* **1987,** *25* (5), 1071-1078.

Sakai, T.; Matsunaga, T.; Yamamoto, Y.; Ito, C.; Yoshida, R.; Suzuki, S.; Sasaki, N.; Shibayama, M.; Chung, U.-i., Design and Fabrication of a High-Strength Hydrogel with Ideally Homogeneous Network Structure from Tetrahedron-like Macromonomers. *Macromolecules* **2008,** *41* (14), 5379-5384.

Salaneck, W. R.; Inganäs, O.; Thémans, B.; Nilsson, J. O.; Sjögren, B.; Österholm, J. E.; Brédas, J. L.; Svensson, S., Thermochromism in poly(3-hexylthiophene) in the solid state: A spectroscopic study of temperature-dependent conformational defects. *The Journal of Chemical Physics* **1988,** *89* (8), 4613-4619.

Samitsu, S.; Shimomura, T.; Heike, S.; Hashizume, T.; Ito, K., Effective Production of Poly(3-alkylthiophene) Nanofibers by means of Whisker Method using Anisole Solvent: Structural, Optical, and Electrical Properties. *Macromolecules* **2008,** *41* (21), 8000-8010.

Samitsu, S.; Shimomura, T.; Heike, S.; Hashizume, T.; Ito, K., Field-Effect Carrier Transport in Poly(3-alkylthiophene) Nanofiber Networks and Isolated Nanofibers. *Macromolecules* **2010,** *43* (19), 7891-7894.

Samitsu, S.; Shimomura, T.; Ito, K., Nanofiber preparation by whisker method using solvent-soluble conducting polymers. *Thin Solid Films* **2008,** *516* (9), 2478-2486.

Sandler, J. K. W.; Kirk, J. E.; Kinloch, I. A.; Shaffer, M. S. P.; Windle, A. H., Ultra-low electrical percolation threshold in carbon-nanotube-epoxy composites. *Polymer* **2003,** *44* (19), 5893-5899.

Schmidt-Rohr, K.; Chen, Q., Parallel cylindrical water nanochannels in Nafion fuel-cell membranes. *Nat Mater* **2008,** *7* (1), 75-83.

Schwartz, B. J., Conjugated Polymers as Molecular Materials: How Chain Conformation and Film Morphology Influence Energy Transfer and Interchain Interactions. *Annual Reviews of Physical Chemistry* **2003,** *54*, 141-172.

Schwarz, K. N.; Kee, T. W.; Huang, D. M., Coarse-grained simulations of the solution-phase self-assembly of poly(3-hexylthiophene) nanostructures. *Nanoscale* **2013,** *5* (5), 2017-2027.

Schweizer, K. S., Order–disorder transitions of π-conjugated polymers in condensed phases. I. General theory. *The Journal of Chemical Physics* **1986,** *85* (2), 1156-1175.

Sears, V. F., Neutron Scattering Lengths and Cross Sections. *Neutron News* **1992,** *3* (3), 29-37.

Seidler, N.; Lazzerini, G. M.; Destri, G. L.; Marletta, G.; Cacialli, F., Enhanced crystallinity and film retention of P3HT thin-films for efficient organic solar cells by use of preformed nanofibers in solution. *Journal of Materials Chemistry C* **2013,** *1*, 7748-7757.

Shaw, P. E.; Ruseckas, A.; Samuel, I. D. W., Exciton diffusion measurements in poly(3-hexylthiophene). *Advanced Materials* **2008,** *20* (18), 3516-3520.

Siram, R. B. K.; Stephen, M.; Ali, F.; Patil, S., Investigation of Phase Separation in Bulk Heterojunction Solar Cells via Supramolecular Chemistry. *The Journal of Physical Chemistry C* **2013,** *117* (18), 9129-9136.

Sirringhaus, H.; Brown, P.; Friend, R.; Nielsen, M.; Bechgaard, K.; Langeveld-Voss, B.; Spiering, A.; Janssen, R.; Meijer, E.; Herwig, P.; de Leeuw, D., Two-dimensional charge transport in self-organized, high-mobility conjugated polymers. *Nature* **1999,** *401*, 685-688.

Smith, L. A.; Liu, X.; Ma, P. X., Tissue engineering with nano-fibrous scaffolds. *Soft Matter* **2008,** *4* (11), 2144-2149.

Sobkowicz, M. J.; Jones, R. L.; Kline, R. J.; DeLongchamp, D. M., Effect of Fullerenes on Crystallization-Induced Aggregation in Polymer Photovoltaics Casting Solutions. *Macromolecules* **2011,** *45* (2), 1046-1055.

Steyrleuthner, R.; Schubert, M.; Howard, I.; Klaumünzer, B.; Schilling, K.; Chen, Z.; Saalfrank, P.; Laquai, F.; Facchetti, A.; Neher, D., Aggregation in a High-Mobility n-Type Low-Bandgap Copolymer with Implications on Semicrystalline Morphology. *Journal of the American Chemical Society* **2012,** *134* (44), 18303-18317.

Subramaniyan, S.; Xin, H.; Kim, F. S.; Shoaee, S.; Durrant, J. R.; Jenekhe, S. A., Effects of Side Chains on Thiazolothiazole-Based Copolymer Semiconductors for High Performance Solar Cells. *Advanced Energy Materials* **2011,** *1* (5), 854-860.

Svenson, S., Controlling surfactant self-assembly. *Current Opinion in Colloid & Interface Science* **2004,** *9* (3–4), 201-212.

Szymanski, C.; Wu, C.; Hooper, J.; Salazar, M. A.; Perdomo, A.; Dukes, A.; McNeill, J., Single Molecule Nanoparticles of the Conjugated Polymer MEH−PPV, Preparation and Characterization by Near-Field Scanning Optical Microscopy. *The Journal of Physical Chemistry B* **2005,** *109* (18), 8543-8546.

Takanezawa, K.; Hirota, K.; Wei, Q.-S.; Tajima, K.; Hashimoto, K., Efficient Charge Collection with ZnO Nanorod Array in Hybrid Photovoltaic Devices. *The Journal of Physical Chemistry C* **2007,** *111* (19), 7218-7223.

Tan, S. T.; Chen, B. J.; Sun, X. W.; Fan, W. J.; Kwok, H. S.; Zhang, X. H.; Chua, S. J., Blueshift of optical band gap in ZnO thin films grown by metal-organic chemical-vapor deposition. *Journal of Applied Physics* **2005,** *98* (1), 013505-5.

Tashiro, K.; Kobayashi, M.; Kawai, T.; Yoshino, K., Crystal structural change in poly (3-alkyl thiophene) s induced by iodine doping as studied by an organized combination of X-ray diffraction, infrared/Raman spectroscopy and computer simulation techniques. *Polymer* **1997,** *38* (12), 2867-2879.

Ten Hoeve, W.; Wynberg, H.; Havinga, E. E.; Meijer, E. W., Substituted 2,2':5',2":5",2"':5"',2"":5"",2""': 5"",2"""':5"""',2"""":5""",2"""":5""",2"""":5"""",2"""""-undecithiophenes, the longest characterized oligothiophenes. *Journal of the American Chemical Society* **1991,** *113* (15), 5887-5889.

Terech, P.; Weiss, R. G., Low Molecular Mass Gelators of Organic Liquids and the Properties of Their Gels. *Chemical Reviews* **1997,** *97* (8), 3133-3160.

Thienpont, H.; Rikken, G. L. J. A.; Meijer, E. W.; ten Hoeve, W.; Wynberg, H., Saturation of the hyperpolarizability of oligothiophenes. *Physical Review Letters* **1990,** *65* (17), 2141-2144.

Traiphol, R.; Charoenthai, N.; Srikhirin, T.; Kerdcharoen, T.; Osotchan, T.; Maturos, T., Chain organization and photophysics of conjugated polymer in poor solvents: Aggregates, agglomerates and collapsed coils. *Polymer* **2007,** *48* (3), 813-826.

Traiphol, R.; Sanguansat, P.; Srikhirin, T.; Kerdcharoen, T.; Osotchan, T., Spectroscopic Study of Photophysical Change in Collapsed Coils of Conjugated Polymers: Effects of Solvent and Temperature. *Macromolecules* **2006,** *39* (3), 1165-1172.

Treat, N. D.; Brady, M. A.; Smith, G.; Toney, M. F.; Kramer, E. J.; Hawker, C. J.; Chabinyc, M. L., Interdiffusion of PCBM and P3HT Reveals Miscibility in a Photovoltaically Active Blend. *Advanced Energy Materials* **2011,** *1* (1), 82-89.

Urade, V. N.; Wei, T.-C.; Tate, M. P.; Kowalski, J. D.; Hillhouse, H. W., Nanofabrication of Double-Gyroid Thin Films. *Chemistry of Materials* **2007,** *19* (4), 768-777.

van Bavel, S.; Sourty, E.; de With, G.; Frolic, K.; Loos, J., Relation between Photoactive Layer Thickness, 3D Morphology, and Device Performance in P3HT/PCBM Bulk-Heterojunction Solar Cells. *Macromolecules* **2009,** *42* (19), 7396-7403.

Vanlaeke, P.; Swinnen, A.; Haeldermans, I.; Vanhoyland, G.; Aernouts, T.; Cheyns, D.; Deibel, C.; D'Haen, J.; Heremans, P.; Poortmans, J.; Manca, J. V., P3HT/PCBM bulk heterojunction solar cells: Relation between morphology and electro-optical characteristics. *Solar Energy Materials and Solar Cells* **2006,** *90* (14), 2150-2158.

Wang, P. S.; Lu, H. H.; Liu, C. Y.; Chen, S. A., Gel Formation via Physical Cross-Linking in the Soluble Conjugated Polymer, Poly[2-methoxy-5-(2-ethylhexyloxy)-1,4-phenylenevinylene], in Solution by Addition of Alkalies. *Macromolecules* **2008,** *41* (17), 6500-6504.

Weigandt, K. M.; Pozzo, D. C.; Porcar, L., Structure of high density fibrin networks probed with neutron scattering and rheology. *Soft Matter* **2009,** *5* (21), 4321-4330.

Wohrle, D.; Meissner, D., Organic Solar-Cells. *Advanced Materials* **1991,** *3* (3), 129-138.

Xin, H.; Kim, F. S.; Jenekhe, S. A., Highly Efficient Solar Cells Based on Poly(3-butylthiophene) Nanowires. *Journal of the American Chemical Society* **2008,** *130* (16), 5424-5425.

Xin, H.; Reid, O. G.; Ren, G.; Kim, F. S.; Ginger, D. S.; Jenekhe, S. A., Polymer Nanowire/Fullerene Bulk Heterojunction Solar Cells: How Nanostructure Determines Photovoltaic Properties. *ACS Nano* **2010,** *4* (4), 1861-1872.

Xing, K. Z.; Fahlman, M.; Chen, X. W.; Inganäs, O.; Salaneck, W. R., The electronic structure of poly(3,4-ethylene-dioxythiophene): studied by XPS and UPS. *Synthetic Metals* **1997,** *89* (3), 161-165.

Xu, W.; Li, L.; Tang, H.; Li, H.; Zhao, X.; Yang, X., Solvent-Induced Crystallization of Poly(3-dodecylthiophene): Morphology and Kinetics. *The Journal of Physical Chemistry B* **2011,** *115* (20), 6412-6420.

Xu, W.; Tang, H.; Lv, H.; Li, J.; Zhao, X.; Li, H.; Wang, N.; Yang, X., Sol-gel transition of poly(3-hexylthiophene) revealed by capillary measurements: phase behaviors, gelation kinetics and the formation mechanism. *Soft Matter* **2012,** *8* (3), 726-733.

Yang, H.; LeFevre, S. W.; Ryu, C. Y.; Bao, Z., Solubility-driven thin film structures of regioregular poly(3-hexyl thiophene) using volatile solvents. *Applied Physics Letters* **2007,** *90* (17), 661-665.

Yang, X. N.; Loos, J.; Veenstra, S. C.; Verhees, W. J. H.; Wienk, M. M.; Kroon, J. M.; Michels, M. A. J.; Janssen, R. A. J., Nanoscale morphology of high-performance polymer solar cells. *Nano Letters* **2005,** *5* (4), 579-583.

Yang, X.; Loos, J., Toward High-Performance Polymer Solar Cells: The Importance of Morphology Control. *Macromolecules* **2007,** *40* (5), 1353-1362.

Yao, Y.; Dong, H.; Hu, W., Ordering of conjugated polymer molecules: recent advances and perspectives. *Polymer Chemistry* **2013,** *4* (20), 5197-5205.

Yin, W.; Dadmun, M., A New Model for the Morphology of P3HT/PCBM Organic Photovoltaics from Small-Angle Neutron Scattering: Rivers and Streams. *ACS Nano* **2011,** *5* (6), 4756-4768.

Yokoyama, A.; Miyakoshi, R.; Yokozawa, T., Chain-Growth Polymerization for Poly(3-hexylthiophene) with a Defined Molecular Weight and a Low Polydispersity. *Macromolecules* **2004,** *37* (4), 1169-1171.

Yook, K. S.; Jeon, S. O.; Joo, C. W.; Lee, J. Y., Color stability and suppressed efficiency roll-off in white organic light-emitting diodes through management of interlayer and host properties. *Journal of Industrial and Engineering Chemistry* **2009,** *15* (3), 420-422.

Yoshino, K.; Love, P.; Onoda, M.; Sugimoto, R.-i., Dependence of Absorption Spectra and Solubility of Poly(3-alkylthiophene) on Molecular Structure of Solvent. *Japanese Journal of Applied Physics* **1988,** *27* (12), L2388-L2391.

Yu, G.; Gao, J.; Hummelen, J. C.; Wudl, F.; Heeger, A. J., Polymer Photovoltaic Cells - Enhanced Effciencies via a Network of Internal Donor-Acceptor Heterojunctions. *Science* **1995,** *270* (5243), 1789-1791.

Yu, G.; Heeger, A. J., Charge Sparation and Photovoltaic Conversion in Polymer Composites with Internal Donor-Acceptor Heterojunctions. *Journal of Applied Physics* **1995,** *78* (7), 4510-4515.

Yu, Z.; Fang, J.; Yan, H.; Zhang, Y.; Lu, K.; Wei, Z., Self-Assembly of Well-Defined Poly(3-hexylthiophene) Nanostructures toward the Structure–Property Relationship Determination of Polymer Solar Cells. *The Journal of Physical Chemistry C* **2012,** *116* (45), 23858-23863.

Zhang, S.; Marini, D. M.; Hwang, W.; Santoso, S., Design of nanostructured biological materials through self-assembly of peptides and proteins. *Current Opinion in Chemical Biology* **2002,** *6* (6), 865-871.

Zhang, Y.; Yip, H. L.; Acton, O.; Hau, S. K.; Huang, F.; Jen, A. K. Y., A Simple and Effective Way of Achieving Highly Efficient and Thermally Stable Bulk-Heterojunction Polymer Solar Cells Using Amorphous Fullerene Derivatives as Electron Acceptor. *Chemistry of Materials* **2009,** *21* (13), 2598-2600.

Zhao, J.; Swinnen, A.; Van Assche, G.; Manca, J.; Vanderzande, D.; Mele, B. V., Phase Diagram of P3HT/PCBM Blends and Its Implication for the Stability of Morphology. *The Journal of Physical Chemistry B* **2009,** *113* (6), 1587-1591.

Zhu, Z.; Wei, B.; Wang, J., Self-assembly of poly(3-hexylthiophene) nanowire networks by a mixed-solvent approach for organic field-effect transistors. *physica status solidi (RRL) – Rapid Research Letters* **2013,** *8* (3), 252-255.

Zuo, F.; Angelopoulos, M.; MacDiarmid, A. G.; Epstein, A. J., ac conductivity of emeraldine polymer. *Physical Review B* **1989,** *39* (6), 3570-3578.

Zuo, L.-J.; Hu, X.-L.; Ye, T.; Andersen, T. R.; Li, H.-Y.; Shi, M.-M.; Xu, M.; Ling, J.; Zheng, Q.; Xu, J.-T.; Bundgaard, E.; Krebs, F. C.; Chen, H.-Z., Effect of Solvent-Assisted Nanoscaled Organo-Gels on Morphology and Performance of Organic Solar Cells. *The Journal of Physical Chemistry C* **2012,** *116* (32), 16893-16900.

Curriculum Vitae

Dr. Gregory M. Newbloom

EDUCATION

University of Washington, Ph.D., Chemical Engineering June 2014
Thesis Title: Engineering the Multi-Length Scale Structure of Self-Assembled Conjugated Polymer Networks
Advisor: Prof. Lilo D. Pozzo

University of Washington, M.S., Chemical Engineering June 2011

Oregon State University, B.S., Chemical Engineering, *magna cum laude* June 2009

Awards/Honors

Soft Matter Award, AIChE National Conference MESD Poster Session (Nov. 2013)
2013 High Impact Publication Award, UW Dept. of Chemical Engineering (Oct. 2013)
American Chemical Society Excellence in Graduate Polymer Research Award (April 2013)
1st Place in the Society of Rheology Graduate Student/Post-Doc Poster Competition (Feb. 2013)
3rd Place in the UW Business Plan Competition (May 2011)
NSF Bioenergy IGERT Fellowship (Sept. 2010 – Sept. 2012)
NSF Bioenergy IGERT Associate (Jan. 2010 – Sept. 2010)
Outstanding AIChE Student Chapter (Nov. 2009)
NASA OSGC Undergraduate Scholar (Sept. 2007 – June 2008)
OSU Rieckmann Engineering Scholar (Sept. 2007 – June 2008)
OSU Diversity Scholar (Sept. 2005 – June 2009)
Clackamas County Community Service Award (May 2003)

RELEVANT EXPERIENCE

PolyDrop, LLC, Seattle, WA
CTO/co-Founder May 2013 - Present

- Start-up company founded on ideas, processes and patents developed in my thesis research
- Responsible for technical aspects of product development including product research and design, scale-up, and cost analysis
- Participated in writing Phase I NSF STTR funding application *(funded FY2014)*
- Led a team to the Rice Business Plan Competition with a Top 30 finish (out of > 500 teams) and a $15k cash prize.

University of Washington, Dept. of Chemical Engineering, Seattle, WA

Graduate Research Assistant Sept. 2009 – June 2014

- Studied the self-assembly of conjugated polymers towards designing interconnected mechanical and electrical network structures for organic electronics
- Developed multi-length scale structure-property relationships for conjugated polymers
- Designed, tested and utilized a novel experimental environment to study developing nanostructure and conductivity simultaneously
- Mentored 6 undergraduate researchers on independent research projects

Teaching Assistant Sept. 2013 – Dec. 2014

- Taught 1 lecture for a class of 30 undergraduate students
- Led and instructed students through laboratory experiments
- Created rubric for grading of lab reports and quizzes

NSF IGERT Bioenergy Fellow Jan. 2010 – June 2011

- Designed, constructed, evaluated and submitted patent application for a mobile pyrolysis blanket for on-site conversion of wasted woody biomass (i.e. slash) to biochar
- Successfully pyrolyzed 250 lbs of biomass while establishing principles for scalability
- Took 3rd place in the UW Business Plan Competition
- Resulted in a spin-off company (Carbon Cultures) that is now selling commercial products

The Boeing Company, Chemical Technologies, Seattle, WA

Summer Intern July 2013 – Oct. 2013

- Invented a new process for the large area deposition of durable superhydrophobic & icephobic coatings
    - Invention disclosure currently being evaluated for patent
- Developed a novel microindentation theory for rapid characterization of ductility and fracturing behavior in thermal spray coatings
- Expanded team research capabilities to include the use of thermoplastic polymers and polymer composites in thermal spray processes

Research Contractor June 2012 – Dec. 2012

- Invented and submitted patent application for a new metal oxide crystallization process
- Engineered functional hybrid photovoltaic devices based around a novel processing idea
- Improved device efficiency by two orders of magnitude through morphology optimization
- Expanded project scope to include new materials that led to beneficial device properties

Oregon State University, Department of Chemical Engineering, Corvallis, OR

Undergraduate Research Assistant Mar. 2009 – June 2009

- Tuned the rheological properties of a hydrogel composite to match the human nucleus pulposus for the purpose of developing an injectable spinal disc replacement
- Developed a rapid gelation process for uniform fiber dispersion within the matrix

Boise Cascade Inc., Paper Manufacturing, St. Helens, OR
Process Engineering Co-op June 2008 – Sept. 2008

- Evaluated and tuned process operating conditions resulting in material and energy savings
- Discovered and initiated a product development change worth $60k annually
- Initiated collaborations with additional Boise paper mills for new product trials
- Proposed an overhaul of an exhaust system for $1.5 million in energy savings (2 year ROI)

NASA Goddard Space Flight Center, Materials Division, Greenbelt, MD
Undergraduate Researcher & Project Manager June 2007 – Dec. 2008

- Studied the mechanical properties and failure mechanisms of polymer-nanotube composites processed in large batches; towards developing light-weight, space-rated materials
- Created a new research collaboration with materials team during following year at OSU

Portland State University, Physics Department, Portland, OR
Undergraduate Research Assistant June 2006 – Sept. 2006

- Optimized the growth and uniformity of carbon nanotube bundles for use in electronic circuits

PUBLICATIONS

1. **Newbloom, G. M.**, Hoffmann, S. M., West, A. F., Gile, M. C., Rice, A. H., Luscombe, C. K., Pfaendtner, J., Pozzo, L. D., "Solvatochromism and Conformational Changes in Fully Dissolved Poly(3-alkylthiophenes)" In preparation, available on request.
2. **Newbloom, G. M.**[*], de la Iglesia, P.[*], Pozzo, L. D, "Controlled Gelation of Poly(3-alkylthiophene)s in Bulk and Thin Film Environments Using Low Volatility Solvent/Poor-Solvent Mixtures" Submitted for Publication in Soft Matter. [*]Co-authors
3. **Newbloom, G. M.**, Ranade, A. N., Matos, M. A., Pozzo, L. D., "Porous Poly(3-hexylthiophene Networks with Conformal Zinc Oxide Coatings for Hybrid Photovoltaic Devices", Submitted for Publication in Synthetic Metals.
4. **Newbloom, G. M.**[*], Weigandt K. M.[*], Pozzo, D. C., "Structure and Property Development of Poly(3-hexylthiophene) Organogels Probed with Combined Rheology, Conductivity and Small Angle Neutron Scattering", Soft Matter, 2012, 8 (34), pp. 8854-8864. [*]Co-authors
5. **Newbloom, G. M.**[*], Weigandt, K. M.[*], Pozzo, D. C., "Electrical, Mechanical and Structural Characterization of Self-Assembly in Poly(3-hexylthiophene) Organogel Networks", Macromolecules, 2012, 45 (8), pp. 3452-3462. [*]Co-authors
6. **Newbloom, G. M.**, Kim, F. S., Jenekhe, S. A., Pozzo, D. C., "Mesoscale Morphology and Charge Transport in Colloidal Networks of Poly(3-hexylthiophene)", Macromolecules, 2011, 44 (10), pp. 3801-3809.

PATENT APPLICATIONS

1. Pozzo, D. C., **Newbloom, G. M.**, 2013, "Nano-composites Incorporating Conductive Polymer Networks", US Patent Application 2013034835, Filed 4/01/2013, *Patent Pending*.
2. **Newbloom, G. M.**, Ranade, A. N., Matos, M. A., 2013, "Low Temperature, Thin Film Crystallization Method and Products Prepared Therefrom", US Patent Application 2013121230, Filed 3/15/2013, *Patent Pending*.
3. Faires, K., Schwartz, D. T., **Newbloom, G. M.**, Richards, J. J., Noon, M. S., Knoth, J. L., 2012, "Blanket for Pyrolysis or Drying of Biomass", US Patent Application 2012037829, Filed 5/14/2012, *Patent Pending*.

PRESENTATIONS

1. **Newbloom, G. M.**, de la Iglesia, P., Pozzo, D. C., "Controlled Gelation of Poly(3-alkylthiophene)s in Bulk and Thin Film Environments Using Low Volatility Solvent/Non-Solvent Mixtures" American Institute of Chemical Engineering National Conference, Nov. 2013, *Poster. (Soft Matter Award)*
2. **Newbloom, G. M.**, Pozzo, D. C., "Engineering the Multi-Length Scale Structure of Conjugated Polymer Networks for Enhanced Charge Transport in Organic Photovoltaics" American Chemical Society National Conference, Apr. 2013, *Award Presentation*.
3. **Newbloom, G. M.**, Weignadt, K. M., De La Iglesia, P., Pozzo, D. C., "Self-Assembly and Gelation of Conjugated Polymers Toward Enhancing Charge Transport in Organic Photovoltaics" Society of Rheology Annual Meeting, Feb. 2013, *Presentation.*
4. **Newbloom, G. M.**, Weignadt, K. M., Richards, J. R., De La Iglesia, P., Pozzo, D. C., "Enhanced Charge Transport through Engineering the Network Structure of Conjugated Polymers for Photovoltaic Applications" Society of Rheology Annual Meeting, Feb. 2013, *Poster. (1st Place in Competition)*
5. **Newbloom, G. M.**, Weignadt, K. M., Pozzo, D. C., "In Situ Structural, Mechanical and Electrical Property Development During the Self-Assembly of Conjugated Polymer Organogels" American Institute of Chemical Engineering National Conference, Oct. 2012, *Presentation.*
6. **Newbloom, G. M.,** Weigandt, K. M., Pozzo, D. C., "Structure and Property Development of Poly(3-hexylthiophene) Organogels Probed with Combined Rheology, Conductivity and Small Angle Neutron Scattering" American Institute of Chemical Engineering National Conference, Oct. 2012, *Poster.*
7. **Newbloom, G. M.,** Matos, M. A., Ranade, A. N., Boeing Research and Technology, Technology Review, Sept. 2012, Presentation. (*Proprietary*)
8. **Newbloom, G. M.**, Weigandt, K. M., Pozzo, D. C., "In Situ Structural, Mechanical and Electrical Property Development during the Self-Assembly of Conjugated Polymer Organogels", UW Chemical Engineering Graduate Student Symposium, Sept. 2012, *Poster.*
9. **Newbloom, G. M.**, Weigandt, K. M., De La Iglesia, P., Richards, J. R., Pozzo, D. C., "Structure and Property Development of Poly(3-hexylthiophene) Organogels Probed with Combined Rheology, Condutivity and Small Angle Neutron Scattering", ORCAS International Conference on Energy Conversion, Sept. 2012, *Poster.*

10. **Newbloom, G. M.**, Weigandt, K. M., De La Iglesia, P., Richards, J. R., Pozzo, D. C., "Structure and Property Development of Poly(3-hexylthiophene) Organogels Probed with Combined Rheology, Condutivity and Small Angle Neutron Scattering", American Conference on Neutron Scattering, Jun. 2012, *Poster.*
11. **Newbloom, G. M.**, Weigandt, K. M., De La Iglesia, P., Pozzo, D. C., "Engineering Networks of Conjugated Polymers", Oak Ridge National Lab SNS & HFIR User Group Conference, Nov. 2011, *Poster.*
12. **Newbloom, G. M.**, Weigandt, K. M., Pozzo, D. C., "Structure-Property Relationships in Conjugated Polymers", UW Chemical Engineering Graduate Student Symposium, Oct. 2011, *Poster.*
13. **Newbloom, G. M.**, Weigandt, K. M., Pozzo, D. C., "Structure-Property Relationships in Conjugated Polymers", NNIN Nanotechnology at the UW, Sept. 2011, *Poster.*
14. **Newbloom, G. M.**, Pozzo, D. C., "Morphology and Characterization of Colloidal Conjugated Polymer Networks", American Chemical Society Northwest Regional Conference, June 2011, *Presentation.*
15. **Newbloom, G. M.**, Weigandt, K. M., Pozzo, D. C., "Structure-Property Relationships in Conjugated Polymers", American Chemical Society Northwest Regional Conference, June 2011, *Poster.*
16. **Newbloom, G. M.**, Weigandt, K. M., Pozzo, D. C., "Structure-Property Relationships in Organogels of Conjugated Polymers", American Chemical Society Colloids and Interfaces Conference, June 2011, *Presentation.*
17. **Newbloom, G. M.**, Weigandt, K. M., Pozzo, D. C., "SANS Investigation of Fiber Networks for Determination of Structure Property Relationships", NIST Center for Neutron Scattering Panel Assessment Meeting, Mar. 2011, *Poster.*
18. **Newbloom, G. M.**, Pozzo, D. C., "Spontaneous Formation of Colloidal Networks for Poly(3-hexylthiophene Dispersed in Aromatic Solvents", UW Chemical Engineering Graduate Student Symposium, Oct. 2010, *Poster.*
19. **Newbloom, G. M.**, Pozzo, D. C., "Spontaneous Formation of Colloidal Networks for Poly(3-hexylthiophene Dispersed in Aromatic Solvents", ORCAS International Conference on Energy Conversion, Sept. 2010, *Poster.*
20. **Newbloom, G. M.**, Powell, D., "Cross-linked Oriented Nanocomposite Extrusion", AIChE Pacific Northwest Regional Student Conference, May 2009, *Presentation.*

LEADERSHIP POSITIONS

Director & Teacher, Calvary Chapel High School Ministry	Aug. 2011 – June 2014
Outreach Director, UW Chem. Eng. Graduate Students	June 2010 – June 2011
President, OSU AIChE Student Chapter	June 2008 – June 2009
President, Suburban Collegiate Ministries	June 2008 – June 2009
Business Manager, OSU AIChE Student Chapter	Sept. 2006 – June 2008

TECHNICAL SKILLS

Expert – Small Angle X-ray Scattering (SAXS), Small Angle Neutron Scattering (SANS), UV-VIS-NIR Absorption Spectroscopy, Transmission Electron Microscopy (TEM), Scanning Electron Microscopy (SEM), Wet Chemistry, Instrumented Indentation

Proficient – Rheology, Dielectric/Impedance/Admittance Spectroscopy, Thermogravimetric Analysis (TGA), Dynamic Light Scattering (DLS), Static Light Scattering (SLS), Bomb Calorimetry, Thermal Spray Technology, Goniometry, Tensiometry

Familiar – Differential Scanning Calorimetry (DSC), Gel Permeation Chromatography (GPC), X-ray diffraction (XRD), Atomic Force Microscopy (AFM), Photolithography, Chemical Vapor Deposition (CVD), Plasma Enhanced Chemical Vapor Deposition (PECVD), X-ray photoelectron spectroscopy (XPS), Field Emission Microscopy, Nanoparticle Synthesis, Cyclic Voltammetry